



HAL
open science

Visible-Light Photocatalysis Promoted by Solid-and Liquid-Phase Immobilized Transition Metal Complexes in Organic Synthesis

Alexei Yakushev, Anton S. Abel, Alexei D. Averin, Irina P. Beletskaya,
Andrey V. Cheprakov, Ilia S. Ziankou, Laurent Bonneviot, Alla G.
Bessmertnykh-Lemeune

► **To cite this version:**

Alexei Yakushev, Anton S. Abel, Alexei D. Averin, Irina P. Beletskaya, Andrey V. Cheprakov, et al.. Visible-Light Photocatalysis Promoted by Solid-and Liquid-Phase Immobilized Transition Metal Complexes in Organic Synthesis. *Coordination Chemistry Reviews*, 2022, 458, pp.214331. 10.1016/j.ccr.2021.214331 . hal-03759523

HAL Id: hal-03759523

<https://hal.science/hal-03759523v1>

Submitted on 24 Aug 2022

HAL is a multi-disciplinary open access archive for the deposit and dissemination of scientific research documents, whether they are published or not. The documents may come from teaching and research institutions in France or abroad, or from public or private research centers.

L'archive ouverte pluridisciplinaire **HAL**, est destinée au dépôt et à la diffusion de documents scientifiques de niveau recherche, publiés ou non, émanant des établissements d'enseignement et de recherche français ou étrangers, des laboratoires publics ou privés.

Visible-Light Photocatalysis Promoted by Solid- and Liquid-Phase Immobilized Transition Metal Complexes in Organic Synthesis

Alexei A. Yakushev,^[a] Anton S. Abel,^{[a]*} Alexei D. Averin,^[a,b] Irina P. Beletskaya,^{[a,b]*} Andrey V. Cheprakov,^[a] Iliia S. Ziankou,^[a] Laurent Bonneviot,^[c] and Alla Bessmertnykh-Lemeune^{[c]*}

[a] Lomonosov Moscow State University, Department of Chemistry, 1-3, Leninskie Gory, Moscow, 119991, Russia. E-mail: antonabel@list.ru

[b] Frumkin Institute of Physical Chemistry and Electrochemistry, Russian Academy of Sciences, Leninsky Pr. 31, Moscow, 119071, Russia. E-mail: beletska@org.chem.msu.ru

[c] ENS de Lyon, UMR 5182, CNRS, Université Claude Bernard Lyon 1, Laboratoire de Chimie, 69342 Lyon, France. E-mail: alla.lemeune@ens-lyon.fr

Abstract

This review summarizes synthetic approaches to reusable photocatalytic systems based on visible light-active transition metal complexes with chelating ligands containing pyridyl residues such as 2,2'-bipyridines, 1,10-phenanthrolines, 2,2':6',2''-terpyridines and related ligands. The use of these materials in organic synthesis is then discussed focusing on 1) most active systems exhibiting a synergy effect between photophysical properties of immobilized complexes and photoactive solid supports and 2) the possibility of repeated uses of the developed catalytic system.

Keywords

photoactive metal complex; reusable catalyst; visible light-driven catalysis; functional material; photoredox catalyst; sustainable organic reaction

Content

1. Introduction
2. Synthesis of immobilized photocatalytic systems
 - 2.1 Immobilization on solid supports
 - 2.2 Supramolecular assembling
 - 2.3 Phase-separable systems
3. Application in photocatalytic reactions
 - 3.1 Oxidative reactions
 - 3.2 Non-redox reactions
 - 3.3 Reductive reactions
 - 3.4 Cocatalyzed transformations
 - 3.5 Continuous flow reactions
 - 3.6 Photoelectrochemical reactions
4. Conclusions
5. Acknowledgments
6. Abbreviations

1. Introduction

Sunlight is currently regarded as the most attractive, abundant, renewable but still under-used source of energy in many practical fields including organic chemistry and industrial manufacture of fine chemicals. Since the beginning of chemistry, scholars inspired by natural processes have been indeed interested to use light as an energy source in organic compound preparation

procedures [1]. Yet, only in this century have we witnessed a new era of organic photochemistry pioneered by Yoon's, Stephenson's and MacMillan's groups research on the photoredox catalysis [2-4]. In contrast to the reactions performed under high energy UV light, these processes do not need specific equipment and, being optimized, proceed selectively affording the target products in good or high yields. These fundamental contributions have encouraged many researchers to focus studies on visible light-driven organic transformations [5-9]. During the last decade, many radical reactions that previously required harsh reaction conditions and/or toxic reagents have been revisited and performed under mild conditions.

To perform these visible light-driven organic reactions, photocatalysts are commonly required since most of organic compounds do not absorb light in the visible region. The addition of an appropriate photosensitizer enables visible light to effect a single-electron or energy transfer to an organic molecule that can initiate many synthetically valuable transformations. Many organic dyes or Visible light-Active Transition Metal (Ru^{II} , Ir^{III} , Re^{II} , Os^{II} , Fe^{II} , Co^{II} and Pt^{II}) complexes with chelating ligands containing PYridyl residues such as 2,2'-bipyridines (bpy), 1,10-phenanthrolines (phen), 2,2':6',2''-terpyridines (tpy) (VATMPY complexes) are now used as photocatalysts for various homogeneous organic reactions. Among these photoactive compounds, $[\text{Ru}(\text{bpy})_3]^{2+}$ and $\text{Ir}(\text{ppy})_3$ (ppy = 2-(pyridin-2-yl- κN)phenyl- κC) complexes and their derivatives are undoubtedly the most extensively studied and powerful homogeneous photocatalysts due to their high brightness, long lifetimes and rich redox chemistry of the $^3\text{MLCT}$ (metal-to-ligand charge transfer) excited states allowing switch between oxidative or reductive quenching cycles in accordance with a given reaction [10]. However, their use in organic synthesis is limited by concerns about contamination of products by toxic metals and inability to recycle and reuse these expensive photocatalysts. It is therefore an important economic and ecological objective to develop immobilized VATMPY complexes which can be easily recovered and reused.

This review summarizes the state of art in this hot and multidisciplinary topic. Some classes of immobilized VATMPY photocatalysts, in particular, metal organic frameworks (MOFs) and covalent organic polymers (COPs) have been reviewed recently [11-14]. However, to our knowledge, a comprehensive and systematic examination of most immobilization methods and their influence on photocatalytic properties of complexes is not yet available. Our review summarizes these methods focusing on materials developed for organic synthesis *per se*. Accordingly, we will not treat those of the immobilized VATMPY complexes designed for light harvesting in dye-sensitized solar-cells (DSSC), for photodegradation of toxic organic compounds, or for chemical energy storage using for instance water oxidation, hydrogen production or carbon dioxide depletion [15-21]. Our review is divided in two parts. First, the synthesis of reusable photocatalytic systems is discussed. Next, the applications of solid- and liquid-phase immobilized photocatalysts in organic synthesis are reviewed, focusing on 1) the most active systems that exhibit a synergy effect between photophysical properties of VATMPY complexes and photoactive solid supports and 2) examples of repeated uses of the developed catalytic systems. Most of immobilization methods reported in this review were developed during the last decade.

2. Synthesis of immobilized photocatalytic systems

To obtain reusable photocatalysts for organic synthesis transition metal complexes can be either immobilized on a variety of solid supports, or incorporated in supramolecular systems, or transformed into amphiphilic or other specific derivatives compatible with liquid-liquid phase-separation conditions. Such photocatalytic systems may present noticeable advantages compared to those operating under homogeneous conditions. Tuning the environment in the vicinity of the photocatalytic centers allows for a better control of the reaction efficiency and selectivity.

Indeed, polarity and porosity of solid supports may affect elementary steps involved in a catalytic process such as light adsorption, energy transfer, generation of redox intermediates, and adsorption-desorption equilibria of substrates, intermediates and final products. The functionalization of the genuine photosensitizer and spatial separation of the catalytic centers after the immobilization may improve both their photostability and decrease the self-quenching process. Furthermore, such photocatalytic systems can be used in those solvents where the complexes *per se* are insoluble or inactive rendering the photocatalyst easier to handle and to recover.

2.1 Immobilization on solid supports

VATMPY complexes immobilized on solid supports can be subdivided according either to the type of interaction with the hosting matrix or to the type of experimental protocols being either direct or stepwise or by the kind of support chosen for the immobilization (Table1).

In terms of bond strength between a photocatalytic site and a solid support, these materials can be formed by either weak interactions such as van der Waals forces and hydrogen bonding or weak electrostatic interactions (class I hybrids) or strong coordinative or covalent bonding (class II hybrids) [22].

There are three experimental strategies for preparing heterogenized photocatalysts: 1) immobilization of stable Ru^{II} and Ir^{III} complexes *per se* (most general approach); 2) inversed procedure involving the complexation of metal ions to immobilized ligands (this approach can deliver higher catalyst loading or help to avoid a difficult introduction of anchoring group in the target complex); 3) a two-step procedure based on the encapsulation of metal salts into a porous zeolite support followed by the complexation of bpy ligands to encapsulated metal ions [23-25].

Though it could be useful to arrange the subject matter according to the means of immobilization in the discussion of material preparation, we have chosen a more straightforward classification based on the nature of supports used that is more convenient for the following discussion of their catalytic properties.

Clay minerals

Among various layered inorganic materials, clay minerals have attracted a special attention as inorganic supports for guest molecules due to their 2D network structure exhibiting cation-exchange properties [26]. Surprisingly, the clay-based materials for photocatalytic applications were scarcely studied.

Yamagishi and coworkers incorporated chiral Δ -[Ru(bpy)₃](ClO₄)₂, Δ - and Λ -[Ru(phen)₃](ClO₄)₂ complexes into montmorillonite clay. They were interested to examine the generation of enantioselectivity in chemical reactions by using weak interactions (dipole–charge, π – π , and van der Waals interactions) between a substrate and a photocatalyst when steric constraints are imposed by a solid support [27]. Functionalized materials Δ -[Ru(bpy)₃]²⁺/MM and Λ -, Δ - Ru(phen)₃²⁺/MM were prepared by stirring solutions of optically active complexes and sodium montmorillonite for 24 h. According to XRD analysis of dispersions of these solids, the Ru^{II}-modified montmorillonite clays are exfoliated to single-layered materials in aqueous media. Therefore, the photochemical reactions occur on an external surface of the material and not in the interlayer spaces.

Table 1. Classification of synthetic approaches to heterogenized VATMPY catalysts.

Support	Immobilization of VATMPY complex		Immobilization of the ligand followed by the complexation
	Chemisorption (class I hybrids)	Coordinative or covalent bonding <i>via</i> anchoring group (class II hybrids)	Covalent bonding <i>via</i> anchoring group (class II hybrids)
Zeolite	[Ru(bpy) ₃] ²⁺ /M ⁺ -Y[25, 28]		
Clay	Δ-[Ru(bpy) ₃] ²⁺ /MM[27] Λ-, Δ- Ru(phen) ₃ ²⁺ /MM[27]		
Silica	[Ru(bpy) ₃] ²⁺ /SiO ₂ [29] [Ru(bpy) ₃] ²⁺ /SiO ₂ -NP[30] [Ru(bpy) ₃] ²⁺ /Ag@SiO ₂ [30] [Ru(bpy) ₃] ²⁺ /Au@SiO ₂ [30] [Ru(bpy) ₃] ²⁺ /MCM-41[31]	[Ru(bpy) ₂ (abpy)] ²⁺ /SiO ₂ -mNP[32] [Ir(ppy) ₂ (vbpy)] ⁺ /MCF[33] [Pt(tpy-1)L ₁] ⁺ /SiO ₂ -XG[34] [Ru(2Si-bpy) ₃] ²⁺ /POS[35]	[Pt(pbp)L] ⁺ /SBA-15[36] [Pt(pbp)L] ⁺ /MCM-41[36] [Pt(tpy)L] ⁺ /MCM-41 [37, 38] [Pt(tpy)L] ⁺ /SBA-15[37, 38] [Pt(tpy)L] ⁺ /MCM-48[37, 38] Ir(mebib)(ppy)L/MCM-41[39] Ir(mebib)(ppy)L/MCM-48[39] Ir(mebib)(ppy)L/SBA-15[39]
Titania	N3/DegP25[40]	[Ru(bpy) ₂ (4dpbpy)] ²⁺ & /BuPO ₃ /TiO ₂ FTO[41-43] [Ru(bpy) ₂ (4dpbpy)] ²⁺ /TiO ₂ FTO[43] [Ru(bpy) ₂ (4dcbpy)] ²⁺ /TiO ₂ FTO[44] [Ru(bpy) ₂ (4dpbpy)] ²⁺ & [Ru(mebimpy) ₂ (4dpmbpy)] ²⁺ /TiO ₂ FTO[45] [Ru(bpy) ₂ (4dpbpy)] ²⁺ & [Ru(mebimpy) ₂ (4dpmbpy)] ²⁺ /TiO ₂ &SI FTO[46]	[Ru ₃ (bpy) ₅ (bpy) ₂] ⁶⁺ /TiO ₂ -NP[47]
GW		[Ru(bpy) ₂ (dppa)] ²⁺ /GW[48] [Ru(phen) ₂ (dppa)] ²⁺ /GW[48]	
GO	[Fe(bpy) ₃] ²⁺ /rGO[49] [Ru(bpy) ₃] ²⁺ /SO ₃ -rGO[50]		
Carbon nitrides	[Fe(bpy) ₃] ²⁺ /npg-C ₃ N ₄ [51] [Ru(bpy) ₃] ²⁺ /g-C ₃ N ₄ [52] [Ru(bpy) ₃] ²⁺ /M ⁺ @nano-C ₃ N ₄ [52]	[Co(bpy) ₂ (Het)N ₃] ⁺ /npg-C ₃ N ₄ [53]	
MOF	[Ru(bpy) ₃] ²⁺ /PCN-99[54] [Ru(bpy) ₃] ²⁺ /InBTB[55] [Ru(phen) ₃] ²⁺ /InBTB[55] [Ru(bpz) ₃] ²⁺ /InBTB[55] [Ru(bpy) ₃] ²⁺ /NPF-201[56] [Ru(bpy) ₃] ²⁺ /PCN-608-SBDC[57] [Ru(bpy) ₃] ²⁺ /MIL-125-NH ₂ [58] [Ru(bpy) ₃] ²⁺ /FJI[59] [Ru(bpy) ₃] ²⁺ /NKMOF-4[31] [Ru(bpy) ₃] ²⁺ /NKMOF-5[31] [Ru(bpy) ₃] ²⁺ /NKMOF-6[31] [Ru(bpy) ₃] ²⁺ /NKMOF-7[31] [Ru(Phphen) ₃] ²⁺ /NKMOF-4[31] Ir(ppy) ₃ /NKMOF-4[31]	[Ru(bpy) ₂ (5dcbpy)] ²⁺ /UiO-67 [60-63] [Ir(ppy) ₂ (5dcbpy)] ⁺ /UiO-67[60] [Ir(F-ppy) ₂ (dbbpy)] ⁺ & Ni(dbbpy)Cl ₂ /Zr ₁₂ -MOF[64] [Ru(bpy) ₂ (5dcbpy)] ²⁺ /UiO-67 & TiO ₂ FTO [65]	[Ru(bpy) ₂ (5dcbpy)] ²⁺ /UiO-67 [63] [Ir(ppy) ₂ (5dcbpy)] ⁺ /UiO-67[66] [Ir(F-ppy) ₂ (5dcbpy)] ⁺ /UiO-67[66] [Ir(F-ppy) ₂ (dbbpy)] ⁺ & Ni(dbbpy)Cl ₂ /Zr ₁₂ -MOF[64]
MOL		[Ir(F-ppy) ₂ (dbbpy)] ⁺ /Hf ₁₂ -OTf-MOL[67]	[Ru(bpy) ₂ (bpya)] ²⁺ /Zr-MOL[68]
Polymer	[Ru(bpy) ₃] ²⁺ /Amb15[50] [Pt(qpy)] ²⁺ /Nafion[69] [Pt(tpy-2)L ₂] ⁺ /Nafion[70] [Ru(bpy) ₃] ²⁺ & Pyc/Nafion[71] Ru(bpy) ₃ ²⁺ /Nf/SiO ₂ [72]	Pt(pbp-1)L ₃ /PS[34] [Ir(vppy) ₂ (d ^b bbpy)] ⁺ /PMA-1[74] [Ir(F-ppy) ₂ (cbpy)] ⁺ /NPS[75] [Ru(4debpy) ₂ (bpy)] ²⁺ /COP-1[76] [Ru(5debpy) ₂ (bpy)] ²⁺ /COP-1[76]	[Ir(ppy) ₂ (py) ₂] ⁺ /PS[84, 85] [Ru(bpy) ₂ (phim)] ⁺ /COP-8[86] [Ru(bpy) ₂ (bdp)] ⁺ /COP-10[87] [Ru(bpy) ₃] ²⁺ /hHPGE-PFPPN[88]

[Ru(bpy)₃]²⁺/COP-11 [73]	Ir(<i>ptppc-H</i>)₃/COP-2 [77] Ir(<i>mtpcc</i>)₃/COP-2 [77] [Ir(<i>ptppc-H</i>)₂(bpy)]⁺/COP-3 [78] [Ir(<i>ptppc-F</i>)₂(bpy)]⁺/COP-3 [78] [Ru(bpy)₃]²⁺/COP-4 [79] [Ir(ppy)₂(bpy)]⁺/COP-4 [79] [Ir(bpppy)₂(d^hbbpy)]⁺/COP-5 [80] [Ir(bbppy)₂(d^hbbpy)]⁺/COP-5 [80] [Ru(bpppy)₂(bpy)]²⁺/COP-5 [81] [Ru(bbppy)₂(bpy)]²⁺/COP-5 [81] [Ru(bpy)₂(5debpy)]²⁺/COP-6 [82] [Ir(ppy)₂(5debpy)]⁺/COP-6 [82] [Ru(bpy)₃]²⁺/COP-7 [83]
SOF	[Ru(bpy)₂(mhppy)]²⁺/SOF-1 [89] [Ru(2pbpy)₃]²⁺/SOF-2 [90]

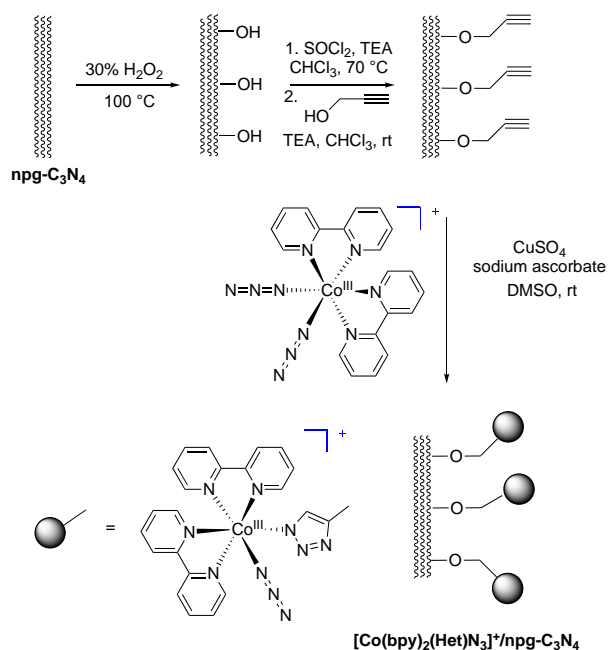
^a **Fe(bpy)₃]²⁺/Mⁿ⁺-Y** (n = 1,2) [23,24] and **[Ru(bpy)₃]²⁺/Mⁿ⁺-Y** [25] were obtained by encapsulation of the metal ions in zeolite pores followed by the complexation of bpy ligand.

Functionalization of nanostructured carbon nitrides

Nanostructured carbon nitrides (CNs) of general formula C₃N₄ exhibit semiconductor properties and can be used as photocatalysts [91]. Such materials can be prepared as one-dimensional nanorods, two-dimensional nanosheets, and three-dimensional mesoporous structures by varying synthetic strategies such as hard/soft templating, exfoliation or solvothermal synthesis [91,92]. However, all these photocatalysts are less effective as compared to other inorganic semiconductors due to their low adsorption coefficients, relatively small specific surface areas and high recombination rates of photogenerated electron-hole pairs [91,92]. To improve their catalytic properties in photoreactions these semiconductors could be functionalized by visible light-active species as, for example, VATMPY complexes. On the other hand, immobilization of metal complexes on photoactive supports not only render their recovery and recycling feasible but also can enhance their photocatalytic efficiency.

Jain and coworkers showed that strong π - π interactions between bpy molecules and the solid support allow for efficient adsorption of [Fe(bpy)₃](PF₆)₂ on the surface of nanoporous graphitic carbon nitride (npg-C₃N₄) from THF solution [51]. According to SEM images, the material **[Fe(bpy)₃]²⁺/npg-C₃N₄** (0.56 wt% of Fe) thus obtained is composed of crumpled and folded thin sheets. The high resolution XPS spectrum confirms that iron retains the +2 oxidation state in this non-porous composite.

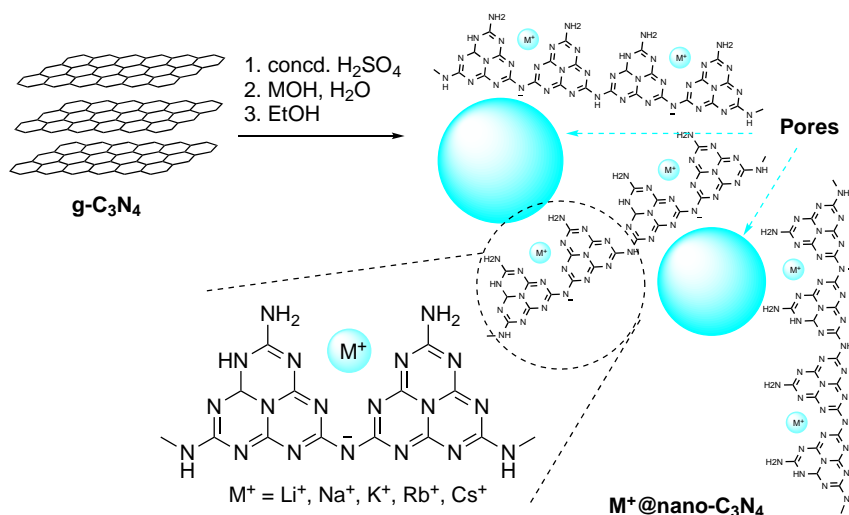
Adsorption of [Co(bpy)₂(N₃)₂]Cl on npg-C₃N₄ affords a functionalized material containing only 0.24 wt% of Co [53]. To increase the loading of Co^{III} complex, the surface of npg-C₃N₄ should be activated, for example, by treatment with hydrogen peroxide. Covalent bonding of [Co(bpy)₂(N₃)₂]Cl to this support bearing hydroxyl groups on the surface was achieved through the copper-catalyzed alkyne-azide cycloaddition reaction after a preliminary treatment of the support by thionyl chloride and propargyl alcohol consecutively (Scheme 1).



Scheme 1. Synthesis of $[\text{Co}(\text{bpy})_2(\text{Het})\text{N}_3]^+/\text{np-g-C}_3\text{N}_4$.

Using this synthetic procedure the material $[\text{Co}(\text{bpy})_2(\text{Het})\text{N}_3]^+/\text{np-g-C}_3\text{N}_4$ with specific surface area of $28 \text{ m}^2 \text{ g}^{-1}$ was obtained and Co content in the material increased up to 1.2 wt%. The +3 oxidation state of cobalt in the solid was confirmed by XPS analysis.

Yamashita and coworkers proposed another approach to increase stability and surface area of $\text{g-C}_3\text{N}_4$ -based photocatalysts, which consisted of the exfoliation of $\text{g-C}_3\text{N}_4$ in concentrated sulfuric acid followed by the neutralization of the solution by alkali metal hydroxides (Scheme 2) [52].



Scheme 2. Synthesis of $\text{M}^+@\text{nano-C}_3\text{N}_4$.

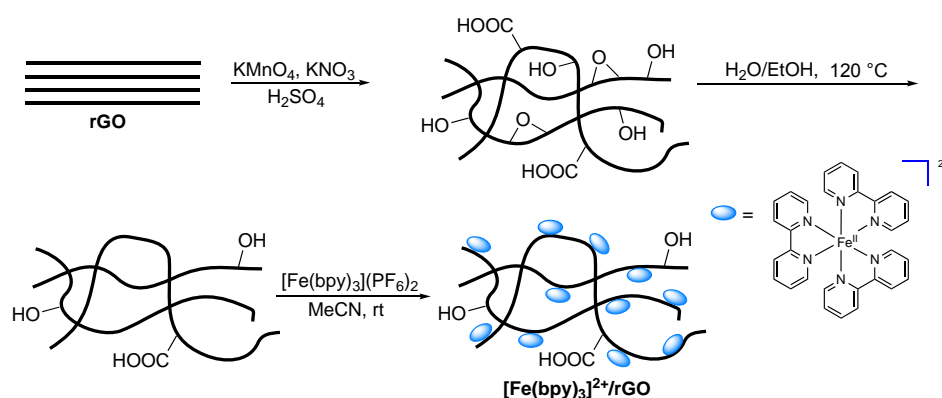
Specific surface areas of materials thus prepared were in the range $135\text{--}170 \text{ m}^2 \text{ g}^{-1}$. Moreover, by varying alkali hydroxides used in the neutralization step, different alkali metal ions ($\text{M}^+ = \text{Li}^+, \text{Na}^+, \text{K}^+, \text{Rb}^+, \text{and Cs}^+$) could be incorporated in C_3N_4 sheets. The treatment of these materials with aqueous solution of $[\text{Ru}(\text{bpy})_3]\text{Cl}_2$ afforded photocatalysts

$[\text{Ru}(\text{bpy})_3]^{2+}/\text{M}^+\text{@nano-C}_3\text{N}_4$ with low loading of the catalytic sites. XANES spectra of these materials revealed an octahedral coordination mode of the ruthenium atoms in all materials. The position of the edge jump was systematically shifted indicating that the electron density of the Ru^{II} species increased when the alkali metal cations varied from Li^+ to Cs^+ . The luminescence of the $[\text{Ru}(\text{bpy})_3]^{2+}/\text{M}^+\text{@nano-C}_3\text{N}_4$ materials was in average about twice as higher as that of $[\text{Ru}(\text{bpy})_3]^{2+}/\text{g-C}_3\text{N}_4$ being only slightly dependent on the alkali metal ion. This enhancement was ascribed to the suppression of self-quenching in these materials displaying a better spatial separation of photoactive species on the $\text{M}^+\text{@nano-C}_3\text{N}_4$ sheets, which exhibit higher specific surface areas as compared to $\text{g-C}_3\text{N}_4$. The increase of luminescence intensity and a small blue shift (from 611 to 604 nm) of the emission maxima on going from Cs^+ to Li^+ in this series probably results from the enhancement of π - π interactions between Ru^{II} complexes and the $\text{M}^+\text{@nano-C}_3\text{N}_4$ supports modified by alkali metal ions of smaller size.

Graphene-supported complexes

Photoactive graphene has attracted considerable interest as a support to prepare composite photocatalysts owing to an advantageous combination of optical, mechanical, thermal, and conductive properties [93]. As in the case of carbon nitrides, many studies are focused on developing heterogenized photocatalysts with large surface areas.

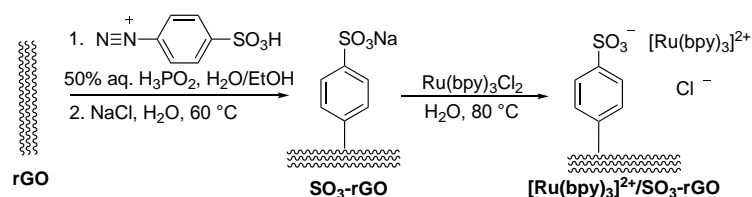
Jain and coworkers prepared reduced graphene oxide (rGO) samples for the immobilization of iron(II) complex $[\text{Fe}(\text{bpy})_3](\text{PF}_6)_2$ (Scheme 3) [49]. First, exfoliated graphene oxide (GO) was obtained by the oxidation of graphite with KMnO_4 in sulfuric acid. This harsh oxidation allowed to introduce oxygen-containing functional groups on the graphite surface and facilitated the separation of graphite sheets. The presence of hydroxy, carboxy, ether groups and epoxide residues on the surface of GO with a specific surface area of $87 \text{ m}^2 \text{ g}^{-1}$ was confirmed by FT-IR and XPS analysis. Then GO thus prepared was treated with ethanol and water at 120°C in autoclave to obtain reduced samples (rGO). This non-selective reduction increases the degree of aromaticity of the sheets but induces a decrease of their specific surface areas to $32 \text{ m}^2 \text{ g}^{-1}$. Finally, the iron(II) complex was immobilized on the surface of these rGO sheets affording a photocatalyst, in which weak π - π interactions of bpy ligands and rGO sheets are believed to serve as the anchoring force.



Scheme 3. Synthesis of $[\text{Fe}(\text{bpy})_3]^{2+}/\text{rGO}$.

Zhang, Li and coworkers proposed another approach for the immobilization of $[\text{Ru}(\text{bpy})_3]\text{Cl}_2$ on the surface of rGO [50]. After reduction of GO by sodium borohydride in water at 90°C to rGO, they treated these samples with 4-sulfonatobenzenediazotium in water/ethanol mixture in the presence of phosphinic acid to prepare rGO functionalized by sulfonate groups (Scheme 4). After ion exchange with aqueous NaCl , sodium ions were

exchanged with the positively charged ruthenium(II) complex in water at 80 °C. Only 27% of reactive sites on the folded surface of rGO were functionalized by Ru^{II} complex likely due to their low accessibility for bulky Ru^{II} species. The FT-IR and XPS spectra of **[Ru(bpy)₃]²⁺/SO₃-rGO** thus obtained confirmed the presence of Ru^{II} complex with sulfonate counterions in this composite material while Raman spectrum and TEM images proved that the graphene sheets were preserved during the immobilization process. The energy-dispersive X-ray spectrometry (EDX) mapping demonstrated uniform distribution of Ru^{II} ions on the surface of the SO₃-rGO sheets with the specific surface area of 125 m² g⁻¹. It is worth noting that the surface area of this material is higher compared to that of **[Ru(bpy)₃]²⁺/rGO** probably due to the presence of the voluminous phenylsulfonate anion.



Scheme 4. Synthesis of **[Ru(bpy)₃]²⁺/SO₃-rGO**.

Inclusion of VATMPY complexes in zeolite pores

Zeolites are crystalline aluminosilicates of general formula $M_{2/n}O \cdot Al_2O_3 \cdot xSiO_2 \cdot yH_2O$, where M is usually a cation belonging to the group IA and IIA and n is the charge of this cation. The 3D-structure is composed of AlO_4 and SiO_4 tetrahedra, which are linked together through oxygen atoms so producing a three dimensional framework containing regular channels and cavities of nano-sized dimensions. As each aluminum-containing tetrahedron incorporated into the framework bears a negative charge, charge-compensation cations are present in the cage cavities and channels. These cations are capable of ion-exchange, e.g. with positively charged VATMPY complexes. The position, size and number (which depend on the Si/Al ratio) of the exchanged species affect the properties of resulting materials and expected content of catalytic centers, which may be loaded into the solid zeolite material.

Zeolites are commonly considered as catalytic microreactors since they exhibit high thermal stability, large internal specific surface area, well-defined and rigid structure [94]. Unfortunately, most of thermally stable zeolites are microporous solids that can induce specific limitations due to a low availability of small pores for bulky substrates.

Though various zeolites are in plenty, only few of them are really popular, and faujasite zeolites Y took the largest share in the preparation of photocatalysts. Yamashita and coworkers encapsulated metal ions in the pores of zeolite Y using $FeCl_2 \cdot 4H_2O$ [23, 24] or $[Ru(NH_3)_6]Cl_3$ [25] as cation sources and then performed the complexation reaction in zeolite pores by adding bpy ligand. This two-step procedure allows to reach high and uniform loading of catalytic $[Fe(bpy)_3]^{2+}$ or $[Ru(bpy)_3]^{2+}$ centers, respectively, in the zeolite cavities. Moreover, the series of materials with various nanoscale environment surrounding the catalytic centers were prepared by exchanging the genuine extra-framework Na^+ cations of zeolite Y by other alkali (M^+) or alkaline earth (M^{2+}) cations. The range of the transition metal content in the materials **[Fe(bpy)₃]²⁺/Mⁿ⁺-Y** and **[Ru(bpy)₃]²⁺/Mⁿ⁺-Y** thus obtained varied from 0.015 to 0.021 and 0.013 to 0.017 mmol g⁻¹, respectively. Increasing the size of the alkali metal cations led to a decrease in Brunauer-Emmett-Teller (BET) surface area of the materials.

The materials thus prepared allow for studies of confinement effects of the host zeolite on the physicochemical properties of encapsulated $[Ru(bpy)_3]^{2+}$ and $[Fe(bpy)_3]^{2+}$ because the size of the complexes (~1.2 nm in diameter) is very close to that of the zeolite Y supercage (~1.3 nm in

diameter). Electronic charge transfer from the basic zeolite framework to the complex induced electronic changes in these encapsulated species. Moreover, it was demonstrated that alkali or the alkali-earth extra-framework cations systematically altered the electronic density on the Ru and Fe atoms, geometric parameters of the encapsulated complexes and their light absorption and emission properties. For example, the larger is the accompanying extra-framework cation M^{n+} , the smaller is the Met–N distance (Met = Ru²⁺ or Fe²⁺) in the encapsulated complex. Noteworthy, the photocatalytic activities of the complexes in the oxidation reactions are also dependent on extra-framework cations M^{n+} (see below).

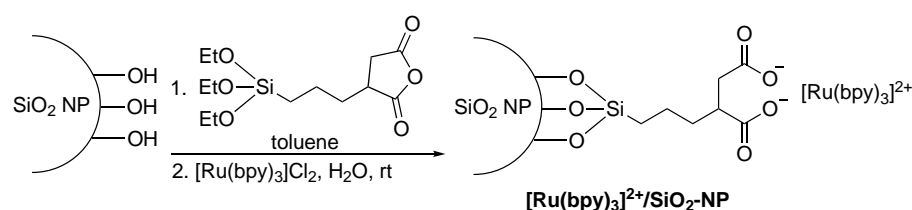
It was also reported that the $[Ru(bpy)_3]^{2+}/Na^+-Y$ can be obtained through the impregnation of $[Ru(bpy)_3]^{2+}$ in zeolite Y [28]. However, entrapping of large $[Ru(bpy)_3]^{2+}$ complex within the zeolite cavities accessible through windows (~1.0 nm in diameter) smaller in size than the complex was not proved by structural studies. It seems that in this material $[Ru(bpy)_3]^{2+}$ ions are located only on the external surface of zeolite Y because the exchange with extra-framework cations through the zeolite lattice apertures is sterically hindered.

Porous silica-based photocatalytic systems

Silica (SiO₂) xerogels have attracted considerable attention in the development of heterogenized photosensitizers [14]. This is mainly due to favorable combination of properties such as transparency to visible light, high specific surface areas, availability of ordered mesoporous (2–50 nm) forms and commercial availability of these supports. Moreover, many synthetic procedures developed for anchoring organic molecules can be easily applied to the immobilization of stable photoactive transition metal complexes. Many hybrid materials belonging both to class I and II materials were thus successfully prepared for catalytic tests (Table 1).

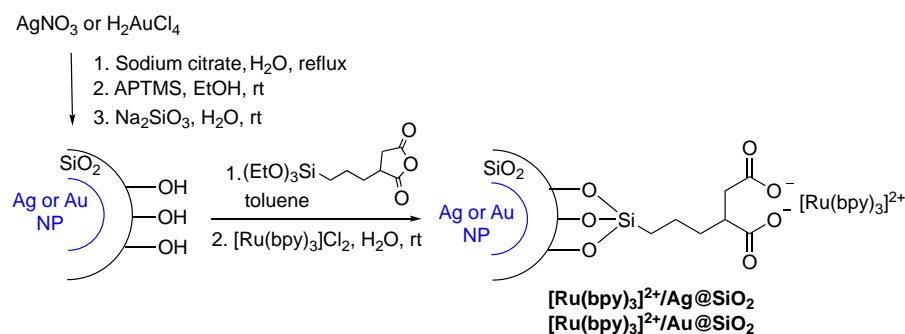
Reusable photocatalysts can be obtained by the direct adsorption of VATMPY complexes on a polar silica surface. Amara and coworkers prepared a $[Ru(bpy)_3]Cl_2$ -functionalized silica $[Ru(bpy)_3]^{2+}/SiO_2$ with catalyst loading of 16 mg g⁻¹ by the adsorption of $[Ru(bpy)_3]Cl_2$ on commercial silica xerogels consisting of 35–70 μm particles exhibiting specific surface areas of 500 m² g⁻¹ (Macherey Nagel) [29]. The adsorption of the complex is believed to be mainly driven by electrostatic interactions because catalyst loading was decreased when the process was performed below the silica isoelectric point (pH < 3.0). Hybrid materials prepared through such non-covalent immobilization of functional molecules on silica surfaces are commonly prone to leaching of guests in solution. However, $[Ru(bpy)_3]^{2+}/SiO_2$ appeared to be quite stable, even after washing several times with polar solvents such as water or ethanol/water solvent mixture due to effective interactions of positively charged species with the negatively charge polar support.

Electrostatic interactions between a VATMPY complex and a silica support can be increased by changing silanol groups on the silica surface by negatively charged carboxylates. To this end, Yamashita and coworkers functionalized spherical silica nanoparticles (NPs) synthesized by Stöber method [95] with (3-(triethoxysilyl)propyl)succinic acid anhydride (Scheme 5) [30]. After hydrolysis of the anhydride to dicarboxylic acid, the negatively charged NPs were obtained and treated with $[Ru(bpy)_3]^{2+}$ to prepare material $[Ru(bpy)_3]^{2+}/SiO_2-NP$.

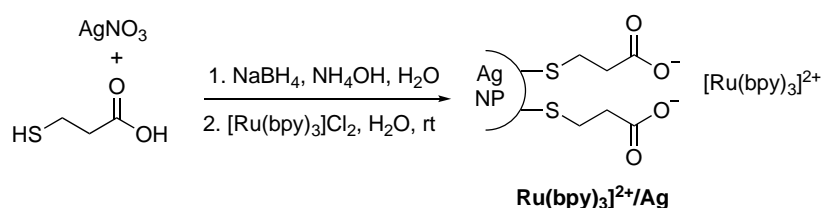


Scheme 5. Preparation of $[\text{Ru}(\text{bpy})_3]^{2+}/\text{SiO}_2\text{-NP}$.

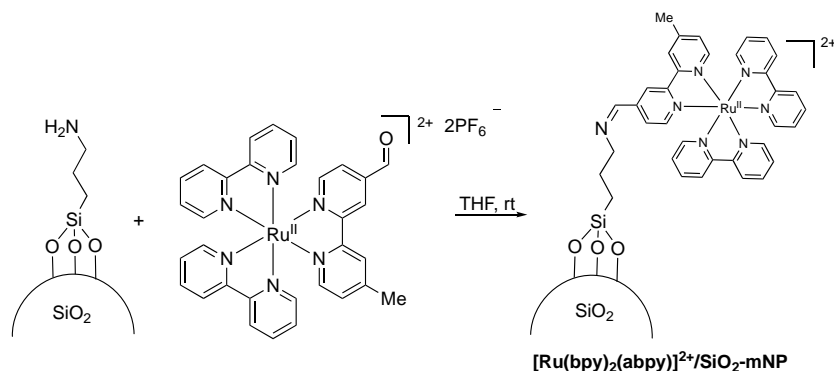
Using this synthetic approach, $[\text{Ru}(\text{bpy})_3]^{2+}$ was also immobilized on the surface of Ag and Au NPs coated with a thin silica shell (Scheme 6) [30]. Ag and Au NPs stabilized by (3-aminopropyl)trimethoxysilane (APTMS) were protected with a SiO_2 thin layer (2–3 nm) by reacting the NPs with sodium silicate. The core-shell nanospheres thus prepared were functionalized with [3-(triethoxysilyl)propyl]succinic acid anhydride. The anhydride groups were subsequently hydrolyzed and functionalized with positively charged $[\text{Ru}(\text{bpy})_3]^{2+}$ species. The structure of $[\text{Ru}(\text{bpy})_3]^{2+}/\text{Ag@SiO}_2$ and $[\text{Ru}(\text{bpy})_3]^{2+}/\text{Au@SiO}_2$ (0.05% Ru) was confirmed by XRD, XAFS and HRTEM techniques.

**Scheme 6.** Synthesis of $[\text{Ru}(\text{bpy})_3]^{2+}/\text{Ag@SiO}_2$ and $[\text{Ru}(\text{bpy})_3]^{2+}/\text{Au@SiO}_2$.

Phosphorescence of the complexes grafted on these NPs was higher compared to that of $[\text{Ru}(\text{bpy})_3]^{2+}$ -modified silica NPs $[\text{Ru}(\text{bpy})_3]^{2+}/\text{SiO}_2\text{-NP}$ probably due to localized surface plasmon resonance effect of metal nanoparticles. The emission intensity of functionalized Ag-NPs was higher compared to that of Au-NPs and roughly twice that of $[\text{Ru}(\text{bpy})_3]^{2+}/\text{SiO}_2\text{-NP}$. In contrast, when $[\text{Ru}(\text{bpy})_3]^{2+}$ was directly anchored on the surface of Ag NPs as shown in Scheme 7, the phosphorescence of the Ru^{II} complex was strongly quenched *via* energy transfer to the core of Ag NPs [30].

**Scheme 7.** Synthesis of $[\text{Ru}(\text{bpy})_3]^{2+}/\text{Ag}$.

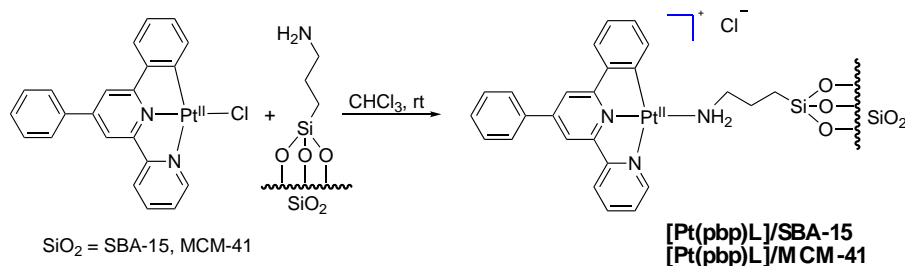
Covalent binding ensures a strong linkage between VATMPY complexes and a silica surface but it requires the ligand functionalization by anchoring groups. Huang and coworkers have immobilized $[\text{Ru}(\text{bpy})_2(\text{abpy})](\text{PF}_6)_2$ (abpy = 4-formyl-4'-methyl-2,2'-bipyridine) complex bearing a formyl-substituted bpy ligand onto mesoporous spherical silica NPs (Scheme 8) [32]. The silica NPs with an average diameter of approximately 100 nm were firstly treated with APTMS to cover the surface by reactive amino groups suitable for anchoring the formyl-functionalized Ru^{II} complex. The immobilization of the complex was performed in THF at room temperature affording the hybrid material $[\text{Ru}(\text{bpy})_2(\text{abpy})]^{2+}/\text{SiO}_2\text{-mNP}$ with catalyst loading of 0.11 mmol g⁻¹.



Scheme 8. Synthesis of $[\text{Ru}(\text{bpy})_2(\text{abpy})]^{2+}/\text{SiO}_2\text{-mNP}$.

Periodic mesoporous silicas are characterized by the presence of *ordered* mesopores (1.5–40 nm) with amorphous silica pore walls and large specific surface areas of ca. $1000 \text{ m}^2 \text{ g}^{-1}$. Among the most cited are MCM-41 and SBA-15, which are composed of a regular hexagonal array of one-dimensional pores, the diameter of which can be varied typically from 2 to 30 nm. In the former, the channel-like pores are altogether not connected while in the latter the longitudinal pores are linked by occasional side channels, which size depends on the temperature of the synthesis. Much less popular is the more elaborate but less readily available MCM-48 material consisting of a uniform array of 3D-connected tubular pores, much better suited for intra-pore molecular transport. Using these diverse silica supports one can explore the effect of nanoconfinement on photophysical and catalytic properties of VATMPY complexes.

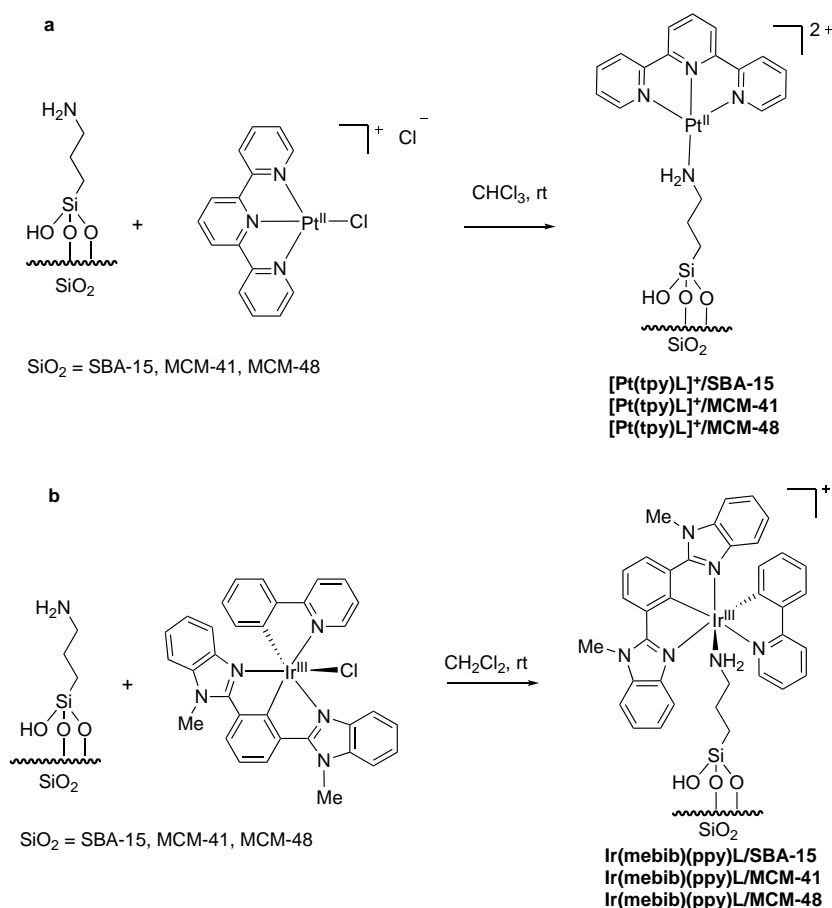
Several synthetic approaches to such hybrid materials were reported by Yamashita's group. First, cyclometalated platinum(II) complex $\text{Pt}(\text{pbp})\text{Cl}$ ($\text{pbp} = 4\text{-phenyl-2-[6-(pyridin-2-yl-}\kappa\text{N)-pyridin-2-yl-}\kappa\text{N)]phenyl-}\kappa\text{C}$) was incorporated into APTES-modified SBA-15 (pore size varied from 2.4 to 13 nm) and MCM-41 silicas by the ligand exchange reaction as shown in Scheme 9 [36].



Scheme 9. Synthesis of $[\text{Pt}(\text{pbp})\text{L}]/\text{SBA-15}$ and $[\text{Pt}(\text{pbp})\text{L}]/\text{MCM-41}$.

The loading of the complex was varied from 0.21 to 12.3 wt% by adapting the reagent amounts. The emission maximum ($\lambda_{\text{em}} = 547 \text{ nm}$) and lifetime ($1.49 \mu\text{s}$) of the complex grafted on the SBA-15 surface (3.3 wt% of $[\text{Pt}(\text{pbp})\text{Cl}]$) were found to be similar to those of $[\text{Pt}(\text{pbp})\text{NH}_2\text{tBu}]\text{ClO}_4$ ($\lambda_{\text{em}} = 547 \text{ nm}$, $\tau = 1.0 \mu\text{s}$) in acetonitrile solution.

The ligand exchange strategy was also used for anchoring $[\text{Pt}(\text{tpy})\text{Cl}]\text{Cl}$ and $[\text{Ir}(\text{mebib})(\text{ppy})\text{Cl}]$ ($\text{mebib} = 2,6\text{-bis}(N\text{-methylbenzimidazol-2-yl})\text{pyridine}$, $\text{ppy} = 2\text{-(2-pyridinyl-}\kappa\text{N)}\text{phenyl-}\kappa\text{C}$) on MCM-41, SBA-15 and MCM-48 silicas (Scheme 10).



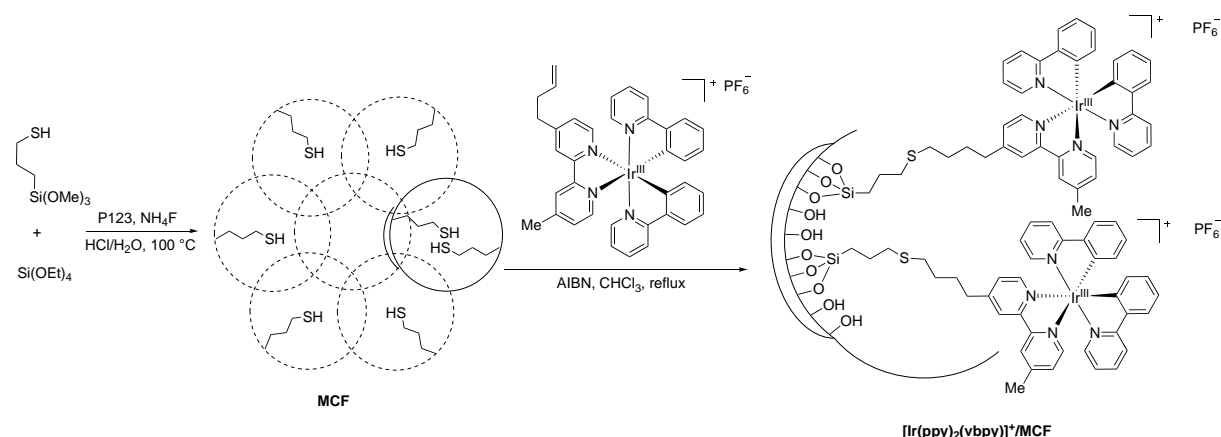
Scheme 10. Anchoring of [Pt(tpy)Cl]Cl (a) and Ir(mebib)(ppy)Cl (b) on the surfaces of MCM-41, SBA-15 and MCM-48.

In this case, APTMS-modified MCM-41 and SBA-15 silicas were treated with [Pt(tpy)Cl]Cl [37,38] or Ir(mebib)(ppy)Cl [39] to obtain materials containing 0.4 wt% of Pt or Ir, respectively. Loading of [Pt(tpy)Cl]Cl on APTMS-modified MCM-48 varied from 0.2 wt% to 1.24 wt% of Pt. The Pt–N and Ir–N bond formation was confirmed by X-ray absorption measurements for all materials thus prepared.

The heterogenized platinum(II) complex **[Pt(tpy)L]⁺** exhibits strong photoluminescence attributed to ligand-centered (³LC) and/or metal-to-ligand charge transfer (³MLCT) transitions. The emission intensity is increased in the order of **[Pt(tpy)L]⁺/MCM-41 < [Pt(tpy)L]⁺/SBA-15 < [Pt(tpy)L]⁺/MCM-48**. In the case of MCM-48-supported complexes, the highest emission intensity was observed for the material containing 0.42 wt% of Pt because further increasing the complex content led to luminescence quenching and appearance of an additional emission band attributed to metal-metal-to-ligand charge-transfer (³MMLCT) transition typically observed in aggregated Pt complexes [38]. The aggregates were also observed by XANES owing to the appearance of the peak corresponding to short non-covalent Pt^{II}–Pt interactions. It is also worth noting that the average Pt–N distances in these hybrids were systematically shortened with the increase of Pt loading. This likely suggests that Pt complexes may undergo slight structural distortions within silica channels due to steric constraints.

The anchored iridium(III) complex was also emissive and displayed 530-nm emission maximum assigned to ³MLCT transitions in all silica-supported complexes. Interestingly, the emission intensity of the solids is increased in a different order (**Ir(mebib)(ppy)L/MCM-41 < Ir(mebib)(ppy)L/MCM-48 < Ir(mebib)(ppy)L/SBA-15**) being the highest for the SBA-15-grafted complex.

Zhang and coworkers proposed mesoporous cellular silica foams (MCFs) as supports for heterogenization of photosensitizers (Scheme 11) [33].

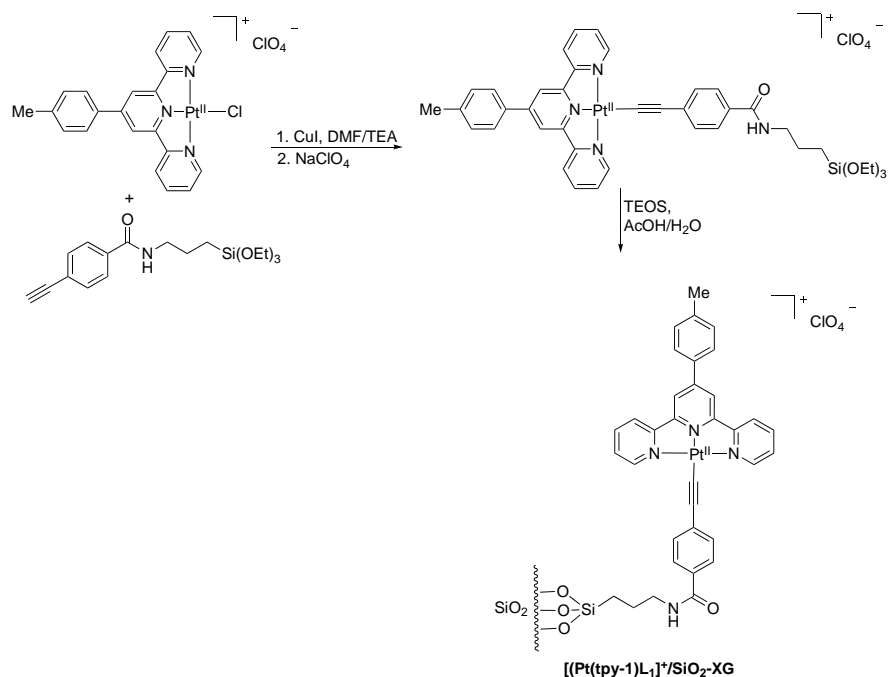


Scheme 11. Preparation of MCFs functionalized by cyclometalated iridium(III) complex $[\text{Ir}(\text{ppy})_2(\text{vbpy})]^+$.

MCFs are highly porous silicas exhibiting specific surface areas up to $1000 \text{ m}^2 \text{ g}^{-1}$ and having an aerogel-like 3D pore system composed of interconnected wide spherical voids. The MCFs average pore size is in the range of 5–50 nm and can be controlled by changing sol-gel process conditions. Moreover, during their synthesis MCFs can be functionalized by appropriate linkers using organic additives. For example, using P123 surfactant and 3-mercaptopropyltrimethoxysilane, it was possible to prepare thiol-functionalized monocellular silica foams (SH-MCFs) involving 3.8–7.4 wt% of S in thiol groups. The Brunauer–Emmett–Teller (BET) surface area, window pore sizes and pore volumes of these materials were gradually decreased with the increase of the thiol-linker content.

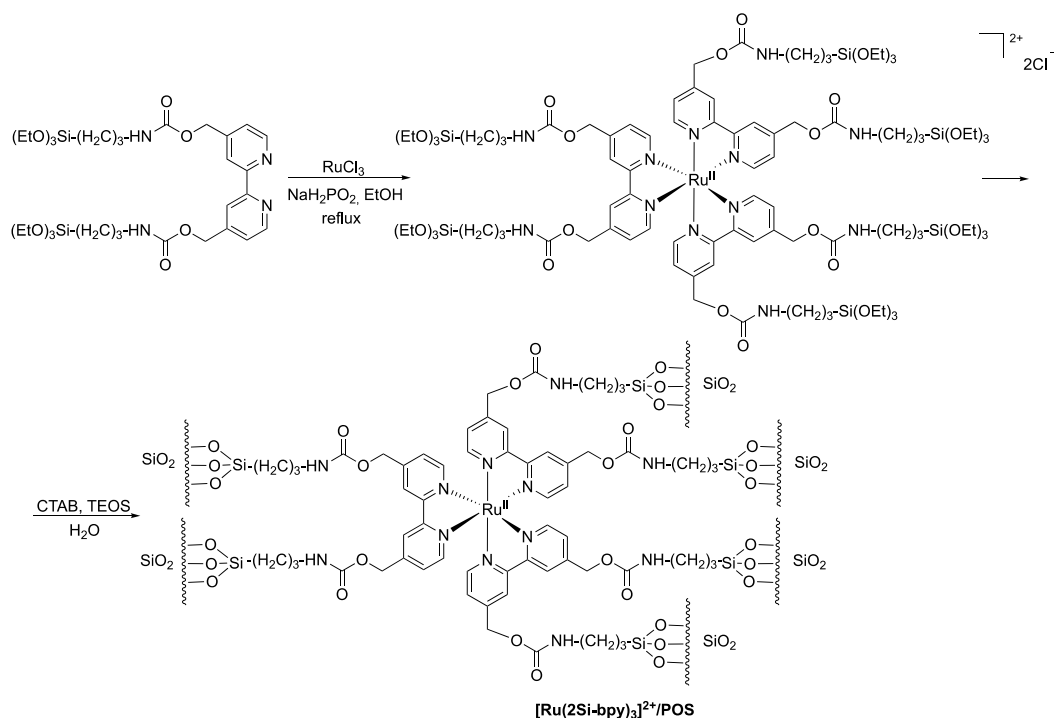
The material with BET surface area of $429 \text{ m}^2 \text{ g}^{-1}$ and charged with 5.3 wt% of S was used as a support to prepare a photoactive material using the thiol-ene coupling reaction with cyclometalated iridium(III) complex $[\text{Ir}(\text{ppy})_2(\text{vbpy})]\text{PF}_6$ (vbpy = 4-(but-3-en-1-yl)-4'-methyl-2,2'-bipyridine) bearing the butenyl-tagged bpy ligand. This coupling reaction afforded $[\text{Ir}(\text{ppy})_2(\text{vbpy})]^+/\text{MCF}$ material with BET surface area of $355 \text{ m}^2 \text{ g}^{-1}$ and pore volume of $0.94 \text{ cm}^3 \text{ g}^{-1}$ containing 0.14 mmol g^{-1} of Ir. Disordered mesoporous structure of this foam-like hybrid was proven by TEM images.

VATMPY complexes can also be incorporated in silica matrices using one-pot sol-gel processes, *i. e.* reacting triethoxysilyl-tethered complexes with tetraalkoxysilanes. This synthetic approach provides a uniform distribution of the catalytic centers in the solid matrices. The structure of functionalized xerogels thus prepared can be tuned varying the structural parameters of transition metal complexes. When complexes with one anchoring group are used in these sol-gel processes, catalytic centers are located in the pores as in case of the above discussed materials prepared through functionalization of pre-formed silica supports. This strategy was used by Wu and coworkers who first prepared platinum(II) complex with 4'-(4-methylphenyl)-2,2':6',2''-terpyridine and a monodentate ligand bearing anchoring triethoxysilyl group ($\text{Pt}(\text{tpy-1})\text{L}_1$) according to the ligand exchange reaction as shown in Scheme 12 [34]. This complex was further reacted with TEOS in aqueous acetic acid to obtain the porous $[\text{Pt}(\text{tpy-1})\text{L}_1]^+/\text{SiO}_2\text{-XG}$ material.



Scheme 12. Synthesis of $[\text{Pt}(\text{tpy-1})\text{L}_1]^+/\text{SiO}_2\text{-XG}$.

Bhaumik, Zhao and coworkers prepared complex $[\text{Ru}(\text{2Si-bpy})_3]^{2+}$ (2Si-bpy = [2,2'-bipyridine]-4,4'-diylbis(methylene) bis[3-(triethoxysilyl)propyl]carbamate) with six trialkoxysilyl groups by the complexation of Ru^{II} ions to a disilylated bpy ligand as shown in Scheme 13 [35]. This complex was reacted with tetraethyl orthosilicate in the presence of cetyltrimethylammonium bromide (CTAB) in water to obtain $[\text{Ru}(\text{2Si-bpy})_3]^{2+}/\text{POS}$ material in which catalytic centers are located in the amorphous silica walls.



Scheme 13. Synthesis of $[\text{Ru}(\text{2Si-bpy})_3]^{2+}/\text{POS}$.

Xerogels of this type possess high chemical stability due to multiple binding of each catalytic center to inorganic supports. The BET surface area of this material was $620 \text{ m}^2 \text{ g}^{-1}$ and the large hysteresis in the high-pressure region of its N_2 adsorption isotherm was attributed to the presence of non-uniform pores. In addition, HRTEM images of $[\text{Ru}(\text{2Si-bpy})_3]^{2+}/\text{POS}$ proved the presence of porous channels with diameters of 3–4 nm distributed homogeneously in the solid.

TiO₂-supported VATMPY complexes

Immobilization of Ru^{II} photoredox catalysts on titania supports takes advantage of a more mature level of expertise achieved in developing technology for the fabrication of photoanodes required by dye-sensitized solar cells (DSSC) and dye-sensitized photoelectrosynthesis cells (DSPECs) [15-21].

DSPECs were introduced with a specific goal to utilize solar energy for preparation of solar fuel but recently their application was extended to perform photoelectrosynthesis of some organic compounds. In DSPECs, a chemical reaction is initiated at photoanode after its visible-light irradiation causing a photo-excitation of absorbed dye molecules (Figure 1).

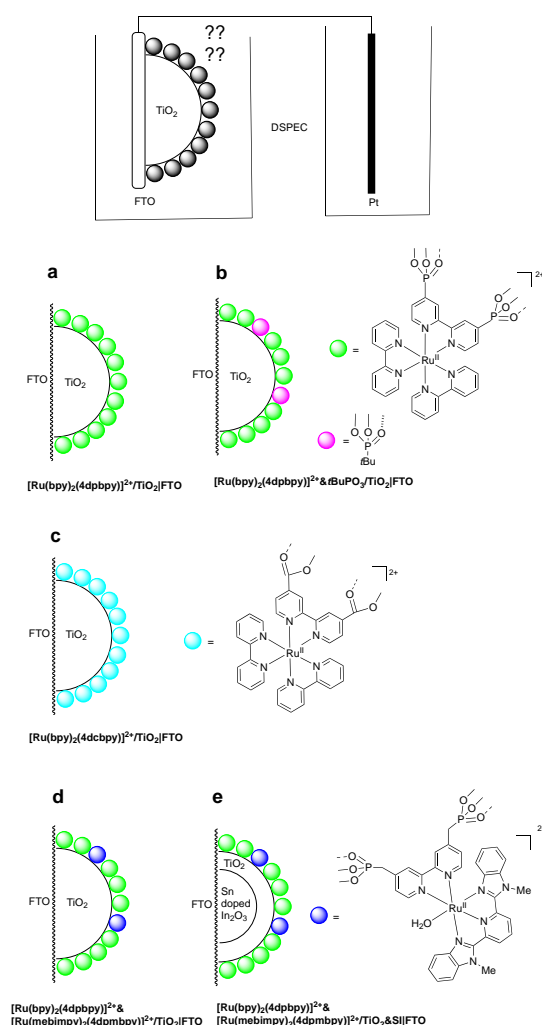


Figure 1. Various photoanodes for organic synthesis in DSPECs (only one TiO_2 nanoparticle of mesoporous nanostructured films is shown).

Then injection of excited electrons into the conduction band of semiconductor is followed by the activation of a redox catalyst through electron transfer. This intermediate species can be involved in a dark catalytic process affording solar fuels or target organic compounds.

Molecular materials for DSSCs and DSPECs are commonly prepared by anchoring a photosensitizer or both a photosensitizer and a transition metal catalyst on wide band gap n-type semiconductors covered by a porous TiO₂ thin film. Ru^{II} polypyridine complexes have been regarded for a long time as dominant chromophores for these devices despite their lower visible light absorptivity as compared to other important but less photostable chromophores. Thus, immobilization of Ru^{II} complexes on photoanodes has been widely explored and particular attention has been paid to the development of anchoring groups providing high stability and efficiency of these light-harvesting devices [96]. Nevertheless, most of such photoanodes has not been yet evaluated for their efficiency in any organic reactions and so far DSPECs for organic synthesis are limited to only a few examples.

In the simplest DSPEC photoanodes, the surface of photoelectrode was modified by only Ru^{II} photosensitizer and the second catalyst was dissolved in the solution environment [41-44]. Photoanodes of this type were obtained adapting the method developed by Grätzel and coworkers for the preparation of DSSC photoelectrodes (Figure 1a) [97]. First, a mesoporous film of TiO₂ nanoparticles was formed on the surface of fluorine-doped tin oxide (FTO) slide [41-44]. Ruthenium(II) complex [Ru(bpy)₂(4dpbpy)]²⁺ (4dpbpy = 2,2'-bipyridine-4,4'-diylidiphosphonic acid) bearing two phosphonate anchoring groups was further prepared [41-43]. Soaking the TiO₂/FTO slide in 150 μM solution of [Ru(bpy)₂(4dpbpy)]²⁺ in a 0.1 M HClO₄ allows for strong binding of the complex on the slide surface through the formation of stable Ti–O(P) bonds. To decrease the reverse electron transfer reactions, the surface of [Ru(bpy)₂(4dpbpy)]²⁺/TiO₂/FTO photoanode was protected by *tert*-butylphosphonic acid (Figure 1b) using a similar soaking procedure [43].

Alternatively, ruthenium(II) complex [Ru(bpy)₂(4dcbpy)]²⁺ (4dcbpy = 4,4'-dicarboxy-2,2'-bipyridine) bearing two carboxylate anchoring groups can be used as a precursor for photoanodes. This complex was deposited on a TiO₂-covered FTO slide according to a similar procedure but using acetonitrile as solvent (Figure 1c) [44].

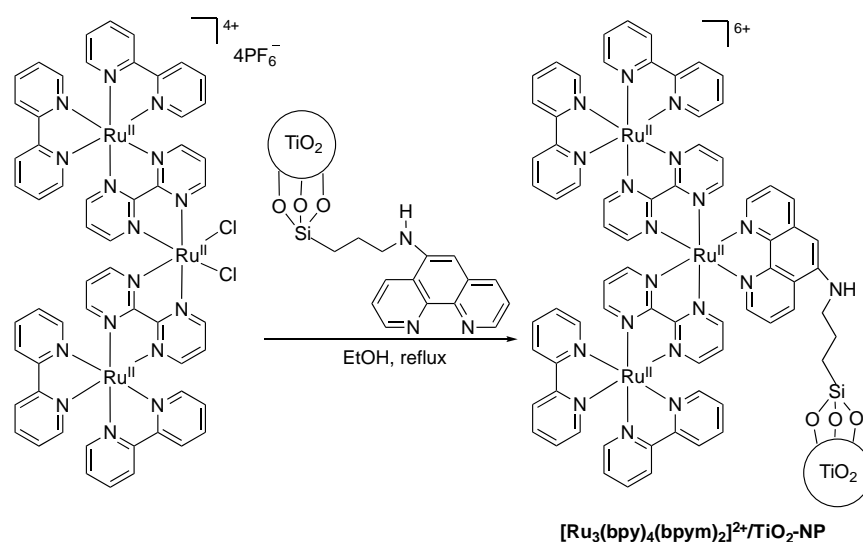
Meyer and coworkers prepared photoanodes for the oxidation of benzylic alcohol to benzaldehyde in DSPECs by grafting both a chromophore and a transition metal catalyst on the photoanode covered by mesoporous films of TiO₂ nanoparticles (TiO₂/FTO slides) (Figure 1d) [45]. First, this TiO₂/FTO slide was soaked in methanol solution of [Ru(bpy)₂(4dpbpy)]²⁺ photosensitizer. Then the catalyst [Ru(mebimpy)₂(4dpmbpy)]²⁺ (mebimpy = 2,6-bis(1-methylbenzimidazol-2-yl)pyridine, 4dpmbpy = 4,4'-bis(methylenephosphonato)-2,2'-bipyridine) bearing two phosphonate anchoring groups was immobilized on the same TiO₂/FTO slide using a similar soaking procedure. The relative surface coverage by the complexes was finely tuned varying the reaction times and controlling the adsorption processes by absorbance measurements. The photoanode thus prepared was capable of cross-surface electron transfer and useful for accumulation of multiple redox equivalents at catalytic sites for performing half-reactions in DSPECs.

To decrease back electron transfer at this doubly (sensitizer/catalyst) functionalized photoanode, mesoporous films of TiO₂ nanoparticles on the surface of TiO₂/FTO slides were replaced by nanostructured films (3.2 μm) composed of a core of tin-doped indium(III) oxide nanoparticles covered by an amorphous TiO₂ shell (2.0–4.0 nm) (nanoITO/TiO₂/FTO slide) (Figure 1e) [46]. Mesoporous films of nanoITO NPs were formed on the FTO surface and coated with TiO₂ by 30–70 cycles of atomic layer deposition. Thereafter, two complexes [Ru(bpy)₂(4dpbpy)]²⁺ and [Ru(mebimpy)₂(4dpmbpy)]²⁺ were grafted on the surface of these films keeping unchanged the experimental procedures used for functionalization of TiO₂/FTO slides.

VATMPY complexes were also immobilized on titania NPs. Anatase, one of the crystalline forms of TiO_2 , is an excellent semiconductor and a common heterogeneous photocatalyst for UV light-driven reactions. To use this support in the preparation of catalysts for visible light-mediated transformations, the choice of immobilization strategy is very important because this photoactive support can not only tune catalytic properties of grafted complexes but also can accelerate the photodegradation of the complexes.

König and coworkers prepared Ru-sensitized TiO_2 NPs by grafting N3-dye (*cis*-di(isothiocyanato)bis(2,2'-bipyridyl-4,4'-dicarboxylato)ruthenium(II) dihydrate) bearing carboxylate anchoring groups [98] on commercial Degussa P25 NPs [40]. The NPs **N3/DegP25** thus obtained were introduced in the photocatalytic reactions without complete characterization of their composition and structure.

Jain and coworkers covalently anchored trinuclear ruthenium(II) complex $[\text{Ru}_3(\text{bpy})_4(\text{bpym})_2\text{Cl}_2]$ (bpym = 2,2'-bipyrimidine) on TiO_2 NPs. To this end, trinuclear chloridoruthenium(II) complex was reacted with TiO_2 NPs bearing phen ligands, which were attached to the surface by using an amine substituent (Scheme 14) [47].



Scheme 14. Immobilization of $[\text{Ru}_3(\text{bpy})_4(\text{bpym})_2\text{Cl}_2]$ onto TiO_2 NPs.

TEM images and EDX analysis of the material prove a uniform distribution of Ru^{II} complex on the surface of TiO_2 NPs having dimension of 10–20 nm. The XRD pattern of the hybrid material $[\text{Ru}_3(\text{bpy})_4(\text{bpym})_2]^{6+}/\text{TiO}_2\text{-NP}$ displays a number of peaks attributed to TiO_2 support and crystalline trinuclear Ru^{II} complex. Titanium oxide NPs were mainly present as anatase phase with rutile phase being an insignificant component.

Photoredox catalysts based on MOFs and MOLs

A large porosity and tunable structural properties make MOFs interesting new materials for development of heterogenized homogeneous catalysts of all kinds [13,99-106]. Their synthesis can be readily adjusted through a proper choice of linker and metal to meet requirement of a particular application. Many MOFs such as ZJU-100, PCN-99, UiO-67, MOL-125, and USF2, have already been used as rigid matrices for the incorporation of VATMPY complexes. Some of these materials display remarkable chemical stability required for catalytic applications in organic synthesis. They can be prepared according to diverse synthetic strategies.

First, the photocatalysts can be encapsulated in the regular pores of MOFs, as in those of zeolites or periodic mesoporous silicas, *via* non-covalent interactions. This approach does not

require prior chemical modification of the complexes and could afford remarkably stable materials due to relatively strong coulombic interactions of positively charged transition metal complexes with porous frameworks.

The MOFs of this type were prepared by encapsulation of VATMPY complexes in pre-formed frameworks or by adding the complexes in the synthetic processes leading to target MOFs.

To encapsulate relatively bulky positively charged species, e. g. $[\text{Ru}(\text{bpy})_3]^{2+}$, MOFs with *meso*-sized pores and negatively charged frameworks are needed. Such MOFs involve exchangeable charge-compensating cations in the pores which can be replaced by VATMPY complexes. Though resembling to zeolites in what concerns the ability of ion exchange and regular structure, MOFs are closer to mesoporous silicas like MCM-41 or SBA-15 with wider pores and channels being able to accommodate more spatially demanding guests.

The increase of pore size in MOFs can be achieved by using bulky linkers, such as 10,15-dihydro-5*H*-diindolo[3,2-*a*:3',2'-*c*]carbazole-3,8,13-tricarboxylate (H_3dcta) [54]. By the reaction of this acid with indium nitrate and tetrafluoroboric acid in a mixture of DMF and ethanol at 120 °C, Zhou and coworkers obtained single crystals of PCN-99 (Figure 2). In this solid, $[\text{In}(\text{COO})_4]^-$ nodes are negatively charged and connected by hydrophobic linkers, which enable π - π stacking between the framework and aromatic guest molecules. Porous system of this MOF involves large cavities connected by wide windows and narrower 1D channels. Impregnation of this MOF with $[\text{Ru}(\text{bpy})_3]\text{Cl}_2$ solution in DMF at room temperature affords the $[\text{Ru}(\text{bpy})_3]^{2+}/\text{PCN-99}$ material, in which the crystalline structure of PCN-99 is preserved.

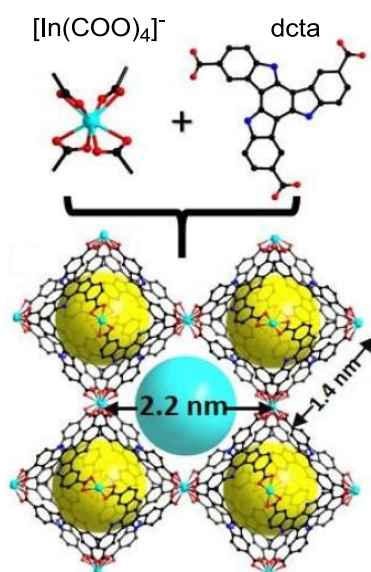


Figure 2. Structure of PCN-99. Reprinted with permission from Ref. [54]. Copyright 2016 Royal Society of Chemistry.

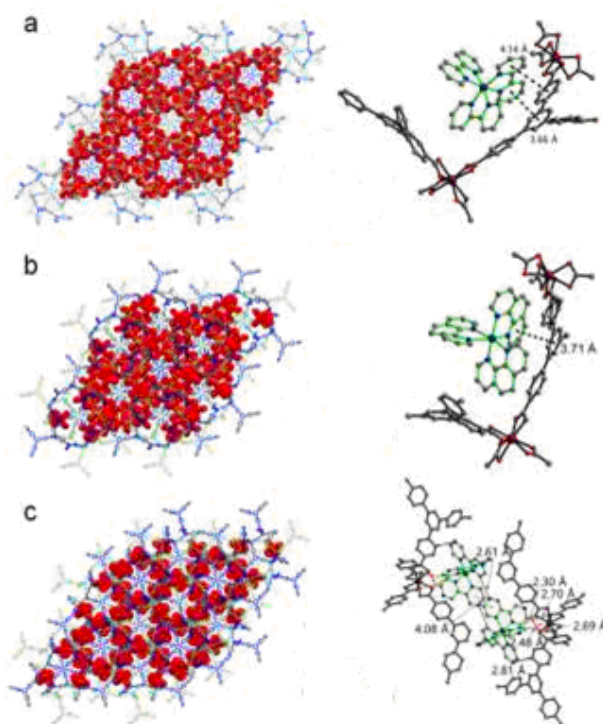


Figure 3. Left panel: Structures of $[\text{Ru}(\text{bpy})_3]^{2+}/\text{InBTB}$ (a), $[\text{Ru}(\text{phen})_3]^{2+}/\text{InBTB}$ (b) and $[\text{Ru}(\text{bpz})_3]^{2+}/\text{InBTB}$ (c). Right panel: Multiple intermolecular interactions between ruthenium cations and the framework in $[\text{Ru}(\text{bpy})_3]^{2+}/\text{InBTB}$ (a), $[\text{Ru}(\text{phen})_3]^{2+}/\text{InBTB}$ (b) and $[\text{Ru}(\text{bpz})_3]^{2+}/\text{InBTB}$ (c). Reprinted with permission from Ref. [55]. Copyright 2020 Wiley-VCH.

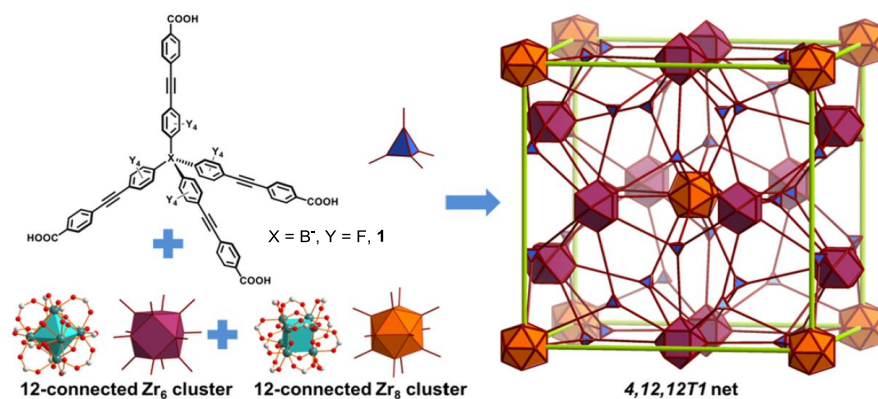
Recently, a similar synthetic strategy was used to encapsulate three Ru^{II} complexes ($[\text{Ru}(\text{bpy})_3]^{2+}$, $[\text{Ru}(\text{phen})_3]^{2+}$ and $[\text{Ru}(\text{bpz})_3]^{2+}$ ($\text{bpz} = 2,2'$ -bipyrazine)) in a negatively charged framework held by $[\text{In}(\text{COO})_4]^-$ nodes and bound by btb ($\text{H}_3\text{btb} = 1,3,5$ -tris(4-carboxyphenyl)benzene) linkers, which can be described as $[\text{Et}_2\text{NH}_2]_3[\text{In}_3(\text{btb})_4] \cdot 10\text{DEF} \cdot 14\text{H}_2\text{O}$ ($\text{DEF} =$ diethylformamide) (Figure 3) [55]. The loading of Ru^{II} complexes in $[\text{Ru}(\text{bpy})_3]^{2+}/\text{InBTB}$, $[\text{Ru}(\text{phen})_3]^{2+}/\text{InBTB}$ and $[\text{Ru}(\text{bpz})_3]^{2+}/\text{InBTB}$ thus obtained was in the range of 33–42 mmol g^{-1} . According to the single crystal X-ray diffraction analysis, all three complexes occupy distinct but different places within the channels of MOF, each apparently corresponding to optimal interaction between the ligands and linkers as shown in Figure 3.

The distribution of luminescent ruthenium(II) species in the crystals of functionalized **InBTBs** was studied by a fluorescence confocal laser scanning microscopy. Authors assumed that a lower emission intensity observed in the central part of the crystals indicated that the migration of ruthenium(II) species inside the mesopores is partly hindered by the accumulation of complexes near the pore entrances.

Photoluminescence properties of $[\text{Ru}(\text{bpy})_3]^{2+}$, $[\text{Ru}(\text{phen})_3]^{2+}$ and $[\text{Ru}(\text{bpz})_3]^{2+}$ species encapsulated in mesopores of **InBTBs** were different from those observed in solution environment due to their specific spatial orientation in the crystals and a distinct nanoscale environment around ruthenium(II) ions entrapped into the frameworks. Surprisingly, the excited state lifetimes were increased after the encapsulation for only $[\text{Ru}(\text{bpy})_3]^{2+}$ and $[\text{Ru}(\text{bpz})_3]^{2+}$ complexes. In contrast, $[\text{Ru}(\text{phen})_3]^{2+}/\text{InBTB}$ exhibited a shorter decay lifetime than that of bulk $[\text{Ru}(\text{phen})_3]\text{Cl}_2$ complex in the given solution probably due to a close spatial arrangement of adjacent ruthenium(II) species (Figure 3).

Anionic frameworks can also be obtained by the introduction of more negative charges in organic linkers. This strategy was used to prepare NPF-201 by the solvothermal reaction of negatively charged tetrahedral linkers **1** with zirconium tetrachloride in DMF using benzoic acid

as a modulator (Scheme 15) [56]. Large pores of NPF-201 are filled with DMF molecules and extra-framework tetrabutylammonium counterions. As all MOFs based on Zr-nodes (Zr-MOFs), NPF-201 displays a remarkable stability due to the presence in the crystals of large zirconium clusters $[\text{Zr}_6(\mu_3\text{-O}_4)(\mu_3\text{-OH})_4]$ and $[\text{Zr}_8(\mu_2\text{-O}(\text{H}))_{12}]$ assembled *via* numerous and strong Zr–O bonds. Incorporation of $[\text{Ru}(\text{bpy})_3]^{2+}$ ions into the cavities of NPF-201 *via* the exchange of tetrabutylammonium cations afforded the $[\text{Ru}(\text{bpy})_3]^{2+}/\text{NPF-201}$ material bearing 0.37 wt% of Ru per ligand. This loading is close to the theoretical limit of uptake (0.5 wt% per ligand) that consistent with a high accessibility of all the pores to species freely diffusing in the channels of the solid.



Scheme 15. The formation of NPF-201 (4,12,12T1 topology). The blue, purple, and orange polyhedra represent 4-, 12-(Zr_6), and 12-(Zr_8)-connected nodes, respectively. Reprinted with permission from Ref. [56]. Copyright 2016 American Chemical Society.

Another example of photoactive MOFs with negatively charged linkers is $[\text{Ru}(\text{bpy})_3]^{2+}/\text{PCN-608-SBDC}$, which was prepared by a two-step procedure from PCN-608, Zr-MOF composed of coordinatively unsaturated $\text{Zr}_6\text{O}_4(\text{OH})_8(\text{H}_2\text{O})_4$ clusters and 4,4'-dimethoxy-3,3',5,5'-tetra(4-carboxyphenyl)biphenyl linkers (Figure 4) [57]. First, negatively charged dicarboxylate linkers with SO_3^- groups were inserted into the framework at the coordination vacancies of the Zr clusters by reacting PCN-608 with 2-sulfoterephthalic acid (H_3SBDC) in DMF. It is worth noting that this MOF can be prepared only by a consecutive installation of the linkers because the one-pot reaction led to impure phases owing to competitive coordination of $-\text{SO}_3^-$ groups to zirconium(IV) ions. Then, the ion exchange in **PCN-608-SBDC** was performed to prepare the target material with the $[\text{Ru}(\text{bpy})_3]^{2+}$ content of about 0.16 wt%, that was in nice agreement with the theoretical expectations supposing that all sodium cations were exchanged with $[\text{Ru}(\text{bpy})_3]^{2+}$ ions.

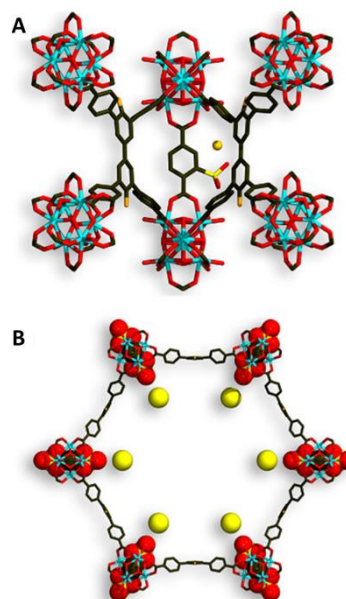


Figure 4. a: Structure of $\text{Na}^+/\text{PCN-608-SBDC}$ viewed along the (1, 2, 0) direction. Only one installed linker of SBDC is shown for clarity. b : The hexagonal 1D channels in $\text{Na}^+/\text{PCN-608-SBDC}$ viewed along the c-axis. Colors: black, C; red, O; dark blue, N; yellow, S; light blue, Zr; light orange -OMe groups ; grey-yellow balls represent disordered Na^+ ions. Reprinted with permission from Ref. [57]. Copyright 2019 American Chemical Society.

MOFs bearing encapsulated photoredox catalysts can also be prepared by one-pot synthesis, reacting metal salts with polycarboxylate ligands under solvothermal conditions in the presence of VATMPY complexes. This strategy is especially useful for the synthesis of microporous crystalline solids with rather small pore apertures, which cannot be obtained by reacting the sterically bulky complexes with pre-formed frameworks. For example, $[\text{Ru}(\text{bpy})_3]\text{Cl}_2$ was incorporated in the pores of MIL-125- NH_2 [107] (pore diameter is ~ 1.25 nm) by conducting the synthesis of MOF from 2-aminoterephthalic acid and titanium isopropoxide in the presence of the Ru^{II} complex (Figure 5) [58].

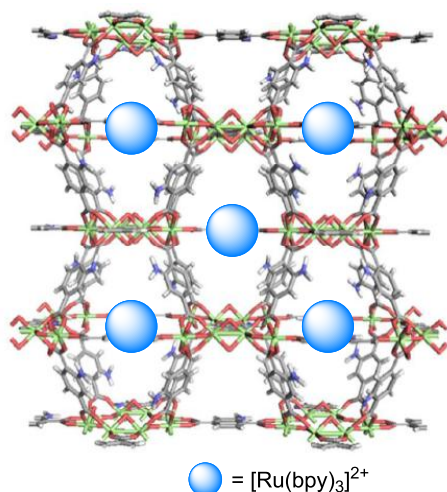


Figure 5. Structure of $[\text{Ru}(\text{bpy})_3]^{2+}/\text{MIL-125-NH}_2$. Adapted with permission from Ref. [108]. Copyright 2017. American Chemical Society.

XRD patterns of this microporous material $[\text{Ru}(\text{bpy})_3]^{2+}/\text{MIL-125-NH}_2$ with specific surface area of $1020 \text{ m}^2 \text{ g}^{-1}$ were similar to that of the parent MIL-125-NH₂. The integrity of the incorporated complex was confirmed by XANES and EXAFS analyses of the solid. Meanwhile, the luminescence of the solid was blue-shifted as compared to that of $[\text{Ru}(\text{bpy})_3]^{2+}$ impregnated onto non-porous fume silica. This shift was most likely related to the confinement effect imposing structural distortions to the $[\text{Ru}(\text{bpy})_3]^{2+}$ complex similar to what was observed after encapsulation of this compound in zeolites.

A MOF bearing photoactive 1,4,5,8-naphthalenediimide (NDI) residues as linkers and $[\text{Ru}(\text{bpy})_3]^{2+}$ as catalytic centers (Figure 6) was prepared by reacting manganese dichloride with *N,N'*-bis(3,5-dicarboxyphenyl)-1,4,5,8-naphthalenediimide (H₄BINDI) in the presence of $[\text{Ru}(\text{bpy})_3]\text{Cl}_2$ in *N,N*-dimethylacetamide (DMA) [59].

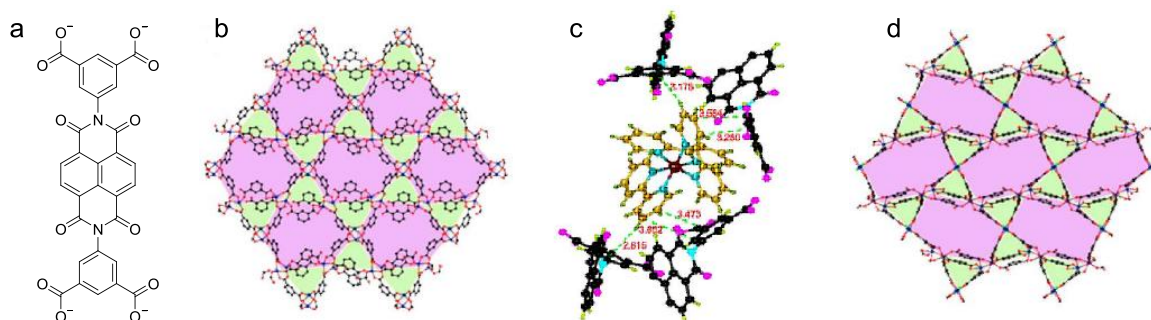


Figure 6. (a) Structure of BINDI linker. (b) Schematic presentation of the $[\text{Ru}(\text{bpy})_3]^{2+}/\text{FJI}$ structure. (c) Multiple intermolecular interactions between BINDI ligands and $[\text{Ru}(\text{bpy})_3]^{2+}$ cations. (d) Schematic presentation of FJI structure. Reprinted with permission from Ref. [59]. Copyright 2018 Elsevier.

The single-crystal X-ray diffraction analysis of this MOF revealed the presence of both dimethylammonium cation (apparently formed from the decomposition of DMA) and $[\text{Ru}(\text{bpy})_3]^{2+}$ species. The crystals with the brutto formula $[\text{Mn}_6(\text{BINDI})_4(\text{H}_2\text{O})_2\text{Cl}_2] \cdot [\text{Ru}(\text{bpy})_3] \cdot 4\text{Me}_2\text{NH}_2$ displayed a complex structure composed of Kagomé lattices pillared by NDI groups (Figure 6b). The manganese ions form two types of SBUs, which are organized into two-dimensional layers adopting the Kagomé topology. The first SBU is a paddle-wheel unit $[\text{Mn}_2(\text{COO})_4\text{Cl}_2]^{2-}$ formed by two square-pyramidal Mn^{2+} ions, each bonded to the other through four bridged carboxyl groups and each bearing one terminal chloride. The second SBU is an asymmetric bimetallic node $[\text{Mn}_2(\text{COO})_6(\text{H}_2\text{O})]^{2-}$, in which Mn^{2+} ions are ligated by only carboxylate functions and a single water molecule. The pillared structural organization of this solid generates porous channels connected by windows of about $8 \times 11 \text{ \AA}^2$, that conforms to the size of the $[\text{Ru}(\text{bpy})_3]^{2+}$ species. NDI residues and $[\text{Ru}(\text{bpy})_3]^{2+}$ counterions are located very closely in the solid. They interact through numerous C–H $\cdots\pi$ contacts and π -stacking of the slipped pyridine ring and the aromatic systems of NDI residues (Figure 6c). The pores are filled with disordered solvent molecules and charge-balancing dimethylammonium cations. Unfortunately, the solvent molecules cannot be removed without decomposition of the framework. Nonetheless, $[\text{Ru}(\text{bpy})_3]^{2+}/\text{FJI}$ being stable in DMA and acetonitrile can be used as a photoredox catalyst in liquid phase organic reactions performed in these solvents.

When manganese dichloride was reacted with H₄BINDI under the same solvothermal conditions but in the absence of $[\text{Ru}(\text{bpy})_3]\text{Cl}_2$, a similar network was obtained (Figure 6d). The solid was crystallized in the same monoclinic space group $P2_1/c$. However, in the absence of sterically bulky counterions, the rotation of the BINDI ligands and change in the coordination

geometry of Mn^{2+} ions in the asymmetric SBU units were observed indicating that $[\text{Ru}(\text{bpy})_3]^{2+}$ can influence the structural organization of MOFs prepared by direct synthesis.

In fact, the templating effect of the $[\text{Ru}(\text{bpy})_3]^{2+}$ complex was recently demonstrated exploring the crystallization of networks formed by cupric chloride and sterically bulky 2,3,6-tris(4-carboxyphenyl)-1,3,5-triazine (H_3tatb), benzo[1,2-*b*:3,4-*b'*:5,6-*b''*]trithiophene-2,5,8-tricarboxylic acid (H_3BTTC) or trimesic acid (H_3btc) in the presence of $[\text{Ru}(\text{bpy})_3]\text{Cl}_2$ (Figure 7) [31]. Since all three ligands have the same C_3 symmetry, three isostructural solids $[\text{Ru}(\text{bpy})_3]^{2+}/\text{NKMOF-4}$, $[\text{Ru}(\text{bpy})_3]^{2+}/\text{NKMOF-5}$ and $[\text{Ru}(\text{bpy})_3]^{2+}/\text{NKMOF-6}$, respectively, were obtained, all displaying a zeolite-like structure. Supramolecular building blocks of sodalite cages with an inner sphere space having diameter of 20 Å, 16 Å and 12 Å, respectively, were formed *via* linking six $[\text{Cu}_4(\text{COO})_8\text{Cl}]^-$ squares with eight planar trianionic ligands. A cubic packing of these cages through sharing metal nodes gave 3D anionic frameworks with intersected channels. MOF $[\text{Ru}(\text{bpy})_3]^{2+}/\text{NKMOF-4}$ based on the largest H_3tatb ligand in this series displayed a 2-fold penetrated framework. The solids with BET surface areas superior to $480 \text{ m}^2 \text{ g}^{-1}$ exhibited a high thermal and chemical stability and maintained their crystallinity up to 220°C .

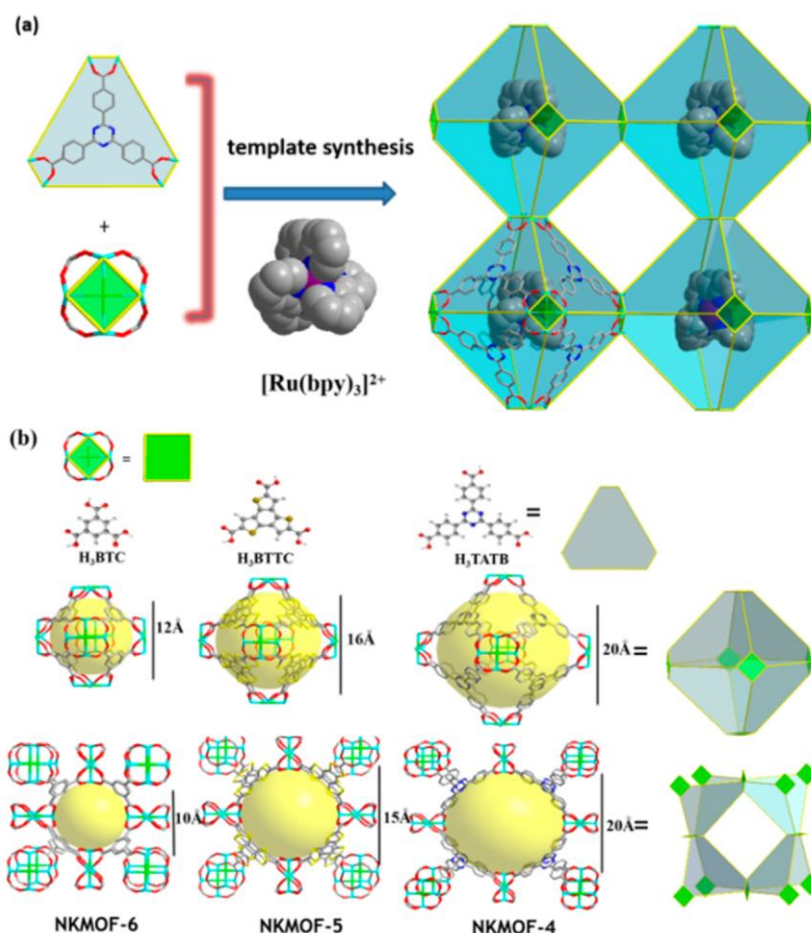


Figure 7. Synthesis of $[\text{Ru}(\text{bpy})_3]^{2+}/\text{NKMOF-4}$, $[\text{Ru}(\text{bpy})_3]^{2+}/\text{NKMOF-5}$ and $[\text{Ru}(\text{bpy})_3]^{2+}/\text{NKMOF-6}$. Reprinted with permission from Ref. [31]. Copyright 2019 American Chemical Society.

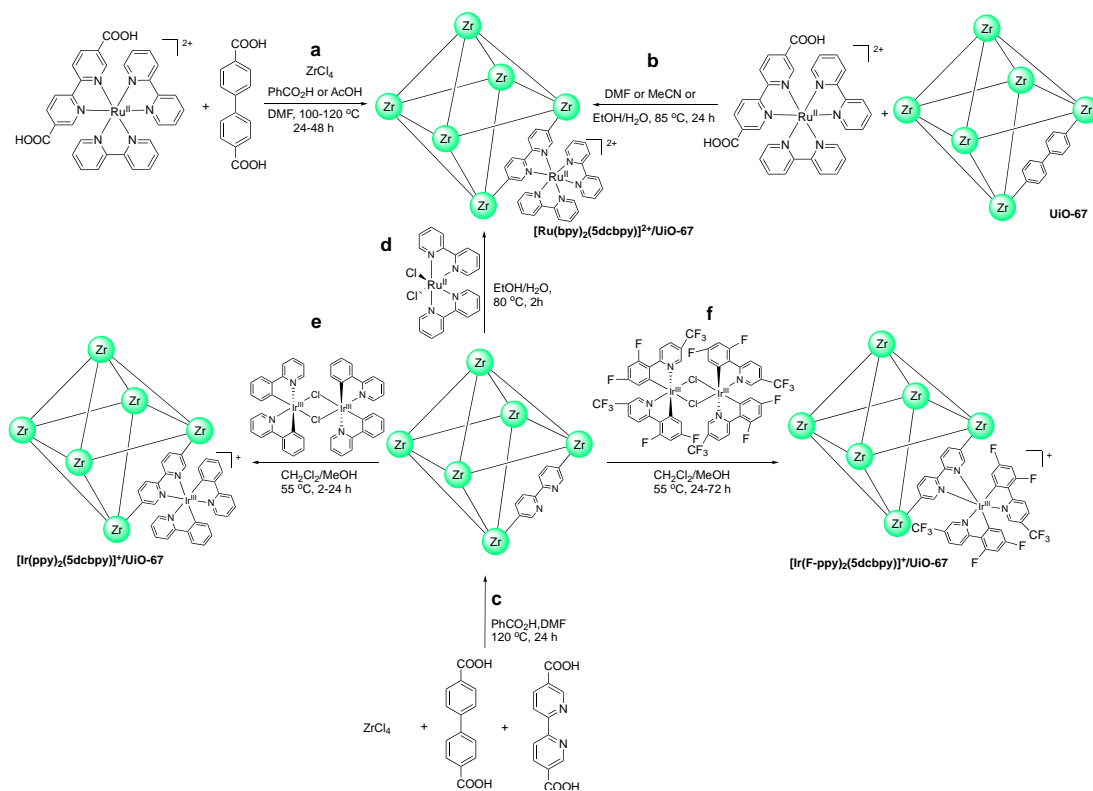
For $[\text{Ru}(\text{bpy})_3]^{2+}/\text{NKMOF-4}$ and $[\text{Ru}(\text{bpy})_3]^{2+}/\text{NKMOF-5}$, templating effect of the ruthenium(II) complex was evidenced by conducting the reaction of the ligand and cupric chloride without addition of the complex. Under these conditions, the crystalline solids were

obtained but their structures were not identical to those prepared with the Ru^{II} complex. In contrast, **NKMOF-6** was successfully formed in the absence of the [Ru(bpy)₃]Cl₂ template.

Interestingly, when tridentate but non-planar tris(4-carboxyphenyl)amine was used as a linker in this solvothermal reaction, a non-porous crystalline solid [Ru(bpy)₃]²⁺/**NKMOF-7** was obtained [31]. Therefore, the coplanarity and C₃ symmetry of the ligands were both important to generate porous zeolite-like structures.

The complexes [Ru(Phphen)₃]Cl₂ (Phphen = 4,7-diphenyl-1,10-phenanthroline) and [Ir(ppy)₃] were also suitable as templating species to prepare photoactive NKMOF-4 frameworks with 20 wt% and 8 wt% catalyst loading, respectively [31]. The porosity of these crystalline solids (564 and 633 m² g⁻¹, respectively) was proven by N₂ adsorption data.

Lin's and Cohen's groups developed another strategy for preparing MOF-based photoredox catalysts, which relies on the incorporation of bpy ligands of VATMPY complexes as linkers into the 3D framework [60-62,59-62]. To simplify the incorporation of bulky complexes with low symmetry in a crystalline framework they prepared mixed-linker MOFs (Scheme 16).



Scheme 16. Synthesis of [Ru(bpy)₂(5dcbpy)]²⁺/UiO-67, [Ir(ppy)₂(5dcbpy)]⁺/UiO-67 and [Ir(F-ppy)₂(5dcbpy)]⁺/UiO-67 by direct synthesis (a), post-synthetic modification of UiO-67 (b) and through a two-step procedure involving the ligand exchange (c) followed by the complexation of ruthenium(II) ions (d-f).

The solvothermal reactions were conducted in the presence of target linker and biphenyl-4,4'-dicarboxylate (bpdca) known to form stable Zr-MOFs. Robust UiO-67-type frameworks, consisting of [Zr₆O₄(OH)₄] clusters, bpdca linkers and ruthenium(II) or iridium(III) polypyridyl complexes were prepared according to different strategies. First, the target MOFs [Ru(bpy)₂(5dcbpy)]²⁺/UiO-67 bearing [Ru(bpy)₂(5dcbpy)]²⁺ (5dcbpy = 5,5'-dicarboxy-2,2'-bipyridine) linkers were obtained by direct synthesis from H₂bpdca, [Ru(bpy)₂(H₂5dcbpy)]²⁺ and zirconium tetrachloride in DMF at 100 °C using benzoic acid or glacial acetic acid as a modulator (Scheme 16, route a) [60-62]. Porous crystalline materials were obtained only when catalyst loading was rather low (1.5–3 wt% of Ru).

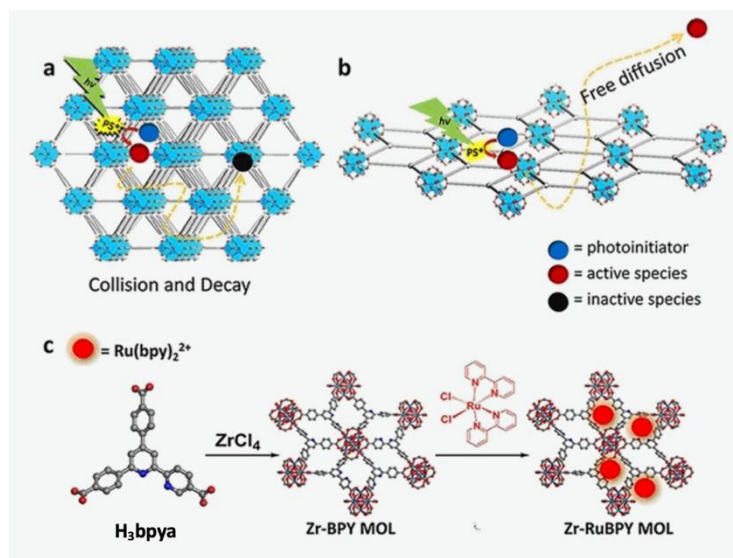
The steady-state emission and the emission lifetime of Ru^{II} complex incorporated in these MOFs depend on the content of the complex [61,109]. By means of transient absorption spectroscopy, Ferrer's and Garcia's groups showed that the behavior of the triplet excited state of the heterogenized Ru^{II} complex is similar to that of [Ru(bpy)₂(5dcbpy)]Cl₂ dissolved in water [62]. Upon visible-light irradiation the localized triplet excited state is generated and decays in part to a very long-lived (millisecond time scale) charge-separated state. The lifetime of this excited state is orders of magnitude longer compared to that of the complex dissolved in organic solvents, a situation that may have a positive effect on the rate of photocatalytic reactions. These observations were rationalized assuming a PET process from the triplet excited state of the Ru^{II} complex to the MOF lattice.

[Ru(bpy)₂(5dcbpy)]²⁺/UiO-67 was also obtained by post-synthetic modification of UiO-67 with [Ru(bpy)₂(H₂5dcbpy)]²⁺ in various organic solvents at 85 °C (Scheme 16, route b). The solid retained its crystallinity though the catalyst loading (1 wt% of Ru) was lower than in the materials synthesized by the one-pot procedure most likely due to the blockage of channels by the bulky Ru^{II} complex [63].

To increase the catalyst loading, another two-step procedure was developed by Cohen's group [63]. First, a mixed-ligand framework UiO-67-bpy bearing bpdc and 5dcbpy linkers was prepared from H₂bpdc, H₂dcbpy and ZrCl₄ in DMF at 120 °C using benzoic acid as a modulator (Scheme 16, route c). Under these conditions, the loading of the 5dcbpy ligand was increased up to 25% of overall ligand content in the crystalline MOF. Post-synthetic modification of this MOF with [Ru(bpy)₂Cl₂] in ethanol/water solvent mixture at 80 °C afforded MOFs **[Ru(bpy)₂(5dcbpy)]²⁺/UiO-67** containing 2–15 wt% of Ru (Scheme 16, route d). ¹H NMR studies of the samples obtained after digesting the **[Ru(bpy)₂(5dcbpy)]²⁺/UiO-67** materials under acidic conditions proved the integrity of the ruthenium(II) complex in the lattice. The MOF bearing 10 wt% of Ru exhibits the BET surface area of ~1800 m² g⁻¹, which is noticeably high, though lower than that of the parent UiO-67-bpy (2425 m² g⁻¹) material.

Similar synthetic strategies were used for incorporation of visible light-active Ir^{III} complexes [60, 66]. Once again, the best results were obtained when [Ir(ppy)₂(5dcbpy)]⁺ and [Ir(F-ppy)₂(5dcbpy)]⁺ (F-ppy = 2-[5-(trifluoromethyl)pyridin-2-yl-κN]-4,6-difluorophenyl-κC) photosensitizers were immobilized in the UiO-67 framework according to the stepwise procedure involving the preparation of mixed-ligand MOF UiO-67-bpy followed by the insertion of iridium(III) centers (Scheme 16, routes e and f) [66]. The loading of complexes was controlled by varying time of the complexation reaction. For example, Ir : Zr molar ratio in **[Ir(ppy)₂(5dcbpy)]⁺/UiO-67** reached 1 : 5.3 when the complexation reaction was performed for 24 h. The formation of fluorinated complex [Ir(F-ppy)₂(5dcbpy)]⁺ proceeded even more slowly giving a solid with the Ir : Zr molar ratio of only 1 : 10.8 after 72 h of the reaction. Photoactive MOFs thus obtained displayed BET surface areas as high as ~ 2000 m² g⁻¹ and nitrogen adsorption isotherms confirmed their microporous structures.

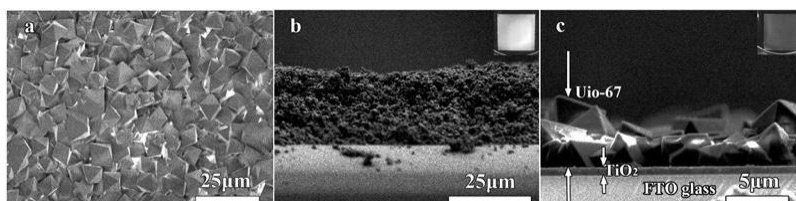
The obvious drawback of microporous catalysts based on MOFs is due to pore size limitations drastically limiting the diffusion of reagents inside their intricate structures that could be especially detrimental for photocatalytic reactions involving short-lived intermediates. Therefore, Lin and coworkers developed synthetic approaches to functionalized metal-organic layers (MOL) with 1-2 nm of thickness in which catalytic centers are located closely to the surface of sheets becoming readily available to substrates [68]. MOL synthesis was achieved very similarly to the synthesis of MOFs through careful choice of organic linkers, modulators and solvents. Thus, heating a mixture of ZrCl₄, 5-carboxy-4',6'-bis(4-carboxyphenyl)-2,2'-bipyridine (H₃bpya) and formic acid in aqueous DMF at 120 °C afforded Zr-BPY material exhibiting a wrinkled nanosheet morphology. The treatment of this solid by [Ru(bpy)₂Cl₂], gave **[Ru(bpy)₂(bpya)]²⁺/Zr-MOL**, in which 71% of the incorporated bpya ligands were coordinated to the ruthenium(II) centers (Scheme 17).



Scheme 17. Synthesis of $[\text{Ru}(\text{bpy})_2(\text{bpya})]^{2+}/\text{Zr-MOL}$. Reprinted with permission from Ref. [68]. Copyright 2018 Wiley-VCH.

Another approach to increase the accessibility of the catalytic centers and mechanical stability of MOFs consists of their deposition as thin films on the surface of transparent to visible light supports. Yang and Fei prepared stable MOF films on the surface of conductive FTO glass support [65]. First, a FTO surface was covered by TiO_2 films using spin-coating and annealing processes (Figure 8). This support was treated with a diluted DMF solution containing biphenyl-3,3',5,5'-tetracarboxylic acid (H_4btca) to obtain a carboxylate-terminated monolayer (CTM). External *meta*-benzenedicarboxylate residues of this CTM are suitable for MOF growth. For instance, UiO-67 films were prepared by heating the CTM-modified substrate in a DMF solution containing H_2bpdcl , ZrCl_4 and acetic acid for 24 h at 120 °C. The thickness of MOF layer deposited on the film was modified by changing experimental conditions (Figure 8). Post-synthetic modification of these films with an aqueous $[\text{Ru}(\text{bpy})_2(5\text{dcbpy})]^{2+}$ solution for 24 h at 75 °C afforded the $[\text{Ru}(\text{bpy})_2(5\text{dcbpy})]^{2+}/\text{UiO-67}\&\text{TiO}_2/\text{FTO}$ slides containing Zr and Ru in the atomic ratio of 1:0.81 which is much higher than in corresponding MOFs (Scheme 16, route b).

A



B

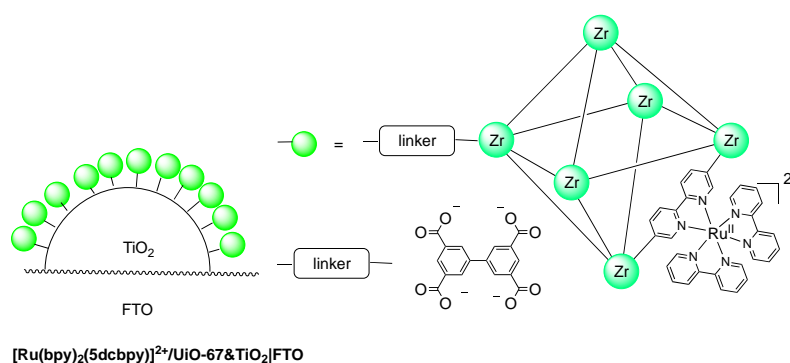


Figure 8. A: Film morphologies: FE-SEM images (a) and cross-sectional FE-SEM images of (b) thicker and (c) thinner UiO-67&TiO₂ films on FTO glass. The insets are optical images of the corresponding films. **B:** schematic presentation of [Ru(bpy)₂(5dcbpy)]²⁺/UiO-67&TiO₂/FTO. Figure 8A reprinted with permission from Ref. [65]. Copyright 2017 Royal Society of Chemistry.

Metal-organic frameworks and layers can be further modified to fabricate materials, in which photoredox catalysts can be combined with Lewis acid centers or other transition metal catalysts. Such hybrid catalysts should be capable of performing tandem multi-step transformations involving both photocatalytic steps, and dark reactions with aid of transition-metal and acid-base catalysts, as recently was demonstrated by Lin and coworkers [64,67]. An extra advantage of such catalysts is that the immobilization could overcome such common flaws of homogeneous catalysts as deactivation due to formation of inactive dimers or loss of important ancillary ligands. Moreover, high local concentrations of both catalytic sites and their periodic arrangement might facilitate the transfer of electrons and radicals between these sites leading to acceleration of sequential catalytic processes.

Dual MOF and MOL catalysts involving photoredox and Lewis acid centers can be obtained by the incorporation of VATMPY complexes as linkers into the framework based on metal ions possessing high Lewis acidity. An important difference between MOL and MOF types of organization is due to better exposure and thus an increased Lewis acidity of metal ions which can possess free valences at layer surfaces in the former.

Hf₁₂-Ir-OTf MOL bearing large triflate-capped Hf₁₂(μ₃-O)₈(μ₃-OH)₈(μ₂-OH)₆ nodes and the [Ir(F-ppy)₂(dbbpy)]⁺ (dbbpy = 5,5'-di(4-carboxyphenyl)-2,2'-bipyridine) photosensitizer in the linkers (Figure 9) was prepared according two-steps procedure [64,67]. First, HfCl₄ and [Ir(F-ppy)₂(H₂dbbpy)]Cl were reacted in DMF in the presence of trifluoroacetic acid and water mediators at 80 °C. In Hf₁₂-Ir-TFA thus obtained, Hf₁₂ nodes are laterally bridged by bidentate ligands belonging to the iridium(III) complex and vertically terminated by trifluoroacetate caps to generate an infinite 2D network.

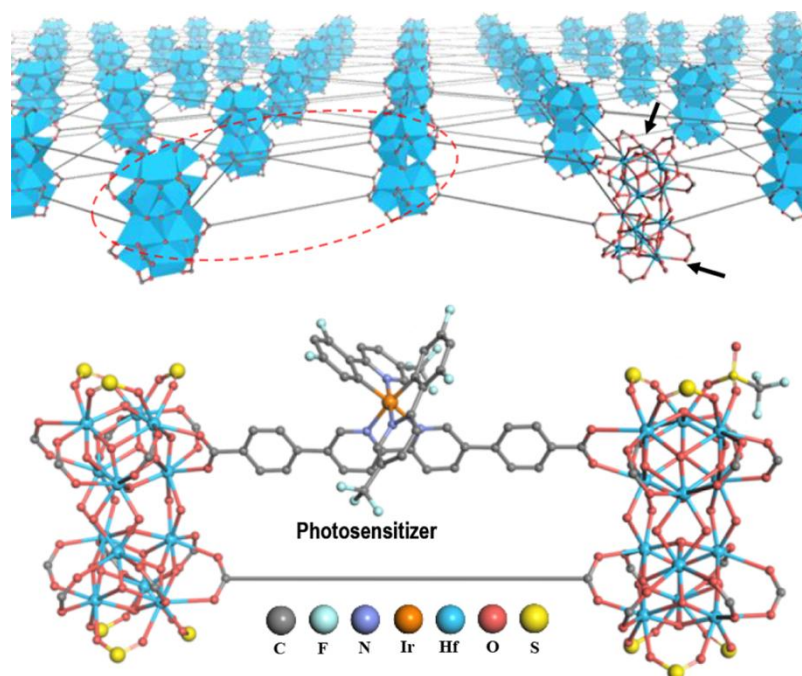


Figure 9. (a) Schematic representation of accessible external Lewis acid sites in the SBUs of Hf₁₂-MOLs (labeled by black arrows). (b) Structure of [Ir(F-ppy)₂(dbbpy)]⁺/Hf₁₂-OTf-MOL. Reprinted with permission from Ref. [67]. Copyright 2020 American Chemical Society.

The morphology of nano-sized plates with a diameter of 300 nm and a thickness of 1.7 nm was confirmed by AFM and TEM imaging, while the amount of TFA residues was calculated by ^{19}F NMR analysis of digested MOL. Next, to increase Lewis acidity of SBUs, trifluoroacetate ligands were replaced by triflate ions (TfO^-) by performing the ligand exchange reaction with trimethylsilyl triflate. The Lewis acidity of Hf_{12} -Ir-OTf MOL was comparable to that of widely used scandium(III) triflate.

Ir–Ni doped Zr-MOF bearing $[\text{Ir}(\text{F-ppy})_2(\text{dbbpy})]^+$ photosensitizer and $[\text{Ni}(\text{dbbpy})\text{Cl}_2]$ pre-catalyst was synthesized combining direct MOF synthesis of the framework bearing Ir(III) centers with a post-synthetic modification of Zr_{12} -type MOF thus obtained by Ni(II) complex [64]. Zr_{12} -type MOF with Ir(III)-modified linkers (Figure 10) was prepared by solvothermal reaction between ZrCl_4 , H_2dbbpy and $[\text{Ir}(\text{F-ppy})_2(\text{H}_2\text{dbbpy})]\text{Cl}$ in DMF at 80 °C using acetic acid as a modulator. Structure of this solid could be obtained by single crystal X-ray analysis, but was deduced comparing XRD, high-resolution TEM imaging and fast Fourier transform of Zr_{12} -Ir nanoplates and those of previously reported isostructural Hf_{12} -dbp MOF (dbp = 5,15-di(4-carboxyphenyl)porphyrin) [110, 111]. Then this MOF was reacted with nickel(II) chloride hexahydrate to insert nickel ions in the free dbbpy ligands. The EXAFS spectrum of the solid agreed well with that of model $\text{Ni}(\text{dbbpy})\text{Cl}_2$ complex, indicating a tetrahedral coordination environment of Ni^{2+} centers in **$\text{Ir}(\text{F-ppy})_2(\text{dbbpy})]^+ \& \text{Ni}(\text{dbbpy})\text{Cl}_2/\text{Zr}_{12}$ -MOF**.

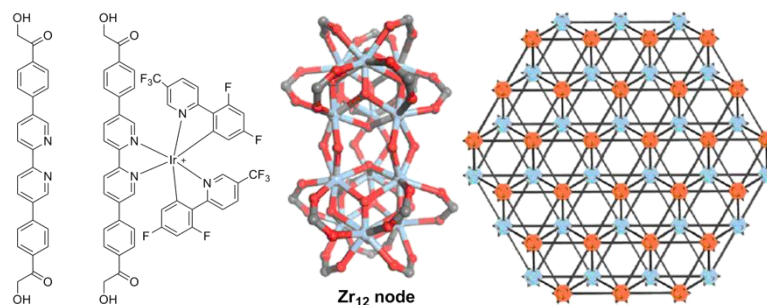


Figure 10. Zr_{12} -type MOF with Ir^{III}-modified linkers. Figure 10b Reprinted with permission from Ref. [110]. Copyright 2017 American Chemical Society.

Polymer-supported VATMPY complexes

Ion-exchange reactions were also widely used to prepare photocatalysts incorporated into polymer supports. For example, to encapsulate $[\text{Ru}(\text{bpy})_3]\text{Cl}_2$ in Amberlyst 15, an aqueous solution of the complex was stirred with this resin at 80 °C for 24 h. Non-porous material **$[\text{Ru}(\text{bpy})_3]^{2+}/\text{Amb15}$** thus obtained was loaded by 0.16 mmol g^{-1} of the complex [50].

Nafion, a rigid, thermally and chemically stable polymer matrix, was widely used for immobilization of photosensitizers. In this polymer, a perfluorinated backbone is functionalized by short pendant chains terminated by sulfonic groups. When swollen in water, the structure of Nafion is believed to resemble the structural organization of the inverse micelles in that the hydrated sulfonic groups are exposed to water phase [112]. Such arrangement of polar groups in polymer led to formation of water-containing pockets of ca. 40 Å in diameter. This material can incorporate high amounts of polar organic or inorganic compounds, thus it could also serve as a support allowing to prepare heterogenized photocatalysts with high loading of catalytic centers. Moreover, the perfluorinated backbone facilitates the oxygen adsorption. The O_2 concentration in water-swollen Nafion is by more than one order of magnitude higher than that usually observed in organic solvents that is of course positive for photooxidation reactions using molecular oxygen as oxidant.

Wu, Tung and coworkers investigated the incorporation of platinum complexes (Figure 11) into water-swollen Nafion membranes by immersing the membrane samples in an aqueous suspension of the platinum(II) complex with polypyridine ligands qpy (qpy = 2,2':6',2'':6'',2''':6''',2''''-quaterpyridine) and tpy-2 (tpy-2 = 4'-(4-methoxyphenyl)-2,2':6',2''-terpyridine) [69, 70].

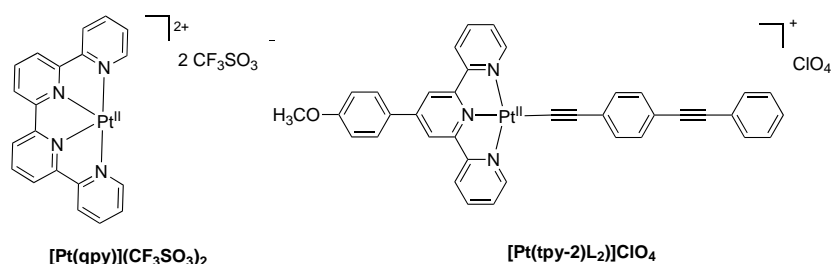
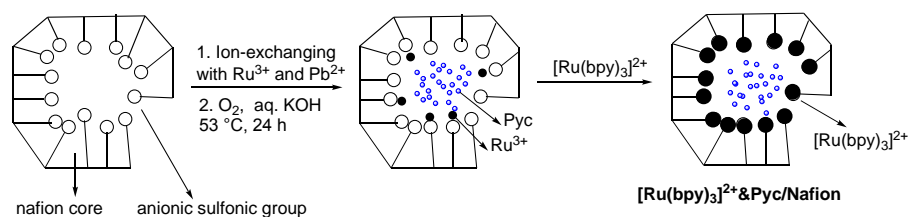


Figure 11. The structure of Pt^{II} complexes encapsulated in Nafion membranes.

Platinum(II)-quaterpyridine complex [Pt(qpy)](CF₃SO₃)₂, which is non-emissive in acetonitrile solution, exhibits a strong luminescence on being incorporated in Nafion membrane (0.1–14 μmol g⁻¹). The emission shape and the excited state lifetime are dependent on the amount of complex incorporated into Nafion, that might be explained by involvement of excimers formed through π–π interactions of the pyridine fragments. In order to avoid this detrimental effect, the catalytic systems [Pt(qpy)]²⁺/Nafion and [Pt(tpy-2)L₂]⁺/Nafion with low photosensitizer loading of 5–7 μmol g⁻¹ were used in photocatalytic reactions.

Nafion membranes are also suitable for the preparation of more sophisticated composite materials through impregnation of two different components. For example, [Ru(bpy)₃]²⁺ and a lead ruthenate pyrochlore mineral (Pyc) were combined in a Nafion membrane to obtain an efficient photocatalytic system for the oxidation of sulfides (Scheme 18) [71]. The membrane was soaked in an aqueous solution of Pb^{II} and Ru^{III} salts (1.5 : 1). Then, it was treated with aqueous potassium hydroxide bubbling molecular oxygen for 24 h to precipitate Pyc. Finally, the ion exchange reaction was used to introduce [Ru(bpy)₃]²⁺ complex in water-containing pockets.

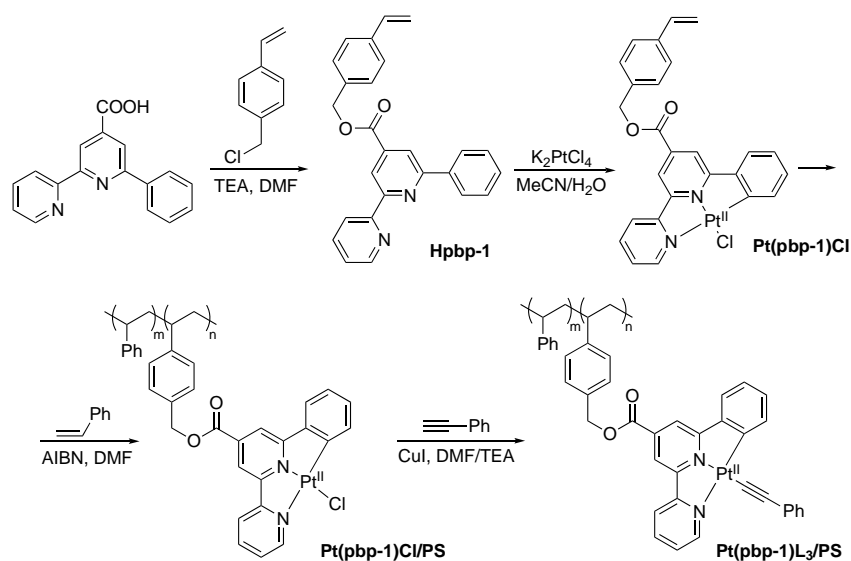


Scheme 18. Illustrative scheme of [Ru(bpy)₃]²⁺ & Pyc/Nafion synthesis.

Nafion films can be used in composite materials to increase photocatalyst loading onto inorganic supports. This was demonstrated by the preparation of [Ru(bpy)₃]²⁺/Nf/SiO₂ material by coating fumed silica (S_{BET} = 192 m² g⁻¹) with a Nafion film followed by the impregnation of [Ru(bpy)₃]Cl₂ from an aqueous solution [72]. The amount of adsorbed complexes in this material was found to be 8.2 wt% that is 5 times of that adsorbed on the surface of parent fumed silica.

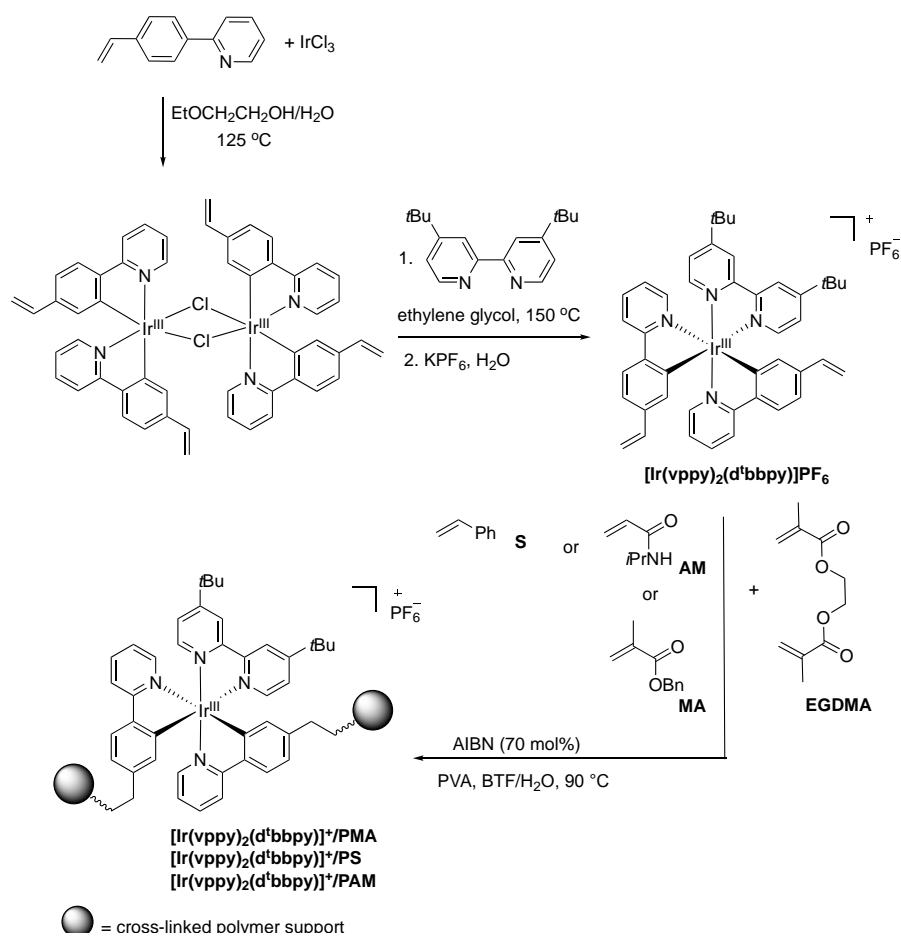
The limited chemical stability of materials prepared through non-covalent interactions of photosensitizers with solid supports (class I, Table 1) prompted the development of solids, in which photoactive complexes are built into polymeric chains by more reliable chemical bonds. To prepare such materials bearing platinum(II) chromophores, Wu and coworkers attached a styrene residue to cyclometalated platinum(II) complex using 4-vinylbenzyl 6-phenyl-2,2'-bipyridine-4-carboxylate (pbp-1) (Scheme 19) [34]. The complex Pt(pbp-1)Cl was then co-

polymerized with styrene and subjected to the ligand exchange reaction to prepare functionalized polymer **Pt(pbp-1)L₃/PS**.



Scheme 19. Synthesis of **Pt(pbp-1)L₃/PS**.

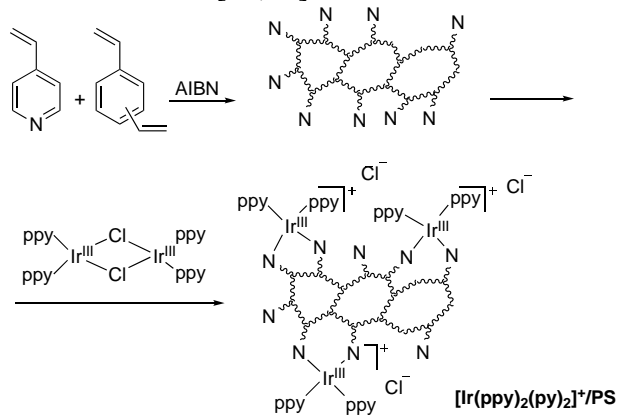
A similar strategy was used for the immobilization of photoactive iridium(III) complexes [74]. In this case, vinyl substituent was introduced in the 2-phenylpyridine ligand as shown in Scheme 20.



Scheme 20. Incorporation of $[\text{Ir}(\text{vppy})_2(\text{d}^t\text{bbpy})]\text{PF}_6$ in polymer matrices.

Next, $[\text{Ir}(\text{vppy})_2(\text{d}^t\text{bbpy})]\text{PF}_6$ ($\text{vppy} = 2\text{-(pyridin-2-yl-}\kappa\text{N)-5-vinylphenyl-}\kappa\text{C}$, $\text{d}^t\text{bbpy} = (4,4'\text{-di-tert-butyl)-2,2'-bipyridine}$) was obtained and copolymerized with ethylene glycol dimethacrylate (EGDMA) and various monomers such as styrene (S), *N*-*i*-propylacrylamide (AM), and benzyl methacrylate (MA). Rapid leaching of Ir(III) complexes into the solution media was observed for all polymers thus obtained probably due to an incomplete polymerization under these conditions. The most stable polymer $[\text{Ir}(\text{vppy})_2(\text{d}^t\text{bbpy})]^+/\text{PMA}$ was covered with an additional protective polymer layer by performing the free-radical copolymerization of EGDMA and MA. $[\text{Ir}(\text{vppy})_2(\text{d}^t\text{bbpy})]^+/\text{PMA-1}$ material exhibited an enhanced stability, thus making possible its use in catalysis.

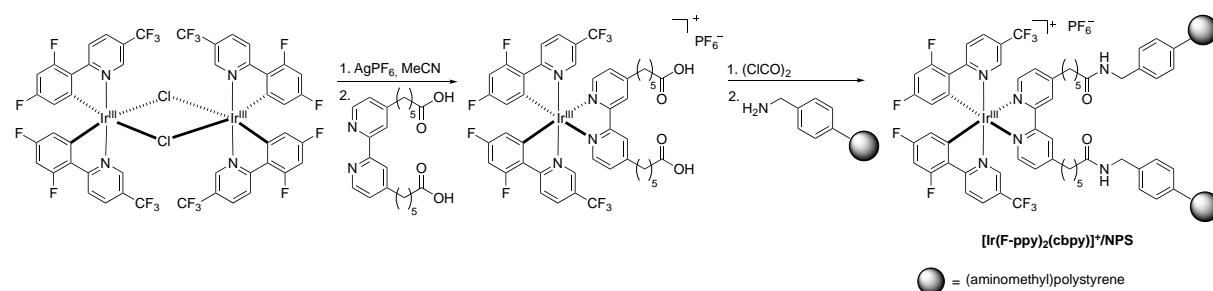
Liang, Shen and coworkers prepared polydivinylbenzene-supported iridium complex $[\text{Ir}(\text{ppy})_2(\text{py})_2]^+/\text{PS}$ by a post-synthetic modification of porous divinylbenzene/4-vinylpyridine (vpy) copolymer as shown in Scheme 21 [84,85].



Scheme 21. Synthesis of $[\text{Ir}(\text{ppy})_2(\text{py})_2]^+/\text{PS}$.

According to SEM imaging, irregular spherical particles with 40–50 nm in diameter were obtained. The rigidity of divinylbenzene monomer allowed for preparation of porous nanoparticles with specific surface areas, which decreased from 865 to 246 $\text{m}^2 \text{g}^{-1}$ with the increase of the Ir content from 5.34 to 7.54 wt%. Although catalyst loading can be partly controlled by varying the relative amount of vpy monomer in the co-polymerization reaction, the uniformity of distribution of iridium(III) sites within the polymer granules is difficult to achieve in this process. Moreover, iridium(III) loading in these polymers was much smaller compared to the amount of available vpy residues likely due to a partial inaccessibility of the py ligands.

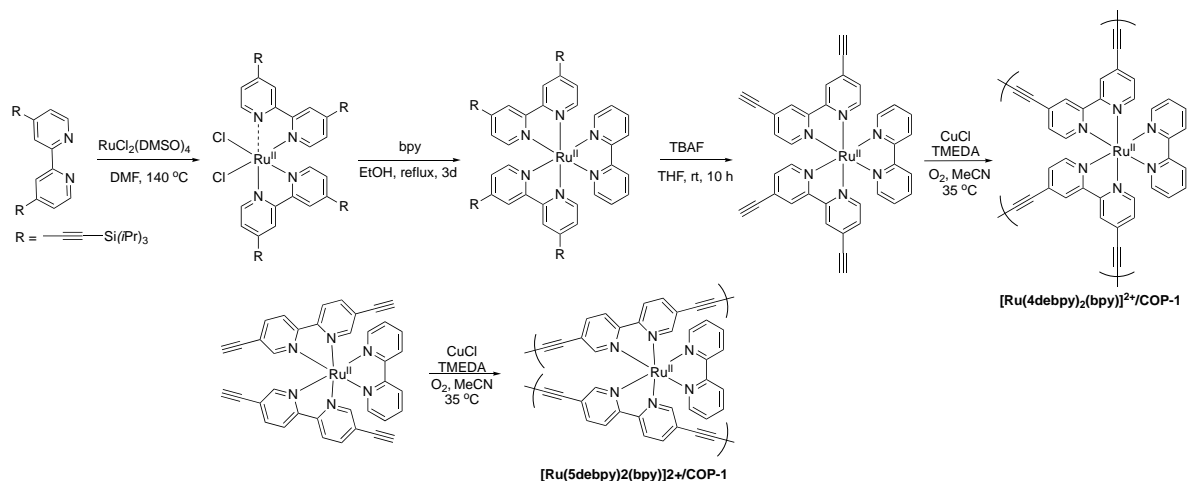
In an attempt to overcome these drawbacks, pre-formed $[\text{Ir}(\text{F-ppy})_2(\text{cbpy})]\text{PF}_6$ ($\text{cbpy} = 4,4'\text{-di(5-carboxypentyl)-2,2'-bipyridine}$) complex was immobilized on available (aminomethyl)polystyrene using carboxylic anchoring groups (Scheme 22) [75]. At the last step of material preparation, the acid groups were activated by oxalyl chloride and reacted with the polymer support to obtain heterogenized catalyst $[\text{Ir}(\text{F-ppy})_2(\text{cbpy})]^+/\text{NPS}$ as orange beads.



Scheme 22. Synthesis of $[\text{Ir}(\text{F-ppy})_2(\text{cbpy})]^{2+}/\text{NPS}$.

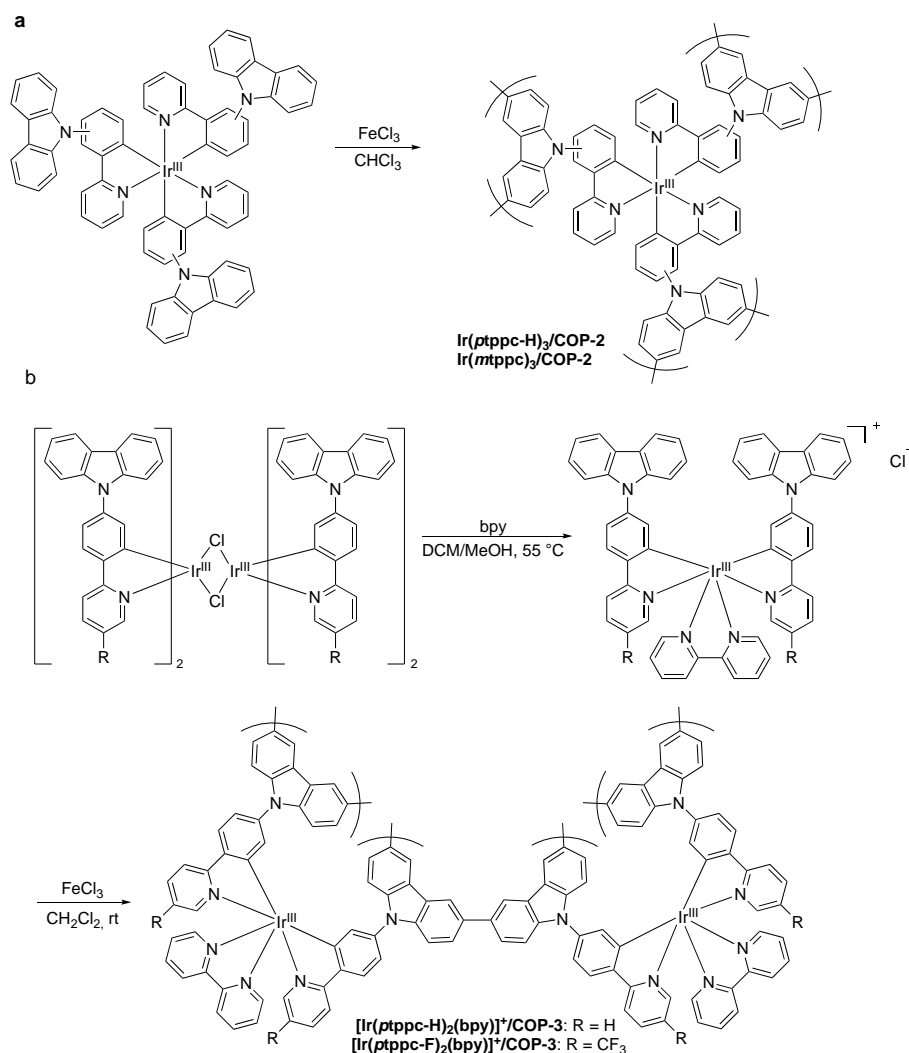
Recently, much attention was drawn to 2D or 3D lightweight nanoporous polymers which are commonly referred to in the recent literature as covalent organic polymers (COPs) or porous organic frameworks (POFs) [101]. These cross-linked polymers are amorphous solid phases, which are insoluble in organic and aqueous solvents and can exhibit a rather high true porosity and chemical stability. As in the case of MOFs, their composition, structural parameters and physicochemical properties can be tuned at the molecular level by an appropriate choice of organic precursors and synthetic strategy. COP supports for photocatalysts may be even advantageous over widely studied MOFs because these networks are assembled by using C–C and C–Het bond forming reactions which afford much more stable frameworks compared to those of MOFs formed by reversible coordination reactions.

The polymers with an extremely high content of potentially photoactive residues were obtained by polymerization of photoactive complexes without addition of any spacer molecules. Lin and coworkers prepared conjugated COPs with 90 wt% of $[\text{Ru}(\text{bpy})_3]^{2+}$ sites according to the oxidative Eglinton coupling of $[\text{Ru}(\text{4debpy})_2(\text{bpy})](\text{NO}_3)_2$ (4debpy = 4,4'-diethynyl-2,2'-bipyridine) or $[\text{Ru}(\text{5debpy})_2(\text{bpy})](\text{NO}_3)_2$ (5debpy = 5,5'-diethynyl-2,2'-bipyridine) (Scheme 23) [76].



Scheme 23. Synthesis of $[\text{Ru}(\text{4debpy})_2(\text{bpy})]^{2+}/\text{COP-1}$ and $[\text{Ru}(\text{5debpy})_2(\text{bpy})]^{2+}/\text{COP-1}$.

The specific surface areas of materials $[\text{Ru}(\text{4debpy})_2(\text{bpy})]^{2+}/\text{COP-1}$ and $[\text{Ru}(\text{5debpy})_2(\text{bpy})]^{2+}/\text{COP-1}$ thus obtained were rather low being equal to $198 \text{ m}^2 \text{ g}^{-1}$ and $15 \text{ m}^2 \text{ g}^{-1}$, respectively. The luminescence lifetimes of heterogenized catalysts were significantly shorter (423 ns and 112 ns, respectively) compared to monomer complexes in solution (962 ns and 574 ns, respectively) likely due to self-quenching observed in polymers, in which the adjacent ruthenium(II) species are electronically coupled *via* ethynyl links. To incorporate Ir^{III} complex in a conjugated microporous framework, $\text{Ir}(\text{ptppc-H})_3$ (ptppc-H = 2-(5-pyridin-2-yl- κN)-5-(9-carbazolyl)phenyl- κC , R = H) and $\text{Ir}(\text{mtppc})_3$ (mtppc = 2-(pyridin-2-yl- κN)-4-(9-carbazolyl)phenyl- κC) complexes were subjected to FeCl_3 -promoted oxidative coupling (Scheme 24) [77]. Polymeric networks $\text{Ir}(\text{ptppc-H})_3/\text{COP-2}$ and $\text{Ir}(\text{mtppc})_3/\text{COP-2}$ (20 wt% of Ir) thus prepared were composed of submicrometer polydisperse spherical particles and displayed specific surface areas of 460 and $480 \text{ m}^2 \text{ g}^{-1}$, respectively.

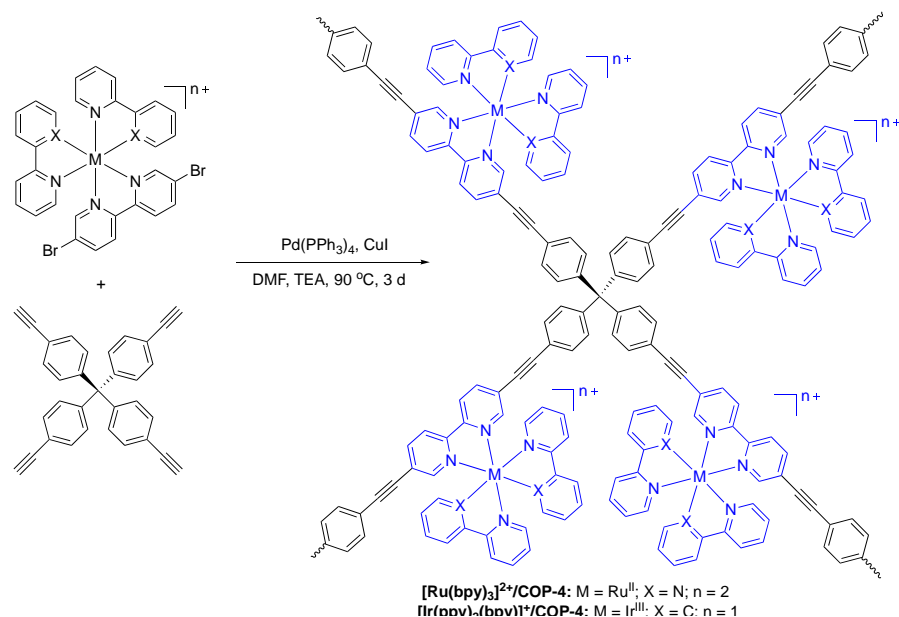


Scheme 24. Synthesis of Ir(tpppc-H)₃/COP-2 and Ir(mtppec)₃/COP-2 (a), [Ir(tpppc-H)₂(bpy)]⁺/COP-3 and [Ir(tpppc-F)₂(bpy)]⁺/COP-3 (b).

Similar strategy was used for the immobilization of [Ir(tpppc-R)₂(bpy)]⁺ (tpppc-R = 2-(5-R-pyridin-2-yl-κN)-5-(9'-carbazolyl)phenyl-κC, R = H (tpppc-H), CF₃(tpppc-F)) complexes in a COP framework (Scheme 24) [78]. Aggregated NPs of [Ir(tpppc-H)₂(bpy)]⁺/COP-3 and [Ir(tpppc-F)₂(bpy)]⁺/COP-3 displayed low specific surface areas of 29 and 129 m² g⁻¹, respectively. The polymers exhibited shorter excited-state lifetimes than corresponding monomers in solutions likely owing to self-quenching processes. The material bearing the trifluoromethyl (CF₃) substituent at the py ring has a much longer excited state lifetime as compared to that of the non-substituted counterpart.

To increase the porosity of COPs and better separate the photo-active catalytic centers, VATMPY complexes were co-polymerized with rigid organic compounds using Sonogashira or Suzuki-Miyaura coupling reactions or the trimerization of alkynes.

The use of *para*-substituted tetraphenylmethane derivatives as spacers could be expected to lead to COPs with ideal diamondoid topology, if the cross-linking effectiveness was qualitative though in reality this is an unrealistic hypothesis. Such attempts were made, e. g. tetrakis(4-ethynylphenyl)methane (TEPB) was reacted with [Ru(bpy)₂(5dbrbpy)]²⁺ (5dbrbpy = 5,5'-dibromo-2,2'-bipyridine) or [Ir(ppy)₂(5dbrbpy)]²⁺ using the Sonogashira coupling to give [Ru(bpy)₃]²⁺/COP-4 (76 wt% of the Ru^{II} complex) and [Ir(ppy)₂(bpy)]⁺/COP-4 polymers (71 wt% of the Ir^{III} complex) (Scheme 25) [79].

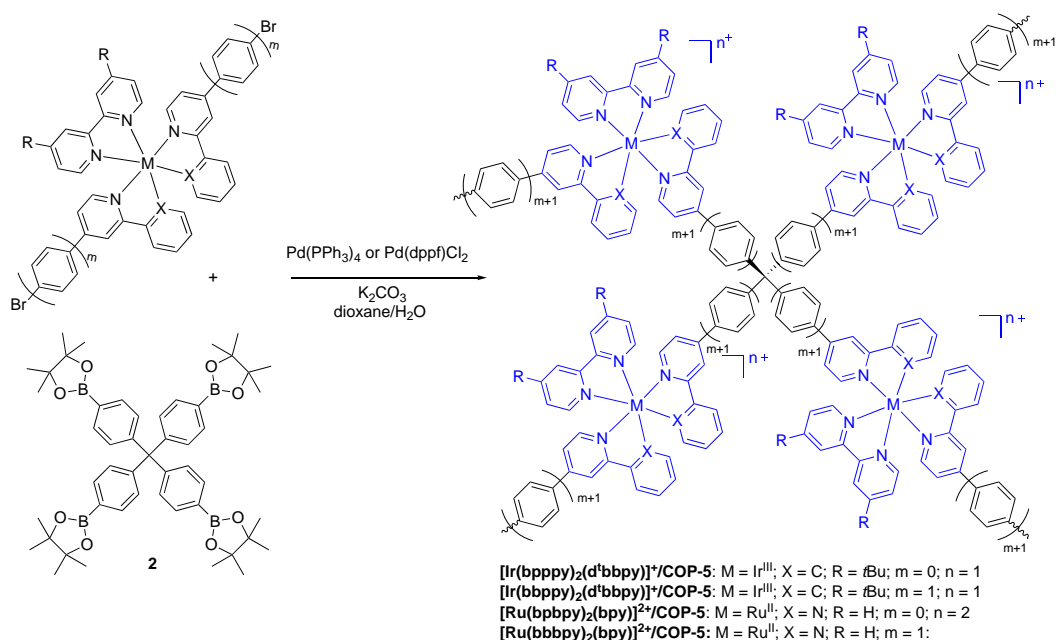


Scheme 25. Synthesis of $[\text{Ru}(\text{bpy})_3]^{2+}/\text{COP-4}$ and $[\text{Ir}(\text{ppy})_2(\text{bpy})]^+/\text{COP-4}$ polymers.

Both polymers were obtained as non-porous solids composed of aggregated NPs with the average dimensions of 100–200 nm. These nanoparticles were believed to be able to serve as light-harvesting antennae to absorb photons in the interior of NPs followed by energy transfer to surface and participating in chemical reactions there. Such processes could be observed only in the solids with high concentration of luminophores, since the probability of energy migration between adjacent chromophore species decreases exponentially with the increase of distance between them. To prove this hypothesis, the photophysics of regular and $[\text{Os}(\text{bpy})_3]^{2+}$ -doped polymers $[\text{Ru}(\text{bpy})_3]^{2+}/\text{COP-4}$ was investigated. Efficient energy transfer from $^*[\text{Ru}(\text{bpy})_3]^{2+}$ to $[\text{Os}(\text{bpy})_3]^{2+}$ was observed at relatively low $[\text{Os}(\text{bpy})_3]^{2+}$ loading (0.1–9 mol%) proving that a photon migration between Ru^{II} complexes must proceed before they reach the $[\text{Os}(\text{bpy})_3]^{2+}$ traps. Such a core-to-surface excited-state transport process, followed by a photocatalytic reaction on the surface, would render all of catalytic centers active, akin to the light-harvesting processes in natural photosynthesis.

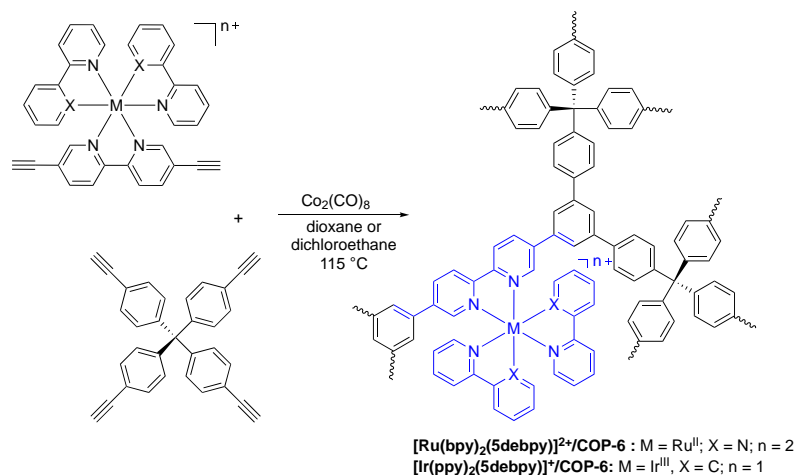
Iridium(III) complex $[\text{Ir}(\text{bppy})_2(\text{d}^t\text{bbpy})]^+$ ($\text{bppy} = 2\text{-}\{[4\text{-}(4\text{-bromophenyl})\text{phenyl}]\text{pyridin-2-yl-}\kappa\text{N}\}\text{phenyl-}\kappa\text{C}$, $\text{d}^t\text{bbpy} = (4,4'\text{-di-tert-butyl})\text{-2,2'-bipyridine}$) and related species $[\text{Ir}(\text{bbppy})_2(\text{d}^t\text{bbpy})]^+$ ($\text{bbppy} = 2\text{-}\{4\text{-}[4\text{-}(4\text{-bromophenyl})\text{phenyl}]\text{pyridin-2-yl-}\kappa\text{N}\}\text{phenyl-}\kappa\text{C}$) were prepared to adjust the size of pores by increasing a distance between iridium centers and the reactive bromine atom (Scheme 26) [80]. These complexes were introduced in the Suzuki–Miyaura reaction with tetraborate **2** to prepare polymers $[\text{Ir}(\text{bppy})_2(\text{d}^t\text{bbpy})]^+/\text{COP-5}$ and $[\text{Ir}(\text{bbppy})_2(\text{d}^t\text{bbpy})]^+/\text{COP-5}$. The replacement of phenylene spacer by a longer biphenylene fragment does allow for an increase a specific surface area of the materials from 29 to 129 $\text{m}^2 \text{g}^{-1}$, respectively.

A similar approach was recently used for immobilization of Ru^{II} complexes. In this case, the porosity of polymers $[\text{Ru}(\text{bpbpy})_2(\text{bpy})]^{2+}/\text{COP-5}$ ($\text{bpbpy} = 4\text{-}(4\text{-bromophenyl})\text{-2,2'-bipyridine}$) and $[\text{Ru}(\text{bbbpy})_2(\text{bpy})]^{2+}/\text{COP-5}$ ($\text{bbbpy} = 4\text{-}[4\text{-}(4\text{-bromophenyl})\text{phenyl}]\text{-2,2'-bipyridine}$) thus prepared was rather low, equal to 15 and 44 $\text{m}^2 \text{g}^{-1}$, respectively [81].



Scheme 26. Synthesis of $[\text{Ir}(\text{bppy})_2(\text{d}^i\text{bbpy})]^+/\text{COP-5}$ and $[\text{Ir}(\text{bbppy})_2(\text{d}^i\text{bbpy})]^+/\text{COP-5}$, $[\text{Ru}(\text{bppy})_2(\text{bpy})]^{2+}/\text{COP-5}$ and $[\text{Ru}(\text{bbppy})_2(\text{bpy})]^{2+}/\text{COP-5}$.

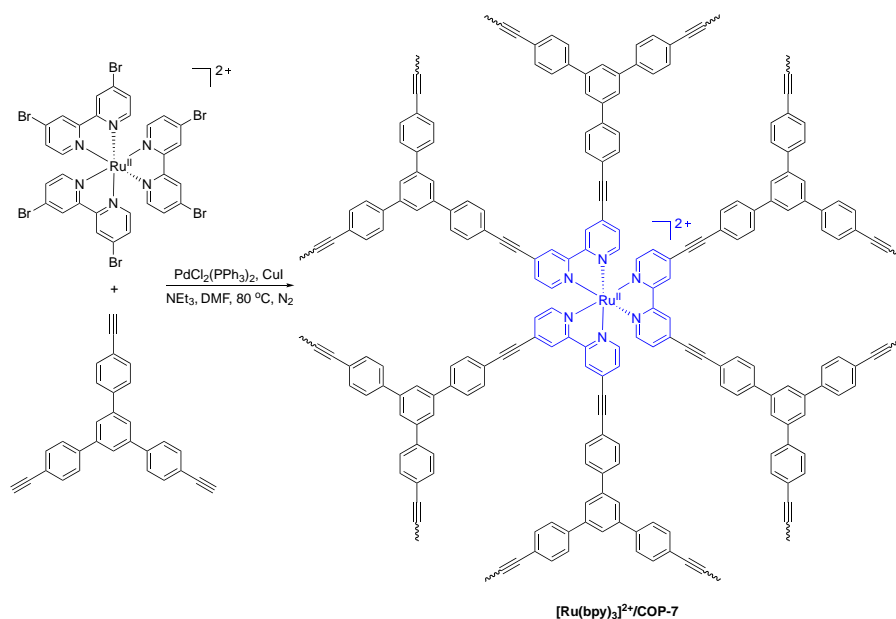
To obtain porous photocatalysts, cobalt carbonyl-mediated trimerization of the terminal alkyne groups on the ligand of the metal complex and tetra(4-ethynylphenyl)methane was used by Lin and coworkers for incorporation of Ru^{II} and Ir^{III} complexes in COPs (Scheme 27) [82]. $[\text{Ru}(\text{bpy})_2(\text{5debpy})]^{2+}/\text{COP-6}$ (4.5 wt% of catalyst) and $[\text{Ir}(\text{ppy})_2(\text{5debpy})]^+/\text{COP-6}$ (2.2 wt% of catalyst) thus prepared display rather similar morphology according to SEM and TEM imaging. Aggregated polymer particles on the order of several micrometers in size with rather rough surfaces appeared to be composed of small nanoparticles with dimensions of about 10 nm. Specific surface areas of Ru^{II} and Ir^{III} -doped materials were as high as 1348 and 1547 $\text{m}^2 \text{g}^{-1}$, respectively, and nitrogen sorption isotherms indicated the presence of micro- and mesopores in these frameworks.



Scheme 27. Synthesis of $[\text{Ru}(\text{bpy})_2(\text{5debpy})]^{2+}/\text{COP-6}$ and $[\text{Ir}(\text{ppy})_2(\text{5debpy})]^+/\text{COP-6}$.

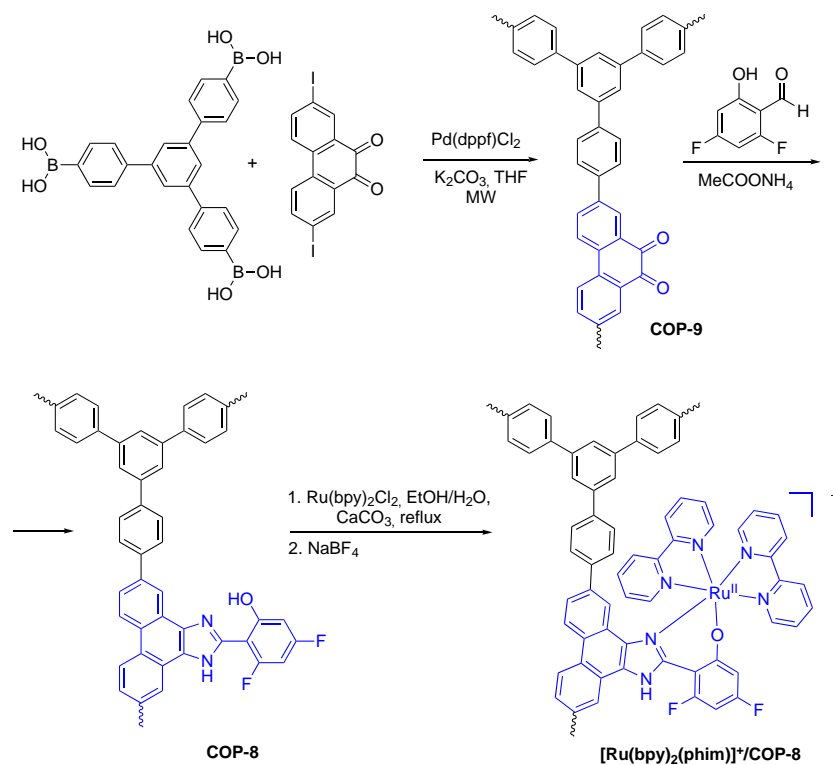
Highly porous COP-based photocatalysts were also prepared by Wang and coworkers reacting $[\text{Ru}(\text{4dbrbpy})_3]^{2+}$ (4dbrbpy = 4,4'-dibromo-2,2'-bipyridine) with a large-size non-planar 1,3,5-tris(4-ethynylphenyl)benzene (TEPB) linker by the Sonogashira reaction (Scheme 28) [83].

The polymer $[\text{Ru}(\text{bpy})_3]^{2+}/\text{COP-7}$ with a specific surface area of $428 \text{ m}^2 \text{ g}^{-1}$ and pore volume of $0.37 \text{ cm}^3 \text{ g}^{-1}$ displayed micro- and mesoporosity.



Scheme 28. Synthesis of $[\text{Ru}(\text{bpy})_3]^{2+}/\text{COP-7}$.

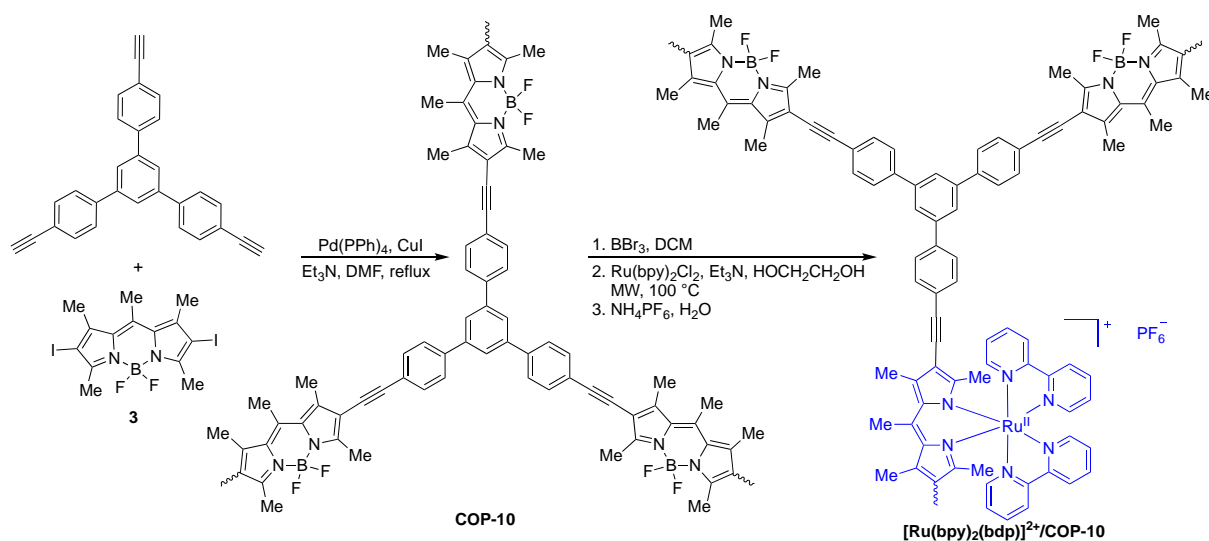
Despite a rather low porosity of most COPs, post-synthetic modification strategy can also be used for the synthesis of photoactive COPs. Sánchez and coworkers synthesized $[\text{Ru}(\text{bpy})_2(\text{phim})]^+/\text{COP-8}$ (phim = 2-(1H-phenanthro[9,10-d]imidazol-2-yl)-3,5-difluorophenol residue) as shown in Scheme 29 [86].



Scheme 29. Synthesis of $[\text{Ru}(\text{bpy})_2(\text{phim})]^+/\text{COP-8}$.

First, porous polymer COP-9 was prepared by the Suzuki-Miyaura reaction between 1,3,5-triphenylbenzene-4',4'',4'''-triboronic acid and 2,7-diiodophenanthrene-9,10-dione under microwave heating. This polymer was further transformed in COP-8 containing free ligand residues, reacting COP-9 with only 0.2 equiv. of 2-hydroxy-3,5-difluorobenzaldehyde to maintain accessibility of catalytic centers in the solid matrix. The target photocatalyst with 1.3 wt% of Ru was obtained reacting COP-8 with $[\text{Ru}(\text{bpy})_3]\text{Cl}_2$ and was isolated after exchange of chloride to tetrafluoroborate counterions. COP-8 exhibited a specific surface area of $285 \text{ m}^2 \text{ g}^{-1}$ which decreased to $49 \text{ m}^2 \text{ g}^{-1}$ after the complexation to Ru^{II} ions.

The synthesis of conjugated microporous polymer COP-10 bearing dipyrromethene moieties starts from the Sonogashira reaction of TEPB and the BODIPY derivative **3** (Scheme 30) [87].



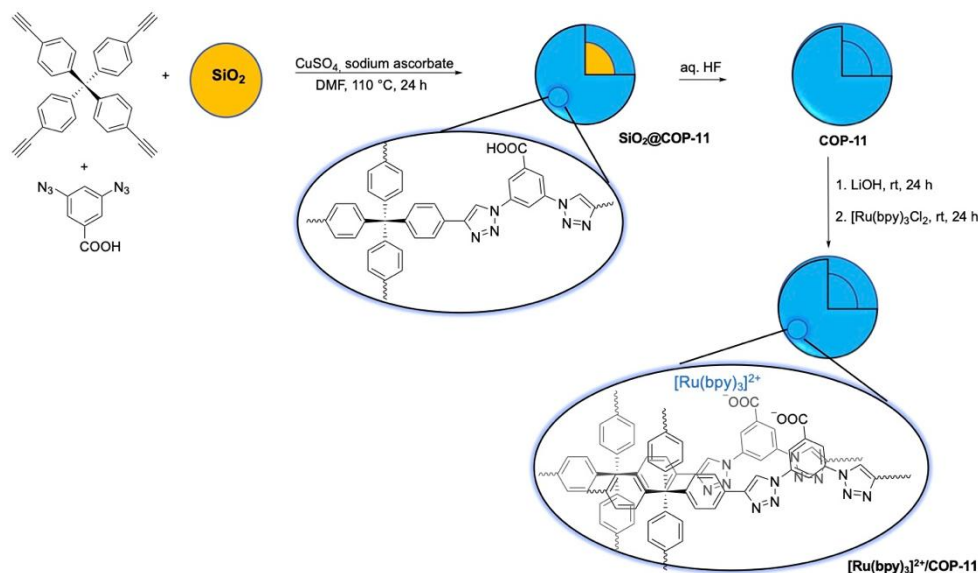
Scheme 30. Synthesis of $[\text{Ru}(\text{bpy})_2(\text{bdp})]^+/\text{COP-10}$.

Deprotection of dipyrin moieties in the polymer thus obtained followed by the complexation of free ligand residues with $[\text{Ru}(\text{bpy})_3]\text{Cl}_2$ affords the target photoredox catalyst $[\text{Ru}(\text{bpy})_2(\text{bdp})]^+/\text{COP-10}$ ($\text{bdp} = 1,3,5,7,9$ -pentamethyldipyrin residue). The overall yield of these two reactions was only 25% and the material thus obtained was doped with 0.61 wt% of Ru and exhibited the BET surface area of $306 \text{ m}^2 \text{ g}^{-1}$.

Thus, most of synthetic approaches developed recently for preparation of photocatalysts embedded in COP afford materials with a rather low internal porosity probably due to partly irregular polymerization reaction and/or strong non-covalent intermolecular interactions of rather flexible organic residues. Most of these materials were obtained as aggregated nanoparticles. The advantages of these nanoparticles lay in their high dispersibility in various solvents, robustness against mechanical damage and rather high external surface areas.

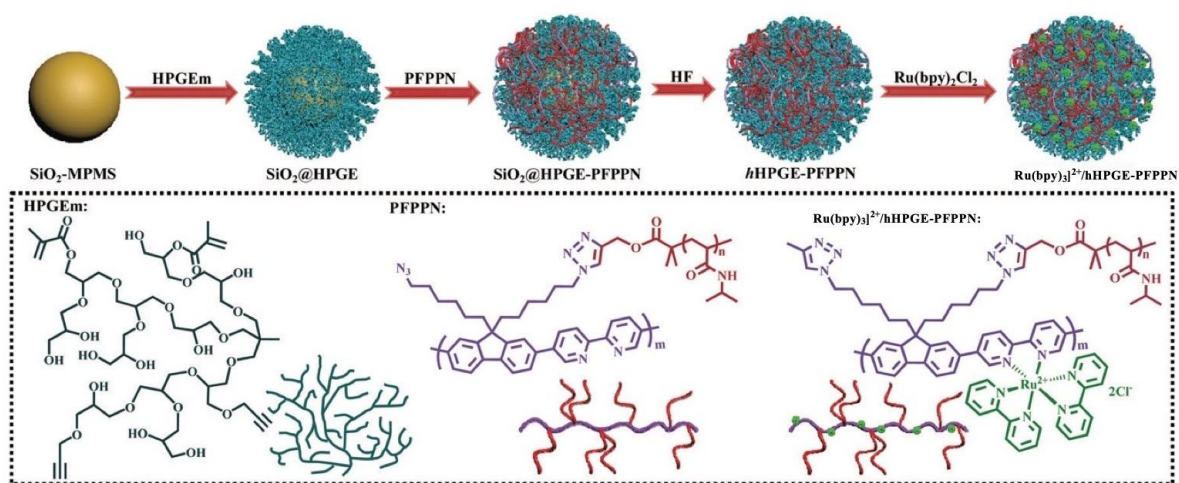
To increase accessibility of photocatalytic centers, hollow nanoparticles of photoactive polymers were developed. Su, Wang and coworkers prepared photocatalyst $[\text{Ru}(\text{bpy})_3]^{2+}/\text{COP-11}$ using hollow nanoparticles COP-11 (Scheme 31) [73]. Monodisperse SiO_2 NPs prepared by Stöber method [95] were modified by APTMS to introduce reactive amino groups. Next, polymer film was grown around the silica core using Cu-catalyzed alkyne–azide cycloaddition (the CuAAC click reaction) of tetrakis(4-ethynylphenyl)methane (TEPM) and 3,5-diazidobenzoic acid in DMF at $110 \text{ }^\circ\text{C}$. The protonation of amino groups by carboxylic acid probably favors the cycloaddition reaction around the NPs. It is also worth noting that the thickness of COP-11 layer can be controlled by tuning the amount of the reagents involved in

this reaction. To go further, the hollow nanospheres were obtained by etching silica core with aqueous hydrofluoric acid. The uniform COP-11 NPs thus obtained were treated with LiOH in water to incorporate Li⁺ cations in the polymer and then reacted with [Ru(bpy)₃]Cl₂ in water to prepare the heterogenized photocatalyst [Ru(bpy)₃]²⁺/COP-11 (2.4 wt% of Ru, 100 m² g⁻¹ BET surface area) by the ion exchange process.



Scheme 31. Synthesis of [Ru(bpy)₃]²⁺/COP-11.

Another photoactive hollow NPs [Ru(bpy)₃]²⁺/hHPGE-PFPPN were synthesized to perform two-stimuli-controlled radical polymerization (Scheme 32) [88]. First, narrow dispersed SiO₂-MPMS NPs with a diameter of 150 nm were prepared by the ammonia-catalyzed sol-gel process followed by the reaction with 3-(trimethoxysilyl)propyl methacrylate to achieve a surface functionalization by methacryl residues (not shown in the Scheme). These NPs were covered with cross-linked hyperbranched shell using precipitation polymerization of methacryloyloxy-functionalized hyperbranched poly(glycerol-co-glycidyl propargyl ether) (HPGEm).

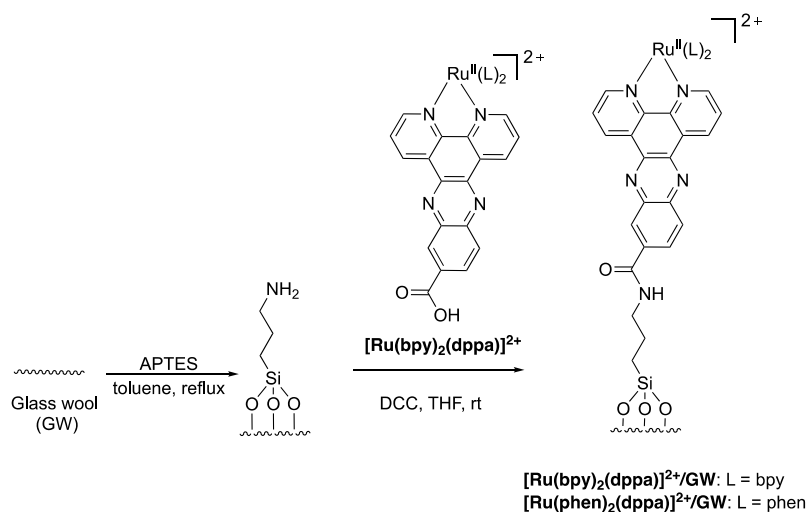


Scheme 32. Synthesis of [Ru(bpy)₃]²⁺/hHPGE-PFPPN Reprinted with permission from Ref. [88]. Copyright 2019 Royal Society of Chemistry.

The peripheral alkyne groups of these core-shell NPs ($\text{SiO}_2\text{@HPGE}$) enable conjugation of these NPs with poly{(9,9-dihexylfluorene)-*alt*-[5,5'-(2,2'-bipyridine)]}-*graft*-poly(*N*-isopropylacrylamide) (PFPPN) *via* Cu-catalyzed azide-alkyne cycloaddition (the CuAAC click reaction) to prepare $\text{SiO}_2\text{@HPGE-PFPPN}$ core-shell NPs. The silica cores were selectively dissolved by hydrofluoric acid treatment and *h*HPGE-PFPPN NPs were further reacted with $[\text{Ru}(\text{bpy})_2\text{Cl}_2]$ to introduce the catalytic centers. The $[\text{Ru}(\text{bpy})_3]^{2+}/\text{hHPGE-PFPPN}$ shells with a thickness of 16 nm and a high cross-linking density provided a firm and robust protection of interior cavities. The Ru^{II} -bpy loading in the NPs was found to be 0.18 mmol g^{-1} , suggesting that around 37% of the bpy sites in the PFP backbone were chelated to ruthenium(II) ions.

Glass wool-supported catalysts

The glass wool was proposed by Scaiano, de Lucas and coworkers as an inexpensive, widely available and potentially versatile inert support for photoactive complexes [48]. Ru^{II} complexes with dipyridophenazine and phen ligands bearing the carboxylate anchoring group were grafted on glass wool according to the synthetic procedure shown in Scheme 33 [48]. The APTES linker which was commonly used for functionalization of silica xerogels (Scheme 8–10) was employed for covalent binding of the complex on the glass wool. The support was treated with APTES to introduce reactive amino groups and then reacted with Ru^{II} complexes in the presence of DCC. The solids thus prepared contained only 0.011–0.012 wt% of Ru. Absorption and emission profiles of the complexes were almost unchanged after their immobilization what is consistent with a high accessibility of the catalytic centers in these materials.



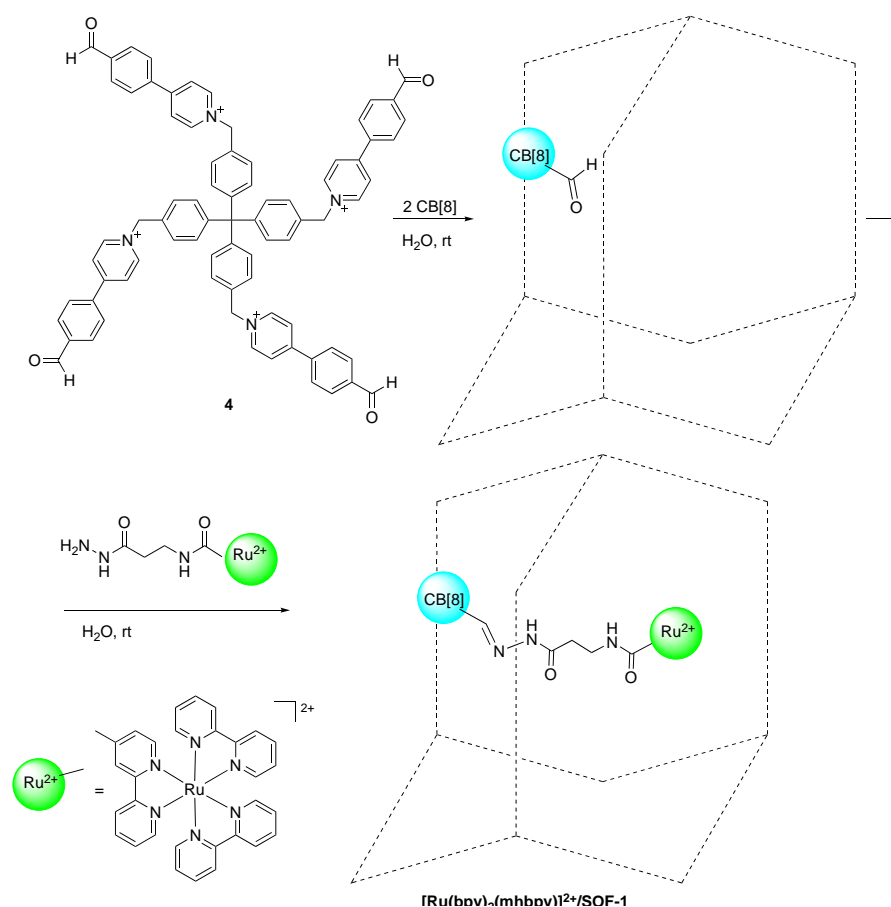
Scheme 33. Functionalization of glass wool with ruthenium(II) photoredox catalyst.

2.2 Supramolecular assembling

Porous supramolecular organic frameworks were prepared by Li, Liu and coworkers reacting cucurbit[8]uril (CB[8]) with rigid organic molecules such as tetra(aryl)methane derivative **4** bearing four 4-phenylpyridinium residues capable of intramolecular self-assembly through π -stacking within the cavity of CB[8] (Scheme 34) [89].

The assembly was performed in water at room temperature and the microcrystals with diamondoid structure were isolated by a slow evaporation of the reaction mixture. To prepare a reusable photoredox catalyst, the formyl-substituted derivative **4** was assembled by using CB[8] and the framework thus prepared was reacted with $[\text{Ru}(\text{bpy})_2(\text{mhbp})]\text{Cl}_2$ (mhbp = *N*-(3-hydrazinyl-3-oxopropyl)-4'-methyl-2,2'-bipyridine-4-carboxamide) in water at room temperature

for 24 h to form hydrazone bonds. The photoactive framework $[\text{Ru}(\text{bpy})_2(\text{mh bpy})]^{2+}/\text{SOF-1}$ was purified by several cycles of dialysis and isolated by a slow evaporation of the reaction mixture.



Scheme 34. Synthesis of $[\text{Ru}(\text{bpy})_2(\text{mh bpy})]^{2+}/\text{SOF-1}$.

The reaction was incomplete and only 5 mol% of the aldehyde groups were reacted under these conditions with the ruthenium complex bearing hydrazine residues. Due to a low content of the complex in the solid, the periodicity of the framework was maintained to a considerable extent after the incorporation of Ru^{II} centers as it was proven by a TEM with selected area electron diffraction (SAED) experiment and the synchrotron XRD profile of solid-state sample. This material is insoluble in non-polar organic solvents that allows for its photocatalytic applications.

To improve the stability of this supramolecular framework two hydrophobic phenyl residues, capable for intramolecular assembly through π -stacking within the cavities of CB[8] were attached to each bpy ligand of $[\text{Ru}(\text{bpy})_3]\text{Cl}_2$ [90, 113]. Encapsulation of six substituents of three bpy ligands gave 3D cubic framework $[\text{Ru}(\text{2pbpy})_3]^{2+}/\text{SOF-2}$ shown in Figure 12. In this porous material, the channel walls were formed by cubic units with Ru centers located in the tops of the cubes. The structure of the solid was confirmed by TEM with SAED imaging, synchrotron small-angle X-ray scattering (SAXS) and the 2D synchrotron X-ray scattering techniques. Thermogravimetric analysis showed that the solid was stable up to 300 °C.

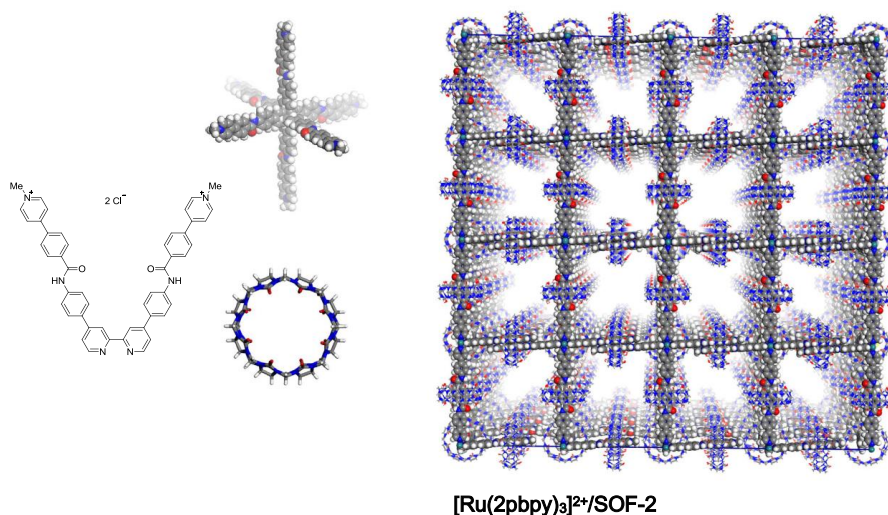


Figure 12. The space-filling structural models of **[Ru(2pbpy)₃]²⁺/SOF-2**: H, white; C, light grey; N, blue; O, red; Ru, cyan (Materials Studio 7.0.) Reprinted from Ref. [113] (Open access journal).

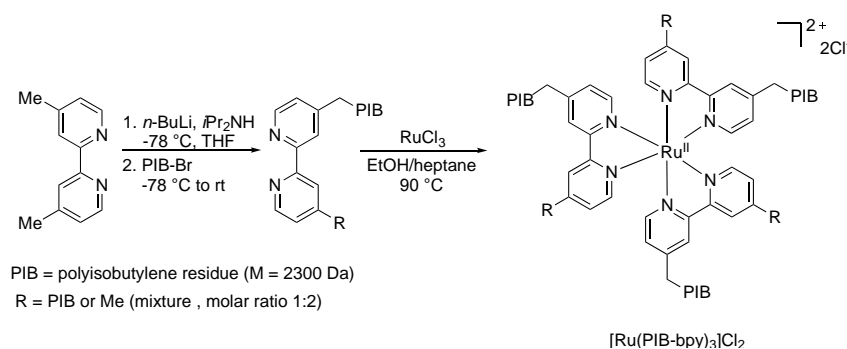
2.3 Phase-separable systems

The solid supported catalysts allow for ready separation of catalysts from reaction products by filtration or centrifugation, but generally are inferior, often dramatically, to homogeneous systems applying the same catalytic species, in what concerns the rate of catalytic reactions and the catalytic efficiency. This can hardly be surprising as the immobilization of catalytic species inevitably restricts their mobility and availability for other participants of catalytic process – a directed transport of reagents towards the surface of support or, which is even more demanding, the diffusion in narrow channels or pores limit the overall reaction rate. Moreover, light utilization in photocatalytic processes is generally higher with homogeneous photocatalysts.

This contradiction between favorable post-reaction processing and unfavorable kinetics of catalytic process severely undermines the usefulness of solid supported systems disregarding how advanced is the structure of material used. Therefore, the other general approach, which aims at combining the best features of homogeneous and heterogeneous catalysis, appeared quite a while ago by taking advantage of numerous liquid systems allowing to perform reactions in a homogeneous liquid phase and to make the products and catalyst to end up in separate and easily separable phases. In some cases, reactions are performed in a biphasic system, where the catalyst and reagents seem to be initially bound to their respective phases. In this approach, catalysts are usually modified to increase the affinity towards this or that liquid. This strategy can be regarded as a special case of immobilization, a liquid phase immobilization. It should be however understood that in such cases reactions usually take place in the interphase boundaries, which are not similar to surface in the solid-liquid catalysis, but rather are thick intermediate liquid layers where the molecules move freely by non-restricted diffusion. In other cases, reactions are run in a single homogeneous liquid phase, and post-reaction phase-separation is achieved by changing miscibility by cooling or addition of “bad” solvents or otherwise, so that the catalyst could be separated from products and easily recycled. Many liquids are capable of serving in such phase-separable systems, including water, fluorinated liquids, ionic liquids, supercritical fluids, even some common solvents. The methods of post-reaction phase separation and catalyst recycling are specific to each case. In this regard, special efforts were focused on the preparation of reusable homogeneous VATMPY complexes, which can be recycled by phase separation.

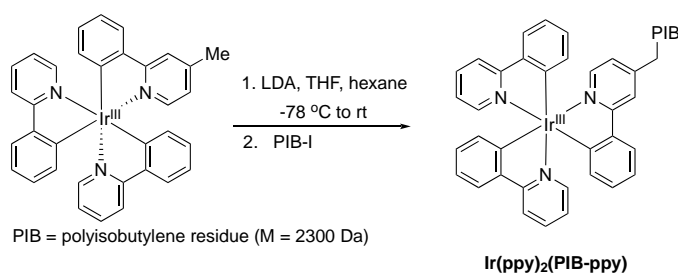
Rueping and coworkers demonstrated that the readily available $[\text{Ir}(\text{ppy})_2(\text{bpy})](\text{PF}_6)$ complex can be used in ionic liquid (1-butyl-3-methylimidazolium tetrafluoroborate) as recyclable catalytic system ($[\text{Ir}(\text{ppy})_2(\text{bpy})](\text{PF}_6)/\text{IL}$), in which the ionic catalyst is bonded to the highly polar ionic liquid phase [114].

On the other hand, Bergbreiter and coworkers proposed to use VATMPY complexes soluble in non-polar alkanes $[\text{Ru}(\text{PIB-bpy})_3]\text{Cl}_2/\text{hep}$ as recyclable photoredox catalysts [115, 116]. In order to be solubilized during the reaction and separated after it, VATMPY complexes were furnished with a non-polar phase-selective polyisobutylene (PIB) chains (Scheme 35). The synthesis started with the transformation of commercially available PIB ($M = 2300$ Da) to halide derivative (not shown in the scheme). Next, the PIB-modified bpy ligand was prepared by the alkylation of lithiated 4,4'-dimethyl-2,2'-bipyridine. Complexation of this chelator to Ru^{II} ions affords $[\text{Ru}(\text{PIB-bpy})_3]\text{Cl}_2$. A mixture of mono- and di-PIB-substituted bpy chelators in molar ratio 6 : 1 was obtained. Moreover, each of these two polymer-modified ligands is polydisperse in molecular weight as a result of diversity in molecular weight of starting PIB-polymers. Nevertheless, all ruthenium(II) complexes with these chelators are soluble in hydrocarbon solvents and can be used as a mixture for performing photocatalytic reaction.



Scheme 35. Synthesis of $[\text{Ru}(\text{PIB-bpy})_3]\text{Cl}_2$.

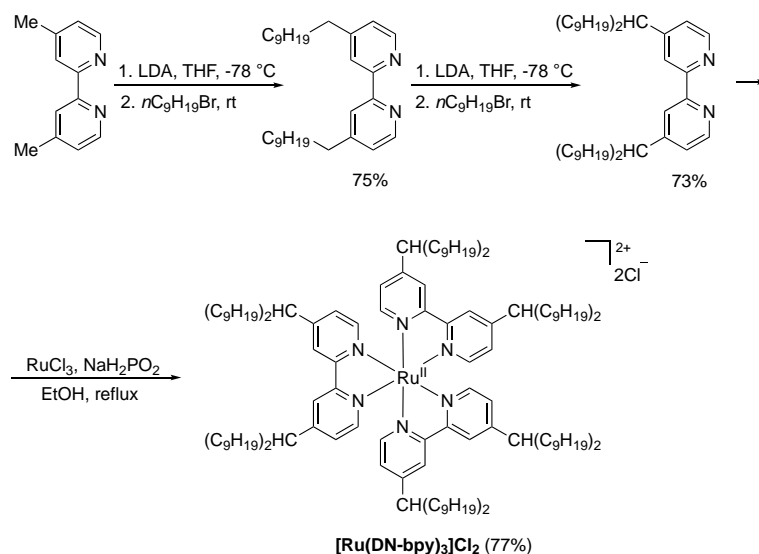
This strategy was also used for the preparation of reusable iridium(III) photoredox catalysts (Scheme 36).



Scheme 36. Synthesis of $[\text{Ir}(\text{ppy})_2(\text{PIB-ppy})]$.

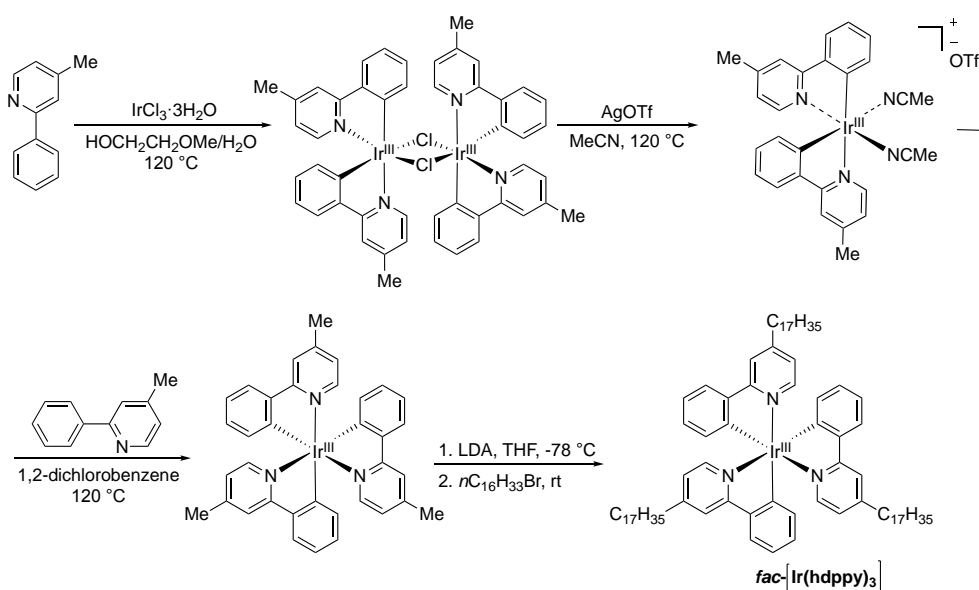
In this case, $[\text{Ir}(\text{ppy})_2(\text{meppy})]$ (meppy = 4-bromo-2-(pyridin-2-yl- κN)phenyl- κC) was a convenient precursor allowing for the selective introduction of only one PIB residue in the ligand molecule [117]. The complex $[\text{Ir}(\text{ppy})_2(\text{PIB-ppy})]$ is soluble in heptane that rendering $\text{Ir}(\text{ppy})_2(\text{PIB-ppy})/\text{hep}$ system useful for photocatalyst recycling.

PIB residues can be replaced by long chain alkyl substituents. Heptane soluble $[\text{Ru}(\text{DN-bpy})_3]\text{Cl}_2$ (DN-bpy = 4,4'-di(nonadec-10-yl)-2,2'-bipyridine) was synthesized performing two successive alkylations of 4,4'-dimethyl-2,2'-bipyridine by 1-bromononane before the complexation of the ligand to the ruthenium(II) ions (Scheme 37) [118].



Scheme 37. Synthesis of [Ru(DN-bpy)₃]Cl₂.

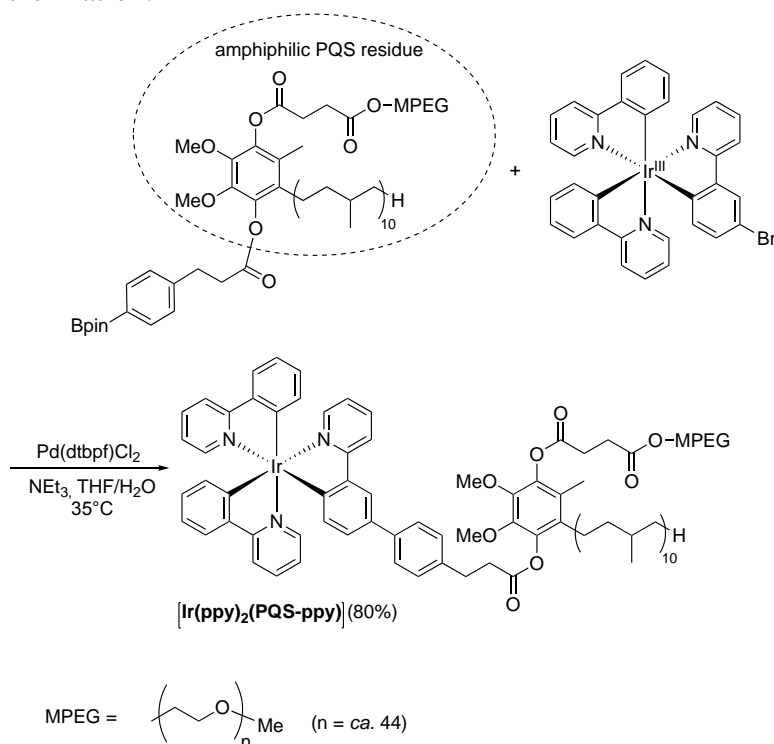
Cyclometalated iridium(III) complex *fac*-[Ir(hdppy)₃] (hdppy = 2-[4-heptadec-1-ylpyridin-2-yl-κN]phenyl-κC) was obtained as a single diastereomer as shown in Scheme 38 [119]. First, the dimer bearing two 4-methyl-2-phenylpyridine (MPP) ligands at each Ir^{III} center was synthesized from iridium(III) trichloride hydrate and MPP. After replacement of chloride ligands by triflates, the dimer was further reacted with an excess of MPP. The lithiation of the complex thus obtained was followed by its alkylation with 1-bromohexadecane afforded the target compound.



Scheme 38. Synthesis of *fac*-[Ir(hdppy)₃].

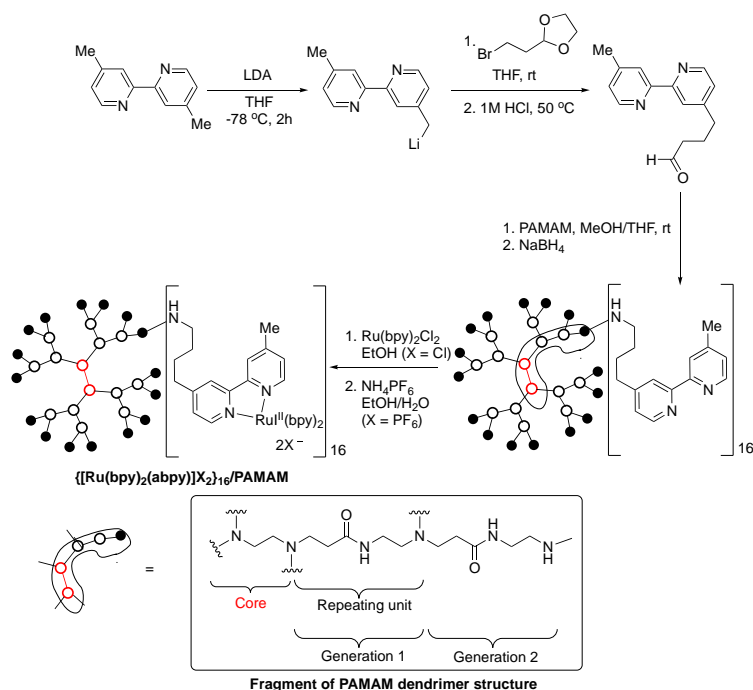
Lipshutz and coworkers used amphiphilic PQS platform shown in Scheme 39 to prepare iridium(III) complex [Ir(ppy)₂(PQS-ppy)] forming stable micelles in aqueous media [120]. After functionalization of the PQS derivative by the boronate ester group as shown in Scheme 39, this compound was reacted with [Ir(ppy)(brppy)] (brppy = 4-bromo-2-(pyridin-2-yl-κN)phenyl-κC) according to the Suzuki-Miyaura reaction to prepare the target complex. Aqueous micellar

solution of this complex $[\text{Ir}(\text{ppy})_2(\text{PQS-ppy})/\text{H}_2\text{O}]$ allows for catalyst recycling in photocatalytic transformation.



Scheme 39. Synthesis of $[\text{Ir}(\text{ppy})_2(\text{PQS-ppy})]$.

To prepare macromolecular photoredox catalyst suitable for nanofiltration separation technology, polyamidoamine (PAMAM) dendrimer was functionalized by bpy residues as shown in Scheme 40 [121]. The synthesis started with the lithiation of 4,4'-dimethyl-2,2'-bipyridine followed by the alkylation reaction and the deprotection of aldehyde group. The key step of this synthetic procedure is the coupling of the oxo-functionalized bpy ligand with amino groups of the second-generation PAMAM dendrimer. Then, the imine bonds in the macromolecular ligand are reduced to increase its chemical stability. Complexation of this chelator to $[\text{Ru}(\text{bpy})_2\text{Cl}_2]$ leads to target macromolecular compound $\{[\text{Ru}(\text{bpy})_2(\text{abpy})]\text{Cl}_2\}_{16}/\text{PAMAM}$ which can be separated from small organic compounds by using nanofiltration through a size exclusion membrane. To simplify this filtration procedure, the chloride counterion was exchanged for hexafluorophosphate according to the ion exchange reaction.



Scheme 40. Synthesis of $\{[\text{Ru}(\text{bpy})_2(\text{abpy})]\text{X}_2\}_{16}/\text{PAMAM}$ ($\text{X} = \text{Cl}, \text{PF}_6$).

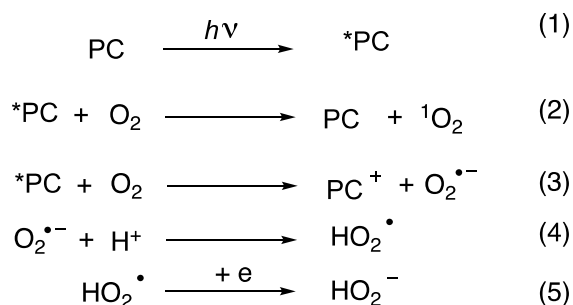
3. Application in photocatalytic reactions

3.1 Oxidative reactions

The oxidation of organic compounds often requires stoichiometric amounts of toxic and hazardous oxidizing agents such as peroxyacids or metal salts in high oxidation states or other such compounds (KMnO_4 , $\text{Na}_2\text{Cr}_2\text{O}_7$, CrO_3 , CeO_2 , or NaIO_4) [122]. These reactions are among the most dangerous and polluting processes in the production of fine chemicals [123]. Replacement of toxic oxidants by molecular oxygen (O_2) or hydrogen peroxide is one of the key objectives in the development of sustainable organic synthesis [124-127]. Photocatalysis is an interesting approach allowing for this purpose.

Molecular oxygen is paramagnetic in its ground state being a triplet able to react *via* branched free-radical reactions, which are non-selective and difficult to control. Oxygen can be made more manageable by transformation through visible light irradiation in the presence of photocatalysts such as VATMPY complexes or organic dyes into the so-called reactive oxygen species (ROS) capable of versatile concerted and polar pathways. The O_2 activation by visible light can proceed according to different mechanisms, which all require the intermediacy of photocatalysts (PC) in their triplet excited state (^3PC) (Eq. 1).

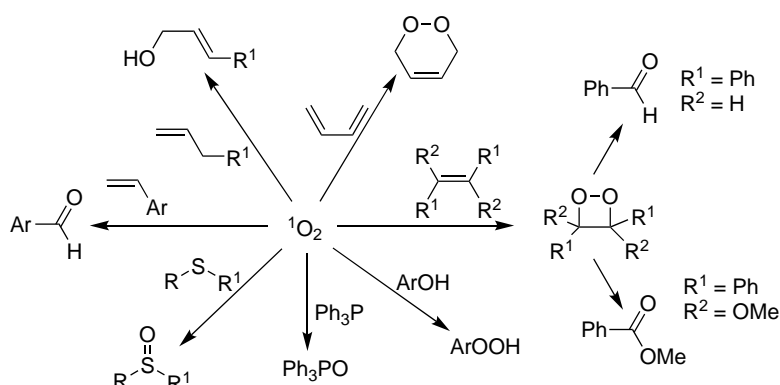
Most commonly, at the primary step of the photocatalytic reaction, the reactive oxygen species (ROS) are generated through energy transfer from $^3\text{MLCT}$ state of VATMPY complex to an oxygen molecule. This energy transfer leads to the formation of singlet oxygen ($^1\text{O}_2$) (Eq. 2). The electron transfer could afford superoxide ($\text{O}_2^{\cdot-}$), which can form the HO_2^{\cdot} radical in the acidic media and be further reduced to hydrogen peroxide anion HO_2^- (Eq. 3-5).



O₂ molecule can also be activated through the formation of metal-oxo complexes. Metal-oxo active sites of enzymes cleave C–H bonds efficiently and selectively giving oxo-functionalized compounds. Many artificial processes catalyzed by transition metal complexes were developed to mimic these reactions [128] and some of them are mediated by visible light, as, for example, oxidation reactions catalyzed by heterogenized [Fe(bpy)₃]²⁺ species [23,24].

Moreover, at the primary photocatalytic step, a substrate molecule can directly react with the excited state of photocatalyst (*PC) [129], but commonly these reactions are more demanding in energy and, thus, less favorable compared to the reaction involving the oxygen molecule.

ROS thus generated can be further involved in various chemical transformations, which proceed without participation of the photocatalyst. Some of them are rather selective and can be used as practical tools in organic synthesis. For example, the reactions of electrophilic singlet oxygen with various electron-rich molecules allow for synthesis of endoperoxides by Diels-Alder reactions, dioxetanes by [2+2] cycloaddition, hydroperoxides from alkenes and phenols, sulfoxides from sulfides and phosphine oxides from phosphines (Scheme 41). It is worth noting that many of the reactions, presented in this scheme, can also proceed *via* the generation of the superoxide anion (O₂^{•-}) or metal-oxo intermediate species. For example, dioxetanes can be formed by using ¹O₂, O₂^{•-} or metal-oxo oxidants depending on the substrates and reaction conditions [23,129,130]. Investigations on the mechanisms of these reactions are challenging and sometimes lead to contradictory results since many reactive oxidant species can be simultaneously generated in the system and their role in the studied reaction varies depending on the reaction conditions.

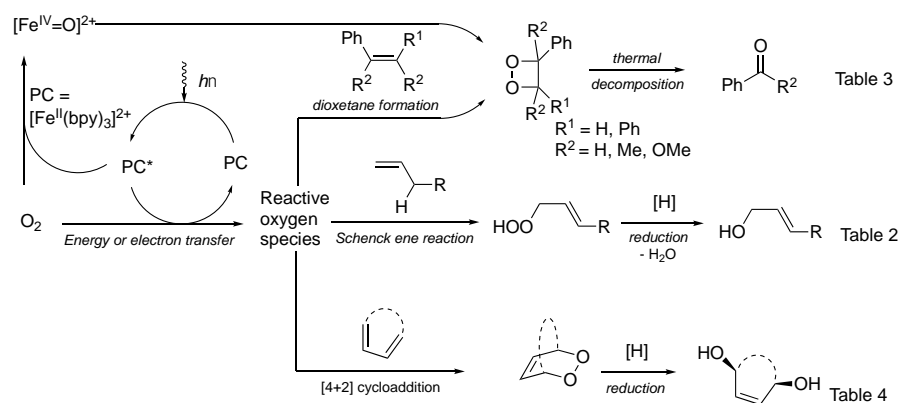


Scheme 41. Oxidation reactions involving ¹O₂.

These reactions are widely used in synthesis of natural products and bioactive molecules [130]. Some of them are already sufficiently mature to be used at the industrial scale. The synthesis of rose oxide, a fragrance, and artemisinin, a well-known antimalarial drug, can be mentioned [130,131].

Oxo-functionalization of unsaturated hydrocarbons

The outcome of photooxidation of unsaturated hydrocarbons by molecular oxygen is strongly dependent on their structure. Many of these reactions are non-selective and accompanied by side reactions such as polymerization of alkenes and isomerization. The synthetically important photocatalytic reactions are summarized in Scheme 42. Heterogenized VATMPY complexes were widely investigated in these reactions, with the focus on recycling the expensive photocatalysts and the increase in the efficiency and selectivity of the oxidation, which can be expected as a positive side effect of some solid supports. These results are detailed in Tables 2–4, including the Schenck ene reaction of olefins containing allylic C–H bonds (Table 2), the cleavage of C–C bond in styrenes (Table 3) and the Diels-Alder reactions of the conjugated dienes and related systems (Table 4).



Scheme 42. Oxo-functionalization of unsaturated hydrocarbons by molecular oxygen upon irradiation with visible light in the presence of heterogenized VATMPY complexes.

As can be seen from these data inorganic compounds and Nafion are generally rather stable to be safely used as photocatalyst supports in the oxidation with molecular oxygen. The heterogenized Ru^{II} , Fe^{II} , Pt^{II} and Ir^{III} catalysts all are generally efficient and afford the products in good yields. Unfortunately, it makes no sense to compare photocatalytic activity of reported materials systematically in the Schenck ene or Diels-Alder reactions since the complexes and supports were varied hazardly and reactions were performed under different irradiation conditions. However, catalyst recycling is of interest and some important information on the positive influence of solid supports on these oxidation reactions can be extracted from these studies despite the fact that reported data are sometimes incomplete or contradictory. We focused our discussion on these results in an attempt to understand why solid photocatalysts sometime exhibit higher catalytic activity than their homogeneous analogues.

Heterogenized Ru^{II} complexes were widely investigated in these oxidation reactions. Glass wool-supported complexes $[Ru(bpy)_2(dppa)]^{2+}/GW$ and $[Ru(phen)_2(dppa)]^{2+}/GW$ (Scheme 33) were useful for photooxidation of 9,10-dimethylantracene and 2-ethylfuran by O_2 (Table 4, entries 8–11) [48]. A high conversion was achieved in the photooxidation of 9,10-dimethylantracene with very low catalyst loading (2×10^{-3} mol%). After the first reaction the catalyst was recovered and reused in four consecutive runs without loss of activity. Unfortunately, comparative studies of these photoactive systems and soluble complexes are still unavailable.

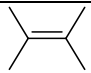
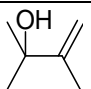
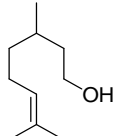
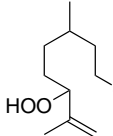
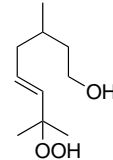
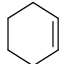
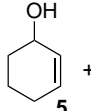
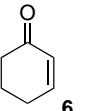
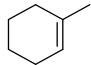
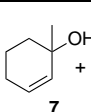
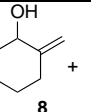
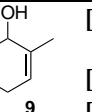

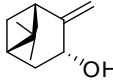
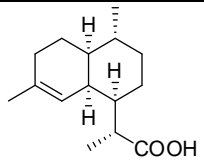
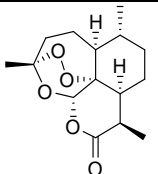
The effect of solid support on the rate of the oxidation reactions was thoroughly studied using a zeolite-encapsulated VATMPY complexes. First, it was shown that ion-exchanged zeolite $[Ru(bpy)_3]^{2+}/Na^+-Y$ mediated the photooxidation of tetramethylethylene (TME) and 1-methylcyclohex-1-ene (Table 2, entries 1 and 4) and in both reactions proceeding with the

participation of singlet oxygen similar results were obtained when functionalized zeolites were replaced by the soluble $[\text{Ru}(\text{bpy})_3]^{2+}$ complex [28]. It was assumed that singlet oxygen generated inside the zeolite at catalytic sites diffuses freely outside to perform its usual transformations in solution. This hypothesis should be nevertheless considered with caution because the incorporation of the Ru^{II} complex into the cages of the host zeolite was not confirmed by spectroscopic techniques and probably bulky Ru^{II} species were adsorbed only at the outer surface of this material.

In contrast, by using well-designed series of zeolite-supported photocatalysts other researches unambiguously demonstrate that the intimate structure of microporous support and distribution of catalytic sites therein can indeed effect the rate and chemoselectivity of the photooxidation reactions [23-25]. In $[\text{Ru}(\text{bpy})_3]^{2+}/\text{M}^+-\text{Y}$ ($\text{M}^+ = \text{Li}^+, \text{K}^+, \text{Rb}^+, \text{Cs}^+$) series, the increase in the photocatalytic activity in the oxidation of α -methylstyrene to acetophenone was observed when large extra-framework K^+, Rb^+ or Cs^+ ions were replaced by smaller Na^+ or Li^+ cations (Table 3, entry 13). The study of the reaction mechanism using scavenging experiments demonstrated that the primary photochemical step was the electron transfer from the excited $^3\text{MLCT}$ state of the Ru^{II} complex to the oxygen molecule leading to the formation of a reactive superoxide ($\text{O}_2^{\cdot-}$). The higher efficiency of $[\text{Ru}(\text{bpy})_3]^{2+}$ in the presence of Na^+ and Li^+ cations was finally explained by their influence on the electronic configuration of excited $^3\text{MLCT}$ state of heterogenized $[\text{Ru}(\text{bpy})_3]^{2+}$ complex.

The photooxidation of styrene under such conditions afforded a mixture of benzaldehyde and 1,2-epoxy-1-phenylethane (Table 3, entry 3). As in the case of α -methylstyrene, TON was increased by two times when large Rb^+ and Cs^+ ions in the zeolite cages were replaced by smaller Na^+ or Li^+ cations. The benzaldehyde/epoxide ratio changed from 6.5 to 8.5 after such exchange of the extra-framework cations. This was explained by an increase in the steric hindrance to the formation of the bulkier epoxide at the catalytic centers in zeolite cages in the presence of large alkali metal cations [25].

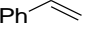
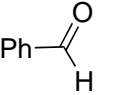
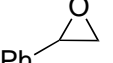
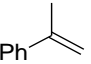
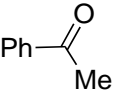
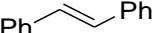
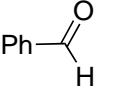
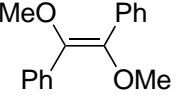
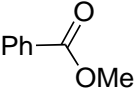
Table 2. Heterogeneous photocatalytic Schenck ene reaction.

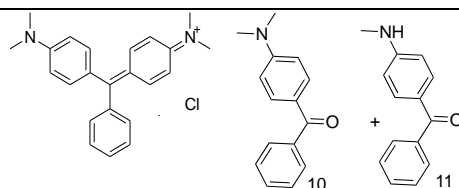
Entry	Substrate	Products ^a	Catalyst, mol% ^b	Light source ^c	Solvent	TON	NMR or GC-MS yield, % (Conversion, %)	Ref
1			[Ru(bpy) ₃] ²⁺ /Na ⁺ -Y	A	MeOH	n/d ^d	(88) ^{e, f}	[28]
2		 + 	[Ru(bpy) ₃] ²⁺ /SiO ₂ (0.1)	B	DCM	n/d	(88–100) ^g	[29]
	+5 similar example:							
3		 + 	[Pt(qpy)] ²⁺ /Nafion	n/a ^h	CH ₃ CN	n/d	18 (5), 82 (6) ⁱ	[69]
4		 +  + 	[Ru(bpy) ₃] ²⁺ /Na ⁺ -Y	A	MeOH	n/d	51 (7), 16 (8), 33 (9) ^{e, j}	[28]
5			[Ru(bpy) ₃] ²⁺ /Ag@SiO ₂ (2 x 10 ⁻³)	C	CH ₃ CN	721	n/d	[30]
6			[Ru(bpy) ₃] ²⁺ /Au@SiO ₂	C	CH ₃ CN	430	n/d	[30]
7			[Ru(bpy) ₃] ²⁺ /SiO ₂ -NP	C	CH ₃ CN	394	n/d	[30]
8			[Ru(bpy) ₃] ²⁺ /Ag-NP	C	CH ₃ CN	63	n/d	[30]
9			[Ru(bpy) ₃] ²⁺ /SiO ₂ (0.1)	B	DCM	n/d	8 ^{k, l}	[29]
10			[Pt(tpy-2)L ₂] ⁺ /Nafion ^m	D	DCM	n/d	95(95) ^{n, o}	[70]
11			Pt(pbp-1)L ₃ /PS (2)	E	DCM	n/d	100 ^{i, k}	[34]
12			[Pt(tpy-1)L ₁] ⁺ /SiO ₂ -XG (0.6)	E	DCM	n/d	100 ^{i, k}	[34]
13			[Pt(pbp)L] ⁺ /SBA-15 (0.8)	F	CH ₃ CN	n/d	100(25) ^{i, k}	[36]
14			[Ru(bpy) ₃] ²⁺ /SiO ₂ (0.1)	B	DCM	n/d	37 ^p	[29]

^aHydroperoxides were obtained as primary products in all reactions. Most of hydroperoxides were reduced to corresponding alcohols to simplify the product characterization. In the case of artemisinic acid (entry 14), the ene reaction was followed by the Hock cleavage of the unsaturated cycle (the acid-catalyzed reaction) and the oxidative ring closure leading to artemisinin (Scheme 43) [131]. ^bThe metal to substrate molar ratio in percentage calculated based on the metal content in the material found by ICP analysis. ^cLight source: A = Hg–Xe lamp, 675 W, $\lambda > 310$ nm; B = white LED, 23 W; C = Xe lamp, 500 W, $\lambda > 400$ nm; D = $\lambda > 450$ nm, the light source was not reported; E = Hg lamp, 500 W,

$\lambda > 400$ nm; F = Hg lamp, 500 W, $\lambda > 450$ nm. ^d n/d = not determined. ^eThe conversion was determined after reduction of the hydrohydroperoxide with trimethylphosphite. ^f In the analogous homogeneous reaction, the conversion was 86%. ^g In the analogous homogeneous reactions, the conversions were 28–94%. ^h n/a = not available. ⁱ The yield and conversion were calculated based on the consumption of the substrate. ^j In the analogous homogeneous reaction, the yields of **7**, **8** and **9** were 50, 17 and 31% respectively. ^k The conversion and the yield were determined after reduction of the hydrohydroperoxide with triphenylphosphine. ^l In the analogous homogeneous reaction, the conversion was 11%. ^m The membrane was swollen in D₂O. ⁿ The yield was determined after reduction of hydrohydroperoxides with sodium bisulfite. ^o Isolated yield. ^p Conversion of artemisinic acid was 96% after 4 h of the reaction under heterogeneous conditions and only 39% under homogeneous conditions in the presence of [Ru(bpy)₃]Cl₂ and TFA. The overall yield of artemisinin under homogeneous conditions was 29%.

Table 3. Photooxidation of styrenes by molecular oxygen in acetonitrile in the presence of heterogenized VATMPY complexes.

En-try	Substrate	Products	Catalyst, mol% ^a	Light source ^b	Reaction time, h	TON (Yield,%)	Ref	
1		 + 	$[\text{Fe}(\text{bpy})_3]^{2+}/\text{M}^+-\text{Y}^c$ (2×10^{-2})	A	24	45–100 ^{d,e}	[23]	
2			$[\text{Fe}(\text{bpy})_3]^{2+}/\text{M}^{2+}-\text{Y}^f$ (3×10^{-2} – 4×10^{-2})	B	24	40–120 ^{d,e}	[24]	
3			$[\text{Ru}(\text{bpy})_3]^{2+}/\text{M}^+-\text{Y}^c$ (3×10^{-2})	A	24	37–85 ^g	[25]	
4			$[\text{Ru}(\text{bpy})_3]^{2+}/\text{Ag}@ \text{SiO}_2$ (2×10^{-3})	C	24	747	[30]	
5			$[\text{Ru}(\text{bpy})_3]^{2+}/\text{Au}@ \text{SiO}_2$	C	24	449	[30]	
6			$[\text{Ru}(\text{bpy})_3]^{2+}/\text{SiO}_2$	C	24	380	[30]	
7			$[\text{Ru}(\text{bpy})_3]^{2+}/\text{Ag}$	C	24	119	[30]	
8			$[\text{Pt}(\text{tpy})\text{L}]^+/\text{SBA-15}$ (2×10^{-3})	D	24	190 ^e	[37, 38]	
9			$[\text{Pt}(\text{tpy})\text{L}]^+/\text{MCM-41}$ (2×10^{-3})	D	24	170 ^e	[37, 38]	
10			$[\text{Pt}(\text{tpy})\text{L}]^+/\text{MCM-48}^h$	D	24	40–260 ^e	[37, 38]	
11			$[\text{Fe}(\text{bpy})_3]^{2+}/\text{M}^+-\text{Y}^c$ (2×10^{-2})	A	24	63–238 ^{d,i}	[23]	
12				$[\text{Fe}(\text{bpy})_3]^{2+}/\text{M}^{2+}-\text{Y}^f$ (3×10^{-2} – 4×10^{-2})	B	24	110–200 ^d	[24]
13				$[\text{Ru}(\text{bpy})_3]^{2+}/\text{M}^+-\text{Y}^c$ (3×10^{-2})	A	24	35–100 ^{g,j}	[23]
14				$[\text{Ru}(\text{bpy})_3]^{2+}/\text{Ag}@ \text{SiO}_2$ (2×10^{-3})	C	24	861	[30]
15				$[\text{Ru}(\text{bpy})_3]^{2+}/\text{Au}@ \text{SiO}_2$	C	24	501	[30]
16				$[\text{Ru}(\text{bpy})_3]^{2+}/\text{SiO}_2$	C	24	420	[30]
17				$[\text{Ru}(\text{bpy})_3]^{2+}/\text{Ag}$	C	24	150	[30]
18				$[\text{Pt}(\text{tpy})\text{L}]^+/\text{SBA-15}$ (2×10^{-3})	D	24	300 ^{d,k}	[38]
19				$[\text{Pt}(\text{tpy})\text{L}]^+/\text{MCM-41}$ (2×10^{-3})	D	24	190 ^{d,k}	[38]
20				$[\text{Pt}(\text{tpy})\text{L}]^+/\text{MCM-48}^h$	D	24	390 ^{d,k}	[38]
21			$[\text{Pt}(\text{ppy})]^{2+}/\text{Nafion}$	n/a ^l	5	(100) ^m	[69]	
22 ⁿ				$\text{Pt}(\text{pbp-1})\text{L}_3/\text{PS}$ (2)	E	2	(100) ^m	[34]
23 ⁿ				$[\text{Pt}(\text{tpy-1})\text{L}_1]^+/\text{SiO}_2\text{-XG}$ (0.6)	E	2	(100) ^m	[34]
24				$[\text{Pt}(\text{pbp})\text{L}]^+/\text{SBA-15}$ (0.8)	F	2	(100)	[36]
25				$\text{Ir}(\text{Mebib})(\text{ppy})\text{L}/\text{SBA-15}$ (1)	B	24	8	[39]
26				$\text{Ir}(\text{Mebib})(\text{ppy})\text{L}/\text{MCM-41}$ (1)	B	24	5	[39]
27				$\text{Ir}(\text{Mebib})(\text{ppy})\text{L}/\text{MCM-48}$ (1)	B	24	6	[39]
28					$[\text{Pt}(\text{ppy})]^{2+}/\text{Nafion}$	n/a ^l	2	(100) ^m
29 ⁿ		$\text{Pt}(\text{pbp-1})\text{L}_3/\text{PS}$ (2)			E	2	(100) ^m	[34]
30 ⁿ		$[\text{Pt}(\text{tpy-1})\text{L}_1]^+/\text{SiO}_2\text{-XG}$ (0.6)			E	2	(100) ^m	[34]
31		$[\text{Pt}(\text{pbp})\text{L}]^+/\text{SBA-15}$ (0.8)			F	1.1	(100)	[36]

32^o**[Fe(bpy)₃]²⁺/Na⁺-Y**

G


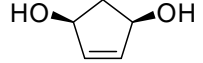
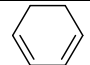
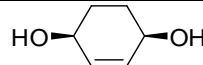
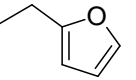
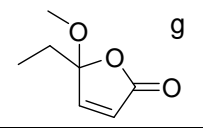
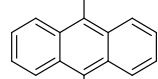
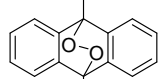
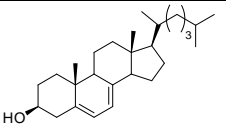
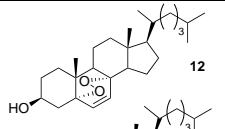
5

(52) **(10)**
(38) **(11)**^p

[132]

^a The metal to substrate molar ratio in percentage was calculated on the basis of the metal content found by ICP analysis. ^b Light Source: A = Xe lamp, 500 W, $\lambda > 430$ nm; B = Xe lamp, 500 W, $\lambda > 420$ nm; C = Xe lamp, 500 W, $\lambda > 400$ nm; D = Xe lamp, 500 W; E = Hg lamp, 500 W, $\lambda > 400$ nm; F = Hg lamp, 500 W, $\lambda > 450$ nm; G = halogen lamp, 500 W, $\lambda > 420$ nm. ^c M = Li⁺, Na⁺, K⁺, Rb⁺, Cs⁺. ^d TON systematically increased with increasing size of metal ions. ^e In the analogous homogeneous reaction the TON was negligible. ^f M = Mg²⁺, Ca²⁺, Sr²⁺, Ba²⁺. ^g TON is systematically decreased with increasing size of metal ions. ^h Catalyst loading varied from 0.001 to 0.012 mol% of Pt. ⁱ Under homogeneous conditions the reaction was not selective. Acetophenone and 1-methyl-1-phenylepoxyde were formed in 44% and 56%, respectively. ^j Under homogeneous conditions the reaction was not selective. Acetophenone, 1-methyl-1-phenyl, and ene-reaction product were formed in 49%, 29% and 22%, respectively. ^k 1-Methyl-1-phenylepoxyde was also obtained as a minor product (< 10%). ^l n/a = not available. ^m The yields were calculated based on the consumption of the substrate. ⁿ Dichloromethane was used as a solvent. ^o H₂O was used as a solvent. ^p Conversion was 98.8%. Methyl benzoate (1.0%), *N,N*-dimethylaniline (0.4%), hydroquinone (6.4 %), 4-aminobenzophenone (0.3%), 4-dimethylamino-4'-methylamino-benzophenone (0.9%) were also identified by GC-MS analysis of the reaction mixture.

Table 4. Heterogeneous photocatalytic Diels-Alder reaction with singlet oxygen.

Entry	Substrate	Products ^a	Catalyst, (mol%) ^b	Light source ^c	Solvent	Conversion, %	NMR or GC-MS yield % (Isolated yield, %)	Ref
1			[Pt(tpy-2)L ₂] ⁺ /Nafion ^d	A	DCM/H ₂ O	> 95	(> 99) ^e	[70]
2			Pt(pbp-1)L ₃ /PS (2)	B	DCM	-	(> 95) ^{e,f}	[34]
3			[Pt(tpy-1)L ₁] ⁺ /SiO ₂ -XG (0.6)	B	DCM	-	(> 95) ^{e,f}	[34]
4			[Pt(pbp)L] ⁺ /SBA-15 (0.8)	C	MeCN	-	> 95 ^{e,f}	[36]
5			Pt(pbp-1)L ₃ /PS (2)	B	DCM	-	> 95 ^{e,f}	[34]
6			[Pt(tpy-1)L ₁] ⁺ /SiO ₂ -XG (0.6)	B	DCM	-	> 95 ^{e,f}	[34]
7			[Pt(pbp)L] ⁺ /SBA-15 (0.8)	C	MeCN	-	> 95 ^{e,f}	[36]
8			[Ru(bpy) ₂ (dppa)] ²⁺ /GW (2 x 10 ⁻³)	D	MeOH	100	n/d ^h	[48]
9			[Ru(phen) ₂ (dppa)] ²⁺ /GW (2 x 10 ⁻³)	D	MeOH	100	n/d	[48]
10			[Ru(bpy) ₂ (dppa)] ²⁺ /GW	D	MeCN	99	n/d	[48]
11			[Ru(phen) ₂ (dppa)] ²⁺ /GW	D	MeCN	99	n/d	[48]
12			[Ru(bpy) ₃] ²⁺ /SiO ₂ (0.1)	E	DCM	99 ⁱ	n/d	[29]
13			[Pt(tpy-2)L ₂] ⁺ /Nafion ^j	E	MeOH- <i>d</i> 4	90	(95) (12) ^{k,1}	[70]
14			[Pt(tpy-2)L ₂] ⁺ /Nafion ^d	E	DCM	95	(80) (12)	[70]
15			Pt(pbp-1)L ₃ /PS (2)	B	DCM	-	76 (12), 24 (13) ^f	[34]
16			[Pt(tpy-1)L ₁] ⁺ /SiO ₂ -XG (0.6)	B	DCM	-	75 (12), 25 (13) ^f	[34]
17			[Pt(pbp)L] ⁺ /SBA-15 (0.8)	C	MeCN- <i>d</i> 3	95	74(12), 26(13)	[36]

^a The endoperoxides were formed as primary products in all reactions and were often directly transformed into corresponding diols by reduction with thiourea to simplify the product characterization. The reaction of 2-ethylfuran in methanol was more complicated (see note g). ^b The metal to substrate molar ratio in percentage was calculated on the basis of the metal content in the material found by ICP analysis. ^c Light source: A = $\lambda > 450$ nm, the light source was not reported; B = Hg lamp, 500 W, $\lambda > 400$ nm; C = Hg lamp, 500 W, $\lambda > 450$ nm; D = blue LED, 450 nm; E = white LED, 23 W. ^d The membrane was swollen in D₂O. ^e The yield obtained after the reduction of the endoperoxide using thiourea. ^f The yields were calculated based on the consumption of the substrate. ^g The Diels-Alder reaction followed by the reaction of the endoperoxide with MeOH [133]. ^h n/d = not determined. ⁱ In the analogous homogeneous reaction the conversion was 97%. ^j The membrane was swollen in CD₃OD. ^k Compound 13 was isolated in trace amount. ¹ In the analogous homogeneous reaction performed in MeOH the conversion was 90%. The isolated yields of compounds **12** and **13** were 75 % and 25%, respectively

Two similar series of $[\text{Fe}(\text{bpy})_3]^{2+}$ -functionalized zeolites $[\text{Fe}(\text{bpy})_3]^{2+}/\text{M}^+-\text{Y}$ and $[\text{Fe}(\text{bpy})_3]^{2+}/\text{M}^{2+}-\text{Y}$, in which the extra-framework cations M^+ and M^{2+} belonged to the group IA or IIA, respectively, were also efficient in the oxidation of styrene and α -methylstyrene by O_2 (Table 3, entries 1, 2, 11 and 12) [23,24]. The mechanistic studies have shown that these reactions proceeded according to mechanism involving $\text{Fe}(\text{IV})=\text{O}$ complexes as intermediates. Interestingly, no oxidation products were obtained when these reactions were performed under homogeneous conditions using $[\text{Fe}(\text{bpy})_3](\text{ClO}_4)_2$ as a photocatalyst. Lower electron density of the iron atom and a longer excited state lifetime observed for the heterogenized $[\text{Fe}(\text{bpy})_3]^{2+}$ complex were evoked for the explanation of its efficiency in these photocatalytic reactions. Both reactions gave the same products as the photooxidations catalyzed by $[\text{Ru}(\text{bpy})_3]^{2+}/\text{M}^+-\text{Y}$ (Table 3, entries 3 and 13). However, in contrast to the Ru^{II} catalytic systems, photosensitizers $[\text{Fe}(\text{bpy})_3]^{2+}/\text{M}^{\text{n}+}-\text{Y}$ bearing large extra-framework metal cations (Cs^+ and Ba^{2+}) allow for the best TON in both series of $[\text{Fe}(\text{bpy})_3]^{2+}/\text{M}^{\text{n}+}-\text{Y}$ catalysts. Since small metal ions should favor the adsorption of substrate molecules in zeolite pores and the reaction acceleration, this process likely is none essential for the oxidation rate. The increase in TON with larger alkali metals was found to correlate with the increase in the intensity of $^3\text{MLCT}$ absorption band and with the decrease in the electron density of the iron atom that probably indicated the influence of electronic structure of heterogenized complexes on the reaction rate.

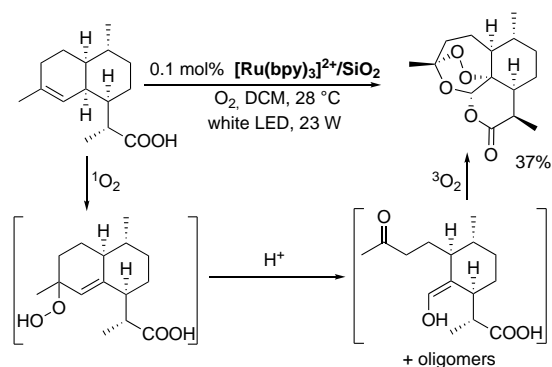
The ratio of benzaldehyde/styrene oxide products in the oxidation of styrene catalyzed by $[\text{Fe}(\text{bpy})_3]^{2+}/\text{M}^{\text{n}+}-\text{Y}$ materials increased along with the increasing size of extra-framework metal cations as it was observed for $[\text{Ru}(\text{bpy})_3]^{2+}/\text{M}^+-\text{Y}$ catalysts. This result is in a good agreement with the hypothesis that the presence of large alkali metal cations in zeolite cages unfavorably influences the formation of the bulkier epoxide.

These studies unambiguously prove that fine tuning of solid matrix offers a tool to alter the photocatalytic properties of heterogenized catalysts without changing their chemical composition on the molecular level. When photoactive complexes are encapsulated in zeolite micropores their electronic structure can be favorably changed. Adsorption of substrates into porous support can also have a positive effect on the photooxidation reaction.

The influence of adsorption was also nicely demonstrated in photooxidation of polar and non-polar compounds by using $[\text{Ru}(\text{bpy})_3]^{2+}/\text{SiO}_2$ catalyst [29]. Oxidation of citronellol and six related compounds bearing various oxygen-containing functional groups by O_2 in dichloromethane (DCM) gave better results (reaction productivity increased by up to 10 times) than the reactions performed under homogeneous conditions (Table 3, entry 2). Probably the adsorption of polar organic compounds by the mesoporous SiO_2 support bearing polar $\text{SiO}-\text{H}$ groups increases a local substrate concentration in a close proximity of the catalytic centers. The reaction acceleration was less pronounced in polar solvents such as acetonitrile and ethanol probably due to their concurrent adsorption on the silica surface. The photooxidation of unsaturated hydrocarbons without hydroxy, carboxy or carbomethoxy groups such as α -pinene and 9,10-dimethylantracene using this photocatalyst $[\text{Ru}(\text{bpy})_3]^{2+}/\text{SiO}_2$ proceeds at a lower rate compared to the reactions with the soluble $[\text{Ru}(\text{bpy})_3]\text{Cl}_2$ complex (Table 2, entry 9 and Table 4, entry 12, respectively) likely due to weak interactions of these substrates with the high polar silica surface [29].

The photosensitizer $[\text{Ru}(\text{bpy})_3]^{2+}/\text{SiO}_2$ can be easily recycled and reused. It was also shown that its photostability is higher than that of $[\text{Ru}(\text{bpy})_3]\text{Cl}_2$ in solution. Nevertheless, a slow catalyst degradation was observed and the conversion was decreased to 70% in the 7th consecutive run of citronellol photooxidation.

A specific role of silica support, was also demonstrated employing $[\text{Ru}(\text{bpy})_3]^{2+}/\text{SiO}_2$ in the synthesis of artemisinin, an antimalarial drug (Table 2, entry 14, Scheme 43) [29].



Scheme 43. The final steps of artemisinin synthesis.

The concluding steps of the artemisinin synthesis involve [4+2] cycloaddition of singlet oxygen followed by the Hock cleavage and the oxidative ring closure. These reactions were more selective and took less irradiation time after the heterogenization of $[\text{Ru}(\text{bpy})_3]\text{Cl}_2$ photocatalyst. Moreover, addition of TFA was not anymore needed because the acidic SiO_2 support served as a catalyst in the Hock cleavage.

Solid supports can also increase the photocatalyst efficiency owing to localized surface plasmon resonance (LSPR). The LSPR-induced enhancement of the catalytic activity of $[\text{Ru}(\text{bpy})_3]^{2+}$ anchored on silica-coated Ag NPs was shown studying the photocatalytic oxidation of 1-methylcyclohex-1-ene and styrenes (Table 2, entry 5 and Table 3, entries 4 and 14) [30]. The reaction TONs provided by this photoactive system were compared to those observed with the complex heterogenized on silica NPs (Table 2, entry 7 and Table 3, entries 6 and 16) and Ag NPs (Table 2, entry 8 and Table 3, entries 7 and 17). For example, in the oxidation of α -methylstyrene with $[\text{Ru}(\text{bpy})_3]^{2+}/\text{Ag}@\text{SiO}_2$ (Table 3, entry 14) TON was twice higher than in the reaction with $[\text{Ru}(\text{bpy})_3]^{2+}/\text{SiO}_2$ (Table 3, entry 16). This increase was consistent with the enhancement of the emission intensity when moving from $[\text{Ru}(\text{bpy})_3]^{2+}/\text{SiO}_2$ to $[\text{Ru}(\text{bpy})_3]^{2+}/\text{Ag}@\text{SiO}_2$ NPs. Moreover, luminescence of $[\text{Ru}(\text{bpy})_3]^{2+}/\text{Ag}@\text{SiO}_2$ was more efficiently quenched by O_2 than that of $[\text{Ru}(\text{bpy})_3]^{2+}/\text{SiO}_2$ that showed a higher efficiency of the interactions between the excited Ru^{II} complex and O_2 at the surface of $[\text{Ru}(\text{bpy})_3]^{2+}/\text{Ag}@\text{SiO}_2$ NPs. This likely is the reason for increasing TONs observed with this material. In contrast, $[\text{Ru}(\text{bpy})_3]^{2+}/\text{Ag}$ NPs were inefficient in the photooxidation reactions. Thus, SiO_2 layer offered not only chemical inertness, transparency, and versatility for conjugation of dyes, but also served as a spacer limiting rapid deactivation of excited Ru^{II} complex by Ag NPs which probably proceeded *via* energy transfer.

Surprisingly, an analogous material $[\text{Ru}(\text{bpy})_3]^{2+}/\text{Au}@\text{SiO}_2$ based on Au core NPs coated with a thin layer of SiO_2 was less efficient compared to the silver analogue (Table 2, entry 6 and Table 3, entries 5 and 15) and exhibited the catalytic activity which only slightly exceeded that of $[\text{Ru}(\text{bpy})_3]^{2+}/\text{SiO}_2$ [30].

The positive effect of solid supports in photocatalytic reactions is particularly high in the case of Pt^{II} photocatalysts. Immobilization of Pt^{II} complexes on silica and Nafion generally leads to a remarkable increase in their emission together with the enhancement of their catalytic efficiency. Polymer- and SiO_2 -supported platinum(II)-quaterpyridine (qpy), platinum(II)-terpyridine complexes (tpy, tpy-1, tpy-2), and cyclometalated platinum(II)-4,6-diphenyl-2,2'-bipyridine (pbp, pbp-1) complexes (Figure 11, Schemes 9, 10, 12 and 19) were investigated in the oxidation by O_2 and most of them exhibited excellent photocatalytic activity.

$[\text{Pt}(\text{qpy})](\text{CF}_3\text{SO}_3)_2$ which is non-emissive in acetonitrile solution was successfully used as a photocatalyst only after its incorporation in a chemically stable fluorinated polymer membrane (Nafion) [69]. Nafion helps to block most of deactivation processes of the triplet excited state of

the complex and the membrane with incorporated Pt^{II} complex shows a long-time and efficient emission. This membrane was used for the generation of singlet oxygen for photooxidation of *trans*-stilbene, *trans*-1,2-dimethoxystilbene and cyclohexene in acetonitrile. The oxidation of both stilbenes proceeded selectively and afforded benzaldehyde or methyl benzoate (Table 3, entries 21 and 28). Cyclohexene gave cyclohex-2-en-1-one as the main product (Table 2, entry 3). This catalyst was easily separated from the reaction mixture and was reused without loss of photocatalytic activity.

Platinum(II)–terpyridine (tpy) complexes incorporated in Nafion [**Pt(tpy-2)L₂**]⁺/Nafion, Figure 11) was efficient for selective photooxidation of cyclopentadiene and α -pinene (Table 4, entry 1; Table 2, entry 10) which probably proceeds in the solution phase outside of Nafion membrane [70]. Interestingly, the rate of these reactions was increased by preliminary swelling of Nafion membrane in D₂O probably owing to the longer lifetime of ¹O₂ in deuterated solvents. The photocatalyst was easily recovered from the reaction mixture when the reaction was completed, and reused in the oxidation of cyclopentadiene 20 times without significant loss of efficiency.

Platinum–tpy complex (Scheme 10) was also incorporated in various periodic mesoporous silicas MCM-41, SBA-15 and MCM-48 to investigate the influence of rigid inorganic support on the oxidation of styrenes by O₂ (Table 3, entries 8–10 and 18–20) [37, 38]. With all materials, the major products of styrene and α -methylstyrene oxidations were benzaldehyde and acetophenone (> 90% selectivity), respectively, and only epoxides were detected as minor side products. The effect of pore size of silica and their arrangement on the TON was clearly observed and the best results were obtained with [**Pt(tpy)L**]⁺/MCM-48. As in the case of [**Ru(bpy)₃**]²⁺/M⁺-Y materials, this most efficient photocatalyst also exhibited the highest intensity of light emission among three studied silica materials. It was assumed that the materials possessing the highest luminescence quantum yield are the best in the generation of ROS that finally may provide the TON increase. Moreover, the oxygen diffusion can be faster in MCM-48 material possessing 3D meso-sized channels that was concluded considering the rate constants of luminescence quenching by oxygen in these materials.

When photooxidation of styrene and α -methylstyrene was performed with [**Pt(tpy)L**]⁺/MCM-48 materials with different loading of the supported Pt^{II} complex (0.2–1.24 wt%) (Table 3, entries 10 and 20), irregular correlation between the reaction rate and the content of Pt^{II} centers was observed. The best results were obtained with the material containing only 0.4 wt% of Pt due to an unfavorable influence of excimers formed in the materials with high photocatalyst loading.

Surprisingly, similar studies of reaction of *trans*-stilbene with molecular oxygen (Table 3, entries 25–27) in the presence of iridium(III) complex [Ir(mebib)(ppy)L] anchored on MCM-41, SBA-15, and MCM-48 mesoporous materials (Scheme 10) showed the advantage of SBA-15 support over other silicas [39]. Thus, the choice of the best silica support can be achieved only by laborious synthesis and investigation of series of relevant materials.

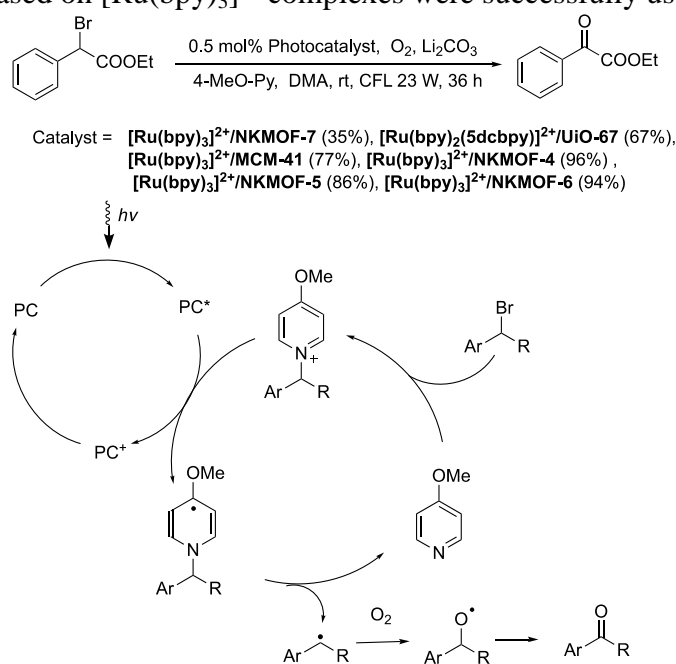
Cyclometalated Pt^{II} 4,6-diphenyl-2,2'-bipyridine (pbp) complex (Scheme 9) incorporated into the channels of mesoporous SBA-15 was also efficient in the photooxidation of various unsaturated hydrocarbons (Table 2, entry 13, Table 3, entries 24 and 31, Table 4, entries 4 and 7) [36]. In the presence of this catalyst, the quantum yield for the product formation in the photooxidation of *trans*-1,2-dimethoxystilbene (Table 3, entry 24) was much higher (up to 100 times) than that observed with the heterogenized catalyst [**Pt(qpy)**]²⁺/Nafion. This was explained by the adsorption of alkenes into silica pores but structural difference of the Pt^{II} complexes in these materials could also contribute to such result. After 10 consecutive runs of this reaction with [**Pt(pbp)L**]⁺/SBA-15 there was almost no leaching of the complex to solution and no significant decrement in the catalyst efficiency.

To compare organic and inorganic supports in the reactions with singlet oxygen, non-porous materials $[\text{Pt}(\text{tpy-1})]^+/\text{SiO}_2\text{-XG}$ (Scheme 12) and $\text{Pt}(\text{pbp-1})\text{L}_3/\text{PS}$ (Scheme 19) were prepared by grafting Pt^{II} complexes on silica and polystyrene, respectively. The photooxidation was performed using a wide series of substrates: 7-dehydrocholesterol, α -pinene, *trans*-stilbene, *trans*-1,2-dimethoxystilbene, cyclopentane, and cyclohexane (Table 2, entries 11 and 12; Table 3, entries 22, 23, 29 and 30; Table 4, entries 2, 3, 5 and 6, respectively) [34]. Both photocatalysts behaved similarly and the expected products were obtained in high yields after 2–4 h of irradiation. Both catalysts can be recycled as was demonstrated by 5 consecutive runs of the photooxidation of *trans*-1,2-dimethoxystilbene.

Though the oxidation is believed to take place in bulk solvent, its outcome sometimes paradoxically depends on the photosensitizer and on the nature of support as discussed above. One additional example is the oxidation of bulky 7-dehydrocholesterol. When singlet oxygen is generated by homogeneous photocatalysts, a mixture of endoperoxide and hydroperoxide *via* [4+2] cycloaddition and Schenck ene reaction, respectively, was obtained. With platinum(II)–tpy and cyclometalated platinum(II)–pbp complexes incorporated in silica $[\text{Pt}(\text{tpy-1})\text{L}_1]^+/\text{SiO}_2\text{-XG}$ (Scheme 12) and $[\text{Pt}(\text{pbp})\text{L}]^+/\text{SBA-15}$ (Scheme 9) as photocatalysts, the oxidation of 7-dehydrocholesterol in DCM or in acetonitrile-*d*₃ was also non-selective and endoperoxide and hydroperoxide were obtained in 3:1 ratio (Table 4, entries 16 and 17) [34]. Cyclometalated platinum(II) 4,6-diphenyl-2,2'-bipyridine complex covalently attached to polystyrene $\text{Pt}(\text{pbp-1})\text{L}_3/\text{PS}$ gave similar results (Table 2, entry 15) [34]. However, when $[\text{Pt}(\text{tpy-2})]/\text{Nafion}$ was used as a photocatalyst in methanol-*d*₄ or DCM, the oxidation became highly chemoselective to yield practically only endoperoxide and the product yield was close to quantitative when the reaction was performed in methanol-*d*₄ (Table 4, entries 13 and 14).

Oxidation of benzyl halides to ketones

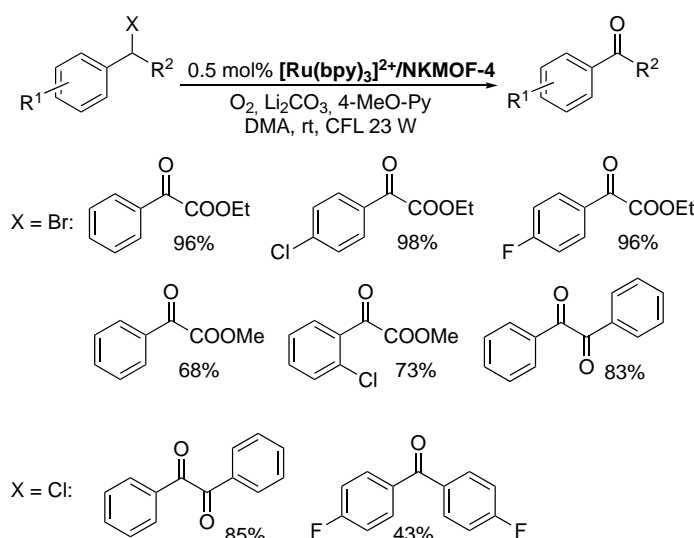
Photocatalytic aerobic oxidation of benzyl halides to ketones under irradiation with visible light proceeds in the presence of lithium carbonate and 4-methoxypyridine (4-MeO-Py) (Scheme 44) [134]. According to proposed reaction mechanism, the radical generated from benzyl halide reacts with O_2 molecule (Scheme 44). Lithium carbonate is required probably to avoid the side reaction of 4-MeO-Py with hydrogen bromide formed in the reaction mixture. Recently solid state photocatalysts based on $[\text{Ru}(\text{bpy})_3]^{2+}$ complexes were successfully used in this reaction.



Scheme 44. Photoredox oxidation of benzyl halides to ketones.

The structure of the solid support strongly influenced the reaction output likely due to the slow diffusion of bulky pyridinium salt formed in the reaction in the pores of materials. When non-porous $[\text{Ru}(\text{bpy})_3]^{2+}/\text{NKMOF-7}$ material was used as catalyst in the aerobic oxidation of ethyl α -bromophenylacetate, the product was obtained in only 35% yield probably due to steric hindrance of the catalytic centers [31]. Better product yields were observed with $[\text{Ru}(\text{bpy})_2(5\text{dcbpy})]^{2+}/\text{UiO-67}$ MOF [61] and the photoredox catalyst prepared by the encapsulation of $[\text{Ru}(\text{bpy})_3]^{2+}$ species in mesoporous MCM-41 silica [31]. However, the silica-based material rapidly released the photocatalyst in solution and could not be reused.

Highly stable and porous zeolite-like MOFs $[\text{Ru}(\text{bpy})_3]^{2+}/\text{NKMOF-n}$ ($n = 4-6$) (Figure 7) showed the highest photocatalytic activity and afforded the product in 86–96% yield [31]. $[\text{Ru}(\text{bpy})_3]^{2+}/\text{NKMOF-4}$ (2,4,6-tri(4-carboxyphenyl)-1,3,5-triazine linkers) was found to be slightly more active among other zeolite-like MOFs and the soluble $[\text{Ru}(\text{bpy})_3]\text{Cl}_2$ complex. Comparative studies of the reactions performed either with the soluble Ru^{II} complex or in the presence of these heterogeneous catalysts demonstrated the superiority of homogeneous conditions during the initial period of 15 h. Nonetheless, on longer exposures the total activity of heterogeneous catalysts was higher likely due to a better photostability of immobilized species. For example, aerobic photooxidation of ethyl α -bromophenylacetate in DMA for 36 h in the presence of 0.5 mol% of $[\text{Ru}(\text{bpy})_3]\text{Cl}_2$ and $[\text{Ru}(\text{bpy})_3]^{2+}/\text{NKMOF-4}$ gave the target product in 85% and 96% yields, respectively. $[\text{Ru}(\text{bpy})_3]^{2+}/\text{NKMOF-4}$ was successfully employed for the oxidation of wide range of benzyl halides (Scheme 45) and reused in 5 catalytic runs of α -bromophenylacetate oxidation showing excellent reproducibility of the products yields.



Scheme 45. Aerobic oxidation of benzyl halides to ketones using $[\text{Ru}(\text{bpy})_3]^{2+}/\text{NKMOF-4}$.

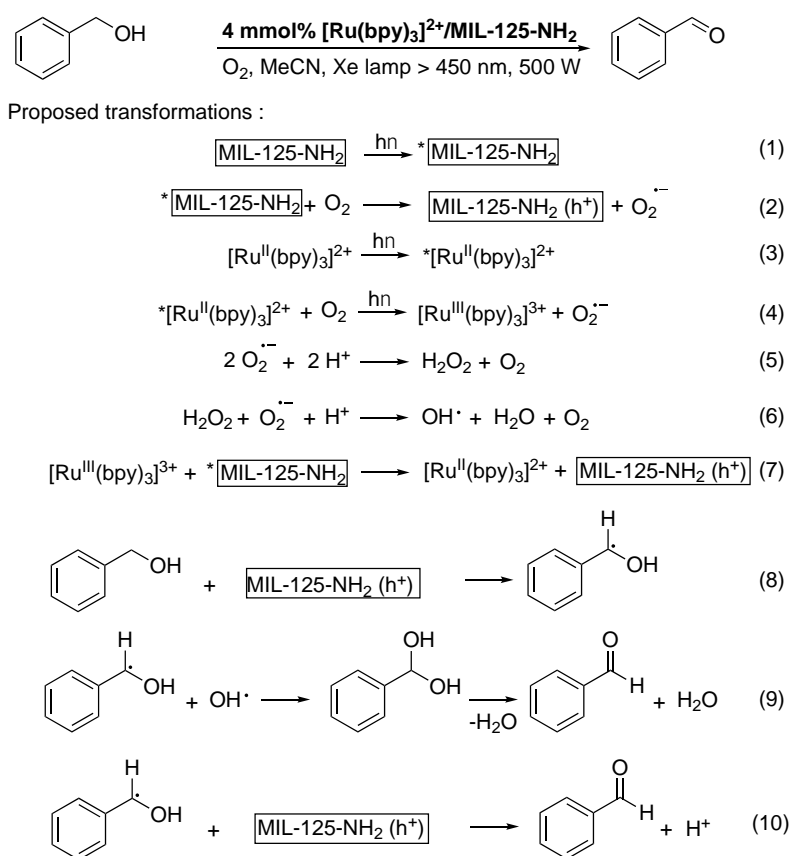
Oxidation of alcohols, phenols and aldehydes

While the photooxidation of alcohols, phenols and aldehydes by O_2 in the presence of VATMPY complexes is widely investigated under homogeneous conditions, the examples of heterogenized complexes suitable for these reactions are rare probably due to a low stability of many reported solid systems in alcoholic media.

Selective photooxidation of benzyl alcohol (BA) by O_2 (Scheme 46) was successful in acetonitrile in the presence of $[\text{Ru}(\text{bpy})_3]^{2+}$ incorporated in the MIL-125- NH_2 MOF

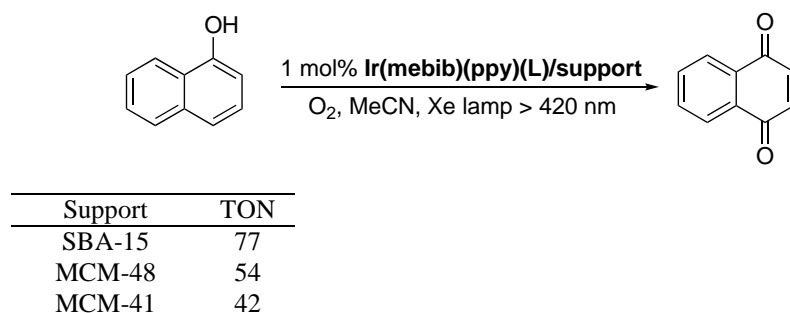
($[\text{Ru}(\text{bpy})_3]^{2+}/\text{MIL-125-NH}_2$, Figure 5) [58]. On the other hand, $[\text{Ru}(\text{bpy})_3]^{2+}$ immobilized in MIL-125 (terephthalic acid linkers) gave only moderate results. This oxidation was less efficient but did proceed when $[\text{Ru}(\text{bpy})_3]^{2+}/\text{MIL-125-NH}_2$ MOF was replaced by bare framework MIL-125-NH₂. When $[\text{Ru}(\text{bpy})_3]\text{Cl}_2$ was employed under homogeneous conditions, the benzaldehyde formation was not observed probably due to inadequate oxidation potential of the complex. Thus, this oxidation is an interesting example of the synergy of photocatalytic properties of $[\text{Ru}(\text{bpy})_3]^{2+}$ complex and the MOF support was observed in the functionalized MIL-125-NH₂ framework which both can be excited under visible-light irradiation.

The most plausible transformations involved in the product formation are shown in Scheme 46. Superoxide generated in the reaction mixture by the electron transfer from excited MIL-125-NH₂ framework and excited $[\text{Ru}(\text{bpy})_3]^{2+}$ complex (Eqs. 2 and 4, respectively) is transformed in the reactive HO[•] radical (Eq. 6). Since $[\text{Ru}(\text{bpy})_3]^{3+}$ cannot oxidize BA, it was assumed that this complex is reduced to $[\text{Ru}(\text{bpy})_3]^{2+}$ by the photoexcited electron located at the Ti₈O₈(OH)₄ cluster of the MIL-125-NH₂ framework (Eq. 7). The photocatalytic oxidation of BA is initiated by the hole of MIL-125-NH₂ formed after the electron transfer (Eq. 8). The radical species (BA[•]) thus generated reacts with the HO[•] radical to give the intermediate aminal which easily undergoes the dehydration giving benzaldehyde. On the other hand, the BA[•] radical probably can accept another hole to yield benzaldehyde without passing through the aminal intermediate (Eq 10).



Scheme 46. Photoredox oxidation of benzyl alcohol.

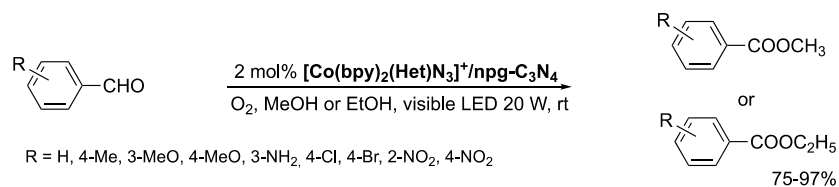
The photooxidation of phenols and naphthols is another benchmark reaction promoted by ¹O₂ [135]. The oxidation of 1-naphthol into 1,4-naphthoquinone under visible light irradiation (Scheme 47) was achieved in the presence of $[\text{Ir}(\text{mebib})(\text{ppy})\text{L}]$ complex grafted on periodic mesoporous silicas (Scheme 10) [39].



Scheme 47. Oxidation of 1-naphthol to 1,4-naphthoquinone.

On the other hand, the reaction was not observed being conducted under the similar experimental conditions in the presence of the soluble $[\text{Ir}(\text{mebib})(\text{ppy})\text{Cl}]$ complex. Excellent catalytic activity of $\text{Ir}(\text{mebib})(\text{ppy})\text{L}/\text{SBA-15}$ was tentatively connected with the high luminescence quantum yield of this material assuming that the complex with the best luminescent properties could provide the highest rate of $^1\text{O}_2$ generation.

Photooxidation can also be used for the preparation of alkyl carboxylates from aldehydes. The most common synthetic routes to carboxylic acid esters involve the transformation of the related acid into more reactive compounds like acyl halide, anhydride, or activated ester which easily participate in the subsequent nucleophilic substitution reactions. An interesting and potentially valuable (in particular, for substrates with reactive functional groups) alternative method of their synthesis is the oxidation of aldehydes in alcoholic media [136,137]. Photoredox catalysts promote the aerobic oxidation of aldehyde under mild conditions (Scheme 48) [138]. This reaction also smoothly proceeds in the presence of the cobalt complex heterogenized on photoactive $\text{npg-C}_3\text{N}_4$ sheets ($[\text{Co}(\text{bpy})_2(\text{Het})\text{N}_3]^+/\text{npg-C}_3\text{N}_4$ material shown in Scheme 1) leading to transformation of electron rich and electron deficient aromatic aldehydes to methyl and ethyl benzoates [53].



Scheme 48. Photocatalytic formation of esters from aromatic aldehydes.

The oxidation of benzaldehyde was also carried out with the analogous cobalt complex under homogeneous conditions and using the non-functionalized photoactive $\text{npg-C}_3\text{N}_4$ sheets. Both these photocatalysts were less efficient as compared to $\text{Co}(\text{bpy})_2(\text{Het})\text{N}_3]^+/\text{npg-C}_3\text{N}_4$ system that demonstrated once again a positive effect of supports capable of efficient charge separation in photocatalyzed reactions.

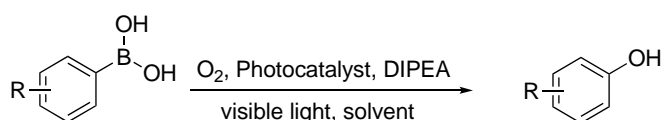
In the oxidation of benzaldehyde, the heterogenized catalyst $[\text{Co}(\text{bpy})_2(\text{Het})\text{N}_3]^+/\text{npg-C}_3\text{N}_4$ was recovered by the centrifugation and reused in 6 consecutive reaction runs without loss of catalytic activity.

Aerobic oxidative hydroxylation of boronic acids

Phenols are versatile intermediates in chemical and pharmaceutical industry. Their synthesis is well developed and they are produced on a large scale [139]. They can be obtained

from various starting compounds, such as aryl halides *via* hydroxylation, arene diazonium salts *via* hydrolysis, and arenes through C–H activation [140,141]. They also can be prepared from readily available aromatic boronic acids using stoichiometric amounts of strong oxidants or molecular oxygen under various catalytic conditions [142]. Many reusable heterogeneous systems were reported for photooxidation of boronic acids by O₂ (Table 5). The reaction proceeds in the presence of a sacrificial electron donor (e. g. DIPEA) through generation of a superoxide as shown in Scheme 49.

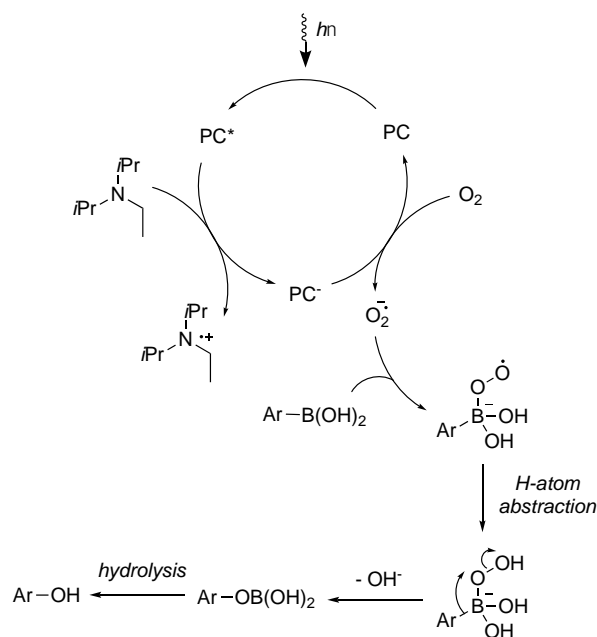
Table 5. Aerobic oxidative hydroxylation of arylboronic acids.



En-try	Substrate	Photocatalyst, mol% ^a	Light Source ^b	Solvent	Time, NMR yield, (Conversion, %)	Ref
1		[Ru(bpy) ₂ (5dcbpy)] ²⁺ /UiO-67 (5)	A	MeOH	48 81 ^c	[63]
2		[Ru(bpy) ₂ (5dcbpy)] ²⁺ /UiO-67 (5)	B	MeOH	48 80 ^c	[63]
3		[Ru(bpy) ₂ (dppa)] ²⁺ /GW (2 x 10 ⁻³)	C	MeCN	6 99	[48]
4		[Ru(phen) ₂ (dppa)] ²⁺ /GW (2 x 10 ⁻³)	C	MeCN	6 >99	[48]
5		[Ru(bpy) ₃] ²⁺ /g-C ₃ N ₄	D	DMF	4 N/D ^d	[52]
6		[Ru(bpy) ₃] ²⁺ /M ⁺ @nano-C ₃ N ₄ ^e	D	DMF	4 N/D ^{f, g}	[52]
7		[Ir(ptppc-H) ₂ (bpy)] ⁺ /COP-3 (2)	E	DMF	48 76	[78]
8		[Ir(ptppc-F) ₂ (bpy)] ⁺ /COP-3 (2)	E	DMF	48 98	[78]
9		[Ir(bpppy) ₂ (d ⁴ bbpy)] ⁺ /COP-5 (1)	F	MeCN	24 >99	[80]
10		[Ir(bbppy) ₂ (d ⁴ bbpy)] ⁺ /COP-5 (1)	F	MeCN	24 >99	[80]
11		[Ru(bpy) ₃] ²⁺ /PCN-99 (2)	G	DMF	48 (65) ^h	[54]
12		[Ir(ptppc-F) ₂ (bpy)] ⁺ /COP-3 (2)	E	DMF	48 85	[78]
13		[Ru(bpy) ₂ (5dcbpy)] ²⁺ /UiO-67 (5)	A	MeOH	48 74	[63]
14		[Ru(bpy) ₂ (5dcbpy)] ²⁺ /UiO-67 (5)	B	MeOH	48 72	[63]
15		[Ru(bpy) ₂ (dppa)] ²⁺ /GW (3x10 ⁻³)	C	MeCN	6 97	[48]
16		[Ru(phen) ₂ (dppa)] ²⁺ /GW (3x10 ⁻³)	C	MeCN	6 98	[48]
17		[Ru(bpy) ₃] ²⁺ /COP-11 (0.5)	H	MeOH	3.5 100 ⁱ	[73]
18		[Ir(bpppy) ₂ (d ⁴ bbpy)] ⁺ /COP-5 (1)	F	MeCN	24 >99	[80]
19		[Ir(ptppc-F) ₂ (bpy)] ⁺ /COP-3 (2)	E	DMF	48 82	[78]
20		[Ru(bpy) ₂ (5dcbpy)] ²⁺ /UiO-67 (5)	A	MeOH	48 76	[63]
21		[Ru(bpy) ₂ (5dcbpy)] ²⁺ /UiO-67 (5)	B	MeOH	48 70	[63]
22		[Ir(bpppy) ₂ (d ⁴ bbpy)] ⁺ /COP-5 (1)	F	MeCN	24 >99	[80]
23		[Ru(bpy) ₂ (5dcbpy)] ²⁺ /UiO-67 (5)	A	MeOH	48 50	[63]
24		[Ru(bpy) ₂ (5dcbpy)] ²⁺ /UiO-67 (5)	B	MeOH	48 47	[63]
25		[Ru(bpy) ₂ (dppa)] ²⁺ /GW (3x10 ⁻³)	C	MeCN	6 96	[48]
26		[Ru(phen) ₂ (dppa)] ²⁺ /GW (3x10 ⁻³)	C	MeCN	6 98	[48]
27		[Ru(bpy) ₂ (dppa)] ²⁺ /GW (3x10 ⁻³)	C	MeCN	6 97	[48]

28		$[\text{Ru}(\text{phen})_2(\text{dppa})]^{2+}/\text{GW}$ (3×10^{-3})	C	MeCN	6	97	[48]
29		$[\text{Ir}(\text{bppy})_2(\text{d}^t\text{bbpy})]^+/\text{COP-5}$ (1)	F	MeCN	24	92	[80]
30		$[\text{Ru}(\text{bpy})_2(\text{dppa})]^{2+}/\text{GW}$ (3×10^{-3})	C	MeCN	6	99	[48]
31		$[\text{Ru}(\text{phen})_2(\text{dppa})]^{2+}/\text{GW}$ (3×10^{-3})	C	MeCN	6	99	[48]
32		$[\text{Ru}(\text{bpy})_3]^{2+}/\text{PCN-99}$ (2)	G	DMF	48	(46) ^j	[54]
33		$[\text{Ir}(\text{ptppc-H})_2(\text{bpy})]^+/\text{COP-3}$ (2)	E	DMF	48	86	[78]
34		$[\text{Ir}(\text{ptppc-F})_2(\text{bpy})]^+/\text{COP-3}$ (2)	E	DMF	48	99	[78]
35		$[\text{Ir}(\text{ptppc-F})_2(\text{bpy})]^+/\text{COP-3}$ (2)	E	DMF	48	99	[78]
36		$[\text{Ir}(\text{bppy})_2(\text{d}^t\text{bbpy})]^+/\text{COP-5}$ (1)	F	MeCN	24	>99	[80]
37		$[\text{Ru}(\text{bpy})_3]^{2+}/\text{PCN-99}$ (2)	G	DMF	48	(59) ^k	[54]
38		$[\text{Ru}(\text{bpy})_2(\text{5dcbpy})]^{2+}/\text{UiO-67}$ (5)	A	MeOH	48	>95	[63]
39		$[\text{Ru}(\text{bpy})_2(\text{5dcbpy})]^{2+}/\text{UiO-67}$ (5)	B	MeOH	48	>95	[63]
40		$[\text{Ir}(\text{ptppc-H})_2(\text{bpy})]^+/\text{COP-3}$ (2)	E	DMF	48	89	[78]
41		$[\text{Ir}(\text{ptppc-F})_2(\text{bpy})]^+/\text{COP-3}$ (2)	E	DMF	48	96	[78]
42		$[\text{Ir}(\text{ptppc-F})_2(\text{bpy})]^+/\text{COP-3}$ (2)	E	DMF	48	99	[78]
43		$[\text{Ir}(\text{ptppc-F})_2(\text{bpy})]^+/\text{COP-3}$ (2)	E	DMF	48	83	[78]
44		$[\text{Ir}(\text{ptppc-F})_2(\text{bpy})]^+/\text{COP-3}$ (2)	E	DMF	48	67	[78]
45		$[\text{Ru}(\text{bpy})_2(\text{5dcbpy})]^{2+}/\text{UiO-67}$ (5)	A	MeOH	48	20	[63]
46		$[\text{Ru}(\text{bpy})_2(\text{5dcbpy})]^{2+}/\text{UiO-67}$ (5)	B	MeOH	48	15	[63]
47		$[\text{Ru}(\text{bpy})_2(\text{5dcbpy})]^{2+}/\text{UiO-67}$ (5)	A	MeOH	48	>95	[63]
48		$[\text{Ru}(\text{bpy})_2(\text{5dcbpy})]^{2+}/\text{UiO-67}$ (5)	B	MeOH	48	91	[63]
49		$[\text{Ir}(\text{bppy})_2(\text{d}^t\text{bbpy})]^+/\text{COP-5}$ (1)	F	MeCN	24	96	[80]

^a The metal to substrate molar ratio in percentage was calculated on the basis of the metal content found by ICP analysis. ^b Light source: A = $\lambda = 365\text{nm}$, the light source was not reported; B = CFL, 23W; C = blue LED, $\lambda = 450\text{nm}$; D = Xe lamp, 500W, $\lambda > 420\text{nm}$; E = white LED, 23W; F = blue LED, 2 x 34W; G = CFL 36W; H = Xe lamp, 300W, $\lambda > 420\text{nm}$; ^c In the analogous homogeneous reaction the yield was >95%. ^d TON was 250. ^e M = Li⁺, Na⁺, K⁺, Rb⁺, Cs⁺. ^f TON was 330–580. ^g TON systematically increased with increasing ionic radii of metal ions. ^h In the analogous homogeneous reaction the conversion was 89%. ⁱ In the analogous homogeneous reaction the conversion was 100% but the reaction was completed after 2 h. ^j In the analogous homogeneous reaction the conversion was 71%. ^k In the analogous homogeneous reaction the conversion was 72%.



Scheme 49. Schematic representation of mechanism of the hydroxylation of arylboronic acids.

Microporous MOF-based photocatalysts showed a low efficiency being involved in this reaction probably due to a slow diffusion of the substrates to the catalytic centers. For example, after encapsulation of $[\text{Ru}(\text{bpy})_3]^{2+}$ species in PCN-99 (Figure 2) the rate of oxidative hydroxylation is decreased for all substrates studied (Table 5, entries 11, 32 and 37) [54].

Better results were obtained when $[\text{Ru}(\text{bpy})_3]^{2+}$ complex was incorporated as linkers in a stable UiO-67-type framework ($[\text{Ru}(\text{bpy})_2(\text{5dcbpy})]^{2+}/\text{UiO-67}$ shown in Scheme 16) [63]. Both electron rich and moderately electron poor aromatic boronic acids were transformed in phenols in good yields in the presence of $[\text{Ru}(\text{bpy})_2(\text{5dcbpy})]^{2+}/\text{UiO-67}$ material (Table 5, entries 1, 2, 13, 14, 20, 21, 23, 24, 38, 39 and 45–48). The heterogenized photocatalyst marginally was a bit less efficient than $[\text{Ru}(\text{bpy})_3]^{2+}$ under homogeneous conditions but was reused in five successive runs of 4-methoxyphenylboronic acid photooxidation.

The importance of material porosity and spatial separation of the catalytic centers in the solid matrix was also observed when aerobic oxidation of phenylboronic acid was conducted using $[\text{Ru}(\text{bpy})_3]^{2+}$ complex grafted on different samples of carbon nitrides [52]. The photocatalytic efficiency of $[\text{Ru}(\text{bpy})_3]^{2+}$ was increased when g- C_3N_4 (Table 5, entry 5) displaying a low specific surface area ($8 \text{ m}^2 \text{ g}^{-1}$) was replaced with the sheets of $\text{Na}^+@ \text{nano-C}_3\text{N}_4$ with a specific surface area of $171 \text{ m}^2 \text{ g}^{-1}$ prepared by the exfoliation of g- C_3N_4 . The spatial separation of the catalytic centers on the surface reduces self-quenching and favors the generation of the reactive superoxide by the electron transfer from excited Ru^{II} complexes to oxygen molecules.

At the next step of optimization of the carbon nitride-based photocatalyst a series of analogous $[\text{Ru}(\text{bpy})_3]^{2+}/\text{M}^+@ \text{nano-C}_3\text{N}_4$ ($\text{M}^+ = \text{Li}^+, \text{Na}^+, \text{K}^+, \text{Rb}^+, \text{Cs}^+$) materials was prepared and investigated in the hydroxylation of phenylboronic acid. TON of the reaction systematically decreased with the increasing size of the alkali metal cations (from 580 to 330 for Li^+ to Cs^+ , respectively, Table 5, entry 6) together with the change of the luminescence intensity of the solids. As reported above, the same systematic correlations were observed in the photooxidation of α -methylstyrene in the presence of $[\text{Ru}(\text{bpy})_3]^{2+}$ species encapsulated in zeolites M^+-Y ($\text{M}^+ = \text{Li}^+, \text{Na}^+, \text{K}^+, \text{Rb}^+, \text{Cs}^+$) (Table 3, entry 13). The favorable changes of the electronic structure of $[\text{Ru}(\text{bpy})_3]^{2+}$ complex were assumed in both cases to explain the positive effect of its immobilization.

Another efficient strategy to prepare the photoredox catalysts for this reaction is the covalent anchoring of Ru^{II} complexes with bpy and phen ligands on the surface of glass wool (Scheme 33) [48]. **[Ru(phen)₂(dppa)]²⁺/GW** and **[Ru(bpy)₂(dppa)]²⁺/GW** photocatalysts thus obtained were stable under mild basic reaction conditions. Both electron rich and electron deficient aromatic boronic acids gave excellent product yields (95–99%) when the reactions were performed in the acetonitrile/water mixture (4:1). For example, irradiation of 4-fluoroboronic acid provided 4-fluorophenol in 96–98% yield (Table 5, entries 25 and 26) while with **[Ru(bpy)₂(5dcbpy)]²⁺/UiO-67** possessing a higher porosity (micropores) this reaction gave the product in only 47% yield (Table 5, entry 24) [63].

In the hydroxylation of phenylboronic acid the **[Ru(phen)₂(dppa)]²⁺/GW** catalyst was successfully recycled 6 times and no catalyst leaching was detected by ICP-OES analysis (detection limit 0.05 ppm).

The photocatalyst prepared from hollow COP NPs and [Ru(bpy)₃]Cl₂ by ion exchange reaction (Scheme 31) gave similarly good results (Table 5, entry 17) despite the presence of only relatively weak electrostatic interactions between Ru^{II} species and the support [73].

Ir^{III} complexes incorporated in COPs work also well. Catalytic activities of two **[Ir(ptppc-H)₂(bpy)]⁺/COP-3** and **[Ir(ptppc-F)₂(bpy)]⁺/COP-3** polymers (Scheme 24) were compared to elucidate the effect of electron-withdrawing CF₃ group in the pyridine ring on the hydroxylation reaction (Table 5, entries 7, 8, 12, 19, 33–35 and 40–44) [78]. Higher product yields were observed in the reactions with the fluorinated complex probably due to a more rapid generation of superoxide anion by the complex possessing a longer excited-state lifetime.

Coordination polymer **[Ir(bbppy)₂(d⁴bbpy)]⁺/COP-5** (Scheme 26) based on another cyclometalated Ir^{III} complex gave similar good results with electron rich and electron deficient boronic acids (Table 5, entries 9, 10, 18, 22, 29, 36 and 49) [80]. Moreover, using this catalyst, 2-naphtheneboronic acid was transformed in 2-naphthol in 96% yield (Table 5, entry 49). The reusability of this photocatalyst seems to be excellent because conversion of phenylboronic acid was as high as 90% after 13 successive runs.

Thus, many heterogenized visible light active complexes were reported to ensure the aerobic hydroxylation of boronic acids. Both organic and inorganic supports gave similar good results.

Oxidation of sulfides to sulfoxides

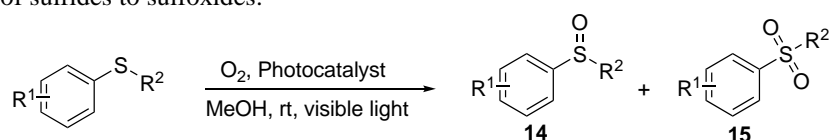
Sulfoxides are widely used in the synthesis of biologically active compounds. Selective oxidation of sulfides to sulfoxides taking place without over-oxidation to sulfone is involved in many synthetic schemes of fine chemical industry. Photocatalytic aerobic oxidation of sulfides in the presence of VATMPY complexes (Table 6) likely proceeds through ¹O₂ generation though there are other mechanistic hypotheses in the literature [143,144]. In the first reported experimental protocol with heterogenized VATMPY complexes, [Ru(bpy)₃]²⁺ immobilized in Nafion membrane was used as a photocatalyst. The oxidation was observed only after incorporation of an electron shuttle, lead ruthenate pyrochlore mineral (Pyc), in the same membrane (Scheme 18). Phenyl sulfides with EDG and EWG were efficiently oxidized by using this membrane (Table 6, entries 1, 13 and 22). When the photocatalyst was recovered and reused in oxidation of thioanisole, almost the same product yields were obtained in three consecutive runs.

Next, Lin and coworkers have found that the electron shuttle was not needed when this photooxidation reaction was performed in methanol [60] and this solvent was widely used to test photocatalytic properties of many novel materials.

Zr-MOFs were often investigated in this reaction proceeding without addition of any basic or coordinating reagents. Firstly, **[Ru(bpy)₂(5dcbpy)]²⁺/UiO-67** in which catalytic centers

are in linkers was used for the oxidation of thioanisole (Table 6, entry 2) [60]. After 22 h of irradiation in the presence of this catalyst under oxygen atmosphere, the sulfide conversion was similar to that obtained with the $[\text{Ru}(\text{bpy})_2(5\text{dcbpy})]\text{Cl}_2$ complex under homogeneous conditions (73% and 72%, respectively). However, an attempt of its reuse failed probably due to a low mechanical stability of the photocatalytic system that is a disadvantage of many reported MOFs [65].

Table 6. Oxidation of sulfides to sulfoxides.



En-try	Substrate	Photocatalyst, mol% ^a	Light Source ^b	Time, h	Conversion, %	Selectivity 14 : 15	Ref
1		$[\text{Ru}(\text{bpy})_3]^{2+}$ & Pyc/Nafion	A	3	>97 ^{c, d}	100	[71]
2		$[\text{Ru}(\text{bpy})_2(5\text{dcbpy})]^{2+}$ /UiO-67 (0.2)	B	22	73 ^e	100	[60]
3		$[\text{Ru}(\text{bpy})_2(5\text{dcbpy})]^{2+}$ /UiO-67 (0.25)	C	-	99 ^c	-	[65]
4		$[\text{Ru}(\text{bpy})_2(5\text{dcbpy})]^{2+}$ /UiO-67 & TiO ₂ /FTO (0.25)	C	-	99 ^c	-	[65]
5		$[\text{Ru}(\text{bpy})_3]^{2+}$ /NPF-201 (1)	B	2.5	>99 ^f	-	[56]
6		$[\text{Ru}(\text{bpy})_2(\text{abpy})]^{2+}$ /SiO ₂ -mNP (0.5)	B	24	89 ^g	-	[32]
7		$[\text{Ir}(\text{bppy})_2(\text{d}^{\text{h}}\text{bbpy})]^{+}$ /COP-5 (1)	D	10	>99	94:5	[80]
8		$[\text{Ir}(\text{ptppc-H})_2(\text{bpy})]^{+}$ /COP-3 (1)	E	10	79	98:2	[78]
9		$[\text{Ir}(\text{ptppc-F})_2(\text{bpy})]^{+}$ /COP-3 (1)	E	10	>99	99:1	[78]
10		$[\text{Ir}(\text{bppy})_2(\text{d}^{\text{h}}\text{bbpy})]^{+}$ /COP-5 (1)	D	18	95	90:5	[80]
11		$[\text{Ir}(\text{ptppc-H})_2(\text{bpy})]^{+}$ /COP-3 (1)	B	10	71	98:2	[78]
12		$[\text{Ir}(\text{ptppc-F})_2(\text{bpy})]^{+}$ /COP-3 (1)	B	10	>99	97:3	[78]
13		$[\text{Ru}(\text{bpy})_3]^{2+}$ & Pyc/Nafion	C	3	90 ^{c, h}	100	[71]
14		$[\text{Ir}(\text{bppy})_2(\text{d}^{\text{h}}\text{bbpy})]^{+}$ /COP-5 (1)	D	20	94	92:2	[80]
15		$[\text{Ir}(\text{ptppc-F})_2(\text{bpy})]^{+}$ /COP-3 (1)	E	10	96	96:4	[78]
16		$[\text{Ir}(\text{ptppc-F})_2(\text{bpy})]^{+}$ /COP-3 (1)	E	13	>99	98:2	[78]
17		$[\text{Ir}(\text{bppy})_2(\text{d}^{\text{h}}\text{bbpy})]^{+}$ /COP-5 (1)	D	20	96	90:6	[80]
18		$[\text{Ir}(\text{ptppc-F})_2(\text{bpy})]^{+}$ /COP-3 (1)	E	16	>99	98:2	[78]
19		$[\text{Ir}(\text{bppy})_2(\text{d}^{\text{h}}\text{bbpy})]^{+}$ /COP-5 (1)	D	10	95	91:4	[80]
20		$[\text{Ir}(\text{ptppc-H})_2(\text{bpy})]^{+}$ /COP-3 (1)	E	15	74	98:2	[78]
21		$[\text{Ir}(\text{ptppc-F})_2(\text{bpy})]^{+}$ /COP-3 (1)	E	15	>99	96:4	[78]
22		$[\text{Ru}(\text{bpy})_3]^{2+}$ & Pyc/Nafion	C	3	96 ^c	100	[71]
23		$[\text{Ir}(\text{bppy})_2(\text{d}^{\text{h}}\text{bbpy})]^{+}$ /COP-5 (1)	D	10	87	84:3	[80]

^a Molar ratio of the metal to substrate in percentage was calculated on the basis of the metal content in the material found by ICP analysis. ^b Light source: A = halogen lamp, 500 W; B = CFL, 26 W; C = blue LED, 3 W; D = blue LED, 2x34W; E = LED, 23W. ^c NMR yield. ^d MeCN/H₂O mixture was used as a solvent. ^e In the analogous homogeneous reaction the conversion was 72%. ^f In the analogous homogeneous reaction the conversion was >99%. ^g In the analogous homogeneous reaction the conversion was 98%. ^h Position of methoxy-group is not specified in the article.

Interestingly, this drawback was overcome by deposition of this MOF as a thin film on the surface of a glass support covered with TiO₂ (Table 6, entry 4) [65]. This slide was reused in five consecutive photooxidation runs affording the product in 95–99%.

The catalytic activity of [Ru(bpy)₃]²⁺/NPF-201 (Table 6, entry 5), in which photocatalyst is non-covalently incorporated in large pores of stable ionic Zr-MOF, was also comparable to that of [Ru(bpy)₃]²⁺ complex in solution [56]. Surprisingly, this photocatalyst was more stable than [Ru(bpy)₂(5dcbpy)]²⁺/UiO-67 despite the presence of only non-covalent interactions between the complex and the framework. It was successively reused in five consecutive runs.

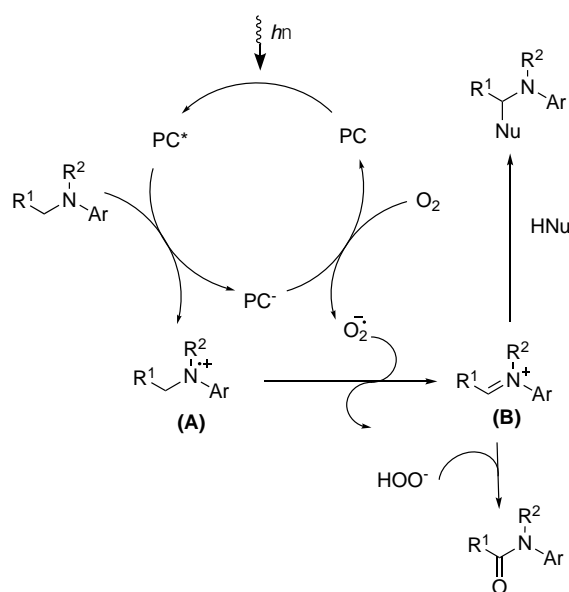
The photocatalyst prepared by covalent binding of [Ru(bpy)₂(abpy)]²⁺ to mesoporous silica NPs (Scheme 8) was similar to [Ru(bpy)₂(abpy)]²⁺ under homogeneous conditions (Table 6, entry 6) and it also was reused 5 times without significant decrease of catalytic activity [32].

The scope of the aerobic photooxidation of sulfides was systematically investigated only with [Ir(ptppc-R)₂(bpy)]²⁺/COP-3 (R = H, CF₃) (Scheme 24) [78] and [Ir(bbppy)₂(d⁴bbpy)]²⁺/COP-5 (Scheme 26) [80]. The aromatic sulfides bearing EDG such as methoxy and methyl groups or EWG such as bromine, chlorine or fluorine were transformed into the corresponding sulfoxides in excellent yields with high selectivity with respect to overoxidation to sulfones (Table 6, entries 7–12, 14–21 and 23). The 90% conversion of sulfides was observed after 5 consecutive catalytic runs for both heterogenized photocatalysts.

Attempts were undertaken to perform asymmetric oxidation of α -ethylbenzyl phenyl sulfide in aqueous methanol using chiral Λ -[Ru(bpy)₃](ClO₄)₂, Δ - and Λ -[Ru(phen)₃](ClO₄)₂ complexes immobilized on montmorillonite clay [27]. The stereoselectivity did not exceed 29% *ee* which was obtained using Δ -[Ru(phen)₃]²⁺-modified clay. Such low stereoselectivity is expected because the transition metal complex and the substrate may communicate only through weak interactions such as dipole–charge, π – π , and van der Waals interactions.

α -Functionalization of amines

C–H functionalization meets the demands of sustainable chemistry and is gaining increasing interest from synthetic chemists. Photoredox catalysis affords convenient protocols to perform many of these transformations, such as α -functionalization of tertiary amines which proceeds *via* the iminium intermediate (Mannich-type reactions) (Scheme 50) [4,145].



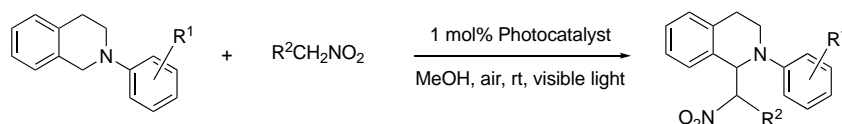
Scheme 50. Transformations involved in α -functionalization of tertiary amines under visible light irradiation in air.

Possible mechanism of this reaction is shown in Scheme 50 [146]. Unlike in the oxo-functionalization reactions, the excited photocatalyst here would rather oxidize the electron-rich amine donor to further pass the electron to oxygen molecule generating superoxide anion $O_2^{\cdot-}$. These species can be transformed to iminium ion according to two pathways (not shown in the scheme). If a hydrogen atom acceptor is present, this species is converted to the iminium ion (**B**). Otherwise the aminium radical cation (**A**) can be deprotonated at the α -position to yield an α -amino radical, which can undergo a second single-electron oxidation, affording the iminium ion (**B**). Iminium cations may be then trapped by nucleophiles to give α -functionalized amines as in the case of Mannich type reactions. It is worth noting that these reactions also slowly proceed in the dark and in the absence of oxygen as it was demonstrated in the detailed mechanistic studies of the reaction of *N*-phenyltetrahydroisoquinoline (THIQ) and nitromethane [146].

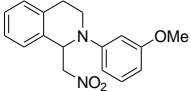
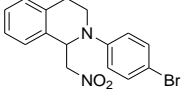
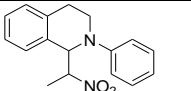
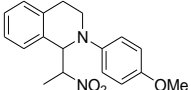
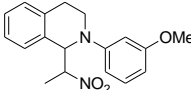
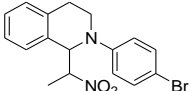
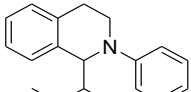
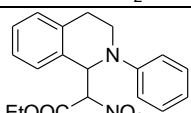
Most of these photoredox catalytic reactions are selective only with THIQs. The photoredox aza-Henry reaction allows the introduction of the α -nitroalkyl group at the THIQ molecules by reacting the intermediate iminium cations with nitroalkanes (Table 7) [146,147].

Fortunately, the conditions are rather similar in most of reported reactions and the reactions can be meaningfully compared. Most of reactions performed with heterogenized Ru^{II} photocatalysts were faster or gave similar conversions as compared to those in the presence of the homogeneous parent photocatalysts likely due to higher stability of these catalysts and more efficient light use by these systems (entries 2–4, 15, 18, 25, 27, 37, 42, 43, 45, 47 and 48) [76,79,82]. The isolated product yields were reported rarely, as shown in Table 7 and, whether available, were in good agreement with the conversions determined by NMR that speaks in favor of the high selectivity of these reactions [76,79]. Many photocatalysts reported were successively reused [60,77,79,82,87].

Table 7. Aza-Henry reaction.



Ent-r	Product	Photocatalyst, mol% ^a	Light source	Time	Conversion (Yield, %)	TON	TOF, ^d	Reference
1		[Ru(bpy) ₂ (phim)] ⁺ /COP-8 (1)	A	72	64	64	1	[86]
2		[Ru(bpy) ₃] ²⁺ /COP-4 (0.2)	B	8	97	485	61	[79]
3		[Ru(4debpy) ₂ (bpy)] ²⁺ /COP-1 (0.2)	B	8	94 (85)	470	59	[76]
4		[Ru(5debpy) ₂ (bpy)] ²⁺ /COP-1 (0.2)	B	8	92 (81)	460	58	[76]
5		[Ru(bpy) ₂ (5debpy)] ²⁺ /COP-6 (0.2)	B	8	90	450	56	[82]
6		[Ru(bpy) ₃] ²⁺ /COP-7 (0.2)	C	4	(97)	485	121	[83]
7		[Ru(bpy) ₂ (bdp)] ²⁺ /COP-10 (1)	D	96	98	98	1	[87]
8		[Ru(bpy) ₂ (5dcbpy)] ²⁺ /UiO-67 (1)	B	12	86	86	7	[60]
9		[Ir(ppy) ₂ (bpy)] ⁺ /COP-4 (0.2)	B	8	55	275	34	[79]
10		[Ir(ptppc-F) ₂ (bpy)] ⁺ /COP-3 (1)	E	24	(96)	96	4	[78]
11		[Ir(ppy) ₂ (5debpy)] ⁺ /COP-6 (1)	B	8	94	94	12	[82]
12		[Ir(ptppc-H) ₃]/COP-2 (2)	F	15	88	44	3	[77]
13		[Ir(mtpc) ₃]/COP-2 (2)	F	15	67	34	2	[77]
14		[Ir(ppy) ₂ (5dcbpy)] ⁺ /UiO-67 (1)	B	12	59	59	5	[60]
15		[Ru(bpy) ₃] ²⁺ /COP-4 (0.2)	B	8	>99	495	62	[79]
16		[Ru(4debpy) ₂ (bpy)] ²⁺ /COP-1 (0.2)	B	8	96 (90)	480	60	[76]
17		[Ru(5debpy) ₂ (bpy)] ²⁺ /COP-1 (0.2)	B	8	96 (82)	480	60	[76]
18		[Ru(bpy) ₂ (5debpy)] ²⁺ /COP-6 (0.2)	B	8	>99	495	62	[82]
19		[Ru(bpy) ₂ (5dcbpy)] ²⁺ /UiO-67 (1)	B	12	97	97	8	[60]

20		$[\text{Ir}(\text{ppy})_2(\text{bpy})]^+/\text{COP-4}$ (0.2)	B	8	>99	495	62	[79]
21		$[\text{Ir}(\text{ppy})_2(5\text{debpy})]^+/\text{COP-6}$ (1)	B	8	91	91	11	[82]
22		$\text{Ir}(\text{ptppc-H})_3/\text{COP-2}$ (2)	F	15	94	47	3	[77]
23		$\text{Ir}(\text{mtppc})_3/\text{COP-2}$ (2)	F	15	89	44	3	[77]
24		$[\text{Ir}(\text{ppy})_2(5\text{debpy})]^+/\text{UiO-67}$ (1)	B	12	96	96	8	[60]
25		$[\text{Ru}(\text{bpy})_2(5\text{debpy})]^{2+}/\text{COP-6}$ (0.2)	B	8	85	425	53	[82]
26		$[\text{Ir}(\text{ppy})_2(5\text{debpy})]^+/\text{COP-6}$ (1)	B	8	98	98	12	[82]
27		$[\text{Ru}(\text{bpy})_3]^{2+}/\text{COP-4}$ (0.2)	B	8	>99	495	62	[79]
28		$[\text{Ru}(4\text{debpy})_2(\text{bpy})]^{2+}/\text{COP-1}$ (0.2)	B	8	99 (89)	495	62	[76]
29		$[\text{Ru}(5\text{debpy})_2(\text{bpy})]^{2+}/\text{COP-1}$ (0.2)	B	8	94 (83)	470	59	[76]
30		$[\text{Ru}(\text{bpy})_2(5\text{debpy})]^{2+}/\text{COP-6}$ (0.2)	B	8	87	435	54	[82]
31		$[\text{Ru}(\text{bpy})_2(5\text{debpy})]^{2+}/\text{UiO-67}$ (1)	B	12	68	68	6	[60]
32		$[\text{Ir}(\text{ppy})_2(\text{bpy})]^+/\text{COP-4}$ (0.2)	B	8	54	270	34	[79]
33		$[\text{Ir}(\text{ppy})_2(5\text{debpy})]^+/\text{COP-6}$ (1)	B	8	97	97	12	[82]
34		$\text{Ir}(\text{ptppc-H})_3/\text{COP-2}$ (2)	F	15	64	32	2	[77]
35		$\text{Ir}(\text{mtppc})_3/\text{COP-2}$ (2)	F	15	71	36	2	[77]
36		$[\text{Ir}(\text{ppy})_2(5\text{debpy})]^+/\text{UiO-67}$ (1)	B	12	62	62	5	[60]
37		$[\text{Ru}(\text{bpy})_3]^{2+}/\text{COP-4}$ (0.2)	B	8	94	470	59	[79]
38		$[\text{Ru}(\text{bpy})_2(5\text{debpy})]^{2+}/\text{COP-6}$ (0.2)	B	8	84	420	53	[82]
39		$[\text{Ru}(\text{bpy})_2(\text{bdp})]^+/\text{COP-10}$ (1)	D	9€	97	97	1	[87]
40		$[\text{Ir}(\text{ptppc-F})_2(\text{bpy})]^+/\text{COP-3}$ (1)	E	24	(95)	95	4	[78]
41		$[\text{Ir}(\text{ppy})_2(5\text{debpy})]^+/\text{COP-6}$ (1)	B	8	94	94	12	[82]
42		$[\text{Ru}(\text{bpy})_3]^{2+}/\text{COP-4}$ (0.2)	B	8	>99	495	62	[79]
43		$[\text{Ru}(\text{bpy})_2(5\text{debpy})]^{2+}/\text{COP-6}$ (0.2)	B	8	95	475	59	[82]
44		$[\text{Ir}(\text{ppy})_2(5\text{debpy})]^+/\text{COP-6}$ (1)	B	8	97	97	12	[82]
45		$[\text{Ru}(\text{bpy})_2(5\text{debpy})]^{2+}/\text{COP-6}$ (0.2)	B	8	91	455	57	[82]
46		$[\text{Ir}(\text{ppy})_2(5\text{debpy})]^+/\text{COP-6}$ (1)	B	8	86	86	11	[82]
47		$[\text{Ru}(\text{bpy})_3]^{2+}/\text{COP-4}$ (0.2)	B	8	88	440	55	[79]
48		$[\text{Ru}(\text{bpy})_2(5\text{debpy})]^{2+}/\text{COP-6}$ (0.2)	B	8	78	390	49	[82]
49		$[\text{Ir}(\text{ppy})_2(5\text{debpy})]^+/\text{COP-6}$ (1)	B	8	75	75	9	[82]
50		$[\text{Ru}(\text{bpy})_2(\text{bdp})]^{2+}/\text{COP-10}$ (1)	D	9€	98	98	1	[87]
51		$[\text{Ru}(\text{bpy})_2(\text{bdp})]^{2+}/\text{COP-10}$ (1)	D	9€	2	2	0	[87]

^a Molar ratio of the metal to substrate in percentage was calculated on the basis of the metal content in the material found by ICP analysis. ^b Light source: A = white CFL, 15 W; B = CFL, 26 W; C = CFL, 24 W; D = LED, 15 W; E = white LED, 23 W; F = CFL, 23 W. Irradiation was performed in air. ^c Isolated yield. ^d TON and TOF were calculated based on experimental data reported in the articles. In most of the works, the reaction time was not optimized that can significantly influence on the TOF values. ^e 2-phenyl-3,4-dihydroisoquinolin-1(2H)-one was also obtained in the yield of 4% (entry 7), 18% (entry 49) and 15% (entry 50).

The reactions between diverse THIQs and nitroalkanes were often performed using COP-supported Ru^{II} complexes (entries 1–7, 15–18, 25, 27–30, 37, 39, 42, 43, 45, 47, 48, 50 and 51). The reactions gave high (>85%) and quite similar conversion of THIQs and both TON and TOF were rather similar for all photoactive COPs based on Ru^{II} complexes with three bpy ligands. The influence of coordination environment of Ru center was demonstrated when one of bpy ligands was replaced by another nitrogen chelator such as phim and bdp. Both TON and TOF of the reactions with $[\text{Ru}(\text{bpy})_2(\text{phim})]^{2+}/\text{COP-8}$ and $[\text{Ru}(\text{bpy})_2(\text{bdp})]^{2+}/\text{COP-10}$ were decreased (entries 1, 7 and 50) as compared to corresponding values obtained with COPs based on complexes belonging to Ru^{II}-3bpy family. $[\text{Ru}(\text{bpy})_2(\text{phim})]^{2+}/\text{COP-8}$ provided only 64% conversion when THIQ reacted with nitromethane under the similar conditions to what was

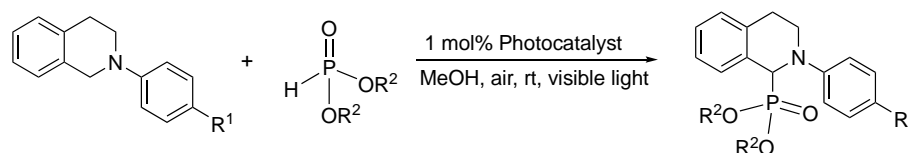
applied in the run in which Ru^{II}-3bpy COPs gave more than 90% of amine conversion (entries 1 and 2–6, respectively) [86]. This decrease of conversion is likely to result from a negative effect of the specific bidentate ligand (phim) coordinated to the ruthenium atom. Moreover, the reaction was not as selective when THIQ reacted with nitroalkanes in the presence of **[Ru(bpy)₂(bdp)]²⁺/COP-10**. A by-product 2-phenyl-3,4-dihydroisoquinolin-1(2*H*)-one was obtained (Table 7, entries 7, 39 and 50) and its yield reached 18 and 15% in the reaction with 1-nitroethane and 1-nitropropane, respectively [87].

Surprisingly, the influence of other factors, such as substituents at the *N*-phenyl ring of THIQ, the structure of nitroalkanes, the porosity of polymer matrix and other features which can be traced to the hypothetical structure of microenvironment of the catalytic center on the reaction were insignificant. However, the impact of porosity deserves attention, though it is rather irregular. On the first hand, the highest TOF of 121 h⁻¹ in the reaction of *N*-phenyl-substituted THIQ with nitromethane was observed with highly porous **[Ru(bpy)₃]²⁺/COP-7** (entry 6) [83]. On the other hand, TON and TOF of the reactions performed in the presence of ruthenium(II) photocatalyst incorporated in highly porous Zr-MOF **[Ru(bpy)₂(5dcbpy)]²⁺/UiO-67** [60] (Table 7, entries 8, 19 and 31) were lower compared to the reactions performed with COP-supported ruthenium(II) photocatalysts possessing significantly lower specific surface and pore volumes. The following example also showed that material porosity is not always needed in this reaction. Photocatalytic centers were incorporated in COP matrices by oxidative coupling of **[Ru(4debpy)₂(bpy)]²⁺** and **[Ru(5debpy)(bpy)₂]²⁺** complexes giving materials **[Ru(4debpy)₂(bpy)]²⁺/COP-1** and **[Ru(5debpy)₂(bpy)]²⁺/COP-1**, respectively, displaying low porosity and containing up to 90 wt% of **[Ru(bpy)₃]²⁺** residues (Scheme 23) [76, 82]. The excited state lifetime of the **[Ru(5debpy)(bpy)₂]²⁺** complex immobilized into this non-porous polymer was much shorter than that of the corresponding complex in solution probably due to self-quenching of luminescence that could be detrimental for its catalytic applications. To circumvent these potential drawbacks, tetra(4-ethynylphenyl)methane spacer was successfully introduced aiming an increase of porosity and a spatial separation of the catalytic sites. BET surface area of polymer **[Ru(5debpy)(bpy)₂]²⁺/COP-6** thus obtained (Scheme 27) was increased from 15 to 1348 m² g⁻¹ after the linker installation. Nevertheless, **[Ru(5debpy)₂(bpy)]²⁺/COP-1** was as active as **[Ru(5debpy)(bpy)₂]²⁺/COP-6** (TOF 58 and 56 h⁻¹, respectively) in the photoreaction of THIQ with nitromethane. The unexpectedly high activity of the non-porous catalyst was explained by the core-to-surface energy transfer which was discussed in the section 2.1.8 (the antennae effect) [76].

Many of COPs modified by Ir^{III} complexes were less efficient than Ru-based photocatalysts, which is consistent with shorter excited-state lifetime of the Ir^{III}-doped polymers. For example, non-porous COPs doped with **[Ru(bpy)₃]²⁺** and **[Ir(ppy)₂(bpy)]²⁺** centers were compared in the reaction of nitromethane with THIQ and its methoxy- and bromo-substituted derivatives MeO-THIQ, and Br-THIQ, respectively (Table 7, entries 2 and 9, 15 and 20, 27 and 32, respectively) [79]. Two photocatalysts have shown a comparable performance only with 4-MeO-THIQ. In contrast, a significant decrease of conversion was observed for THIQ and Br-THIQ when Ru^{II} complex was replaced by Ir^{III} catalysts. Replacement of COP supports by highly porous MOFs in the case of Ir^{III} complexes does not allow for an increase in the efficiency of Ir^{III}-photocatalyzed reactions, as was shown in all cases reported (Table 7, entries 9, 20 and 32 (COP), entries 14, 24 and 36 (Zr-MOF)).

Reactive iminium ions formed in photocatalyzed reactions could also be involved in the C–P bond forming reactions (Scheme 51). Homogeneous photoredox catalytic reactions using both Ru^{II} or Ir^{III} complexes were reported to serve as useful tools in their synthesis [148]. Examples of photoredox C–P bond forming reactions performed in the presence of heterogenized VATMPY complexes are summarized in Table 8.

Table 8. Photoredox C–P bond formation.



Ent-Substrate	R ²	Catalyst	Light Source	Time, h	NMR yield (isolated yield, %)	Reference
1	Me	[Ru(bpy) ₃] ²⁺ /FJI	A	12	(82) ^b	[59]
		[Ir(vppy) ₂ (d ⁴ bbpy)] ⁺ /PMA-1	B	14	(95)	[74]
2	Et	[Ru(bpy) ₃] ²⁺ /FJI	A	12	(80) ^b	[59]
		[Ir(vppy) ₂ (d ⁴ bbpy)] ⁺ /PMA-1	B	14	92 (87)	[74]
		[Ir(vppy) ₂ (d ⁴ bbpy)] ⁺ /PS	B	12	74	[74]
		[Ir(vppy) ₂ (d ⁴ bbpy)] ⁺ /PAM	B	12	83	[74]
		[Ir(vppy) ₂ (d ⁴ bbpy)] ⁺ /PMA	B	12	90	[74]
		[Ir(ptppc-H) ₂ (bpy)] ⁺ /COP-3	C	24	83	[78]
		[Ir(ptppc-F) ₂ (bpy)] ⁺ /COP-3	C	24	92	[78]
		[Ru(bpy) ₃] ²⁺ /FJI	A	12	(69) ^b	[59]
		[Ir(vppy) ₂ (d ⁴ bbpy)] ⁺ /PMA-1	B	14	(67)	[74]
3	nBu	[Ir(vppy) ₂ (d ⁴ bbpy)] ⁺ /PMA-1	B	14	(88)	[74]
		[Ir(ptppc-H) ₂ (bpy)] ⁺ /COP-3	C	24	94	[78]
4	Me	[Ru(bpy) ₃] ²⁺ /FJI	A	12	(78) ^b	[59]
		[Ru(bpy) ₃] ²⁺ /FJI	A	12	(77) ^b	[59]
5	Et	[Ir(vppy) ₂ (d ⁴ bbpy)] ⁺ /PMA-1	B	14	(97)	[74]
		[Ru(bpy) ₃] ²⁺ /FJI	A	12	(62) ^b	[59]
		[Ru(bpy) ₃] ²⁺ /FJI	A	12	(84) ^b	[59]
		[Ru(bpy) ₃] ²⁺ /FJI	A	12	(85) ^b	[59]
		[Ir(vppy) ₂ (d ⁴ bbpy)] ⁺ /PMA-1	B	24	(87)	[74]
		[Ir(ptppc-F) ₂ (bpy)] ⁺ /COP-3	C	24	80	[78]
		[Ru(bpy) ₃] ²⁺ /FJI	A	12	(66) ^b	[59]
		[Ru(bpy) ₃] ²⁺ /FJI	A	12	(89) ^b	[59]
		[Ru(bpy) ₃] ²⁺ /FJI	A	12	(86) ^b	[59]
6	Et	[Ir(vppy) ₂ (d ⁴ bbpy)] ⁺ /PMA-1	B	14	(39)	[74]
		[Ir(ptppc-F) ₂ (bpy)] ⁺ /COP-3	C	24	89	[78]
7	Et	[Ir(vppy) ₂ (d ⁴ bbpy)] ⁺ /PMA-1	B	14	(47)	[74]

^a Light Source: A = CFL, 14 W; B = white LED, 7.1 W; C = white LED, 23 W. Irradiation was performed in air. ^b MeCN was used as a solvent. ^c 2 mol% of catalyst were used.

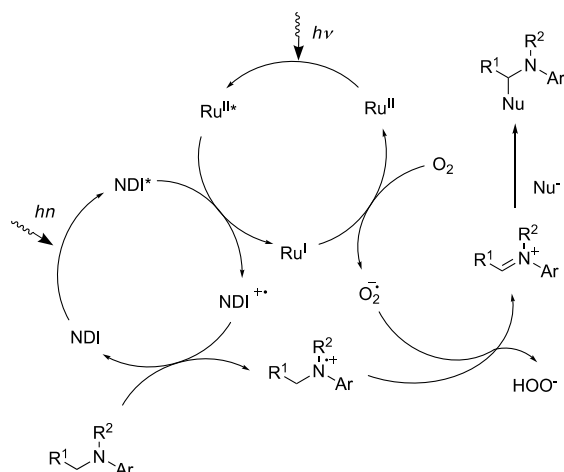
The reactions of THIQs with dialkyl H-phosphonates were carried out with Ir^{III} complexes incorporated in polymers (Table 8, entries 2, 4–11, 13–15, 18, 22 and 26–28) and Ru^{II} complexes supported by FJI MOF (Table 8 entries 1, 3, 12, 16, 17, 19–21 and 23–25). The stability of these heterogenized photoredox catalysts was dependent to a great extent on the immobilization method. All photocatalysts obtained by free radical copolymerization of [Ir(vppy)₂(d⁴bbpy)]PF₆ and various unsaturated monomers were prone to lose the Ir^{III} complex under reaction conditions [74]. It seems that a high extent of catalyst leaching of these polymers is associated with the incomplete polymerization of monomers in benzotrifluoride (BTF)

(Scheme 20). To achieve the reusability of these catalysts the most stable polymer **Ir(vppy)₂(d⁴bbpy)/PMA** was covered by an additional protective polymer layer. The photoredox catalyst **Ir(vppy)₂(d⁴bbpy)/PMA-1** thus prepared was successfully used in five consecutive runs of phosphonylation of THIQ with diethyl phosphite affording the phosphonate in 88–95% yield. The catalyst leaching in solution was less than 0.3% in each cycle.

As in the case of aza-Henry reaction, the conversion was practically independent on the substituent nature. THIQs bearing EWG such as halogen atoms seem to be less reactive only in the reactions catalyzed by **[Ir(vppy)₂(d⁴bbpy)]/PMA-1** (Table 8, entries 25 and 27) [74]. The photoredox phosphonylation of THIQ smoothly proceeded with dimethyl, diethyl and dibutyl H-phosphonates but the product yields were lower with bulky di-*i*-propyl H-phosphonate (Table 8, entries 12, 13, 19 and 23). It is also worth noting that photoredox reactions of THIQs with diethyl H-phosphonate (Table 8, entry 8) and nitroalkanes (Table 7, entries 9 and 39) performed under similar conditions with photocatalyst **[Ir(ptppc-F)₂(bpy)]⁺/COP-3** ran with similar rates and gave products in 92–96% yields after 24 h of irradiation. Accordingly, the reaction of the iminium cation with a nucleophile seems not to be a rate determining step of these reactions.

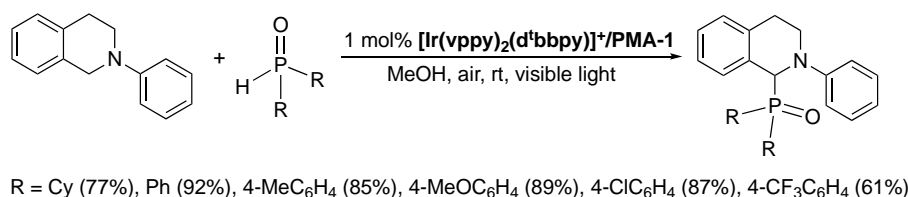
Comparative studies of two photoactive COPs **[Ir(ptppc-H)₂(bpy)]⁺/COP-3** and **[Ir(ptppc-F)₂(bpy)]⁺/COP-3** (Scheme 24) have demonstrated the influence of electron-withdrawing CF₃ group at the *ptppc*-R ligand on the catalyst photoactivity [78]. Fluorinated polymer **[Ir(ptppc-F)₂(bpy)]⁺/COP-3** was found to be more efficient as it was also observed in the oxidation of sulfides by O₂ (Table 6) and aerobic hydroxylation of arylboronic acids (Table 5) despite different mechanisms of these reactions. As it was discussed above, **[Ir(ptppc-F)₂(bpy)]⁺** possesses a longer excited state lifetime as compared to **[Ir(ptppc-H)₂(bpy)]⁺** that can be advantageous for various chemical reactions proceeding with this excited species.

Interesting results in phosphonylation of THIQs were obtained when **FJI** MOF bearing photoactive 1,4,5,8-naphthalenediimide (NID) residues in the linkers was doped with **[Ru(bpy)₃]²⁺** catalytic centers (**[Ru(bpy)₃]²⁺/FJI**, Figure 6). The photocatalyst thus obtained was more efficient compared to **[Ru(bpy)₃]Cl₂** under homogeneous conditions and afforded the desired phosphonates in good yields even with the THIQs having EWG at the *N*-phenyl ring (Table 8, entries 23 and 24). As a plausible explanation of the high efficiency of this photocatalytic system, the authors privileged the synergy in excitation of NDI residues and **[Ru(bpy)₃]²⁺** complexes located very closely in the porous solid (Scheme 51 shows the suggested reaction mechanism proposed by authors. It involves the reaction of the excited Ru complex with the excited NDI residue which is quite picaresque as lifetimes of both species are rather short). It is worth noting that in **[Ru(bpy)₃]²⁺/FJI** the photocatalytic centers and the FJI framework are not connected by covalent bonding but non-covalent forces such as coulombic attractions and multiple intramolecular π - π and C-H \cdots π contacts of bpy ligands and NDI residues apparently safeguarded a prominent level of stability of this solid. The same sample of catalyst **[Ru(bpy)₃]²⁺/FJI** was successfully used over three successive catalytic cycles for all studied transformations.



Scheme 51. Proposed mechanism of photoredox-catalyzed phosphonylation reaction under visible light irradiation in air.

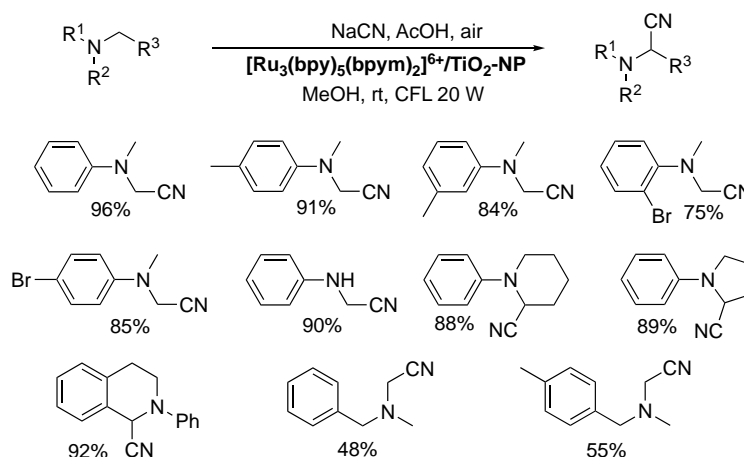
The photoredox reactions of THIQs with secondary phosphine oxides (Scheme 52) were investigated only in the presence of **[Ir(vppy)₂(d^tbbpy)]⁺/PMA-1** polymer (Scheme 20) [74]. The products were obtained in good yields (85–92%) for diphenylphosphine oxides bearing EWG and EDG at the phenyl ring with the only exception of compound with such a strong EWG as CF₃ substituent (Table 8, entry 33). Diphenylphosphine oxide was found to be more reactive than dicyclohexyl derivative.



Scheme 52. Photoredox coupling of THIQs with secondary phosphine oxides under visible light irradiation in air.

The iminium ions are also useful intermediates in photoredox-catalyzed synthesis of α -aminonitriles which are useful for the preparation of α -amino acids and heterocyclic compounds such as imidazoles, alkaloids and other biologically important molecules [149]. Among various methods of their synthesis, the aerobic oxidative cyanation of tertiary amines performed using a homogeneous photoredox catalyst allows for their synthesis under mild conditions [150].

TiO₂-supported trinuclear ruthenium(II) complex (Scheme 14) worked well as a photocatalyst when the reaction was performed in methanol in the presence of air or molecular oxygen (Scheme 53) [47].

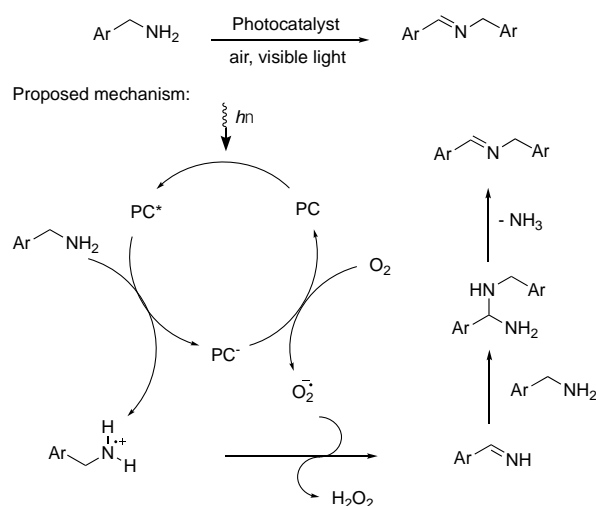


Scheme 53. Oxidative cyanation of tertiary amines under visible light irradiation in air or molecular oxygen.

THIQ, *N,N'*-dimethylanilines, and *N*-arylated cyclic amines afforded α -aminonitriles in high yields (75–96%). *N,N'*-dimethylbenzylamine was less reactive and gave the product of cyanation of methyl group in 48% yield. Secondary aromatic amine and *N*-methylaniline also yielded the target product in 90% yield. The 8 consecutive reactions of *N,N'*-dimethylaniline were successfully performed to investigate the catalyst reuse.

Oxidative coupling of benzylic amines

Imines are important electrophilic intermediates in the preparation of fine chemicals and pharmaceuticals [151, 152]. They can be readily obtained by the condensation of carbonyl compounds with amines. However, this reaction is inconvenient for design of multi-step synthetic routes owing to a high reactivity of the carbonyl group. To circumvent this drawback, the synthesis of imines *via* the oxidation of amines can be regarded. Although this reaction can be performed using special oxidants such as 2-iodoxybenzoic acid, efforts have been devoted to develop functional group-tolerant photocatalytic processes, in which molecular oxygen is used as a terminal oxidant (Scheme 54) [145,153,154]. The reaction was supposed to run through the formation of an imine intermediate as shown in Scheme 54. The second amine molecule reacts with this intermediate to form an aminal which gives the expected substituted imine by elimination of ammonia. The suggested catalytic cycle is thus very close to other photooxidative α -functionalization of amines already discussed (Scheme 50). Here, however, it is much more difficult to achieve selectivity and to avoid the reaction of intermediate imine with other nucleophiles, such as e.g. hydroperoxide anion formed in the reaction mixture. Therefore, good product yields were reported only for benzylic amines. Many heterogenized Ru^{II} photoredox catalysts, which are efficient in the α -functionalization of amines are also useful for oxidative coupling of benzylic amines (Table 9). However, Ir^{III} -based catalysts for this transformation were not reported so far.

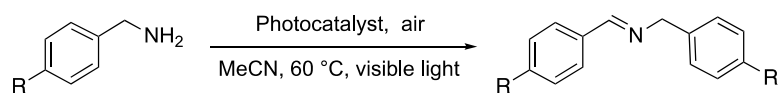


Scheme 54. Aerobic oxidation of benzylic amines.

The reactions of benzylamine and its electron rich derivatives were investigated by using COP-supported complexes $[\text{Ru}(\text{4debpy})_2(\text{bpy})]^{2+}/\text{COP-1}$, $[\text{Ru}(\text{5debpy})_2(\text{bpy})]^{2+}/\text{COP-1}$ and $[\text{Ru}(\text{bpy})_3]^{2+}/\text{COP-4}$ and Zr-MOF $[\text{Ru}(\text{bpy})_2(\text{5dcbpy})]^{2+}/\text{UiO-67}$ bearing photoactive catalytic centers in the linkers [60, 76, 79]. The use of non-porous $[\text{Ru}(\text{5debpy})_2(\text{bpy})]^{2+}/\text{COP-1}$ catalyst exhibited a different pattern of substrate selectivity, as the conversion of substituted benzylic amines was found to vary significantly depending on substituents and the presence of electron-donating groups in the aromatic ring resulted in a significant decrease of conversion (entries 3, 8 and 13) [76]. The product yield was also rather low in the coupling of *p*-methoxybenzylamine performed by using the microporous $[\text{Ru}(\text{bpy})_2(\text{5dcbpy})]^{2+}/\text{UiO-67}$ photocatalyst (entry 11). However, kinetic studies of coupling photoreactions with $[\text{Ru}(\text{bpy})_2(\text{5dcbpy})]^{2+}/\text{UiO-67}$ (entries 1, 6 and 11) demonstrated that the initial reaction rates were similar for all substrates including *p*-methoxybenzylamine. Therefore, the drop of yield was more likely associated not with the reactivity in the rate-limiting step, but with a low stability of the product due to acid-catalyzed decomposition, supposedly caused by $[\text{Zr}_6\text{O}_4(\text{OH})_4]$ clusters in the catalyst support.

Comparative studies of photoredox catalysts $[\text{Ru}(\text{4debpy})_2(\text{bpy})]^{2+}/\text{COP-1}$, $[\text{Ru}(\text{bpy})_3]^{2+}/\text{COP-4}$ and $[\text{Ru}(\text{bpy})_2(\text{5dcbpy})]^{2+}/\text{UiO-67}$ and the respective free complexes showed that efficiency of Ru^{II} complexes did not significantly decrease after their heterogenization with the exception of the non-porous $[\text{Ru}(\text{5debpy})_2(\text{bpy})]^{2+}/\text{COP-1}$ photocatalyst. With this COP, the product yields were much lower in the oxidative coupling of 4-methyl- and 4-methoxybenzylamines (entries 8 and 13) than those observed under homogeneous conditions. Recycling experiments were successful for all these heterogenized catalysts at least in two additional reaction runs.

Table 9. Heterogeneous photocatalytic aerobic oxidative coupling of benzylic amines



Entry	R	Photocatalyst, mol% ^a	Light source	Time, h	Conversion	NMR or GC yield, % (isolated yield, %)	Reference
1	H	$[\text{Ru}(\text{bpy})_2(\text{5dcbpy})]^{2+}/\text{UiO-67}$ (1)	A	1	n/d ^c	83 ^d	[60]
2	H	$[\text{Ru}(\text{4debpy})_2(\text{bpy})]^{2+}/\text{COP-1}$ (1)	B	1	99	93	[76]
3	H	$[\text{Ru}(\text{5debpy})_2(\text{bpy})]^{2+}/\text{COP-1}$ (1)	B	1	99 ^e	88	[76]

4	H	[Ru(bpy) ₃] ²⁺ /COP-4 (1)	B	1	99 ^f	n/d ^c	[79]
5 ^g	H	[Fe(bpy) ₃] ²⁺ /npg-C ₃ N ₄ (10)	C	8	n/d ^c	(94) ^h	[51]
6	Me	[Ru(bpy) ₂ (5dcbpy)] ²⁺ /UiO-67 (1)	A	1	n/d ^c	90	[60]
7	Me	[Ru(4debpy) ₂ (bpy)] ²⁺ /COP-1 (1)	B	1	99	88	[76]
8	Me	[Ru(5debpy) ₂ (bpy)] ²⁺ /COP-1 (1)	B	1	76 ⁱ	52	[76]
9	Me	[Ru(bpy) ₃] ²⁺ /COP-4 (1)	B	1	95	n/d ^c	[79]
10 ^g	Me	[Fe(bpy) ₃] ²⁺ /npg-C ₃ N ₄ (10)	C	7.5	n/d ^c	(91)	[51]
11	MeO	[Ru(bpy) ₂ (5dcbpy)] ²⁺ /UiO-67 (1)	A	1	n/d ^c	46	[60]
12	MeO	[Ru(4debpy) ₂ (bpy)] ²⁺ /COP-1 (1)	B	1	99	87	[76]
13	MeO	[Ru(5debpy) ₂ (bpy)] ²⁺ /COP-1 (1)	B	1	67 ^j	51	[76]
14	MeO	[Ru(bpy) ₃] ²⁺ /COP-4 (1)	B	1	84	n/d ^c	[79]
15 ^g	MeO	[Fe(bpy) ₃] ²⁺ /npg-C ₃ N ₄ (10)	C	7	n/d ^c	(94)	[51]
16 ^g	Cl	[Fe(bpy) ₃] ²⁺ /npg-C ₃ N ₄ (10)	C	8.5	n/d ^c	(86)	[51]
17 ^g	Br	[Fe(bpy) ₃] ²⁺ /npg-C ₃ N ₄ (10)	C	8.5	n/d ^c	(81)	[51]
18 ^g	CN	[Fe(bpy) ₃] ²⁺ /npg-C ₃ N ₄ (10)	C	10	n/d ^c	(85)	[51]

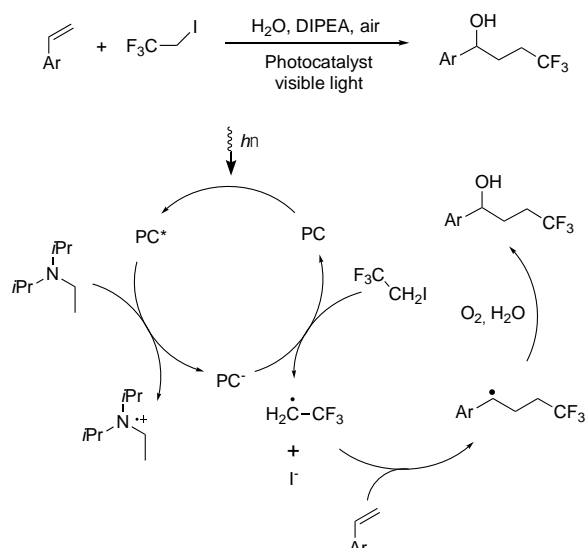
^a The metal to substrate molar ratio in percentage calculated based on the metal content found by ICP analysis. ^b Light Source: A = Xe lamp, 300 W; B = Xe lamp, 450 W; C = white LED, 70 W m⁻², λ > 400 nm. ^c n/d = not determined. ^d In the analogous homogeneous reaction the yield was 96%. ^e In the analogous homogeneous reaction the conversion was 99%, the yield was 89%. ^f In the analogous homogeneous reaction the conversion was 97%. ^g The reaction was performed at room temperature. ^h In the analogous homogeneous reaction the isolated yield was 98%. ⁱ In the analogous homogeneous reaction the conversion was 97%, the yield was 87%. ^j In the analogous homogeneous reaction the conversion was 90%, the yield was 79%.

Interestingly, the least expensive [Fe(bpy)₃]²⁺ complex immobilized on photoactive npg-C₃N₄ support also gave the coupling products in excellent yields under irradiation by visible light in acetonitrile at room temperature (Table 9, entries 5, 10 and 15–18) [51]. However, Fe^{II}-catalyzed coupling reactions proceeded slower than those mediated by heterogenized ruthenium(II) complexes. Under these conditions, benzylic amines bearing EDG in the ring were more reactive than those with EWG likely due to the easier formation of the imine intermediate. Despite increased irradiation time in each catalytic run, no significant loss in the catalytic activity was observed for the recycled photocatalyst [Fe(bpy)₃]²⁺/npg-C₃N₄ and the product yield remained almost unchanged after 6 recycling experiments.

Oxidative difunctionalization of styrenes and functionalized alkenes

Difunctionalization of double bonds is a powerful tool in the synthesis of highly functionalized organic compounds [155]. Among various synthetic applications of these transformations, the reactions allowing for the introduction of a trifluoromethyl group into organic molecules have been widely explored with aim of tuning physical properties of organic compounds such as polarity, lipophilicity, membrane permeability.

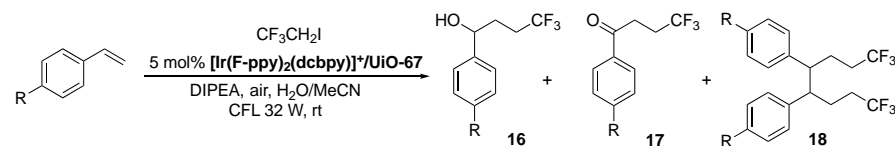
Photoredox catalysts allow for performing the oxidative trifluoroethylation of styrenes in aqueous media at room temperature (Scheme 55, Table 10) [156].



Scheme 55. 2,2,2-Trifluoroethylation of styrenes in aqueous media using photoredox catalysis.

The heterogeneous version of this reaction was carried out using two Ir^{III} complexes covalently incorporated in UiO-67-type MOFs, e. g. **[Ir(ppy)₂(5dcbpy)]⁺/UiO-67** and **[Ir(F-ppy)₂(5dcbpy)]⁺/UiO-67** frameworks [66].

Table 10. Photocatalytic reaction of styrenes with 1,1,1-trifluoro-2-iodoethane and water.



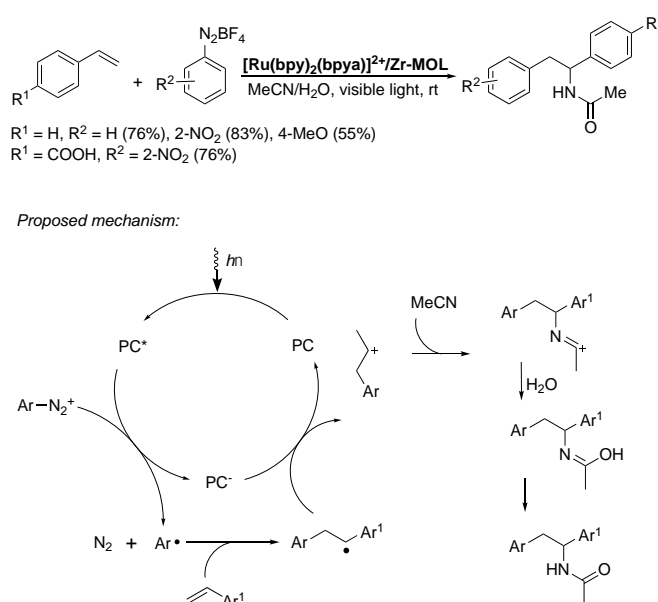
Entry	R	Catalyst	Con, % ^a	Yield A/B/C, % ^b
1	OMe	[Ir(ppy)₂(5dcbpy)]⁺/UiO-67	99	60/11/28
2	OMe	[Ir(F-ppy)₂(5dcbpy)]⁺/UiO-67	99	76/18/2
3	OMe	Ir(ppy) ₃	99	10/9/80
4	OMe	[Ir(F-ppy) ₂ (Et ₂ 5dcbpy)]Cl ^c	99	20/7/72
5	OMe	[Ir(F-ppy) ₂ (Et ₂ 5dcbpy)]Cl	99	32/8/60
6	H	[Ir(F-ppy)₂(5dcbpy)]⁺/UiO-67	95	70/20/4
7	Me	[Ir(F-ppy)₂(5dcbpy)]⁺/UiO-67	83	74/9/0
8	Br	[Ir(F-ppy)₂(5dcbpy)]⁺/UiO-67	49	43/6/0
9	Ph	[Ir(F-ppy)₂(5dcbpy)]⁺/UiO-67	97	60/30/0

^a Conversion. ^b GC-MS yield. ^c Et₂dcbpy = 5,5'-ethoxycarbonyl-2,2'-bipyridine.

First, 4-methoxystyrene and 1,1,1-trifluoro-2-iodoethane were irradiated in the presence of DIPEA in a MeCN/water solvent mixture in air (entries 1 and 2). The fluorinated **[Ir(F-ppy)₂(5dcbpy)]⁺/UiO-67** photocatalyst showed a higher selectivity than **[Ir(ppy)₂(5dcbpy)]⁺/UiO-67** and afforded the target product **16** in 76% yield along with the corresponding ketone **17** (the overoxidation product, 18%) and the dimer of benzyl radical (**18**, 2%). Interestingly, being performed with soluble Ir^{III} complexes, the reaction gave dimer **18** as the major product (entries 3–5). The change of the reaction course in the presence of microporous MOF photocatalysts was likely induced by a steric hindrance imposed by solid frameworks to the side dimerization reaction. A high conversion was observed only for electron-rich styrenes while a good selectivity was achieved in all studied reactions (entries 5–9). No significant leaching of this catalyst was observed for these heterogenized catalysts, as evidenced

by ICP-OES analysis of the filtrates (< 0.1 ppm of Ir). Photoredox catalyst $[\text{Ir}(\text{Fppy})_2(\text{5dcbpy})]^+/\text{UiO-67}$ was successfully reused in 3 consecutive reaction runs.

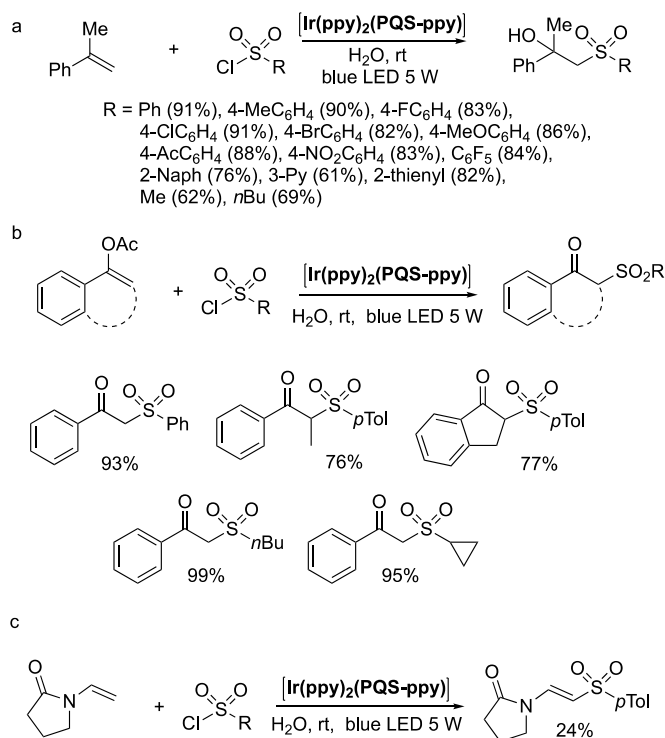
The free-radical Meerwein arylation reaction is well-known as a legacy method in organic synthesis, largely superseded by new and more selective reactions. There are however still some efforts to revisit this classical method and make it more useful [157]. Quite naturally, the photoredox chemistry capable of furnishing methods of the generation of free-radicals of varied nature could be of use in attempts to update the Meerwein chemistry [158]. The proposed mechanism of the photoredox-catalyzed amido-arylation of alkenes is shown in Scheme 56 [158]. The primary photocatalytic step consists of the generation of an aryl radical from diazonium salt by a single-electron transfer from excited $^*[\text{Ru}(\text{bpy})_3]^{2+}$ complex. It was suggested that the addition of this radical to alkene followed by the oxidation of the radical thus formed affords a carbenium intermediate, which reacts with nitrile to give amido arylated product. Such selective reaction of the cation with nitrile in aqueous media is rather doubtful and additional experiments are needed to prove this mechanism.



Scheme 56. Photocatalyzed Meerwein arylation-addition reaction.

Performing multicomponent reactions with heterogenized photoredox catalysts is only possible when catalytic centers inside the material are accessible to freely diffusing molecules as otherwise the reaction involving three or more molecules becomes extremely improbable. Comparative studies of the photocatalytic activity of Ru^{II} complexes incorporated in UiO-67-type Zr-MOFs and in Zr-MOL sheets were performed reacting styrenes with diazonium salts and nitriles as shown in Scheme 56 [68]. The layered material $[\text{Ru}(\text{bpy})_2(\text{bpya})]^{2+}/\text{Zr-MOL}$ showed a superior activity as compared to $\text{Ru}(\text{bpy})_2(\text{5dcbpy})^{2+}/\text{UiO-67}$ MOF and gave the products in 55–83% yields. Unfortunately, catalyst recycling in these reactions was not reported.

Photo-induced difunctionalization of alkenes by sulfonyl chloride in aqueous media proceeds under irradiation in inert atmosphere through generation of sulfonyl radicals and leads to β -hydroxysulfones (Scheme 57) [159]. Lipshutz and coworkers have demonstrated the reactivity of the sulfonyl radical in micellar media using amphiphilic $[\text{Ir}(\text{ppy})_2(\text{PQS-ppy})]$ photocatalyst, which forms stable micelles in aqueous media [120]. Upon completion the reaction products were extracted with an organic solvent, and the aqueous layer containing the micellar photocatalyst was reused.



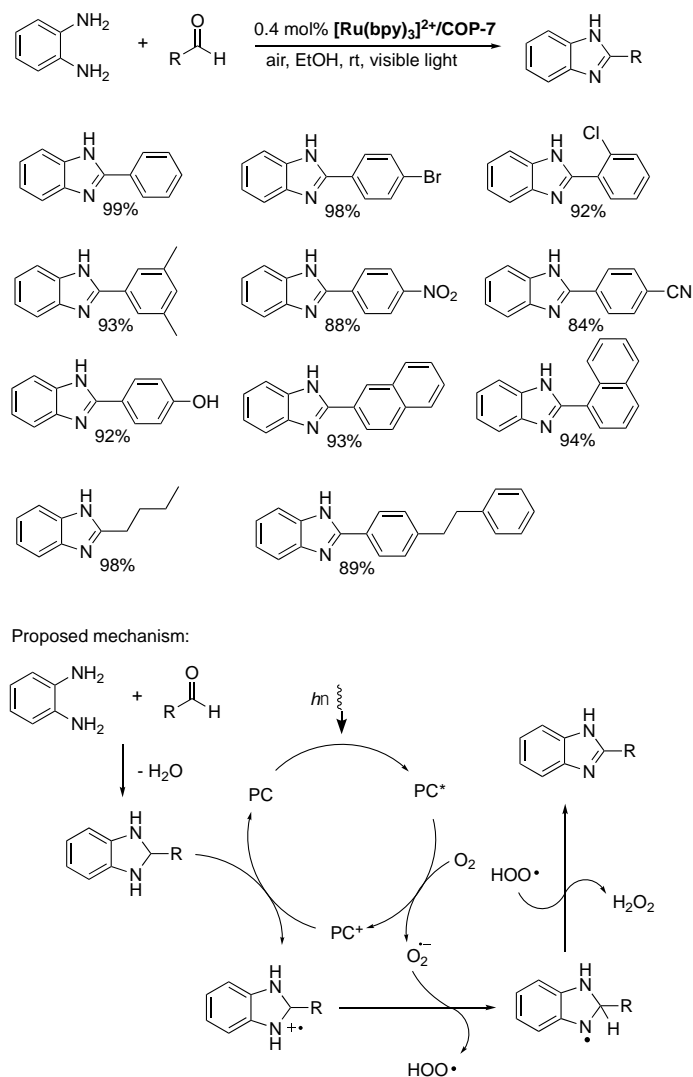
Scheme 57. Photoredox-catalyzed difunctionalization of α -methylstyrene (a) and functionalized alkenes (b and c) by sulfonyl chlorides in aqueous media.

A variety of benzenesulfonyl chlorides with EWG, EDG or electron-neutral substituents at the *para* position smoothly reacted with α -methylstyrene affording the desired products in good yields. Heteroaryl sulfonyl chlorides also gave β -hydroxysulfones successfully but modest yields were obtained with alkyl sulfonyl chlorides. Other variations in the styrene, styrene-like or enol acetates partners were also tested and led to the expected products (Scheme 57). However, sulfonylation of an enamide gave the β -hydroxysulfone in low yield (24%).

Catalyst recycling was investigated in the sulfonylation of α -methylstyrene with *p*-toluenesulfonyl chloride. The aqueous medium containing [Ir(ppy)₂(PQS-ppy)] (1 mol%) was recycled in four consecutive runs with the products isolated in yields from 70 to 88%, before an additional amount (0.5 mol%) of the catalyst was added. The resulting aqueous solution was then recycled in five reaction runs. Overall, the total loading of iridium catalyst for these ten reactions was as low as 1.5 mol%.

Oxidative heterocyclizations

Benzimidazoles are usually prepared from *o*-phenylenediamines either by acid catalyzed reaction with carboxylic acids or with aldehydes under oxidative conditions. Photoredox catalysis allows to perform the last reaction using air as a terminal oxidant (Scheme 58), that is important for increasing functional group tolerance and meeting the standards of the sustainable pharmaceutical industry [160].

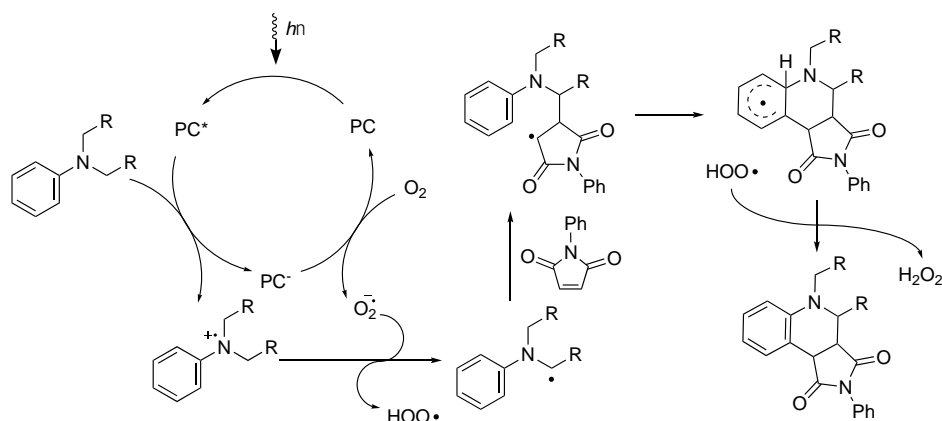


Scheme 58. Photoredox catalytic synthesis of benzimidazoles from aldehydes.

Efficient heterogenized photoredox catalysts for this visible light-induced reaction were reported recently. Excellent results were obtained with $[\text{Ru}(\text{bpy})_3]^{2+}/\text{COP-7}$ polymer with easily accessible photocatalytic centers in the mesoporous polymer network (Scheme 28) [83]. Aromatic aldehydes with both EDG and EWG were smoothly converted to the corresponding benzimidazoles in good to excellent yields (84–99%), although the electron poor substrates reacted more slowly under these conditions. Moreover, aliphatic aldehydes were also suitable for this reaction and afforded benzimidazoles in high yields (89–99%).

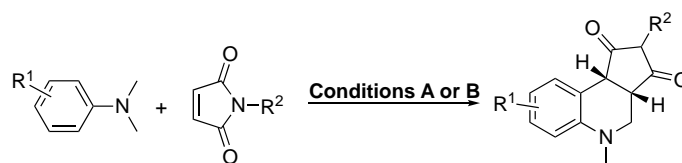
The recyclability of $[\text{Ru}(\text{bpy})_3]^{2+}/\text{COP-7}$ was studied in the reaction of *o*-phenylenediamine with benzaldehyde. The photocatalyst was recovered by centrifugation and successfully reused 12 times. The structural stability of the recovered powder was confirmed by UV–vis and FT–IR spectroscopies, SEM and element mapping.

Photoredox catalysts can also be used for the cyclization of tertiary *N,N*-dialkylanilines with maleimides, which affords biologically relevant tetrahydroquinolines [161]. As shown in Scheme 59, this reaction proceeds in the presence of air through the formation of amine cation radical.



Scheme 59. Proposed mechanism for aerobic oxidative heterocyclization of tertiary amines with maleimides.

Photoactive zeolite-like MOFs bearing encapsulated Ru^{II} complexes $[\text{Ru}(\text{bpy})_3]^{2+}/\text{NKMOF-4}$, $[\text{Ru}(\text{bpy})_3]^{2+}/\text{NKMOF-5}$ and $[\text{Ru}(\text{bpy})_3]^{2+}/\text{NKMOF-6}$ (Figure 7) gave the products in 68–93% yield when catalyst loading was increased up to 3 mol% (Scheme 60, conditions A).



Conditions A: 3 mol% $[\text{Ru}(\text{bpy})_3]^{2+}/\text{NKMOF-4}$, air, DMF, rt, CFL

$\text{R}^1 = 4\text{-Me}$; $\text{R}^2 = \text{Ph}$ (93%), Me (91%), Bn (85%), 4- FC_6H_4 (90%), 4- ClC_6H_4 (83%), 4- BrC_6H_4 (86%), 4- MeOC_6H_4 (68%)

$\text{R}^2 = \text{Ph}$; $\text{R}^1 = \text{H}$ (71%), 4-F (92%), 4-Br (70%), 3-Me (90%)

Conditions B: 1.2 mol% $[\text{Ir}(\text{ppy})_2(\text{py})_2]^+/\text{PS}$, air, NMP, blue LED 3 W

$\text{R}^1 = \text{H}$; $\text{R}^2 = \text{Ph}$ (72%), 4- MeC_6H_4 (87%), 4- FC_6H_4 (50%), 4- ClC_6H_4 (59%), Bn (52%)

$\text{R}^1 = 4\text{-Me}$; $\text{R}^2 = \text{Ph}$ (86%), 4- MeC_6H_4 (89%), 4- FC_6H_4 (62%), 4- ClC_6H_4 (76%), Bn (66%)

$\text{R}^1 = 4\text{-F}$; $\text{R}^2 = \text{Ph}$ (69%), 4- MeC_6H_4 (91%), 4- FC_6H_4 (53%), 4- ClC_6H_4 (72%), Bn (54%)

$\text{R}^1 = 4\text{-MeO}$; $\text{R}^2 = \text{Ph}$ (59%), 4- MeC_6H_4 (72%)

$\text{R}^1 = 4\text{-Cl}$; $\text{R}^2 = 4\text{-MePh}$ (95%)

$\text{R}^1 = 3\text{-Me}$; $\text{R}^2 = \text{Ph}$ (65%)

Scheme 60. Heterogenized photoredox cyclization of tertiary anilines with maleimides.

$[\text{Ru}(\text{bpy})_3]^{2+}/\text{NKMOF-4}$ was found to be the most active photocatalyst in the series as was also observed in aerobic oxidation of benzyl halides to carbonyl compounds by using the same catalysts (Scheme 44) [31]. Under optimal conditions, 93% product yield was obtained in the condensation of *N,N*-dimethyl-*p*-toluidine with *N*-phenylmaleimide in contrast to the analogous homogeneous reaction with $[\text{Ru}(\text{bpy})_3]\text{Cl}_2$, which afforded the product in only 76% isolated yield. In the recycling experiments, $[\text{Ru}(\text{bpy})_3]^{2+}/\text{NKMOF-4}$ was reused 5 times with only small decreasing of the product yield to 85% in the last run. Moreover, the filtrate obtained after the photocatalytic reaction contains less than 0.3 wt% of Ru involved in the studied cyclization reaction. Non-porous $[\text{Ru}(\text{bpy})_3]^{2+}/\text{NKMOF-7}$ gave only 32% yield of the tetrahydroquinoline under the same conditions that might reveal problems in diffusion of substrates to the catalytic centers.

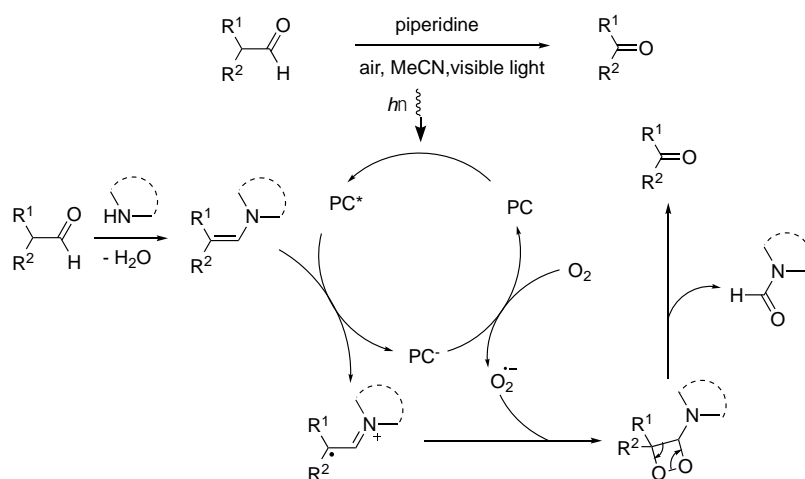
$[\text{Ru}(\text{bpy})_3]^{2+}/\text{NKMOF-4}$ was also more active than $\text{Ru}(\text{bpy})_2(5\text{dcbpy})^{2+}/\text{UiO-67}$ [61] and $[\text{Ru}(\text{bpy})_3]^{2+}/\text{MCM-41}$ [31]. Moreover, $[\text{Ru}(\text{bpy})_3]^{2+}/\text{MCM-41}$ prepared by the

encapsulation of $[\text{Ru}(\text{bpy})_3]^{2+}$ complex into mesopores of MCM-41 silica rapidly released the photocatalyst in solution and could not be reused.

A solid photocatalyst prepared by incorporation of $[\text{Ir}(\text{ppy})_2(\text{py})_2]^+$ complex in the divinylbenzene/vinylpyridine copolymer (PS) (Scheme 21) was also efficient in this cyclization (Scheme 60, conditions B) [84]. Maleimides with EDG and EWG gave the target products in good yields but electron poor compounds were less reactive. The same trend was observed among the substituted anilines. The photoredox catalyst which was prepared as spherical particles with the diameter about 20–50 nm was separated by centrifugation, and reused 5 times in the cyclization of *N,N*-dimethylaniline with *N*-phenylmaleimide.

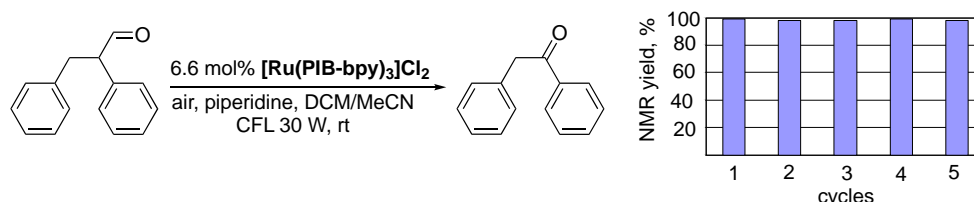
Oxidative decarbonylation of aldehydes

The aerobic photo-induced C–C bond cleavage in aldehydes requires the presence of amine and proceeds through the formation of enamine intermediate as shown in Scheme 61 [162].



Scheme 61. Proposed mechanism for oxidative C–C bond cleavage in aldehydes.

The cleavage of 2,3-diphenylpropanal in the presence of piperidine in $\text{CH}_2\text{Cl}_2/\text{MeCN}$ mixture is a such rare case of photo-induced reaction in which soluble $[\text{Ru}(\text{PIB-bpy})_3]\text{Cl}_2$ bearing hydrophobic PIB-modified bpy ligands could be successfully reused for 5 cycles (Scheme 62) [116].



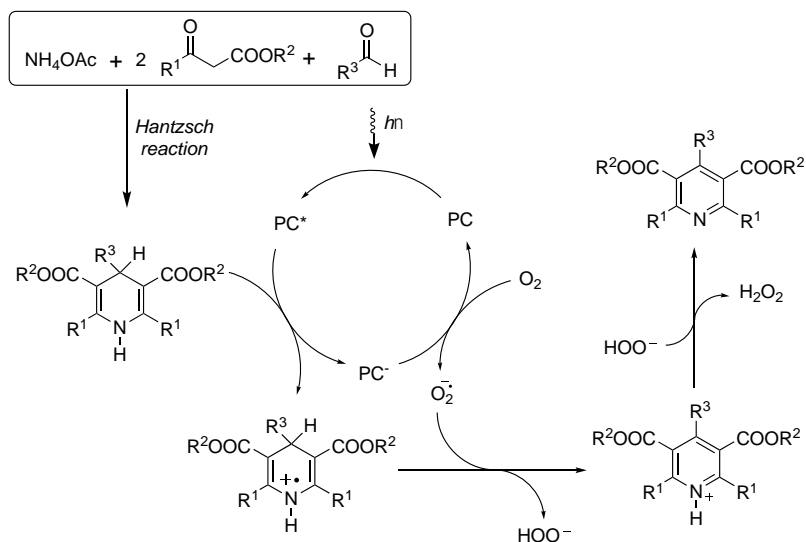
Scheme 62. Photocatalytic cleavage of 2,3-diphenylpropanal.

After each cycle, the solvent was removed under reduced pressure. The reaction mixture was redissolved in heptane and the product was separated from the catalyst by the extraction with MeCN. The $[\text{Ru}(\text{PIB-bpy})_3]\text{Cl}_2/\text{hep}$ layer was evaporated to recover the photoredox catalyst and the residue was introduced in the next run. Leaching of the catalyst in polar phase was as low as 0.9% (in the third catalytic run taken as an example). However, the reaction scope seems

to be strongly limited because different solubility of the photocatalyst and the final product in biphasic mixture of organic solvents is needed for the successful recovery process.

Oxidative aromatization of dihydropyridines

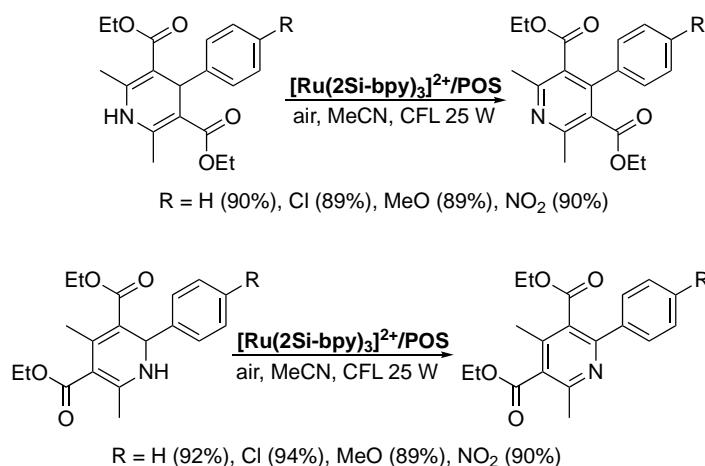
It was demonstrated that aerobic oxidative aromatization in the presence of $[\text{Ru}(\text{bpy})_3]\text{Cl}_2$ takes place smoothly for both 1,4- and 1,2-isomers of dihydropyridine (DHP), available in good yields *via* the Hantzsch reaction [163]. The primary photocatalytic step of this reaction is the electron transfer from DHP molecule to excited Ru^{II} complex as shown in Scheme 63 taking the aromatization of 1,4-DHP as an example.



Scheme 63. Aerobic oxidative aromatization of 1,4-DHPs under irradiation with visible light.

Many DHPs are commercially available and commonly used in photochemistry as sacrificial reductants. However, the oxidative aromatization reaction of DHPs might be also useful in the organic synthesis in particular for preparation of highly functionalized 2-arylpyridines, useful compounds in the coordination and material chemistry.

To prepare reusable photoredox catalysts for this reaction, triethoxysilyl-tethered Ru^{II} complex was incorporated in silica xerogels according to a sol-gel process (Scheme 13) [35]. Using $[\text{Ru}(\text{2Si-bpy})_3]^{2+}/\text{POS}$ photocatalyst thus obtained, 3,5-diethoxycarbonyl-4,6-dimethyl-2-phenylpyridine was successfully obtained in 10 consecutive reactions (Scheme 64).

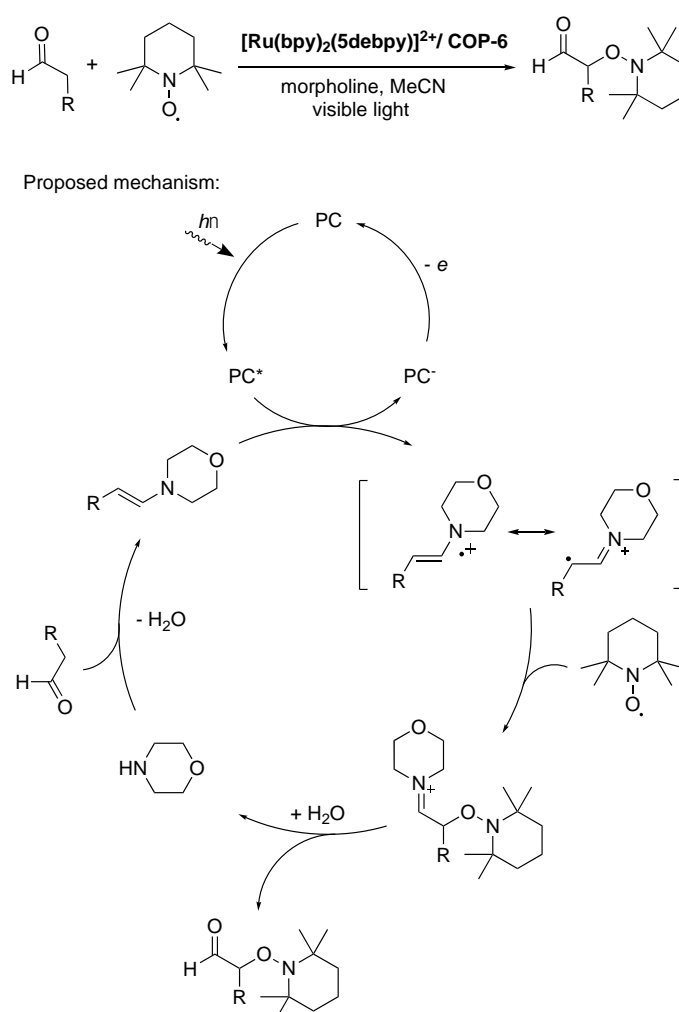


Scheme 64. Heterogeneous photoredox aromatization of 1,2- and 1,4-DHPs.

The powder recovered after 10 reuses preserved its original structure and Ru content. The catalyst was then employed for the oxidative aromatization of isomeric 1,2-DHPs and 1,4-DHPs bearing EWG and EDG at the phenyl substituent (Scheme 64). Comparable TOF (about 450 h⁻¹) was observed in all studied reactions, in which the products were isolated in 89–92% yields.

Aminoxylation of enolizable aldehydes

The **[Ru(bpy)₂(5debpy)]²⁺/COP-6** material (Scheme 27) was employed for aminoxylation of enolizable aldehydes with TEMPO [164] as shown in Scheme 65 [82]. The reaction was carried out using 3-phenylpropanal as a model compound. The product was isolated in 45% yield as in the analogous homogeneous reaction (48%). The recovered catalyst gave the product in 43% yield.



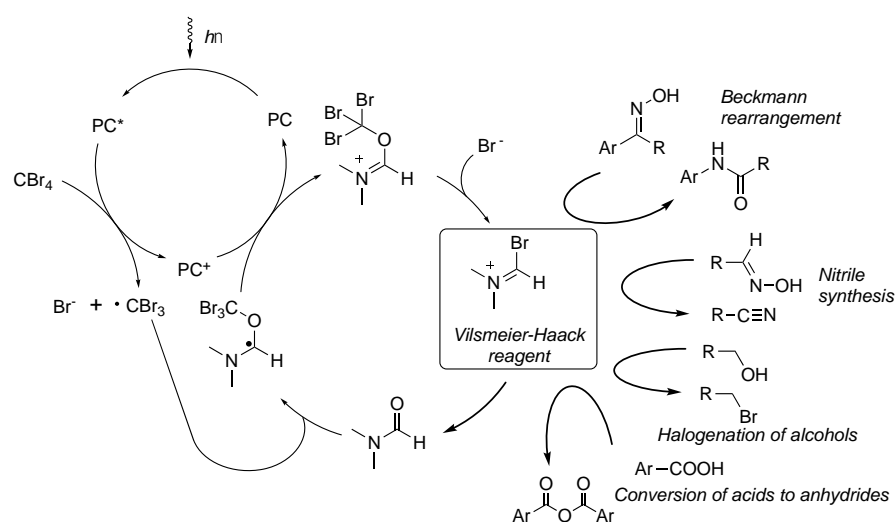
Scheme 65. Photoredox oxyamination of aldehydes under heterogeneous conditions.

3.2 Non-redox reactions

Transformations involving the generation of Vilsmeier-Haack reagent

Halomethyleneiminium salts (Vilsmeier-Haack reagent) are efficient electrophilic reagents to perform formylation, cyclizations and nucleophilic displacement reactions [165,166]. Many of them are valuable in the small-scale production of fine chemicals in agro- and pharmaceutical industries.

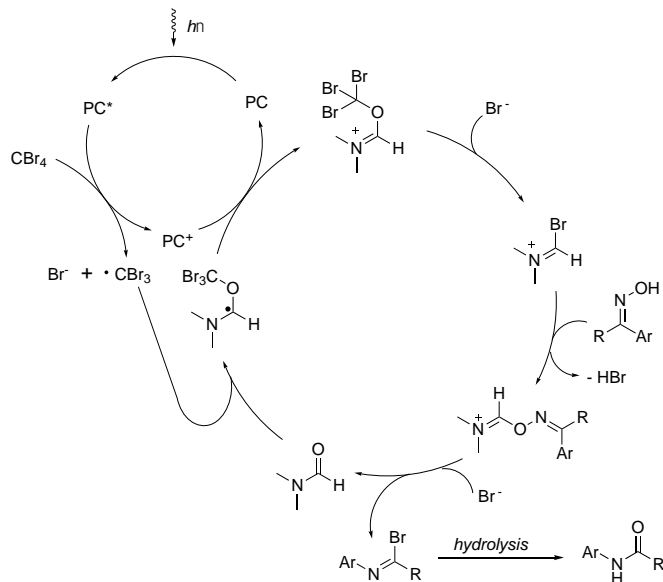
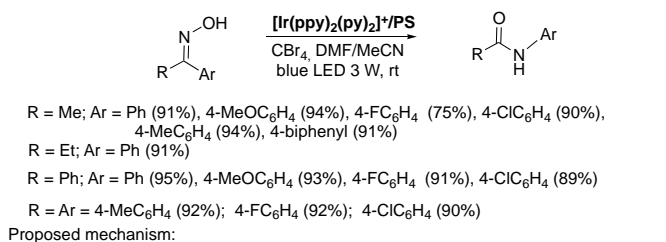
Vilsmeier-Haack reagents are usually generated *in situ* reacting *N,N*-disubstituted formamides with POCl₃, SOCl₂ or other reactive acid chlorides. Moreover, this reagent can be formed using tetrahalomethanes and an excess of Cu and Fe powder under harsh conditions. To increase the functional group tolerance and avoid aggressive and toxic reagents, the generation of the iminium salts by visible-light irradiation of *N,N*-disubstituted formamides and tetrabromomethane at room temperature in the presence of 1 mol% of [Ru(bpy)₃]Cl₂ is of particular interest (Scheme 66) [167].



Scheme 66. Photoredox reactions proceeding *via* generation of Vilsmeier-Haack reagent and suggested mechanism of its formation under photocatalytic conditions.

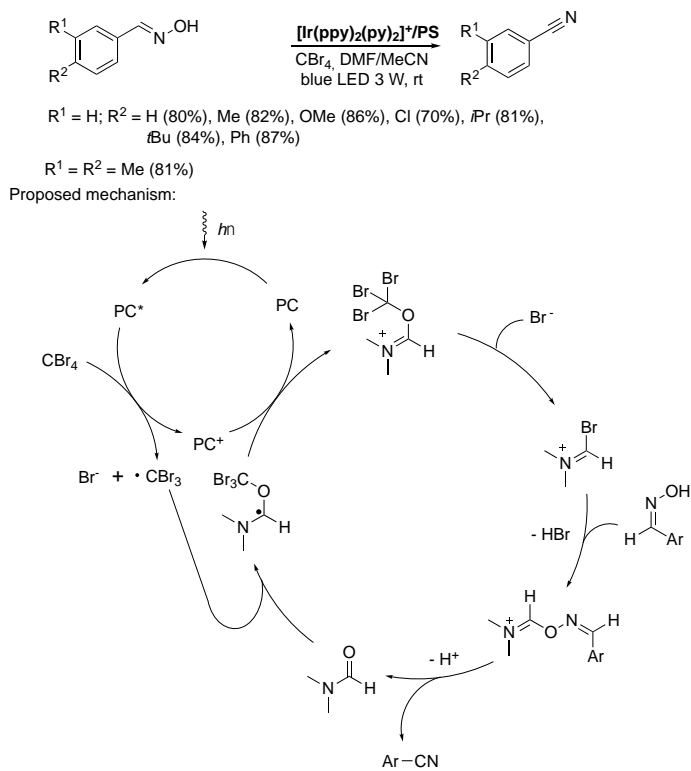
This homogeneous photocatalytic protocol was successfully applied to convert alcohols into halides [167], carboxylic acids into anhydrides [168], primary amides into nitriles [169] and to perform Beckmann and Lossen rearrangements [170, 171] (Scheme 66). However, difficult purification of products from trace amounts of toxic transition metals interfered with large-scale applications of this method, in particular in the pharmaceutical industry.

When the photoactive divinyl-based polymer [Ir(ppy)₂(py)₂]⁺/PS (Scheme 21) was used to perform the visible light-mediated Beckmann rearrangement, excellent product yields were obtained in acetonitrile for diphenyl and methyl phenyl ketoximes bearing EWG and EDG substituents (Scheme 67) [85]. In comparative studies of soluble *fac*-[Ir(ppy)₃] and heterogenized [Ir(ppy)₂(py)₂]⁺/PS using diphenyl ketoxime as model compound, the target amide was obtained in comparable yields (90% and 97%, respectively).



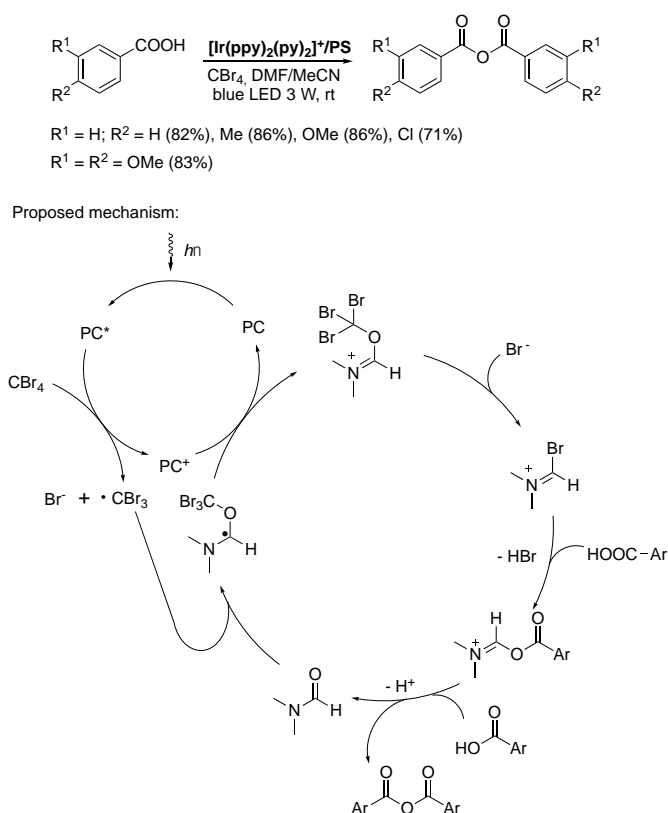
Scheme 67. Photoredox-catalyzed Beckmann rearrangement.

Aldoximes were converted to nitriles in good yields (70–87%) under the same experimental conditions (Scheme 68).



Scheme 68. Photoredox-catalyzed dehydration of aldoximes to nitriles.

Finally, this heterogeneous catalyst was used in the synthesis of anhydrides from benzoic acids as shown in Scheme 69. The overall high product yields were noticeably lower (by ~ 10% less) in the case of benzoic acids bearing EWG.

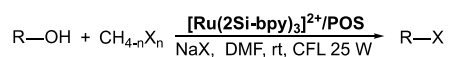


Scheme 69. Photoredox-catalyzed synthesis of carboxylic acid anhydrides.

Recycling of $[\text{Ir}(\text{ppy})_2(\text{py})_2]^+/\text{PS}$ photocatalyst was investigated in all these transformations using benzophenone oxime, 4-phenylbenzaldoxime and 4-methylbenzoic acid. The yield of the target products decreased by 5–10% (from 85–96% to 75–90%) after 5 consecutive photocatalytic cycles of each reaction without loss of selectivity.

To develop a reusable photocatalyst for transformation of alcohols to halides, the soluble PIB-polymer-tagged Ru^{II} complex (Scheme 35) was investigated [116]. However, the limited choice of solvents suitable for this reaction makes recovering of this soluble complex impossible.

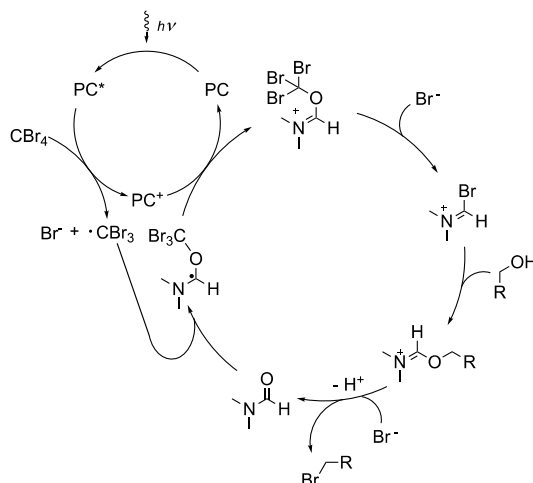
Silica-supported Ru^{II} complex $[\text{Ru}(\text{2Si-bpy})_3]^{2+}/\text{POS}$ gave excellent yields of target halides when the reaction was carried out in DMF in the presence of an external halogen source (NaBr or NaI) as shown in Scheme 70 [35]. Both alkyl bromide and iodide were obtained in high yields but catalyst recycling was not reported.



$\text{CH}_{4-n}\text{X}_n = \text{CBr}_4$:
 $\text{X} = \text{Br}$; $\text{R} = \text{Bz}$ (89%), Cy (85%), $n\text{C}_{12}\text{H}_{25}$ (90%), $i\text{Pr}$ (93%),
 2-propynyl (88%)

$\text{CH}_{4-n}\text{X}_n = \text{CHI}_3$:
 $\text{X} = \text{I}$, $\text{R} = \text{Bz}$ (92%), Cy (82%), $n\text{C}_{12}\text{H}_{25}$ (91%), $i\text{Pr}$ (91%),
 2-propynyl (76%)

Proposed mechanism:

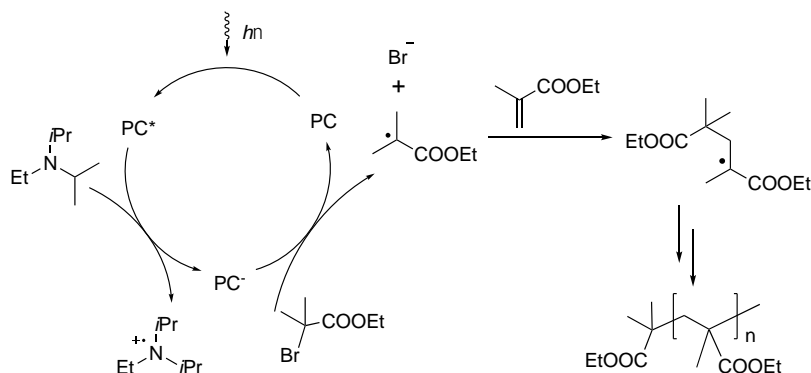


Scheme 70. Photoredox-catalyzed synthesis of alkyl halides from alcohols.

Polymerization of acrylates and acrylamides

Ruthenium(II) and iridium(III) polypyridyl complexes can also be used for the initiation of diverse light-mediated polymerization processes such as free radical polymerization (FRP), cationic and ring-opening metathesis polymerizations and so forth [172-174]. Light is particularly interesting for developing external stimuli-controlled polymerization procedures due to possibility to achieve high selectivity using mild reaction conditions in relatively simple experimental setup. Photo-induced polymerization can be stopped by switching off the irradiation and then continued by exposing the reaction mixture to the light.

In photo-induced FRP processes initiated by Ru^{II} photoredox catalysts, addition of a sacrificial reductant is needed to generate a powerful single electron reductant $[\text{Ru}(\text{bpy})_3]^{+}$ which gave reactive carbon-centered radicals reacting with activated organic halides (Scheme 71). These radicals further react with monomer molecules, for example, methacrylate, giving the final product in free-radical chain polymerization.

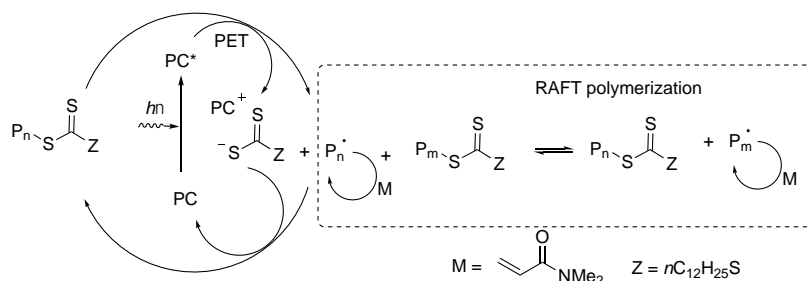


Scheme 71. Proposed mechanism for the initiation of radical polymerization under visible light irradiation.

The photoredox FRP of various methacrylates (methyl (MMA), *n*-butyl, cyclohexyl, benzyl and glycidyl(GMA)) smoothly proceeds in the presence of $[\text{Ru}(\text{bpy})_3]^{2+}$ encapsulated in the Nafion-covered SiO_2 NPs ($[\text{Ru}(\text{bpy})_3]^{2+}/\text{Nf}/\text{SiO}_2$) [72]. The photo-induced reaction was carried out in acetonitrile at room temperature adding DIPEA and ethyl 2-bromoisobutyrate for the initialization of the chain process. The average molecular weight (M_n) of polymers thus prepared was dependent on the monomer structure and varied in the range of 39000 – 90000 as was observed in homogeneous reaction. Despite the high viscosity of the reaction mixture, the catalyst was successfully separated by centrifugation, washed with organic solvents and then reused in 5 repeated runs of MMA polymerization.

Another catalyst recycling strategy was used in the visible light-driven FRP of ethyl (EMA), 2-ethoxyethyl (2E-EMA) methacrylates and GMA performed in heptane in the presence of $[\text{Ru}(\text{PIB-bpy})_3]\text{Cl}_2$ [115]. This complex was soluble in heptane solutions of monomers and was separated from the products after spontaneous precipitation of the polymers. According to ICP-MS analysis of the crude 2E-EMA polymer thus prepared, Ru content in the sample was 1.9 ppm that is much less than Ru content (48.4 ppm) found in polymer prepared using classical $[\text{Ru}(\text{bpy})_3](\text{PF}_6)_2$ photocatalyst in DMF and separated by precipitation adding an excess of MeOH. The heptane-soluble photoredox catalyst was reused 3 times in the polymerization of EMA affording a slightly lower yield in the 3rd run probably due to physical losses of the catalyst in the recycling work-up or its partial decomposition under a long irradiation with visible light.

Photoinduced electron/energy transfer reversible addition–fragmentation chain transfer (PET-RAFT) polymerization also can be performed under visible light irradiation in the presence of VATMPY complexes [175]. In this process, the reaction is initiated by electron or energy transfer from $^*\text{PC}$ to trithiocarbonate derivatives which also serve as chain transfer agents (CTA) (Scheme 72).



Scheme 72. Proposed mechanism of PET-RAFT polymerization.

It was demonstrated that the photo-induced RAFT polymerization can be stopped by switching off the irradiation. Moreover, the use of the second orthogonal external switcher (pH changing, for example) is possible in this reaction to achieve fine tuning of the polymer structure [175, 176].

Recently, PET-RAFT polymerization of *N,N*-dimethylacrylamide (DMA), *N,N*-diethylacrylate, *N*-isopropylacrylate, 2-hydroxyethyl acrylate, glycidyl methacrylate, poly(ethylene glycol) methyl ether methacrylate, and styrene in various solvents (DMSO, MeCN, MeOH and toluene) was investigated using $[\text{Ru}(\text{bpy})_3]^{2+}/\text{hHPGE-PFPPN}$ material as a photoredox catalyst and 2-(dodecylthiocarbonothioylthio)-2-methylpropionic acid as a CTA [88]. After optimization of reaction conditions, polymers with molecular weights $M_n = 9\text{--}19.0 \text{ kg mol}^{-1}$ and rather homogeneous molecular weight distribution ($D < 1.2$) were obtained for all monomers except 2-hydroxyethyl acrylate and styrene. In the polymerization of 2-hydroxyethyl acrylate, side *trans*-esterification reaction was observed leading to an increase of dispersity of

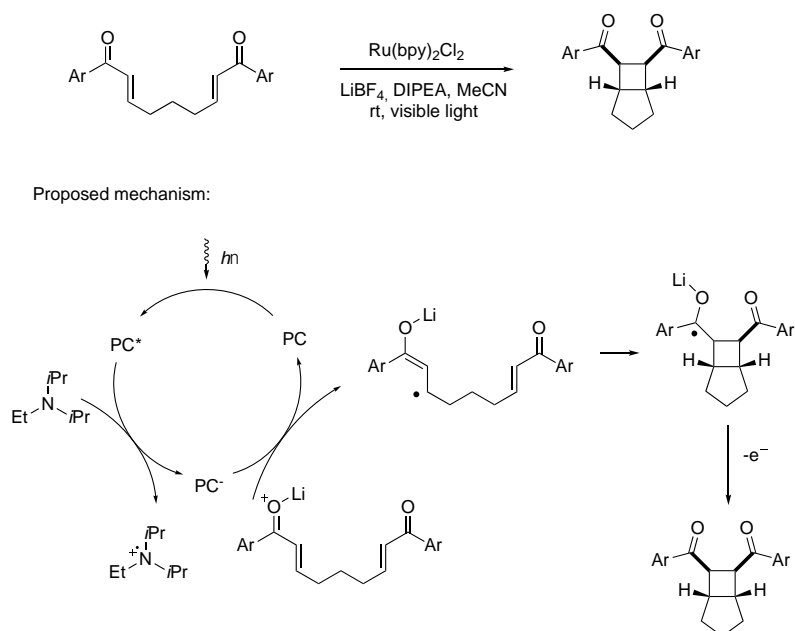
polymer thus obtained up to 1.25. On the other hand, polymerization of styrene was slow and after 24 h of irradiation the conversion of monomer was only 25%.

The presence of poly(*N*-isopropylacrylamide) residues (PNIPAM) in **[Ru(bpy)₃]²⁺/hHPGE-PFPPN** shells conferred this photocatalyst with thermo-responsive behavior. Coil-to-globule phase transition of PNIPAM residues was observed at 32 °C. Therefore, the polymerization of DMA was accelerated significantly above 32 °C due to the increase of accessibility of the photocatalyst. Thus, the control of the radical polymerization by two external stimuli, namely light and heat, was feasible.

The catalyst recycling was investigated in the RAFT-polymerization of DMA using 20 ppm of **[Ru(bpy)₃]²⁺/hHPGE-PFPPN** photocatalyst. The average monomer conversion after 6 h of irradiation decreased from 90 to 70% in the 4th run due to leaching of ruthenium complex to solution. **[Ru(bpy)₃]²⁺/hHPGE-PFPPN** material sample was regenerated by treatment of the recovered solid with Ru(bpy)₂Cl₂ in ethanol/THF solvent mixture. Four consecutive reaction runs with material thus obtained gave the results similar to those obtained in the first series of four experiments.

Cycloaddition reactions

Visible light-mediated cycloaddition reactions can proceed through photoinduced electron transfer or triplet energy transfer. The first mechanism was proposed for [2+2] cycloadditions of aryl enones. As a representative example, intramolecular [2+2] cycloaddition of bis(arylenone)s is shown in Scheme 73 [177]. This reaction takes place only in the presence of lithium salts and DIPEA. As in the free radical polymerization reactions, the addition of a sacrificial reductant is needed to generate **[Ru(bpy)₃]⁺** complex, which reacts, in this case, with an bis(arylenone) molecule activated by Li⁺ cation. Only aryl-substituted enones are suitable for this reaction presumably due to the greater ease of generating the requisite radical intermediates. In contrast, the reacting partner could be any Michael acceptor [178].



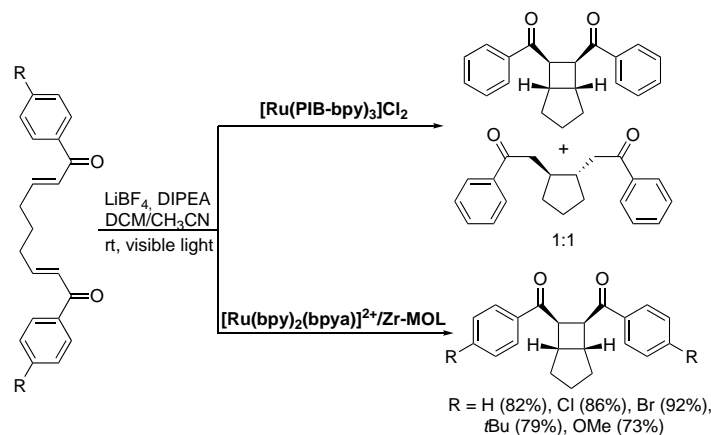
Scheme 73. [2+2] Cycloaddition of bis(arylenone)s.

The development of reusable photocatalysts for this [2+2] cycloaddition reaction is challenging because the reaction is quite demanding towards solvents and the mass diffusion

process involving these flexible bulky bis(enone) molecules has strong influence on the reaction rate when the reactions are carried out with heterogeneous solid photocatalysts.

UiO-67 MOF doped with $[\text{Ru}(\text{bpy})_3]^{2+}$ catalytic centers [60] failed to promote [2+2] cycloaddition of bis(enone)s [68]. It seems that the formation of sterically demanding intermediates in the narrow pores of this solid was impossible.

When soluble amphiphilic photoredox catalyst $[\text{Ru}(\text{PIB-bpy})_3]\text{Cl}_2$ is employed to develop reusable photocatalytic system for a phase-separated process, the reaction should be performed in $\text{CH}_2\text{Cl}_2/\text{MeCN}$ mixture (9:1), due to a low solubility of this catalyst in acetonitrile [116]. Under these conditions, [2+2] cycloaddition was accompanied by the reductive cyclization and two products were obtained in the molar ratio 1:1 (Scheme 74).

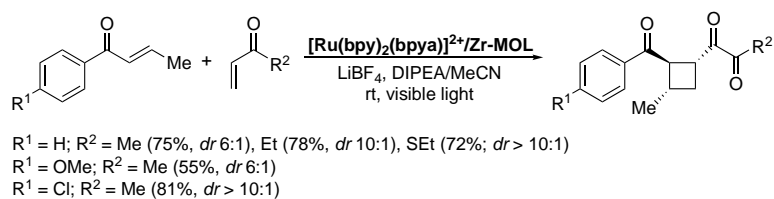


Scheme 74. Photocatalytic intramolecular bis(enone)s [2+2] cycloaddition.

This switch of the reaction course is rather unexpected. Reduced product can be obtained selectively when the cyclization of bis(enone)s is performed in acidic reaction medium (see below for a discussion, Scheme 93) [179]. Under the studied experimental conditions, the reduced product is most likely formed through another mechanism reported recently for non-catalytic reductive reactions in dichloromethane solutions of DIPEA [180].

Finally, the selective intramolecular [2+2] cycloaddition of aryl bis(enone)s using heterogenized catalysts was achieved by using $[\text{Ru}(\text{bpy})_2(\text{bpya})]^{2+}/\text{Zr-MOL}$ sheets with 1-2 nm of thickness in which catalytic centers are more accessible than in $[\text{Ru}(\text{bpy})_2(5\text{dcbpy})]^{2+}/\text{UiO-67}$ [68]. Bicyclic compounds were obtained in 73–92% yield as single *meso* isomers when bis(enone)s were irradiated with blue LED in acetonitrile. The aryl bis(enone)s bearing EDG at the phenyl ring required longer reaction times than electron-deficient aromatics. The catalyst was stable under reaction conditions and leaching of both Ru and Zr into the solution environment was negligible (2.3 and 0.3% for Ru and Zr, respectively). The photoactive powder was recovered and reused in three repeated cycloaddition runs without loss of activity and diastereoselectivity.

Intermolecular [2+2] cycloaddition reactions of phenyl enones and diverse Michael acceptors were investigated under the same heterogeneous conditions [68]. As shown in Scheme 75, $[\text{Ru}(\text{bpy})_2(\text{bpya})]^{2+}/\text{Zr-MOL}$ gave the target products in 55–81 % yields which were comparable to those observed with the soluble $[\text{Ru}(\text{bpy})_3]\text{Cl}_2$ complex. However, while all homogeneous reactions proceeded with excellent selectivity (> 10:1), the heterogeneous reactions with methylacrylate afforded two diastereoisomers in lower (up to 6:1) molar ratio.

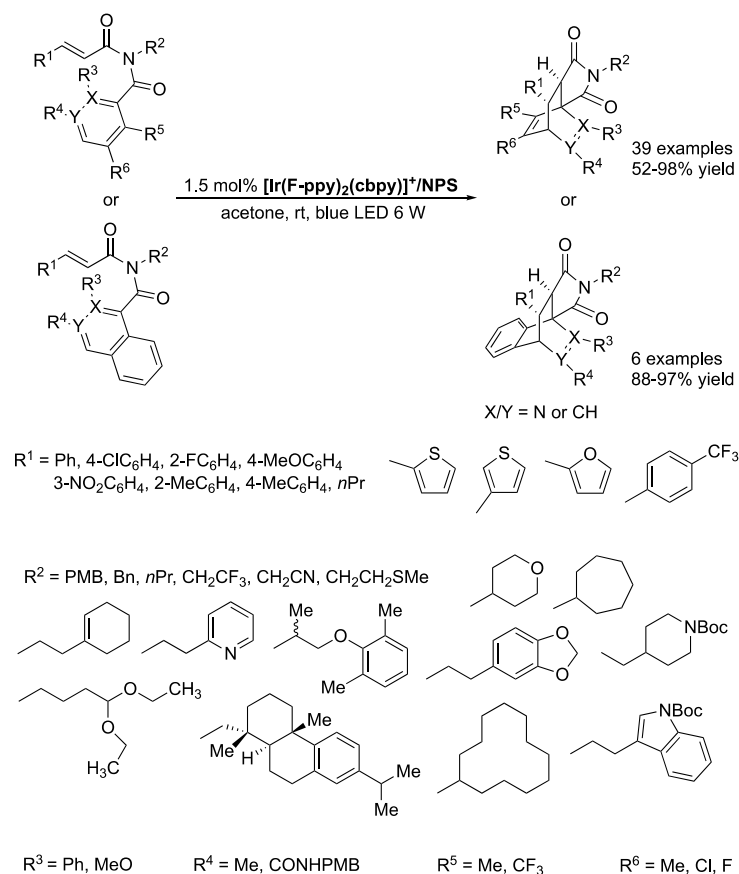


Scheme 75. Photocatalytic intermolecular [2+2] cycloaddition of phenyl enones and Michael acceptors.

Under the same conditions, MOF $[Ru(bpy)_2(5dcbpy)]^{2+}/UiO-67$ gave the products in the same diastereomer ratio (*dr*) but in only 50–60% yields that likely reflected a slow diffusion of intermediate radicals in MOF pores [68].

The photoinduced energy transfer process is also useful for organic synthesis. Many oxo-functionalization reactions proceed after the generation of singlet oxygen through energy transfer from 3MLCT state of photosensitizer to an oxygen molecule. An interesting example of photocatalyzed cycloaddition reactions proceeding *via* triplet energy transfer without participation of molecular oxygen was reported recently by Glorius and coworkers [75].

Intramolecular [4+2] cycloaddition leading to the formation of isoquinuclidines (2-azabicyclo[2.2.2]octanes) is of particular interest among various reactions used for the dearomatization of pyridines (Scheme 76).



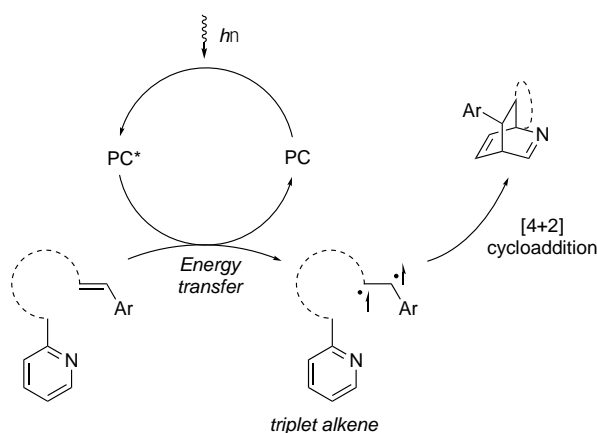
Scheme 76. Intramolecular [4+2] cycloaddition reactions leading to dearomatization of pyridines.

Isoquinuclidines and their dehydrogenated derivatives are found in various bioactive natural products and pharmaceuticals and can be used as valuable intermediates for organic synthesis. Recently, intramolecular [4+2] cycloadditions to the pyridine ring were performed under visible light irradiation using the $[Ir(F\text{-}ppy)_2(cbpy)]^+/NPS$ polystyrene beads (Scheme

22). Being irradiated by blue LED for 5 h in acetone, pyridine-containing cinnamyl amides afford the desired products in excellent yields as mixtures of two diastereomers. Various substituents can be introduced at both aromatic ring and at the amide nitrogen atom without a significant decrease in product yields.

Dearomatization of pinacolamide with 4-methoxybenzyl ether (PMB) protecting group in dichloromethane, THF, MeCN, DMF and water using as low as 0.75 mol% of the $[\text{Ir}(\text{F-ppy})_2(\text{cbpy})]^+/\text{NPS}$ photocatalyst was also successful. Unfortunately, the *dr* was only slightly dependent on the solvent and varied within a range of 1.1 to 2.0. In contrast, when dichloromethane was replaced by acetone in the reaction of *N*-benzyl-protected compound *dr* was increased from 2.0 to 20.0.

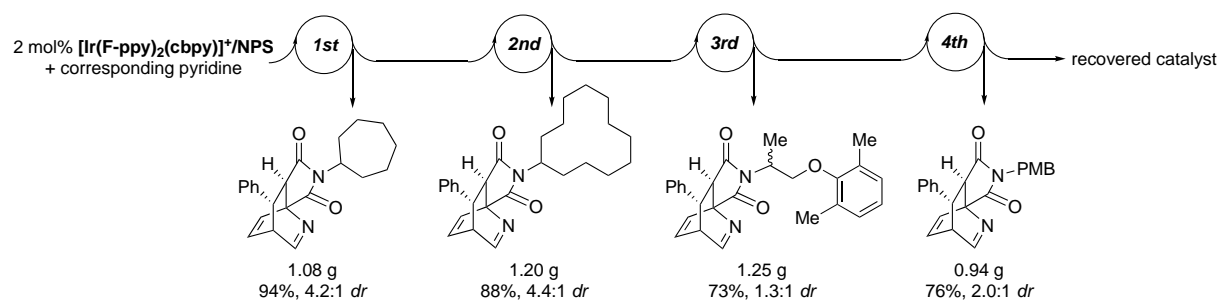
Mechanistic investigations have shown that the reaction proceeded through a 1,2-biradical intermediate *via* triplet energy transfer as shown in Scheme 77. This intermediate was trapped by adding 2,3-dimethylbuta-1,3-diene or styrene to a reaction mixture of PMB-protected derivative.



Scheme 77. Proposed mechanism of visible light-mediated intramolecular [4+2] cycloaddition.

A series of dearomatized products was also obtained from isoquinolines with excellent yields (88–97%) and in high *dr* of 8:1 to 20:1 (Scheme 76). Both naphthyl- and phenyl-substituted cinnamyl amides also smoothly reacted under these conditions affording the products in high yields. The arene substituent at double bond can also be replaced by furanyl or thienyl residues. In contrast, when aromatic residues were replaced by *n*-propyl group, no target product was obtained.

After demonstrating the reusability of $[\text{Ir}(\text{F-ppy})_2(\text{cbpy})]^+/\text{NPS}$ in 10 consecutive reaction runs, four sequential gram scale reactions were successfully performed using substrates bearing different substituents (PMB, cycloheptyl, cyclododecyl, and 1-methyl-2-(2,6-dimethylphenoxy)ethyl) at the amide nitrogen atom as shown in Scheme 78.

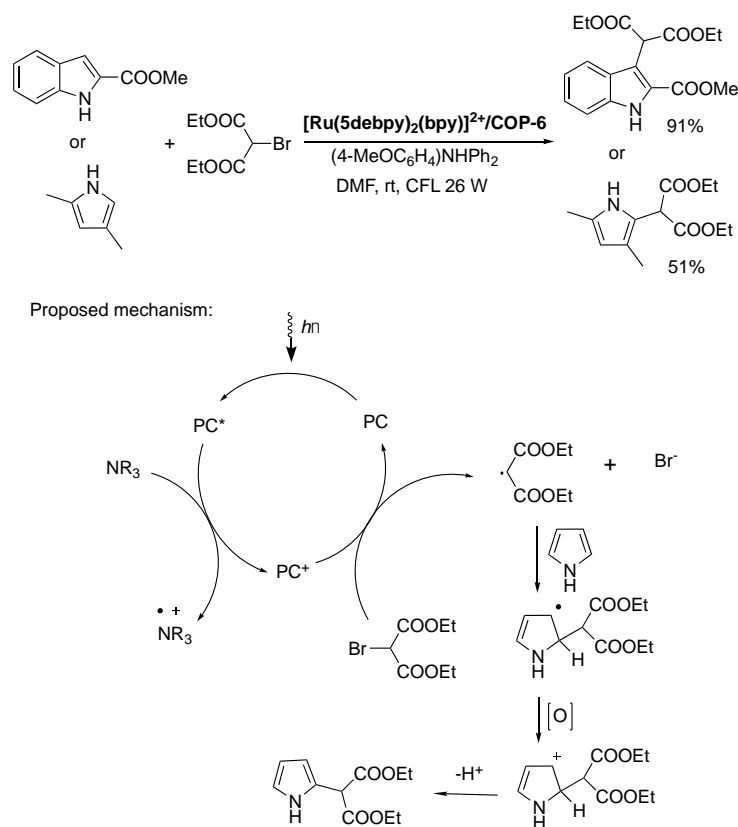


Scheme 78. The sequential gram scale [4+2] cycloaddition reactions carried out using reusable $[\text{Ir}(\text{Fppy})_2(\text{cbpy})]^{2+}/\text{NPS}$ catalyst.

α -(Hetero)arylation of malonates

Reactive carbon-centered free radicals can be easily generated by the reductive cleavage of organic halides in photoredox catalytic process [181-183]. This primary photocatalytic step can be followed by different radical transformations leading to many valuable organic products. For example, α -(hetero)arylation of malonates can be performed under these conditions as shown in Scheme 79.

The porous cross-linked polymer $[\text{Ru}(\text{5debpy})_2(\text{bpy})]^{2+}/\text{COP-6}$ (Scheme 27) efficiently catalyzed the α -arylation of diethyl bromomalonate by 2-methoxycarbonylindole and 2,5-dimethylpyrrole giving the products in 91 and 51% yield, respectively [82]. These yields are comparable to those obtained in control reactions under homogeneous conditions but $[\text{Ru}(\text{5debpy})_2(\text{bpy})]^{2+}/\text{COP-6}$ can be reused without any significant decrease in the product yields.



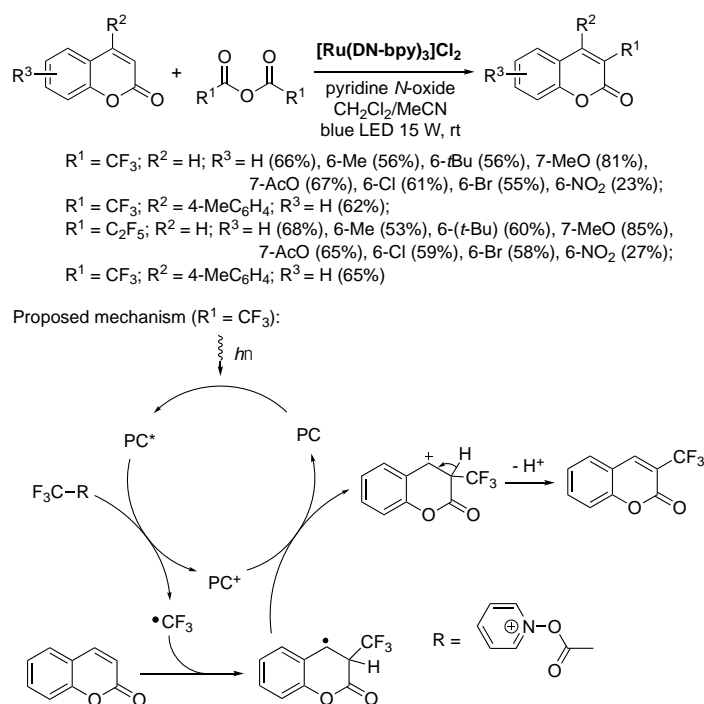
Scheme 79. Suggested mechanism of α -(hetero)arylation of malonates.

Fluoroalkylation reactions

The fluoroalkylation of unsaturated bonds is widely used in medicinal chemistry. Fluorinated derivatives of coumarin can be obtained under visible-light irradiation in the presence of photoredox catalysts by reacting coumarins or phenyl alkynoates with fluorinated compounds, which can generate free-radical intermediates [184, 185]. For example, coumarins reacted with trifluoroacetic or pentafluoropropionic anhydrides in the presence of pyridine *N*-

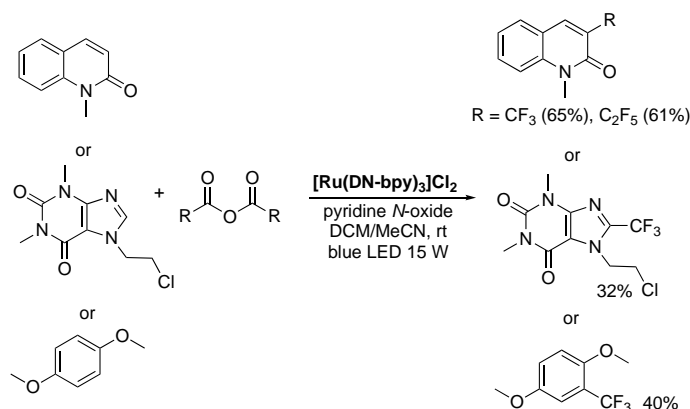
oxide and $[\text{Ru}(\text{DN-bpy})_3]\text{Cl}_2$ complex (Scheme 37) in $\text{CH}_2\text{Cl}_2/\text{MeCN}$ mixture under irradiation with blue LED affording perfluoroalkylated derivatives (Scheme 80) [118]. The suggested mechanism for the generation of fluorinated alkyl radicals involves the acetylation of *N*-oxide to form an intermediate undergoing reductive cleavage (not shown in the scheme). Addition of this radical to double bond of the heterocyclic ring is followed by the oxidation of the carbon-centered free radical to carbocation and base-catalyzed elimination.

When parent coumarin and its acetoxy or halogen-substituted derivatives were introduced in this reaction, the products were obtained in 52–85% yields with both fluorinated anhydrides. However, the product yields dropped down to 23–27% when the reactions were performed with the heterocycle bearing a strong electron-withdrawing nitro group presumably due to instability of starting compound under the reaction conditions.



Scheme 80. Photoredox-catalyzed synthesis of CF_3 -substituted coumarins and suggested mechanism of this reaction.

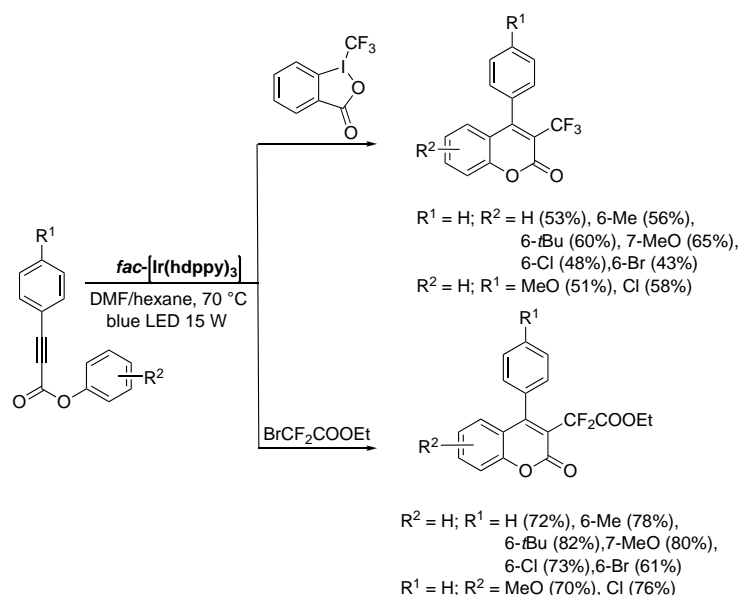
N-Methyl quinolinone also reacts with trifluoroacetic or pentafluoropropionic anhydrides under these conditions affording fluorinated products in good yields (Scheme 81) [118]. Photo-induced trifluoromethylation of 7-(2-chloroethyl)theophylline and *p*-dimethoxybenzene was also observed though the products were obtained in moderate 32% and 40% yields (Scheme 81) [118].



Scheme 81. Synthesis of fluorinated derivatives of nitrogen heterocycles and electron-rich arenes.

The heptane-soluble $[\text{Ru}(\text{DN-bpy})_3]\text{Cl}_2$ complex can be separated by liquid/liquid extraction as previously was done in the photocatalytic processes mediated by $[\text{Ru}(\text{PIB-bpy})_3]\text{Cl}_2$ complex [116,117]. The catalyst recycling was investigated only in the trifluoromethylation of unsubstituted coumarin with trifluoroacetic anhydride. For these substrates, the difference in the solubility of the reaction product and the photoredox catalyst allowed for the rather efficient catalyst recovery but the product yield progressively decreased from 66% to 51% in 6 consecutive catalytic runs performed with the same catalyst sample. The relative amount of recovered catalyst was estimated after the 6th run and found to be at the level of 53% of the initial loading.

Trifluoromethylated derivatives of coumarins were also obtained by difunctionalization of phenyl alkynoates as shown in Scheme 82 [119].



Scheme 82. Photoredox-catalyzed difunctionalization of phenyl alkynoate with Togni's reagent.

In this case, CF_3 radical was generated from Togni's reagent in the presence of K_2HPO_4 and the catalyst recycling was achieved after attaching hydrophobic substituents at the bpy ligands of the Ir^{III} catalyst (Scheme 38). Thermomorphic DMF/hexane solvent mixture was used to perform the reaction under homogeneous conditions at 70 °C. The photoredox catalyst was easily separated

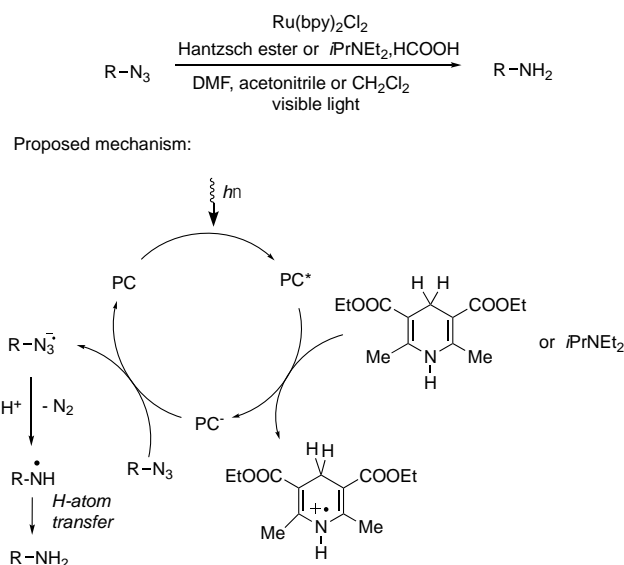
after cooling of the reaction mixture because DMF and hexane are immiscible at room temperature. A wide range of trifluoromethylated 4-aryl-substituted coumarins was obtained in moderate yields (43–65%) by this reaction. The repeated experiments with the recycled catalyst performed with phenyl ester of 3-phenylpropiolic acid gave nice results. The product yields did not decrease in 5 consecutive runs and 79% of the catalyst were recovered after the 5th cycle.

This reusable catalyst was also successfully employed in the synthesis of 3-(etoxy-carbonyl)difluoromethyl-substituted coumarins through the reaction of arylalkynes with ethyl bromodifluoroacetate as shown in Scheme 82 [119].

3.3 Reductive transformations

Synthesis of amines

Azides are convenient and readily available amine precursors [186]. Photoredox catalysts allow for their reduction in DMF, acetonitrile or CH₂Cl₂ solutions at room temperature [187]. The homogeneous photocatalyzed reduction can be carried out using DIPEA as a sacrificial agent but the reaction proceeds faster and affords the products in higher yields being performed using both ammonium salts and Hantzsch esters as sources of electrons and protons. The key steps of the suggested mechanism of this reduction are shown in Scheme 83. The reduction starts with reductive quenching of the excited photoredox catalyst by tertiary amine or Hantzsch ester. Then single-electron reduction of the azide molecule by [Ru(bpy)₃]⁺ affords a radical anion which is further transformed to the aminyl radical upon expulsion of dinitrogen and protonation. This radical is finally converted to a primary amine through the abstraction of a hydrogen atom.



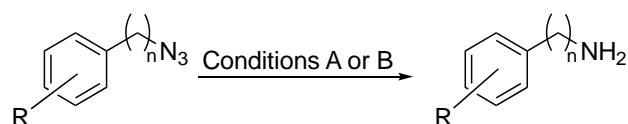
Scheme 83. Reduction of azidobenzenes to corresponding amines under irradiation with visible light in the presence of the photoredox catalyst and key steps of the catalytic process (see text for some additional details).

The mild experimental conditions of this method allow for the use of hybrid molecular materials formed by non-covalent binding of components in this reaction (Table 11). For example, supramolecular 3D framework [Ru(bpy)₂(mhbpy)]²⁺/SOF-1 assembled through CB[8] units (Scheme 34) worked well and was reused up to 11 times in the reduction of 1-azido-4-cyanobenzene in the presence of Hantzsch ester, DIPEA and formic acid in a CH₂Cl₂/hexane solvent mixture at room temperature (entry 4) [89]. The reduction of aromatic azides bearing EWG such as 4-methoxycarbonyl, 4-carboxy, 4-halogen, 4-trifluoromethyl and 3-cyano groups

also smoothly took place under these conditions giving the substituted anilines in quantitative yields (entries 1–6, 9–15). In all these reactions, the heterogenized catalyst showed the catalytic activity comparable to that of soluble $[\text{Ru}(\text{bpy})_2(\text{mhbp})]\text{Cl}_2$ complex. Unfortunately, electron-rich azidobenzenes gave the target products in moderate yields (43% and 20%, respectively, entries 7 and 8) which are significantly lower than those obtained in the homogeneous reduction with $[\text{Ru}(\text{bpy})_2(\text{mhbp})]\text{Cl}_2$ (69% and 43%, respectively).

The recycling and reuse of this heterogeneous catalyst in the reduction of 3-cyanophenylazide and 4-carboxyphenylazide were less successful compared to the reaction of 1-azido-4-cyanobenzene. Partial hydrolysis of the hydrazone bond and decomposition of supramolecular framework due to a slow inclusion of aromatic products into CB[8] cavities might have accounted for a rapid decrease of the product yields in these recycling experiments. ICP-OES experiments revealed the loss of 89% of Ru by the catalyst after the cumulative 11th run of the reduction of 1-azido-4-cyanobenzene.

Table 11. Photocatalytic reduction of azides.



Entry	R	n	Condi- tions ^a	Time	Yield	Reference
1	3-CN	0	A	8	99	[89]
2	3-CN	0	B	12	91	[90]
3	4-CN	0	A	18	99	[89]
4	4-CN ^b	0	A	1	98	[89]
5	4-CN	0	B	9	96	[90]
6	4-CN	0	B ^c	1	95	[90]
7	4-Me	0	A	38	43	[89]
8	4-MeO	0	A	38	20	[89]
9	4-COOH	0	A	9	99	[89]
10	4-COOMe	0	A	6	99	[89]
11	4-COOMe	0	B	12	92	[90]
12	4-CONHC ₃ H ₁₁	0	A	18	99	[89]
13	4-F	0	A	48	99	[89]
14	4-CF ₃	0	A	20	99	[89]
15	4-Cl	0	A	38	99	[89]
16	2-naphthylazide	0	A	38	99	[89]
17	4-CN	1	B	30	92	[90]
18	4-Me	1	B	40	87	[90]
19	4-MeO	1	B	40	64	[90]
20	4-COOMe	1	B	30	92	[90]
21	4-Cl	1	B	40	84	[90]
22	H	1	B	30	89	[90]
23	4-CN	2	B	30	92	[90]
24	4-Me	2	B	30	81	[90]
25	4-MeO	2	B	30	78	[90]
26	4-Cl	2	B	30	94	[90]
27	H	2	B	30	92	[90]
28	H	3	B	70	73	[90]

^a Conditions A: $[\text{Ru}(\text{bpy})_2(\text{mhbp})]^{2+}/\text{SOF-1}$, Hantzsch ester, DIPEA, HCOOH, DCM/n-hexane (1:1), rt, CFL, 26 W. Conditions B: 0.1 mol% $[\text{Ru}(\text{2pbpy})_3]^{2+}/\text{SOF-2}$, Hantzsch ester, DIPEA, HCOOH, MeCN, rt, CFL, 50 W.

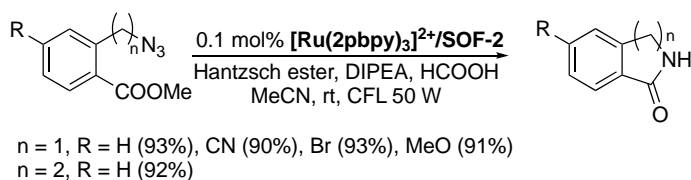
^b CFL, 300 W was used as a light source. ^c MeCN/H₂O (1:1) solvent mixture was used.

To increase stability of ruthenium(II) catalysts prepared by the assembly of molecular components within CB[8] units, each of the three bpy ligands was furnished with two

substituents suitable for the intramolecular assembly within CB[8] units and thus a supramolecular framework $[\text{Ru}(\text{2pbpy})_3]^{2+}/\text{SOF-2}$ was prepared (Figure 12) [90]. This photoactive material was efficient in the reduction of azidobenzenes, benzyl and 2-phenylethyl azides (Table 11). The comparative studies have demonstrated that homogeneous reactions catalyzed by $[\text{Ru}(\text{bpy})_3]\text{Cl}_2$ took place slowly and gave the respective amines in lower yields as compared to the reductions catalyzed by this supramolecular assembly. It was assumed that the photo-induced reduction in pores of $[\text{Ru}(\text{2pbpy})_3]^{2+}/\text{SOF-2}$ was accelerated due to the presence of several catalytic centers close to each other and adsorption of azide molecules by the porous solid.

Unfortunately, the recovered $[\text{Ru}(\text{2pbpy})_3]^{2+}/\text{SOF-2}$ material usually lost its activity. However, in the most successful case, the reduction of 1-azido-4-cyanobenzene, the catalyst was recycled 11 times and the product was obtained in 70% yield in the 12th run after increasing the reaction time from 9 h to 20 h.

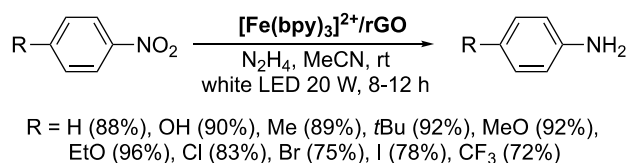
This photoredox catalyst is also efficient in tandem reactions leading to formation of lactams from methyl 2-(azidomethyl)- and 2-(2-azidoethyl)benzoates through the azide reduction followed by the cyclization reaction (Scheme 84) [90]. The target lactams were isolated in high yields (90–93%).



Scheme 84. Photocatalytic synthesis of lactams under visible-light irradiation.

Nitrobenzenes can also be reduced to anilines under irradiation with visible light using photoredox catalysts if hydrazine hydrate is employed as a stoichiometric reductant (Scheme 85) [188]. rGO-Supported $[\text{Fe}(\text{bpy})_3](\text{PF}_6)_2$ complex $[\text{Fe}(\text{bpy})_3]^{2+}/\text{rGO}$ shown in Scheme 3) is an efficient heterogenized photocatalyst for this reaction [49]. With this material formed through rather weak π - π interactions of the complex and the support, the reduction of nitrobenzene in acetonitrile proceeded faster than the analogous reaction carried out with $[\text{Fe}(\text{bpy})_3](\text{PF}_6)_2$ complex under homogeneous conditions. When a mixture of rGO and $[\text{Fe}(\text{bpy})_3](\text{PF}_6)_2$ with the same amount of Fe^{II} complex as in the pre-formed $[\text{Fe}(\text{bpy})_3]^{2+}/\text{rGO}$ material was used in the reduction of nitrobenzene, the acceleration of reaction was not observed. Electron transfer from excited $^*[\text{Fe}(\text{bpy})_3]^{2+}$ complex to the rGO support could favor the photoreduction since the efficient charge separation increases the probability of the electron transfer to an organic molecule. Considering a low content of iron(II) complex in this composite material and aromatic nature of rGO support, adsorption of nitrobenzene on rGO surface also may be responsible for the enhancement of the reaction rate in the presence of $[\text{Fe}(\text{bpy})_3]^{2+}/\text{rGO}$ photocatalyst.

Among the substituted nitrobenzenes investigated in this reaction, compounds bearing EWG were less reactive and gave the lower product yields (72–83%) compared to those with EDG (90–96%). The catalyst was reused in 6 consecutive runs affording anilines with similar yields. The ICP-AES analysis have showed that less than 10% of Fe was lost in total after the 6th run.

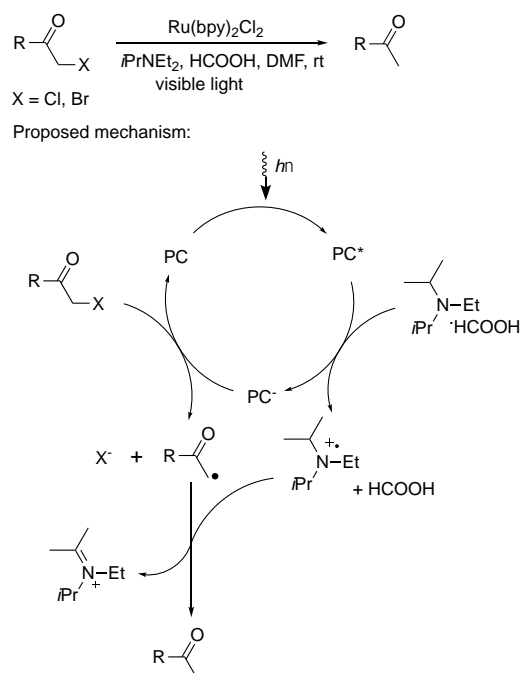


Scheme 85. Reduction of nitrobenzenes to anilines.

Hydrodehalogenation of alkyl halides

The reductive cleavage of organic halides is a fundamental process involved in many synthetic, as well as spontaneous, environmental processes. The study of photocatalytic approaches towards this transformation helps to probe new possibilities for its incorporation into various useful applications.

The photo-induced hydrodebromination under irradiation by visible light was firstly developed under homogeneous conditions using $[\text{Ru}(\text{bpy})_3]\text{Cl}_2$ as a photoredox catalyst and DIPEA with either formic acid or Hantzsch esters as a stoichiometric reductant and a hydrogen atom source [182]. The proposed reaction mechanism is shown in Scheme 86.



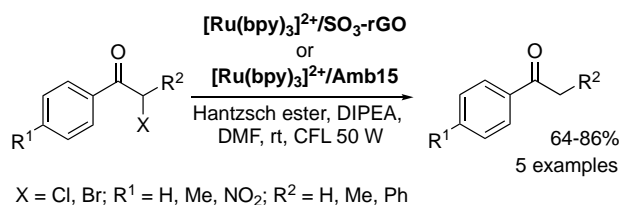
Scheme 86. Suggested mechanism of hydrodehalogenation of α -carbonyl-substituted halides.

Reductive quenching of $^*\text{PC}$ by DIPEA generates the PC^- , which reduces alkyl halide to a carbon-centered radical. This radical may abstract hydrogen atom from α -position of the amine radical anion. When Hantzsch ester or formate ion are employed in the reaction, they also may serve as hydrogen atom donors. Excellent selectivity, relatively short reaction times and mild conditions make this photocatalytic reaction an excellent model for investigations of newly prepared heterogenized photoredox systems.

Initial attempts to increase the efficiency of photoredox catalyst in the reduction of α -bromoacetophenones by combining the ruthenium(II) complex and the conductive rGO support ($[\text{Ru}(\text{bpy})_3]^{2+}/\text{SO}_3\text{-rGO}$ material shown in Scheme 4) were unsuccessful due to the presence of bulky phenylsulfonate counterion attached to rGO surface. This linker prohibited electronic interactions between the complex and the support rendering the participation of rGO support in charge separation process negligible [50].

The complex $[\text{Ru}(\text{bpy})_3]\text{Cl}_2$ immobilized on Amberlyst 15 resin also exhibited an inferior performance as compared to the homogeneous analogue photocatalyst giving the acetophenone in 72–78% yield [50].

Nonetheless, both of the heterogenized catalysts served well in the reduction of a wide series of substituted α -bromoacetophenones and afforded the respective acetophenones in good yields (64–86%) with $[\text{Ru}(\text{bpy})_3]^{2+}/\text{SO}_3\text{-rGO}$ catalyst giving consistently somewhat better yields (by 5–15 %) (Scheme 87). The advantage of $[\text{Ru}(\text{bpy})_3]^{2+}/\text{SO}_3\text{-rGO}$ was also shown in recycling experiments. The catalyst $[\text{Ru}(\text{bpy})_3]^{2+}/\text{Amb15}$ lost 27% of Ru after the 5th consecutive use that resulted in a significant decrease (30%) in the product yield. In contrast, on being recycled 5 times, $[\text{Ru}(\text{bpy})_3]^{2+}/\text{SO}_3\text{-rGO}$ is as active as the initial sample despite the loss of about 8% of Ru and a small aggregation of rGO sheets.



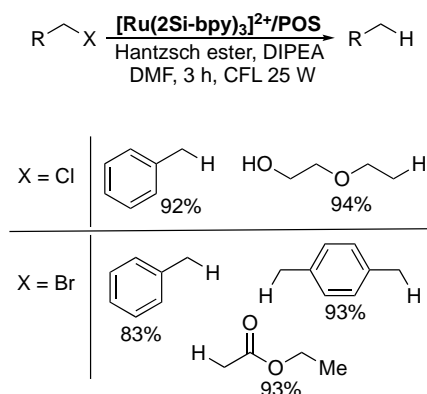
Scheme 87. Hydrodehalogenation of α -bromoacetophenone derivatives under visible-light irradiation in the presence of $[\text{Ru}(\text{bpy})_3]^{2+}/\text{SO}_3\text{-rGO}$ and $[\text{Ru}(\text{bpy})_3]^{2+}/\text{Amb15}$.

The most interesting results in the reduction of α -bromoacetophenone were obtained when $[\text{Ru}(\text{bpy})_3]^{2+}$ was immobilized in microporous Zr-MOF framework (Scheme 16) [62]. The hydrodehalogenation reaction was significantly accelerated compared to that performed under homogeneous conditions. When the reduction was performed in acetonitrile at room temperature using triethanolamine (TEOA) as a sacrificial reductant, the halide conversion was quantitative after 2h of the reaction in the presence of $[\text{Ru}(\text{bpy})_2(\text{5dcbpy})]^{2+}/\text{UiO-67}$ as compared to about 30% obtained when $[\text{Ru}(\text{bpy})_2(\text{dcbpy})]\text{Cl}_2$ was employed under similar homogeneous conditions. Based on photophysics studies of the $[\text{Ru}(\text{bpy})_2(\text{5dcbpy})]^{2+}/\text{UiO-67}$ by TAS, the authors assumed that the long lifetime of the charge separation state of the heterogenized complex was a key factor responsible for this reaction acceleration. The stabilization of this state was believed to be due to participation of the metal nodes and linkers of MOF in electron migration processes.

Excellent stability of $[\text{Ru}(\text{bpy})_2(\text{5dcbpy})]^{2+}/\text{UiO-67}$ was confirmed performing three reaction runs with the recycled catalyst and comparing initial reaction rates, rate of consumption, and final conversion of the starting halide in these reactions. Moreover, the Ru content was monitored in the organic phases to show that Ru leaching to solution do not exceed 0.15%.

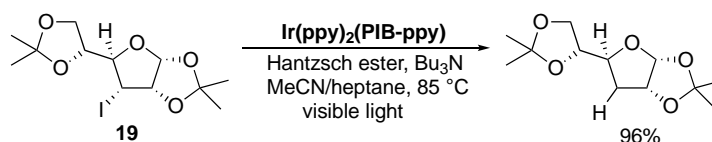
The cross-linked polymers $[\text{Ru}(\text{bpy})_3]^{2+}/\text{COP-4}$ [79] (Scheme 25), $[\text{Ru}(\text{4debpy})_2(\text{bpy})]^{2+}/\text{COP-1}$ [76] and $[\text{Ru}(\text{5debpy})_2(\text{bpy})]^{2+}/\text{COP-1}$ [76] of low porosity or altogether non porous but involving a very high catalyst content (76 wt%, 91 wt% and 90 wt%, respectively) (Scheme 23) were efficient in the reduction of benzyl bromoacetate in the presence of DIPEA and Hantzsch ester. The photocatalytic reduction with non-porous $[\text{Ru}(\text{bpy})_3]^{2+}/\text{COP-4}$ was performed in DMF at room temperature. As in the case of homogeneous reaction proceeding with $[\text{Ru}(\text{bpy})_3]\text{Cl}_2$, a complete conversion of the halide was achieved after 8 h of irradiation and benzyl acetate was isolated in 84% yield. The reactions catalyzed by $[\text{Ru}(\text{4debpy})_2(\text{bpy})]^{2+}/\text{COP-1}$ and $[\text{Ru}(\text{5debpy})_2(\text{bpy})]^{2+}/\text{COP-1}$ were performed in a methanol/THF solvent mixture and also gave benzyl acetate in high yields (92% and 86%, respectively). The high activity of these photoredox catalysts of low porosity was explained by the excellent light-harvesting properties of these materials involving an extraordinary number of photocatalytic centers at surface.

Wide range of activated alkyl bromides and chlorides was reduced using silica-based photoredox catalyst $[\text{Ru}(\text{2Si-bpy})_3]^{2+}/\text{POS}$ shown in Scheme 13 [35]. Reduced products were obtained in high yields for all alkyl halides studied (Scheme 88) but the catalyst recycling was not investigated.



Scheme 88. Reductive dehalogenation of alkyl halides under visible-light irradiation with the $[\text{Ru}(\text{2Si-bpy})_3]^{2+}/\text{POS}$ photoredox catalyst.

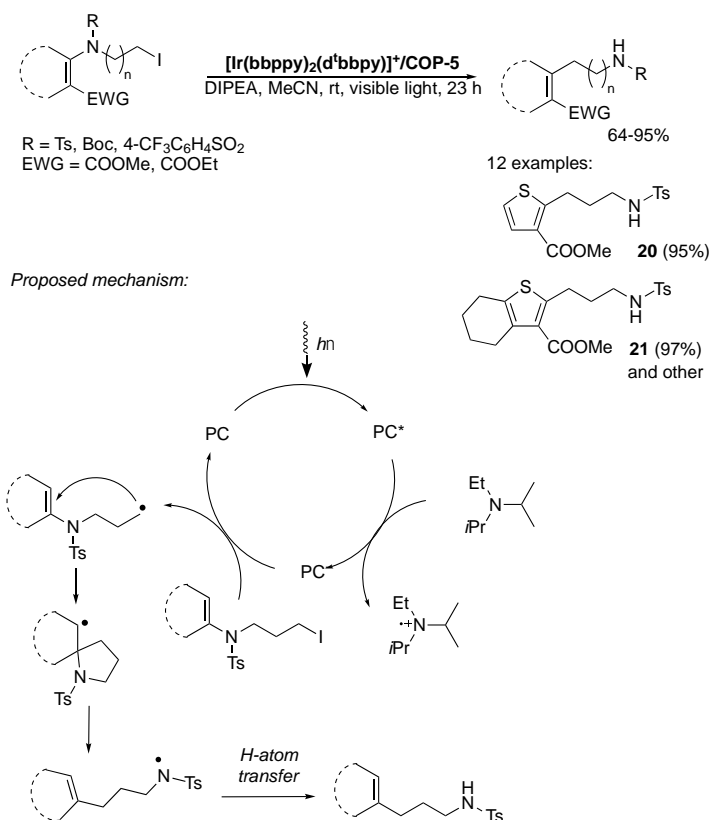
Amphiphilic complex $[\text{Ir}(\text{ppy})_2(\text{PIB-ppy})]$ is useful in the reduction of specific organic halides which can be reduced in a thermomorphic MeCN/heptane solvent mixture [189]. The iodide **19** was quantitatively reduced using tributylamine and Hantzsch esters under homogeneous conditions at 85 °C (Scheme 89). The Ir^{III} complex was recycled after cooling the reaction mixture by a simple separation of two organic phases because reaction products were insoluble in heptane. In the second reaction run, an increase of product yield from 78 to 96% was observed. This rise was explained by non-negligible solubility of the reaction product in the heptane phase, thus, after the initial run the non-polar phase was saturated by the product, and no more losses could take place in subsequent runs. In the following 8 runs the product yields were constantly high. This liquid/liquid phase recycling approach is particularly interesting for continuous flow reaction conditions discussed below.



Scheme 89. Hydrodeiodation of **19** by using recyclable $[\text{Ir}(\text{ppy})_2(\text{PIB-ppy})]$ photoredox catalyst.

Smiles-Truce rearrangement

The primary steps of the photoredox catalytic cycle of the Smiles-Truce rearrangement are similar to those of hydrodehalogenation reaction (Scheme 86) and involve the reductive quenching of excited catalyst by tertiary amine affording the strong PC^- reductant which transforms an alkyl halide into a free carbon-centered radical [190]. Once generated, this radical can either abstract a hydrogen atom, as already described or take part in other reactions. In Smiles-Truce rearrangement (Scheme 90) [191], an *exo-trig* ring closure followed by hemolytic cleavage of a rather weak C–N bond, and terminated by H atom abstraction, fulfils the light-driven transformation.



Scheme 90. Photocatalytic Smiles-Truce rearrangement.

COP **[Ir(bbppy)₂(d^tbbpy)]⁺/COP-5** shown in Scheme 26 was suitable for performing this rearrangement in acetonitrile in the presence of DIPEA (Scheme 90) [80]. The heterogeneous reactions with this catalyst were slower than the control experiment in homogeneous conditions, but the preparative reaction scope was as broad as in the later.

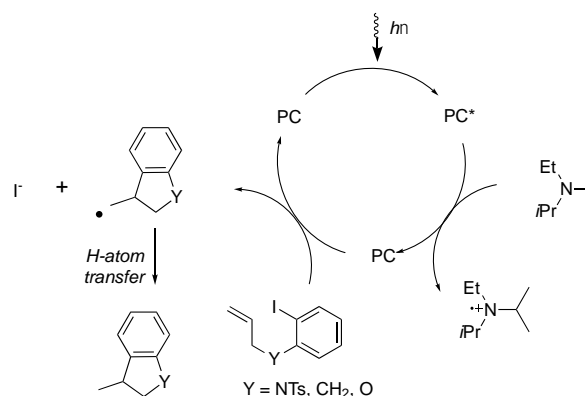
The recycled **[Ir(bbppy)₂(d^tbbpy)]⁺/COP-5** was used for reactions leading to compounds **20** and **21**. The product yields were decreased only up to 90% after 8 and 5 consecutive catalyst uses for **20** and **21**, respectively. However, in attempts to perform more runs the product yields decreased more steeply. ICP-OES analysis of the recycled catalyst confirmed its negligible leaching in the solution environment. Therefore, the initially slow but eventually faster catalyst deactivation was more likely to be caused by degradation of the supported complex under long irradiation by visible light.

A very similar COP **[Ir(bbppy)₂(d^tbbpy)]⁺/COP-5** bearing phenylene linkers instead of biphenylene residues and thus possessing smaller pores (Scheme 26) was much less efficient under the same conditions probably due to a slow diffusion of bulky substrates into the pores. For example, compound **20** was obtained in only 52% yield when this catalyst was employed.

Intramolecular reductive cyclization reactions

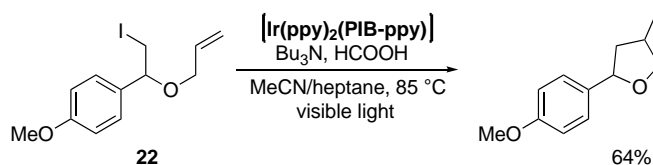
Free carbon-centered radicals generated under visible-light irradiation in the presence of photoredox catalysts prone to participate in the intramolecular reductive cyclization reactions [2-4]. The first example is the reductive cyclization of organic halides bearing double and triple carbon bonds [4]. The reductive cleavage step can be followed by the intramolecular addition of the carbon-centered radical thus formed to unsaturated C-C bonds as shown in Scheme 91 for aryl iodides. Hydrogen atom abstraction presumably from the amine radical cation then furnish

the cyclized product. As in the case of the hydrodehalogenation reaction, this transformation is commonly performed in the presence of formic acid and DIPEA or Hantzsch ester [189].



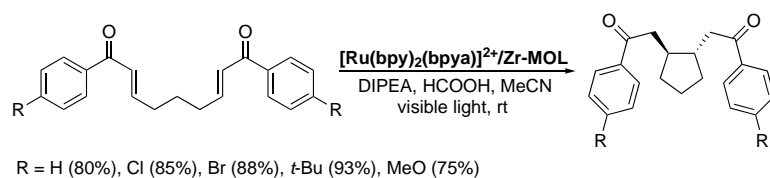
Scheme 91. Proposed mechanism for reductive cyclization reactions.

A reusable photoredox catalyst was reported only for the cyclization of iodide **22** [117]. The reaction was performed with amphiphilic complex $[\text{Ir}(\text{ppy})_2(\text{PIB-ppy})]$ in the presence of DIPEA and formic acid in MeCN/heptane solvent mixture at 85 °C (Scheme 92). Though the product yield was slightly lower than in homogeneous reaction in the presence of $[\text{Ir}(\text{ppy})_3]$ in acetonitrile at room temperature, this catalyst was successfully recycled by partitioning the reaction mixture between heptane and MeCN on cooling to room temperature, the catalyst ended up in the heptane layer and was reused without isolation. The reaction was thus repeated 10 times using the same solution of the catalyst and the product was obtained in each run in 60–76% yield without noticeable deterioration.

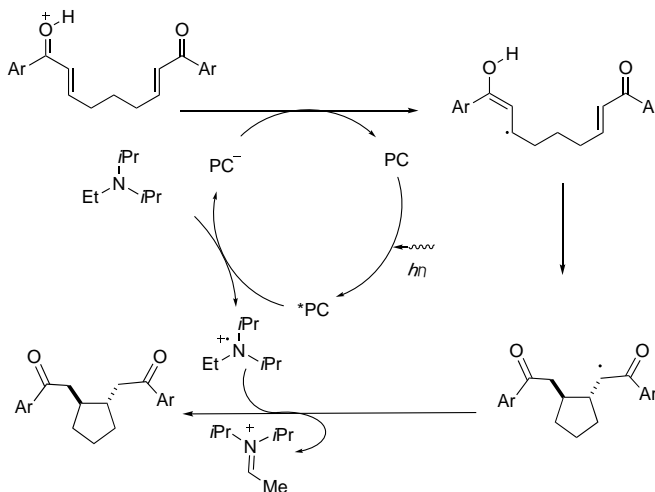


Scheme 92. Reductive cyclization of iodide **22** with recyclable $[\text{Ir}(\text{ppy})_2(\text{PIB-ppy})]$ photocatalyst.

Another photocatalytic reductive cyclization reaction which was mediated by a reusable catalyst employs the bis(arylene)s (Scheme 93). The photoredox transformation of bis(arylene)s in acetonitrile in the presence of DIPEA can be directed to the formation of bicyclic compounds (Scheme 73) or cyclopentane derivatives (Scheme 93) by adding LiBF_4 or acids, respectively [177,179]. The primary photoredox steps of these two catalytic cycles involve as usual the formation of strong reductant $[\text{Ru}(\text{bpy})_3]^+$ which further reacts with enol in the presence of protic acid or lithium cation lending the Lewis' acid assistance towards the one-electron-reduction, leading to free-radical intermediates. These intermediates either undergo the [2+2] cycloaddition reaction as shown in Scheme 73 or are engaged in exo-trig cyclization onto the second enone residue as shown in Scheme 93. In either pathway the cyclized radicals are quenched by appropriate H-atom donor, e. g. the photogenerated amine radical cation [179].



Proposed mechanism:



Scheme 93. Photocatalytic reductive cyclization reaction of bis(arylenone)s.

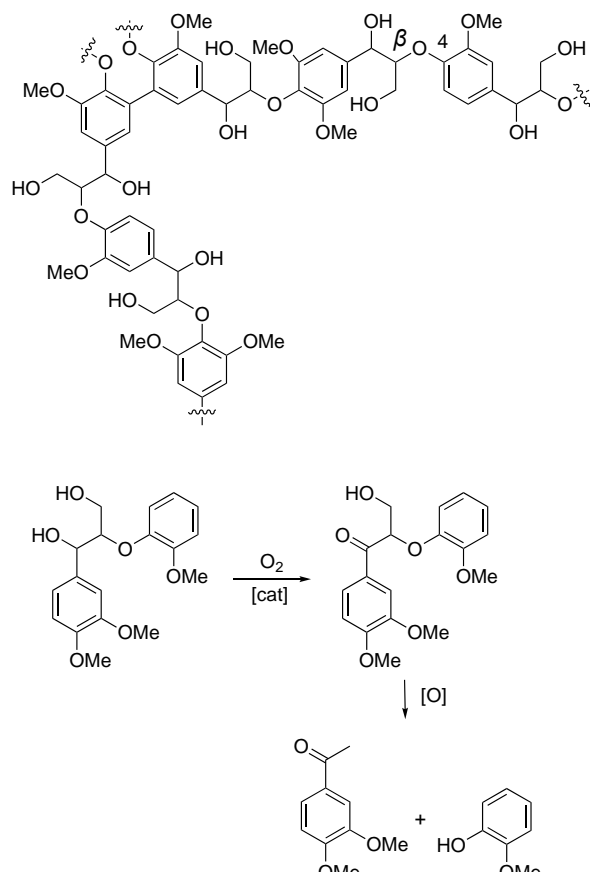
Both reductive cyclization and [2+2] cycloaddition reactions smoothly take place with Ru^{II}-doped MOL $[\text{Ru}(\text{bpy})_2(\text{bpya})]^{2+}/\text{Zr-MOL}$ in which photoredox catalytic centers are attached to the coordination polymer 2D sheets, and are more accessible for the freely diffusing substrate molecules than in 3D MOFs such as $[\text{Ru}(\text{bpy})_2(\text{5dcbpy})]^{2+}/\text{UiO-67}$ [68]. The cyclized products were obtained in 75–93% yield as pure *trans*-diastereoisomers when bis(arylenone)s were irradiated with blue LED in acetonitrile in the presence of formic acid and DIPEA. The symmetrical bis(enone)s bearing EDG and EWG are both excellent substrates for this reaction but electron-poor compounds react faster than electron-rich derivatives similar to what was observed in the [2+2] cycloaddition reaction of the same series of bis(enone)s. Such sterically bulky substituents as *tert*-butyl groups have a negative effect on the reaction rates.

Interestingly, when this reaction was carried out with $[\text{Ru}(\text{bpy})_2(\text{5dcbpy})]^{2+}/\text{UiO-67}$ MOF (shown in Scheme 16 (route d)) the products were obtained in 75–93% yield while this photocatalyst is inefficient in [2+2] cycloadditions of bis(arylenone)s [68]. Molecular mechanics (UFF) calculations were performed to visualize a 3D structure of the reaction products in the pores. The large octahedral voids of $[\text{Ru}(\text{bpy})_2(\text{5dcbpy})]^{2+}/\text{UiO-67}$ are occupied by Ru^{II} complexes and only smaller tetrahedral pores could accommodate arylated bis(enone) substrates. The size of these pores is intermediate between the dimensions of the products formed in the reduction and cycloaddition reactions that explains why the [2+2] cycloaddition reaction in the pores is uneasy. The recycling experiments with this photoredox catalyst have not reported so far.

Reductive cleavage of ethers

The photo-induced cleavage of C–O bonds is observed in many synthetically important reactions such as the reductive ketoepoxide opening, the oxidative deprotection of *para*-methoxybenzyl ethers or reductive cleavage of model compounds for the development of controlled depolymerization of lignin [2-4]. Among them, reactions for the lignin depolymerization are of particular interest since valorization of lignin is one of the key

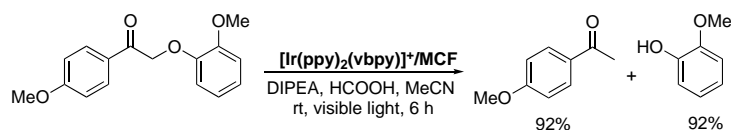
challenges in the biomass utilization. The lignin is a biopolymer constituting ca. 30% of non-fossil organic carbon composed of diversely linked 3-arylpropan-1-ol units bearing electron-rich phenol residues (Scheme 94), and thus can be regarded as rich renewable source of aromatic compounds. Although many types of C–O bonds are found in this biopolymer, the most common type is the β -O-4 linkage and reactions leading to its cleavage are required. Recently, a promising light-mediated process which tolerates the presence of diverse functional groups found in native and processed lignin samples was developed for the cleavage of such a linkage (Scheme 94) [192].



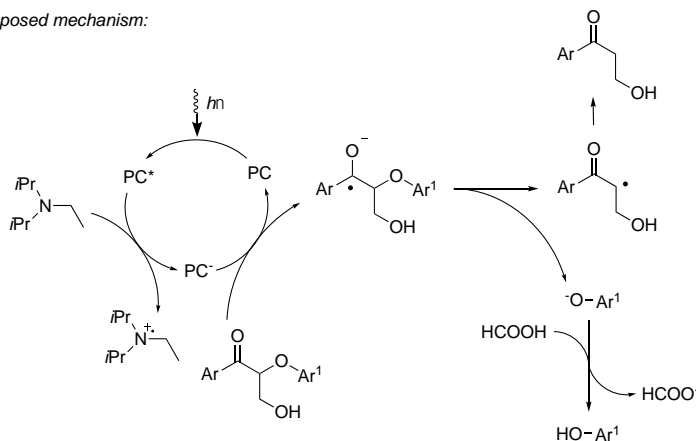
Scheme 94. The structure of lignin (top) and synthetic strategy of its degradation shown on the model compound (bottom).

As in the case of the C–halogen bond cleavage in alkyl halides, photocatalytic C–O bond rupture in ethers is facilitated by the α -carbonyl substituent. As soon as there are no such motifs in the native lignin, this biopolymer should be preprocessed to introduce such functionality, e.g. by selective oxidation of benzylic hydroxyl groups using a recyclable Bobbitt's salt ([4-AcNH-TEMPO]BF₄), for example [193]. In the next step, model compounds containing keto-groups in the vicinity of the cleavable C–O bonds were subjected to photocatalytic reductive C–O bond cleavage.

The proposed mechanism of this fragmentation reaction (Scheme 95) is analogous to that of the reductive dehalogenation of alkyl halides (Scheme 86). The reaction starts with the generation of the PC[−] reductant which performs a single electron transfer to the aromatic substrate (one of the possible structures is shown in the scheme) to generate a radical anion. This species undergoes a C–O bond cleavage to generate an aryloxy anion and the corresponding α -carbon-centered radical. Protonation of the anion and the hydrogen atom abstraction by the carbon-centered radical (likely from phenol) lead to the final products.



Proposed mechanism:



Scheme 95. Proposed mechanism for the photocatalytic C–O bond cleavage in phenacyl ethers.

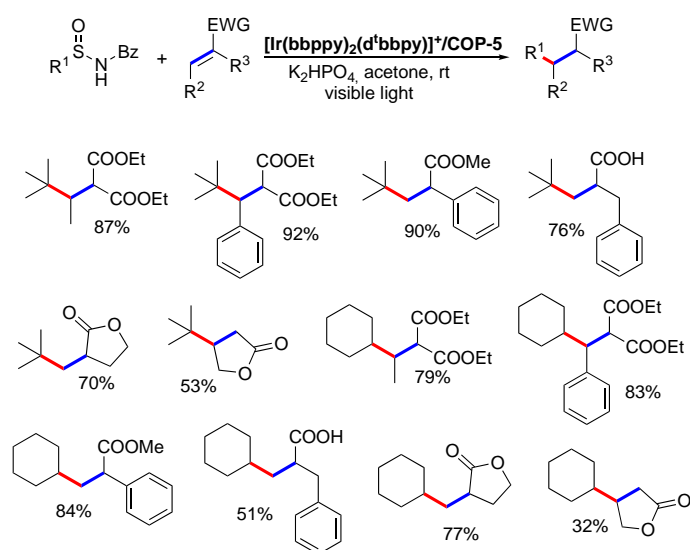
To demonstrate industrial potential of this approach, reusable photocatalysts are required because iridium(III) photoredox catalysts are expensive and toxic compounds. Recently, the photoactive silica gel $[\text{Ir}(\text{ppy})_2(\text{vbpy})]/\text{MCF}$ (Scheme 11) was investigated in this reaction following standard conditions of the homogeneous reaction (Scheme 95) [33]. Exploring the fragmentation of various phenacyl ethers with substituent patterns related to natural lignin, it was demonstrated that both functional group tolerance and the reaction selectivity do not suffer after the immobilization of the photoredox catalyst on MCF support. High visible light transparency of silicas and large size of 3D channels of the MCF support presumably contribute to the catalyst performance.

The reusability of $[\text{Ir}(\text{ppy})_2(\text{vbpy})]/\text{MCF}$ catalyst was checked studying the fragmentation of 2-(2-methoxyphenoxy)-1-(4-methoxyphenyl)ethanone. The recycled catalyst was employed in 5 repeated uses without significant loss of catalytic efficiency. TEM images of the recycled material showed that its morphology remained intact in this fragmentation reaction. Moreover, ICP analysis revealed that iridium content (0.13 mmol g^{-1}) in the recovered material is almost the same as in the original material (0.14 mmol g^{-1}).

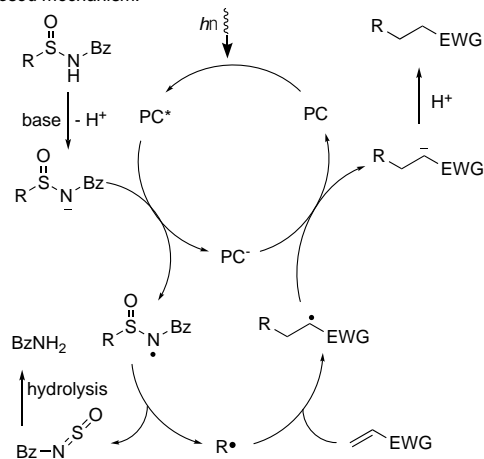
Conjugate addition reaction of *N*-benzoyl alkylsulfonamides

Among different methods for the generation of alkyl radicals in visible light photoredox catalytic reactions, desulfuration of *N*-benzoyl alkylsulfonamides (Scheme 96) is of interest because these compounds can be readily prepared from thiols or sulfides, are easy to handle and store. The deprotonation of *N*-benzoyl alkylsulfonamide affords an amidyl anion which reacts with excited photoredox catalyst $^*\text{PC}$ through a single electron transfer to yield nitrogen-centered radical. This radical undergoes fragmentation leading to the formation of *N*-sulfanylbenzamide and a carbon-centered alkyl radical. After generation of the alkyl radical, the free radical addition to the double bond takes place followed by one-electron reduction giving formally the same product as the Michael conjugate addition reaction, as shown in Scheme 96.

Two COPs $[\text{Ir}(\text{bppy})_2(\text{d}^t\text{bbpy})]^+/\text{COP-5}$ and $[\text{Ir}(\text{bbppy})_2(\text{d}^t\text{bbpy})]^+/\text{COP-5}$ shown in Scheme 26 were investigated as photoredox catalysts in this reaction employing dipotassium phosphate in acetone at room temperature (Scheme 96) [80].



Proposed mechanism:



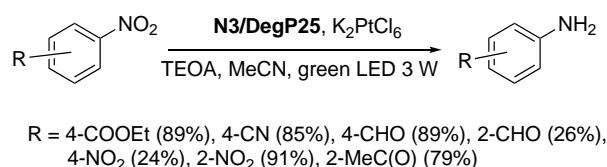
Scheme 96. Photocatalytic conjugative addition of *N*-benzoyl alkylsulfonamides to Michael acceptors.

These porous polymers display very similar structures but differ in the pore size. A strong influence of mass transfer processes on the reaction rate was observed for the $[\text{Ir}(\text{bbppy})_2(\text{d}^t\text{bbpy})]^+/\text{COP-5}$ photocatalyst. For example, the reaction of *N*-benzoyl *tert*-butylsulfonamide with diethyl (methylmethylene)malonate afforded the target product in only 19% yield. In contrast, the reaction performed with $[\text{Ir}(\text{bbppy})_2(\text{d}^t\text{bbpy})]^+/\text{COP-5}$ under the same conditions gave the product in 92% yield. The reactions catalyzed by this photoactive polymer and analogous soluble complex $[\text{Ir}(\text{bbppy})_2(\text{d}^t\text{bbpy})]\text{PF}_6$ ($\text{bbpy} = 2$ -[4-(4-phenylphenyl)pyridin-2-yl- κN]phenyl- κC) took place at similar rates to give the product in 92 and 96% yield, respectively. The heterogeneous reaction tolerated diverse Michael acceptors including acrylic acids and acrylates, α - and β -butyrolactones and diethyl methylenemalonate derivatives. Recycling experiments gave excellent results. After six reaction runs, the reaction of *N*-benzoyl *tert*-butylsulfonamide with diethyl (methylmethylene)malonate afforded the product in 91% yield without the loss of the selectivity. However, in the subsequent runs the yields began to deteriorate faster to reach only 76% in the 12th consecutive run similar to what was observed in the Smiles-Truce rearrangement performed with this catalyst.

3.3 Cocatalyzed transformations

Modern synthetic methods often take advantage of combining different modes of catalysis (transition metal catalysis, acid-base catalysis, organocatalysis etc.) in a single process achieving better performance, versatility and selectivity. The photocatalysis should not be an exception, and we have actually already seen some examples of such multimodal catalysis in the preceding chapters (for example, Scheme 43) but they are still rather limited despite their considerable potential.

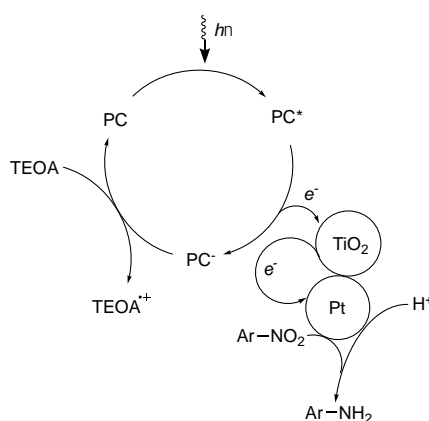
König and coworkers developed a dual catalytic system combining noble metal (Pd, Pt and Au) nanoparticles and **N3**-dye (*cis*-di(isothiocyanato)bis(2,2'-bipyridyl-4,4'-dicarboxylato)ruthenium(II) dihydrate) grafted on the surface of Degussa P25 nanoparticles (Scheme 97) [40].



Scheme 97. Reduction of nitrobenzenes to anilines under irradiation by green light in the presence of the Ru^{II} photoredox catalyst and noble metal nanoparticles.

The reduction of nitrobenzenes to anilines was investigated with the objective to replace hazardous hydrazine by *in situ* generated hydrogen using triethanolamine as a sacrificial reductant and proton source. The reaction mixture containing TEOA and the photocatalyst was charged with Pd^{II}, Pt^{II} and Au^{III} salts to prepare *in situ* the metal nanoparticles. The reaction was performed in acetonitrile at room temperature under irradiation with green LED for 24 h.

In this system, ruthenium(II) complex presumably served only for the injection of electrons into the conduction band of TiO₂ under irradiation with visible light as it is observed in DSSCs (Scheme 98). Pt^{II} and Pd^{II} salts were identified as efficient pre-catalysts when their loading did not exceed 0.01–0.5 mol%. Au^{III} salts were more efficient and provided a quantitative nitrobenzene conversion being loaded at the level of 10⁻⁴ mol%.

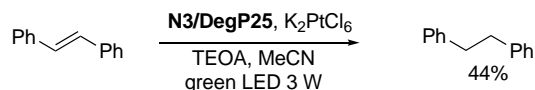


Scheme 98. Suggested mechanism of reduction of nitrobenzenes to anilines.

The substrate scope was investigated in the reaction with K₂PtCl₆. Only ethyl 4-nitrobenzoate, 4-nitrobenzotrile and 4-nitrobenzaldehyde afforded corresponding anilines in good yields. Reduction of 2-nitrobenzaldehyde and 2-nitroacetophenone expectedly gave

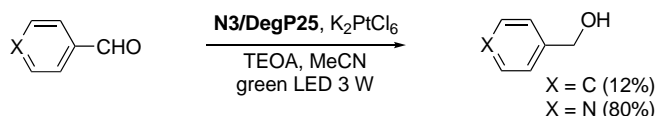
benz[c]isoxazoles as side products. The hydrodehalogenation side reaction was observed in the reduction of 4-bromonitrobenzene but the target aniline was obtained in high yield decreasing K_2PtCl_6 loading up to 10^{-3} mol%. 1,2-Dinitrobenzene was reduced to 1-amino-2-nitrobenzene in 91% yield, but 1,4-isomer gave the product in low yield (21–24%). A repeated use of this catalytic system was not reported and seems to be hardly possible because the morphology of such bizarre multicomponent systems is hardly possible to control and maintain.

The reduction of stilbene has also been shown to be of low practical interest (Scheme 99).



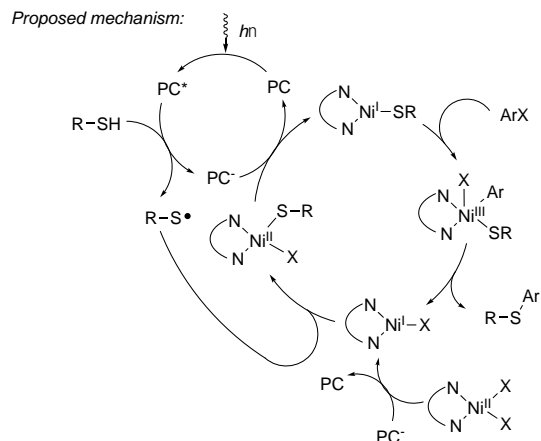
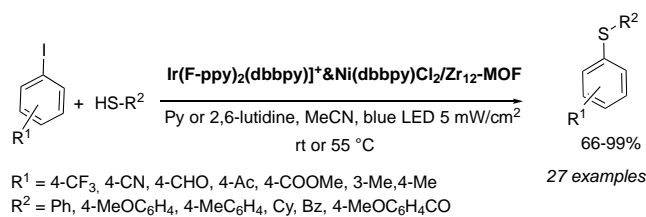
Scheme 99. Photoreduction of stilbene in the presence of the Ru photoredox catalyst and noble metal nanoparticles.

Aldehydes gave under these conditions the reduction product in good yields only for more reactive derivatives such as 4-pyridinecarbaldehyde (Scheme 100).



Scheme 100. Reduction of active aldehydes under irradiation by green light in the presence of the Ru photoredox catalyst and noble metal nanoparticles.

In order to combine catalytic activity of photo-active complexes and redox-active complexes, Ir–Ni doped Zr-MOF (Figure 10) was developed by Lin and coworkers and investigated in C–S bond forming reactions [64]. Many transition metal catalysts are employed to catalyze cross-coupling reactions of aryl halides with thiols, but most reactions proceed in the presence of strong bases and specific air-sensitive ligands at high temperatures, which limit functional group tolerance [194]. Recently, photoredox reactions combining a Ir^{III} photosensitizer and a Ni^{II} complex were proposed to perform the C–S bond forming reactions under irradiation at room temperature in the presence of rather weak bases (Scheme 101) [195,196].



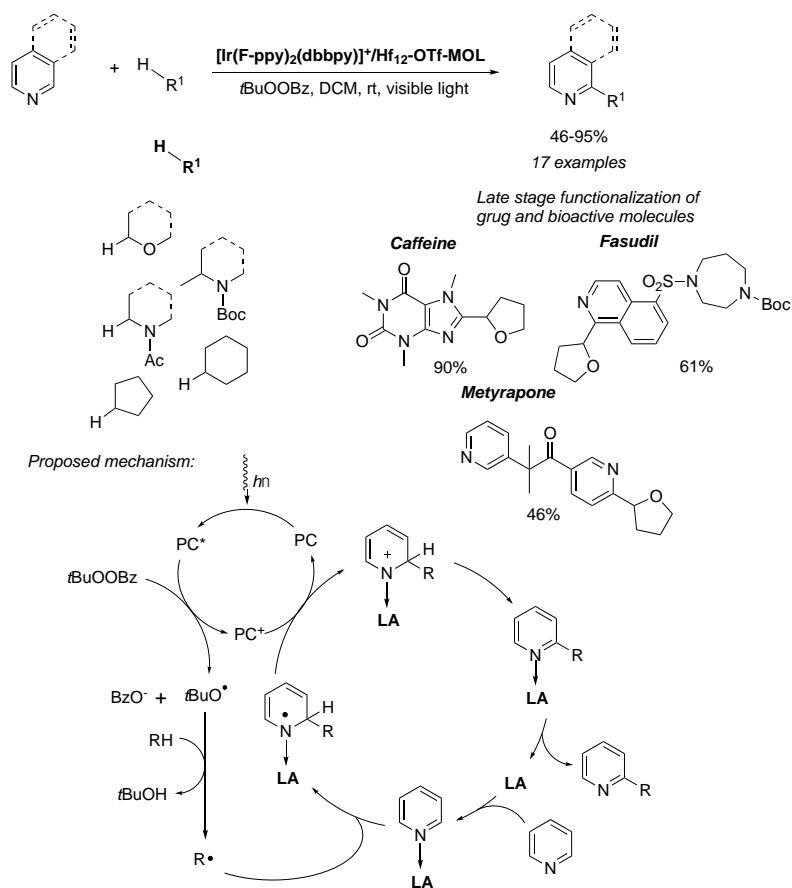
Scheme 101. Photoredox mediated nickel catalyzed cross-coupling of aryl iodides with thiols.

The postulated reaction mechanism is presented in Scheme 101 and involves the formation of a thiyl radical as a key step [195]. The Ir-based photoredox cycle and Ni-based organometallic cycle are connected by both electron and radical transfers.

TON was significantly decreased when this reaction was performed using soluble Ir^{III} and Ni^{II} complexes or a mixture of the soluble Ni^{II} complex and Zr-MOF doped with only Ir^{III} photosensitizer. In the reaction of 4-methoxythiophenol with 4-iodobenzotrifluoride, TON of 22500 was achieved varying the catalyst loading but the best conversion of 91% was obtained when the reaction was performed in the presence of 0.02 mol% of Ir–Ni Zr-MOF. Aryl halides bearing EWG such as trifluoromethyl, cyano, formyl, acetyl, and carbomethoxy afforded the target products in the reaction with thiophenol and other electron rich aryl thiols in excellent yields (86–96%). At 55 °C, the reaction scope was extended to iodotoluenes, benzylic thiols, cyclohexanethiol and a *N*-protected cysteine derivative.

These results are of particular importance for the development of dual catalyzed C–C, C–Het (Het = O, N, S) bond forming reactions which are extensively studied employing homogeneous photoredox and transition metal catalysts [197,198].

To prepare dual catalytic system combining photoredox and Lewis acid catalytic sites, Ir^{III} photoredox catalyst was incorporated in Hf-MOL [Ir(F-ppy)₂(dbbpy)]⁺/Hf₁₂-OTf-MOL shown in Figure 9 [67]. Dehydrogenative cross-coupling reactions of heteroarenes with ethers, protected amines or inactivated alkanes were investigated as shown in Scheme 102. TONs of all these reactions affording functionalized heteroarenes were higher than those observed in analogous reactions performed with soluble [Ir(F-ppy)₂(H₂dbbpy)]Cl and stoichiometric amounts of Brønsted acids or substoichiometric amounts (20 mol%) of Lewis acids.



Scheme 102. Photoredox-catalyzed dehydrogenative cross-coupling of heteroarenes with ethers, protected amines or inactivated alkanes.

Cyclic and acyclic ethers smoothly underwent coupling reactions with pyridine, phenanthridine and isoquinoline to afford target products in 70–93% isolated yields and with excellent regioselectivity. Carbamates reacted with isoquinoline, quinoline and benzothiazole affording the products in good yields. This photocatalytic system was also used for functionalization of bioactive and drug molecules such as caffeine (the most widely consumed a central nervous system stimulant), Fasudil (a potent Rho-kinase inhibitor and vasodilator), and Metyrapone (a diagnostic agent for adrenal insufficiency).

The mechanism of these reactions [191] seems not to change after the immobilization of the catalysts. Synergy of two catalytic sites separated in solid catalytic systems by only ~ 1.2 nm and the increased photostability of the heterogenized photosensitizer were evoked by the authors to explain excellent catalytic properties of $[\text{Ir}(\text{F-ppy})_2(\text{dbppy})]^+/\text{Hf}_{12}\text{-OTf-MOL}$.

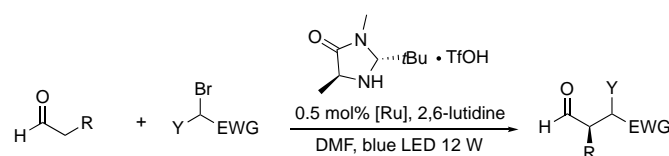
In addition, this photoredox catalyst was recovered and used in five consecutive runs of dehydrogenative cross-coupling of isoquinoline with tetrahydrofuran without significant decrease in catalytic activity.

Being combined with organocatalysts, photoredox catalysts allow to perform enantioselective transformations such as α -alkylation of aldehydes. The use of photoredox catalysts in asymmetric synthesis is challenging despite easy accessibility of two optical isomers (Λ and Δ) of octahedral $[\text{Ru}(\text{bpy})_3]\text{Cl}_2$ complex. A photoredox catalyst typically serves only for generation of reactive radical species. Thus, the photocatalyst does not participate in the bond-forming event and therefore does not influence the transition states leading to bond-forming event. This accounts for very low optical yields in the photoredox reactions with rare exceptions.

To overcome this limitation, Nicewicz and MacMillan combined a photoredox catalyst with an organocatalyst [181]. This enantioselective reaction exploited enamine catalysis concept.

Enamine catalysis allows for the aldehyde activation due to formation of an enamine in the reaction of an aldehyde with a secondary amine [199]. Being activated, the aldehydes smoothly react with diverse electrophiles affording α -substituted derivatives. When the secondary amine is chiral, the reaction leads to optically active aldehydes.

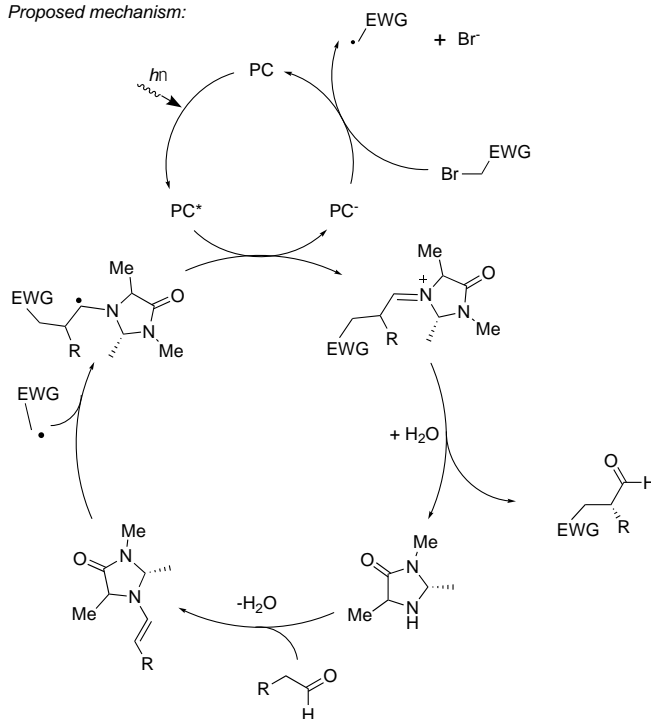
In the presence of photoredox catalysts, the reactions catalyzed by imidazolidinones proceeded through another mechanism if reactive carbon-centered free radicals were present in the reaction mixture (Scheme 103) [181]. Electron-deficient halides are commonly used as a source of these radicals. After the generation of the chiral enamine intermediate, addition of an electrophilic carbon-centered radical to the less hindered face of the enamine takes place leading to the α -amino radical. The two catalytic cycles then intersect with the single-electron oxidation of this α -amino radical by excited $^*[\text{Ru}(\text{bpy})_3]^{2+}$ species to yield the iminium and $[\text{Ru}(\text{bpy})_3]^+$ species. Hydrolysis of the iminium affords the α -alkylated product and regenerates the organocatalyst. Photoredox catalysis thus serves not only to form the reactive radical species but also to perform a key oxidation in the organocatalytic cycle.



$[\text{Ru}] = [\text{Ru}(\text{bpbpy})_2(\text{bpy})]^{2+}/\text{COP-5}$ or $[\text{Ru}(\text{bbppy})_2(\text{bpy})]^{2+}/\text{COP-5}$

R = Bn, Y = EWG = COEt: 92% yield, 90% ee
 R = Bn, Y = H, EWG = PhCO: 78% yield, 95% ee
 R = Bn, Y = H, EWG = 4-MeOC₆H₄CO: 80% yield, 95% ee
 R = Bn, Y = H, EWG = 4-ClC₆H₄CO: 77% yield, 94% ee
 R = Hex, Y = H, EWG = PhCO: 81% yield, 93% ee
 R = Hex, Y = H, EWG = 4-MeOC₆H₄CO: 84% yield, 94% ee

Proposed mechanism:



Scheme 103. Asymmetric α -alkylation of aldehydes in presence of Ru^{II} photocatalyst and imidazolidinone co-catalyst.

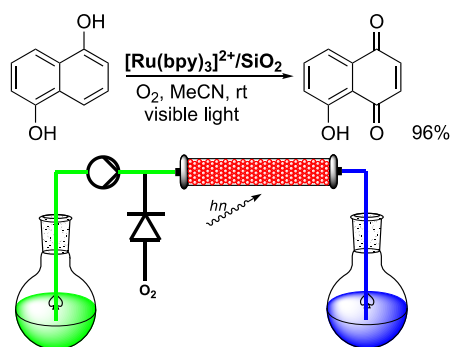
Recently, it was shown that the photoredox Ru^{II} catalyst can be recovered after reaction completing and reused. Being mediated by non-porous COPs $[\text{Ru}(\text{bppy})_2(\text{bpy})]^{2+}/\text{COP-5}$ and $[\text{Ru}(\text{bbpy})_2(\text{bpy})]^{2+}/\text{COP-5}$ (Scheme 26) and the soluble organocatalyst, the enantioselective alkylation of hydrocinnamaldehyde and octanal with diverse electron-deficient bromoalkanes provided comparable product yields (77–92%) and stereoselectivity (90–95% *ee*) as the $[\text{Ru}(\text{bpy})_3]\text{Cl}_2$ catalyst under homogeneous conditions (Scheme 103) [81]. In the reaction of hydrocinnamaldehyde with diethyl bromomalonate, $[\text{Ru}(\text{bppy})_2(\text{bpy})]^{2+}/\text{COP-5}$ was used repeatedly 10 times, observing a decrease of product yield from 92% to 73% in the last run and the almost intact optical purity of the target product.

3.5 Continuous flow reactions

In general, visible-light photocatalytic processes are not used by industry for large-scale chemical production in part due to the specific equipment and lighting demands [200]. The design of glass flow reactors transparent for visible light is a vital topic for industrial photochemistry [131,201,202]. The progress in photocatalyst recycling in flow continuous processes is rather slow despite three types of continuous flow setups were investigated recently.

The first type of setup is a fixed-bed photoreactor, which facilitates the product purification procedures by anchoring photocatalysts to a solid support. These reactors may promote a fast substrate conversion owing to generation of a localized catalyst excess by circulation of the substrate over packed catalytic beds.

A column packed with the Ru^{II} complex heterogenized on available silica $[\text{Ru}(\text{bpy})_3]^{2+}/\text{SiO}_2$ was employed by Amara and coworkers in the oxidation of 1,5-dihydroxynaphthalene to juglone, commercially important compound used in the synthesis of diverse anthraquinone derivatives (Scheme 104) [127]. This reaction was investigated in a homogeneous system implemented in a batch reactor long ago [203,204] but only recently was performed under the continuous flow conditions.

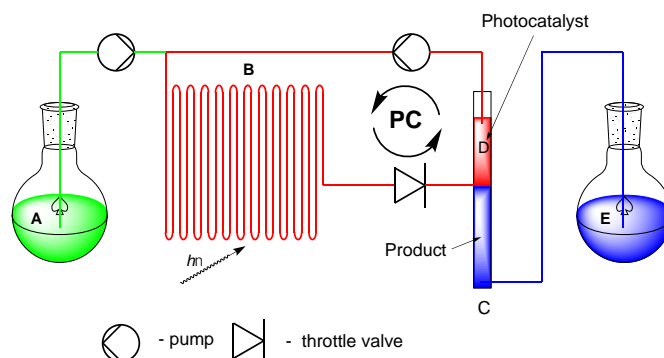


Scheme 104. Photochemical oxidation of 1,5-dihydroxynaphthalene in a flow fixed-bed photoreactor.

The best results were obtained with 0.006 mol L⁻¹ solution of 1,5-dihydroxynaphthalene, which gave juglone in 81% yield when air was used as an oxidant. Replacing air with pure oxygen the almost quantitative conversion was achieved. However, when a more concentrated substrate solution of 1,5-dihydroxynaphthalene (0.01 mol L⁻¹) was used to increase the productivity of the system, the product yield dropped to 78%. In all experiments, the conversion level was maintained within 6–8 hours of irradiation.

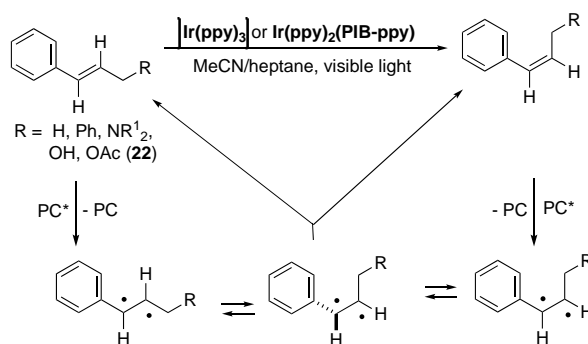
In spite of occasional success as in the already cited work, the fixed-bed photoreactors are considered as being not fully conforming to the requirements of photocatalytic chemistry, not only because of poor light penetration, but also because most photocatalysts, available as powders, impart a high flow resistance.

The second type of continuous flow apparatus benefits from a simple recovery of soluble photoredox catalysts after performing reactions in a narrow channel microreactor (**B**), which allows for a uniform and efficient irradiation of the reaction mixture (Scheme 105). The target products are isolated in a liquid/liquid phase separator (**C**) due to a difference in solubility of the photocatalyst and these compounds in a biphasic solvent mixture used in the reaction. A recovered solution of the photocatalyst can be continuously pumped in the reactor as shown in the Scheme 105.



Scheme 105. Continuous flow apparatus for photochemical reactions with in-line biphasic separation of photoredox catalysts.

Heptane soluble VATMPY complexes are convenient photocatalysts for this setup. Using these complexes and thermomorphic solvent mixtures, the reaction can be performed under homogeneous conditions at elevated temperature and the catalyst recycling can be achieved at room temperature as in batch reactions described above (Schemes 89 and 92). As a proof-of-concept research, the visible light-mediated *E/Z* isomerization of styrene and its functionalized derivatives [114,136] was studied by Reiser and coworkers (Scheme 106) [117]. According to proposed mechanism, the key step of the process is the energy transfer from the excited photocatalyst to alkene leading to a biradical species (Scheme 106) [114, 136].



Scheme 106. *E/Z* photoisomerization of styrenes and proposed mechanism of this reaction.

The reuse of $[\text{Ir}(\text{ppy})_2(\text{PIB-ppy})]$ was investigated in the photoisomerization of polar acetate **22** in heptane/MeCN solvent mixture. The solution of unsaturated acetate in acetonitrile (**A**) was pumped into a microreactor (**B**) along with a heptane solution of $[\text{Ir}(\text{ppy})_2(\text{PIB-ppy})]$ complex (**D**) (Scheme 105). The photoreaction was performed in the microreactor at 90 °C. The reaction mixture was then introduced in a cooled phase separator (**C**) from which the heptane solution of the catalyst was pumped back into the microreactor while an acetonitrile solution of *Z*-isomer (**E**) was collected to isolate the product. The *Z*:*E* isomer ratio of 82:18 was maintained

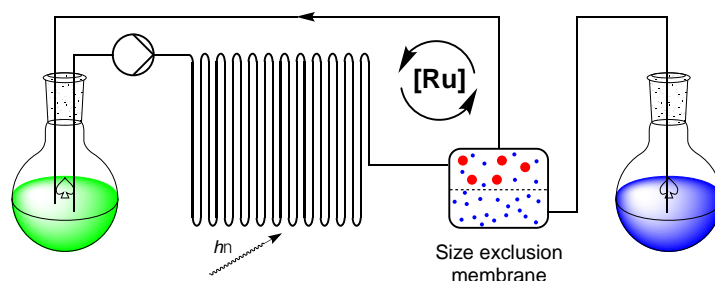
for 2.5 h of the reaction. Using this setup, the catalyst loading was decreased at least 30 times compared to that employed in the analogous batch reaction.

Another reusable photoredox catalytic system for this setup was developed by Rueping's group who studied the *E/Z* isomerization of non-polar stilbene [114]. They benefited from the difference in the solubility of $[\text{Ir}(\text{ppy})_2(\text{bpy})]\text{PF}_6$ complex and low-polar organic molecules in $[\text{bmim}]\text{BF}_4$ ($\text{bmim} = 1\text{-butyl-3-methylimidazolium}$) ionic liquid. The photoisomerization was performed in a biphasic mixture of ionic liquid and toluene or pentane in which stilbene isomers are highly soluble. Continuous recycling of the ionic liquid phase was successfully realized using flow rates up to $10\text{--}20\ \mu\text{L h}^{-1}$ that allowed to achieve the quantitative isomerization of *E*-stilbene in 1.8 g-scale reaction.

Trifluoromethylation of coumarin with trifluoroacetic anhydride in the presence of pyridine N-oxide was carried out using a simplified continuous flow setup [118]. Continuous catalyst recycling was impossible in this reaction because the reaction was not observed in acetonitrile and $\text{MeOH}/\text{CH}_2\text{Cl}_2$ solvent mixture was employed to obtain the desired products. This mixture should be evaporated before separation of catalyst using a $\text{MeCN}/\text{heptane}$ biphasic system. However, continuous flow conditions allowed for an efficient light utilization that led to reaction acceleration. The product was obtained in 65% yield for a resident time of 5 h while 24 h were needed to obtain the same reaction output under batch conditions.

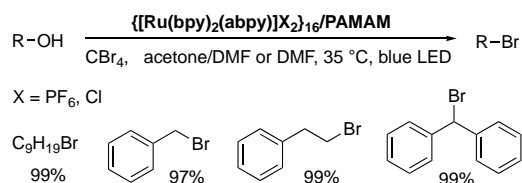
Recycling of non-functionalized $[\text{Ru}(\text{bpy})_3]^{2+}$ complex using a simplified continuous flow setup was possible in the synthesis of artemisinin (Scheme 43) [205]. In this case, the process was performed in $\text{THF}/\text{H}_2\text{O}$ or $\text{EtOH}/\text{H}_2\text{O}$ solvent mixture adding sulfuric acid in tubular photoreactor filled with glass beads. After partial evaporation of EtOH or THF , the product was obtained in 37% yield by filtration. The filtrate containing water soluble $[\text{Ru}(\text{bpy})_3](\text{SO}_4)$ complex, the acid and side products formed in the reaction was introduced in the next run. The reuse of this aqueous solution and evaporated EtOH was demonstrated for three runs with no loss in yield of artemisinin. It is worth noting that water solubility of $[\text{Ru}(\text{bpy})_3]\text{X}_2$ complexes is dependent on the nature of counterion X and can be increased replacing hexafluorophosphate anion by chloride, nitrate or sulfate anions that was used in the development of this reusable photocatalytic system.

The liquid-liquid recycling technology has serious limitations in the substrate scope. To overcome this drawback, the catalyst recycling in a separator equipped with size exclusion membrane was investigated preparing photoactive dendrimer macromolecules. This third continuous flow setup involves a module equipped with a size exclusion membrane (Scheme 107). Proof-of-concept research was performed with macromolecular photoredox catalysts $\{[\text{Ru}(\text{bpy})_2(\text{abpy})]\text{X}_2\}_{16}/\text{PAMAM}$ ($\text{X} = \text{Cl}, \text{PF}_6$) shown in Scheme 40 [121]. Three model photoredox-catalyzed reactions were investigated varying solvents, reagent concentrations and a resident time.



Scheme 107. Continuous flow apparatus for photochemical reactions equipped by column with size-exclusion membrane for nanofiltration of photoredox catalysts.

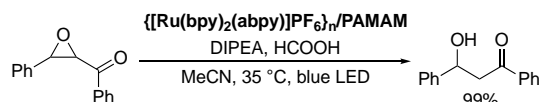
First, photocatalytic transformation of alcohols into bromides using carbon tetrabromide (Scheme 70) was adapted to flow conditions performing reaction in a DMF/acetone solvent mixture (Scheme 108). High conversion of primary, secondary and tertiary alcohols was obtained but the in-line catalyst recycling was impossible because a pressure required for the nanofiltration of the catalyst was superior to the working limit of the continuous flow photoreactor.



Scheme 108. Photoredox-catalyzed transformation of alcohols to bromides using carbon tetrabromide in DMF performed under continuous flow conditions.

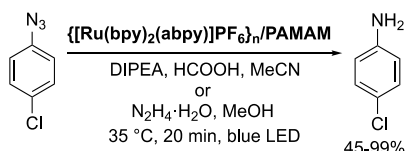
Off-line nanofiltration of the catalyst in the reaction of 1-nonanol was also difficult for $\{[\text{Ru}(\text{bpy})_2(\text{abpy})](\text{PF}_6)_2\}_{16}/\text{PAMAM}$ but worked well for the reaction performed in DMF with $\{[\text{Ru}(\text{bpy})_2(\text{abpy})]\text{Cl}_2\}_{16}/\text{PAMAM}$ material bearing chloride counterions. However, after the second successful run, the catalyst recycling was impossible likely due to decomposition of macromolecules.

The photoredox-catalyzed reductive opening of chalcone- α,β -epoxide using DIPEA and formic acid [206] was also investigated in the presence of both $\{[\text{Ru}(\text{bpy})_2(\text{abpy})]\text{X}_2\}_{16}/\text{PAMAM}$ (X = Cl, PF₆) photocatalysts (Scheme 109). Once again, the experimental conditions were found to obtain the product in quantitative yield but both recycled catalysts partially lost their efficiency in the second successive reaction run.



Scheme 109. Reductive opening of chalcone- α,β -epoxide performed under continuous flow conditions.

The reduction of 1-azido-4-chlorobenzene to related amine by hydrazine hydrate in the flow microreactor proceeded with a rather low (45–55%) but constant conversion in four consecutive reaction runs performed with the off-line recycled photoredox catalyst (Scheme 110). In contrast, the reduction of this azide by a mixture of DIPEA and formic acid gave the reduced product in quantitative yield but the catalyst recycling after reaction completing was impossible even in off-line mode.



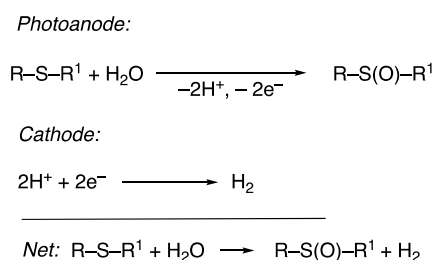
Scheme 110. Reduction of 1-azido-4-chlorobenzene performed under continuous flow conditions.

3.6 Photoelectrochemical reactions

Dye-sensitized photoelectrochemical cells (DSPECs) (Figure 1) have gained increasing attention for the production of solar fuels. In these devices, the photoexcited electrons of the light

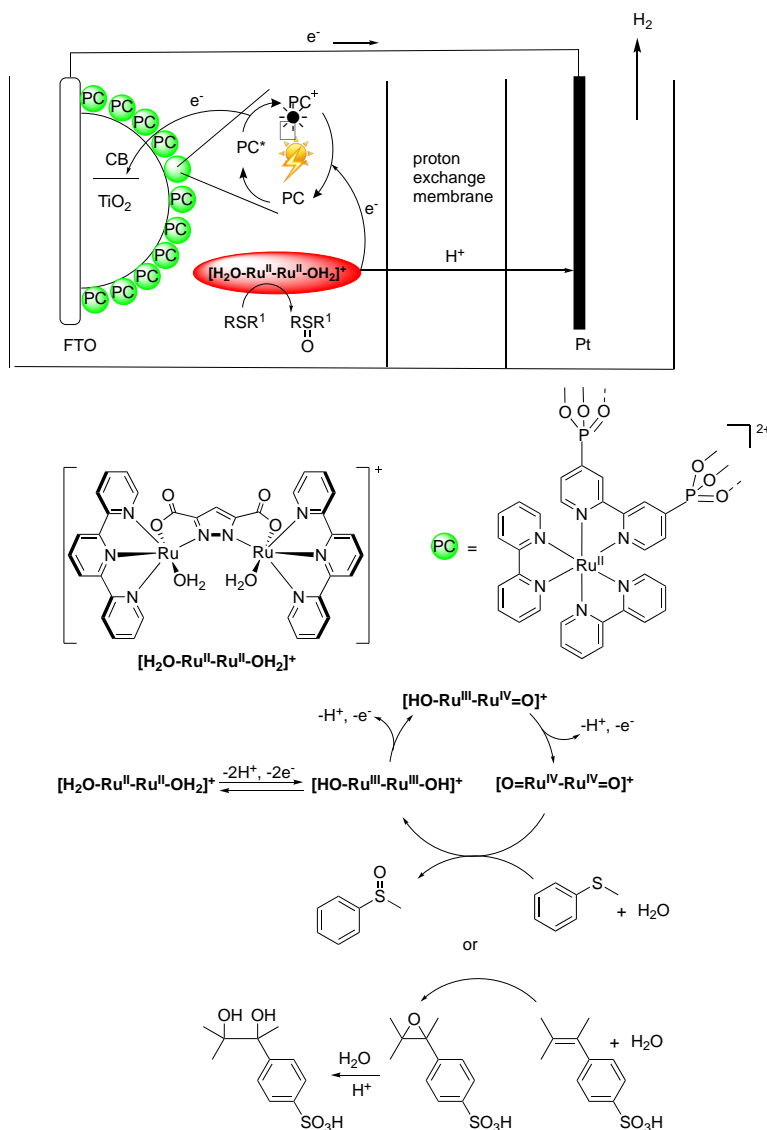
sensitive electrode can be used to drive reduction reactions while the holes can be employed in the oxidation reactions. Intensive studies of electrochemical water splitting and reduction of CO₂ coupled to water oxidation generated serious doubts on the practical usefulness of these devices for solar energy valorization leading to the studies of alternative targets for artificial photosynthesis which had high chemical value [207]. Organic oxidation reactions are considered among possible anode reactions and several concepts have been proposed over last decades including transformations of glycerol into dihydroxyacetone, or benzene into phenol [207]. Photoredox catalysis also can be used for such transformations, as was demonstrated by a relatively small number of researches which are still very far from any practical systems.

For example, the oxidation of sulfides to sulfoxides coupled with the proton reduction to hydrogen at a Pt cathode was studied by Palomares, Llobet and coworkers (Scheme 111) [42].



Scheme 111. Oxidation of sulfides in DSPEC cell.

Chemoselective thioanisole oxidation to sulfoxide using water as oxidant was performed by using the FTO|TiO₂-supported [Ru(bpy)₂(4dpbpy)]²⁺ complex as a photosensitizer (Figure 1). The soluble Ru-aqua complex [H₂O-Ru^{II}-Ru^{II}-OH₂]⁺ (Scheme 112) [208] was used as a redox catalyst and the reaction was performed in a mixture of phosphate buffer, DMF and 2,2,2-trifluoroethanol. Under irradiation of the photoanode, the Ru-aqua complex was likely transformed into the [O=Ru^{IV}-Ru^{IV}=O]⁺ species through PCET (proton-coupled electron transfer) processes (Scheme 112) and this species reacted with



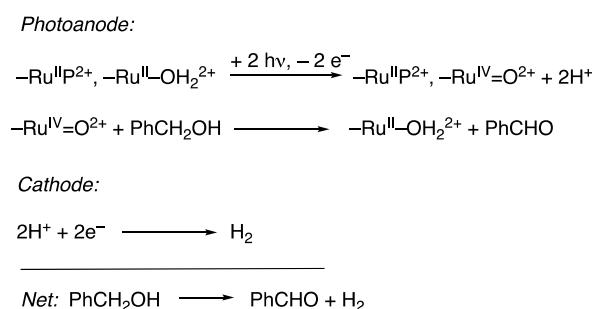
Scheme 112. Photoelectrochemical oxidation of styrenes and thioanisole in a DSPEC.

thioanisole to afford methyl phenyl sulfoxide. In the cathodic compartment, hydrogen was formed with Faradaic efficiency of 89%. Sulfoxide was characterized by ¹H NMR spectroscopy but its quantification was not performed.

A very similar DSPEC anodic compartment was used for the oxidation of 4-styrene sulfonic acid to related epoxide which was spontaneously hydrolyzed to 4-(1,2-dihydroxyethyl)benzenesulfonic acid under acidic reaction conditions [43]. Photoanode [Ru(bpy)₂(4dpbpy)]²⁺/TiO₂/FTO was protected with *tert*-butylphosphonic acid (Figure 1) and a half-cell was charged with 0.1 M solution of lithium perchlorate, [H₂O-Ru^{II}-Ru^{II}-OH₂]⁺ complex dissolved in a 0.1 M perchloric acid solution and 4-styrene sulfonic acid. The irradiation of the photoanode was continued until no more hydrogen was produced in the cathodic half-cell. Conversion of starting styrene derivative was 7% and diol was formed with 70% selectivity. The catalytic system was completely deactivated after 24 h of irradiation due to leaching of photosensitizer to solution.

Meyer and coworkers reported on the benzaldehyde synthesis in DSPEC [46]. In the developed setup, mesoporous films of TiO₂ nanoparticles or of appropriate core/shell nanoparticles with thin layer of TiO₂ (nanoITO/TiO₂) were used as a photoanode. These inorganic films were co-loaded with the [Ru(bpy)₂(4dpbpy)]²⁺ photosensitizer (–Ru^{II}P²⁺) and the

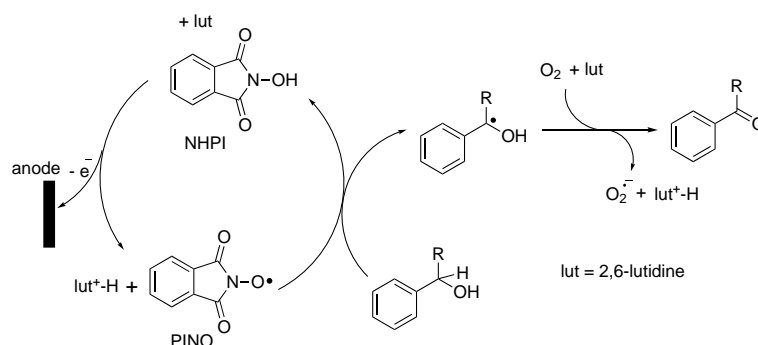
$[\text{Ru}(\text{mebimpy})_2(4\text{dpmbpy})]^{2+}$ catalyst ($-\text{Ru}^{\text{II}}-\text{OH}_2^{2+}$) as shown in Figure 1. The oxidation of benzyl alcohol (BA) was coupled with proton reduction to hydrogen at a Pt counter electrode (Scheme 113).



Scheme 113. Benzyl Alcohol Oxidation in DSPEC cell.

The photoelectrolysis of a 0.1 M BA solution in supporting electrolyte solution (20 mM pH 4.5 acetate buffer with 0.1 M LiClO_4) was performed for 3–5 h with Ru-modified $\text{TiO}_2|\text{FTO}$ and nanoITO/ $\text{TiO}_2|\text{FTO}$ photoanodes. The oxidation was selective and gave benzaldehyde with Faradaic efficiency of 26% on TiO_2 and 37% on nanoITO/ TiO_2 films. Controlled potential electrolysis on $-\text{Ru}^{\text{II}}-\text{OH}_2^{2+}$ -modified nanoITO under the same conditions afforded benzaldehyde in 66% Faradaic efficiency. The low efficiency of benzaldehyde photoproduction was explained by competing oxidation of water and decomposition of Ru^{II} sensitizer under irradiation by visible light.

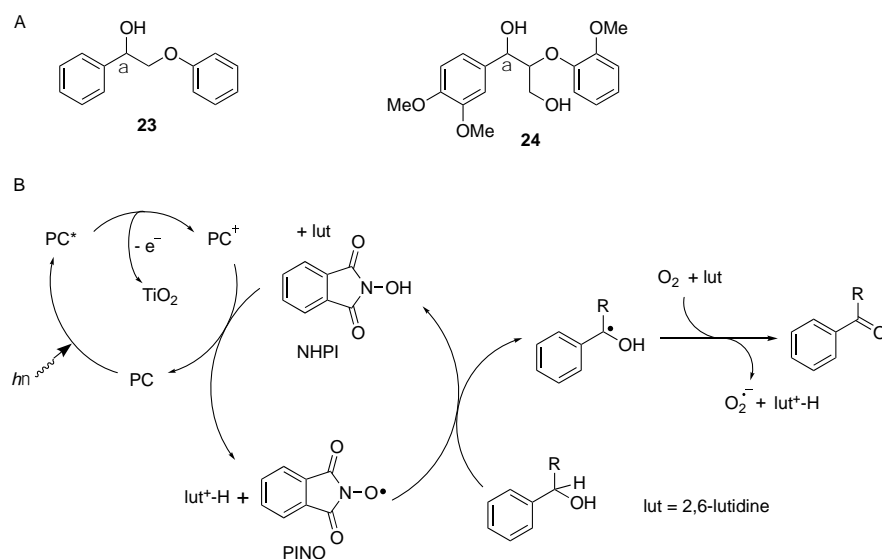
Based on these results, a photoelectrochemical strategy for lignin oxidation *via* hydrogen atom transfer (HAT) was proposed. Selective oxidation of benzylic alcohol moieties of lignin represents an initial step of lignin depolymerization as discussed above (Scheme 94). Recently, Leem, Sherman and coworkers developed the electrochemical oxidation of model compounds of lignin in the presence of 2,6-lutidine and *N*-hydroxyphthalimide (NHPI) (Scheme 114) [44]. The reaction is initiated by anodic oxidation of NHPI to phthalimide *N*-oxide (PINO), which is facilitated in the presence of 2,6-lutidine owing to a proton transfer (PCET process). Then HAT would provide the carbon-centered α -hydroxy radical, which is oxidized with oxygen and deprotonated with 2,6-lutidine (PCET) affording the target ketone.



Scheme 114. Suggested mechanism for electrochemical and DSPEC oxidation of model compounds of lignin.

This oxidation reaction can be performed in DSPECs replacing the electrochemical PINO generation by the visible-light promoted process as shown in Scheme 115. Selective oxidation of the benzylic alcohol group, $\text{C}_\alpha\text{-OH}$, of alcohols **23** and **24** was performed using $\text{FTO}|\text{TiO}_2$ -supported $[\text{Ru}(\text{bpy})_2(4\text{dcbpy})]^{2+}$ complex as a photosensitizer (Figure 1). Electron transfer from

excited ruthenium(II) complex to TiO_2 affords Ru^{III} complex, which produces PINO from NHPI in the presence of 2,6-lutidine through a PCET process.



Scheme 115. Photocatalytic oxidation of alcohols in DSPEC: A) structures of model compounds B) proposed mechanism.

After 20 h of irradiation of the half-cell with visible light, more than 90% of 2-phenoxy-1-phenylethanol (**23**) was oxidized to the corresponding ketone. The veratrylglycerol- β -guaiacyl ether (**24**) was less reactive and gave $\sim 70\%$ conversion under the same experimental conditions. Unfortunately, the oxidation of hot-water extracted maple lignin was less successful and gave $\sim 15\%$ of carbonyl compounds under the best conditions. The repeated uses of the photoanode in the oxidation of alcohol **23** were possible but a decrease of the product yield (from 92% to 60%) over the prolonged irradiation times (from 20 h to 80 h) was observed in four consecutive reaction runs. Both decomposition of ruthenium(II) photosensitizer and its leaching to solution were likely responsible for this loss of photocatalytic efficiency of DSPEC setup.

4. Conclusions

Immobilization of VATMPY complexes has gained increasing attention within the last decades due to a wide application of photoactive materials containing these complexes in advanced technologies dealing with light-harvesting, preparing energy-storing compounds and creating value-added products. In this review, synthetic approaches to the preparation of reusable photocatalysts for organic reactions are systematically discussed. At the end of this manuscript it seems appropriate to summarize some of the conclusions that can be drawn from literature concerning the efficiency of different approach to reusable photocatalytic systems based on VATMPY complexes.

The use of sunlight represents a new frontier for sustainable organic chemistry and chemoselective visible light-driven reactions are highly desirable. To perform these reactions, photocatalysts are commonly required since most of organic compounds do not absorb photons in the visible region. Complexes containing precious metals, such as platinum, ruthenium and iridium, are now used as photocatalysts for a vast variety of organic reactions. Therefore, their cost, toxicity and future availability are brothing researchers and many strategies are exploring for their recovery and reuse in photocatalytic processes.

Conception of homogeneous reusable catalysts is particularly attractive in the photocatalysis because liquid-phase immobilized VATMPY complexes allow for efficient use of light sources and compatible with continuous flow processes. However, the development of such photocatalytic systems is laborious and boring because most visible light-driven reactions afford polar organic compounds being proceeded in polar solvents, in which positively charged VATMPY complexes are highly soluble. Thus, they can be recovered only under specific conditions using expensive ionic liquids or cheap hydrocarbon-containing phases but in combination with costly amphiphilic photoredox catalysts. The recovery procedures based on the phase separation are very limited in the substrate scope even after careful optimization of the reaction conditions. Moreover, this strategy has only low value for diminishing metal content in reaction products due to a relatively high solubility of the photoredox catalysts in the liquid phase containing the reaction products.

Immobilization of precious metal complexes using solid supports has been proven to be a more feasible strategy for developing reusable photocatalysts. The complexes were immobilized using diverse organic and inorganic supports and both class I and class II hybrid materials were prepared. Covalent anchoring of the VATMPY complexes on the solid support requires a substitution of one or several bpy ligands by chelators bearing anchoring groups. Replacement of bpy ligand by another nitrogen or oxygen chelator and even its functionalization by an anchoring group may decrease the photocatalytic efficiency and stability of VATMPY complexes. Therefore, their immobilization through non-covalent interactions was widely investigated. Surprisingly, most of materials thus prepared exhibit excellent chemical stability due to the strong π - π stacking and coulombic interactions between positively charged complexes with heteroaromatic ligands and solid supports, in particular when the complexes are encapsulated into negatively charged porous networks such as zeolites and specific MOFs.

The reuse of photocatalysts in heterogeneous catalytic reactions allows for a noticeable decrease of the total investment of expensive and toxic VATMPY complexes for consecutive reaction runs. However, it was demonstrated that both leaching of the complexes in solution and their limited photostability under long irradiation by visible light can be detrimental for their reuse.

Heterogenized photocatalysts provide not only an easy and effective recovery of expensive catalysts but also allows for additional noticeable benefits. Spatial separation of catalytic sites after immobilization may improve their photo- and chemical stability and decrease the self-quenching process. Such photocatalytic systems can be used in those solvents where the VATMPY complexes *per se* are insoluble or inactive rendering the photocatalyst easier to handle. Though many light-driven reactions are believed to take place in bulk solvent, their outcome sometimes paradoxically depends on the photocatalyst and on the nature of support in particular in photoredox catalyzed reactions proceeding without participation of molecular oxygen. Heterogenized complexes especially those which are encapsulated into microporous solid matrices often exhibit specific structural and physicochemical properties due to steric and electronic constraints within the restricted void spaces and the presence of the functional groups on the host surface. These weak but numerous interactions influence the photophysical properties of the complexes and may finally provide the acceleration of photocatalytic reactions. Solid supports can participate in the photoredox reactions through adsorption of substrates at the vicinity of the catalytic site and/or control on the diffusion in narrow channels or pores. It is worth noting that a synergistic action of photoactive supports and VATMPY complexes was established in many cases. Photoactive supports may indeed participate in the charge separation processes and light-harvesting accelerating the photoredox catalyzed reactions. Finally, many recently developed materials offer a possibility of a simultaneous incorporation of two or more orthogonal catalysts within the same solid in controlled molar ratio. Surprisingly, research on

dual-catalyzed reactions involving photoredox catalysts remains limited and its further development is required.

It is now unambiguously proven that optimized heterogenized photocatalysts exhibit a superior catalytic efficiency in a given reaction as compared to homogeneous systems applying the similar catalytic species, in what concerns the rate of catalytic reaction and product yield. Nevertheless, the catalytic performance of most reported reusable photoactive systems does not exceed that of soluble complexes operating under homogeneous conditions because many non-predictable variables should be control during the optimization process.

It is also worth noting that visible light-driven reactions employing reusable photocatalysts are believed to be essential in sustainable organic chemistry though many important reaction parameters such as quantum efficiency, *E(nvironmental)* factors and the atom efficiency were not estimated in most of cases.

Despite rapid development of reusable photoredox catalysis during the last decade, there are many reactions of interest in organic photochemistry, for which such catalysts are unknown. Development of this field which demands synergistic efforts of organic chemists and material scientists promises to be rapid and interesting.

5. Acknowledgments

This work was supported by the Russian Foundation for Basic Research (grant N 18-29-04030). It was accomplished in the frame of the collaborative agreement between ENS de Lyon and Lomonosov Moscow State University (2012-2021). A. Yakushev is grateful to the French government and French embassy in Russia for Mechnikov 2020 Grant.

6. Abbreviations

¹H NMR – proton nuclear magnetic resonance
2E-EMA – 2-ethoxyethyl methacrylate
2Si-bpy – [2,2'-bipyridine]-4,4'-diylbis(methylene) bis[3-(triethoxysilyl)propyl]carbamate
³MLCT – triplet metal-to-ligand charge transfer
4-MeO-Py – 4-methoxypyridine
4dbrbpy – 4,4'-dibromo-2,2'-bipyridine
4dcbpy – 4,4'-dicarboxy-2,2'-bipyridine
4debpy – 4,4'-diethynyl-2,2'-bipyridine
4dpbpy – 2,2'-bipyridine-4,4'-diyl diphosphonic acid
4dpmbpy – 4,4'-bis(methylenephosphonato)-2,2'-bipyridine
5dbrbpy – 5,5'-dibromo-2,2'-bipyridine
5dcbpy – 5,5'-dicarboxy-2,2'-bipyridine
5debpy – 5,5'-diethynyl-2,2'-bipyridine
abpy – 4-formyl-4'-methyl-2,2'-bipyridine
AFM – atomic force microscopy
AIBN – 2,2'-azobisisobutyronitrile
AM – *N*-i-propylacrylamide
APTES – (3-aminopropyl)triethoxysilane
APTMS – (3-aminopropyl)trimethoxysilane
BA – benzyl alcohol
bdp – 1,3,5,7,9-pentamethyldipyrrin residue
bmim – 1-butyl-3-methylimidazolium
Bobbitt's salt – 4-acetamido-2,2,6,6-tetramethyl-1-oxopiperidinium tetrafluoroborate

BODIPY – dipyrrometheneboron difluoride
 bbbpy – 4-[4-(4-bromophenyl)phenyl]-2,2'-bipyridine
 bpbpy – 4-(4-bromophenyl)-2,2'-bipyridine
 bpdc – biphenyl-4,4'-dicarboxylate
 bbppy – 2-{4-[4-(4-bromophenyl)phenyl]pyridin-2-yl- κN }phenyl- κC
 bpppy – 2-{[4-(4-bromophenyl)]pyridin-2-yl- κN }phenyl- κC
 bppy – 2-[4-(4-phenylphenyl)pyridin-2-yl- κN]phenyl- κC
 bpy – 2,2'-bipyridine
 bpym – 2,2'-bipyrimidine
 bpz – 2,2'-bipyrazine
 brppy – 4-bromo-2-(pyridin-2-yl- κN)phenyl- κC
 Br-THIQ – 2-(4-bromophenyl)-1,2,3,4-tetrahydroisoquinoline
 BTC – 1,3,5-benzenetricarboxylate
 BTF – benzotrifluoride
 CB[8] – cucurbit[8]uril
 cbpy – 4,4'-di(5-carboxypentyl)-2,2'-bipyridine
 CF₃ – trifluoromethyl
 CN – carbon nitride
 CO₂ – carbon dioxide
 COP – covalent organic polymer
 CTA – chain transfer agent
 CTAB – cetyltrimethylammonium bromide
 CTM – carboxylate-terminated monolayer
 CuAAC – Cu-catalyzed azide-alkyne cycloaddition
 dbbpy – 5,5'-di(4-carboxyphenyl)-2,2'-bipyridine
 dbp – 5,15-di(4-carboxyphenyl)porphyrin
 dcta – 10,15-dihydro-5*H*-diindolo[3,2-*a*:3',2'-*c*]carbazole-3,8,13-tricarboxylate acid
 DCC – *N,N'*-dicyclohexylcarbodiimide
 DCM – dichloromethane (CH₂Cl₂)
 DEF – diethylformamide
 DHP – dihydropyridine
 DIPEA – diisopropylethylamine
 DMA – *N,N*-dimethylacetamide
 DMF – *N,N*-dimethylformamide
 DMSO – dimethyl sulfoxide
 DN-bpy – 4,4'-di(nonadec-10-yl)-2,2'-bipyridine
 dppa – dipyrido[3,2-*a*:2',3'-*c*]phenazine-11-carboxylic acid
dr – diastereomer ratio
 DSSC – dye sensitized solar cells
 DSPEC – dye-sensitized photoelectrochemical cell
 d^tbbpy – (4,4'-di-*tert*-butyl)-2,2'-bipyridine
 EDG – electron-donating group
 EDX – energy-dispersive X-ray spectroscopy
ee – enantiomeric excess
 EGDMA – ethylene glycol dimethacrylate
 EMA – ethyl methacrylate
 EWG – electron-withdrawing group
 EXAFS – extended X-ray absorption fine structure
 F-ppy – 2-[5-(trifluoromethyl)pyridin-2-yl- κN]-4,6-difluorophenyl- κC
 FE-SEM – field emission scanning electron microscopy

phen – 1,10-phenanthroline
 FRP – free radical polymerization
 FTO – fluorine-doped tin oxide
 ICP – inductively coupled plasma
 ICP-AES – inductively coupled plasma atomic emission spectroscopy
 ICP-MS – inductively coupled plasma mass spectrometry
 ICP-OES – inductively coupled plasma optical emission spectroscopy
 ITO – indium tin oxide
 H₃bpya – 5-carboxy-4',6'-bis(4-carboxyphenyl)-2,2'-bipyridine
 H₃atb – 2,3,6-tris(4-carboxyphenyl)-1,3,5-triazine
 H₃btb – 1,3,5-tris(4-carboxyphenyl)benzene
 H₃bttc – benzo[1,2-*b*:3,4-*b'*:5,6-*b''*]trithiophene-2,5,8-tricarboxylic acid
 H₃SBDC – 2-sulfoterephthalic acid
 H₄BINDI – *N,N'*-bis(3,5-dicarboxyphenyl)-1,4,5,8-naphthalenediimide
 H₄btca – biphenyl-3,3',5,5'-tetracarboxylic acid
 HAT – hydrogen atom transfer
 hdppy – 2-[4-(heptadec-1-yl)pyridin-2-yl-κ*N*]phenyl-κ*C*
 Hpbp-1 – 4-vinylbenzyl 6-phenyl-2,2'-bipyridine-4-carboxylic acid
 HPGEm – methacryloyloxy-functionalized hyperbranched poly(glycerol-*co*-glycidyl propargyl ether)
 HRTEM – high resolution transmission electron microscopy
 g-C₃N₄ – graphitic carbon nitride
 GMA – glycidyl methacrylate
 K₂HPO₄ – dipotassium hydrogen phosphate
 LiBF₄ – lithium tetrafluoroborate
 LiClO₄ – lithium perchlorate
 LSPR – localized surface plasmon resonance
 MA – benzyl methacrylate
 mebib – 2,6-bis(*N*-methylbenzimidazol-2-yl)pyridine
 mebimpy – 2,6-bis(1-methylbenzimidazol-2-yl)pyridine
 MeCN – acetonitrile
 MeOH – methanol
 MeO-THIQ – 2-(4-methoxyphenyl)-1,2,3,4-tetrahydroisoquinoline
 meppy – 4-bromo-2-(pyridin-2-yl-κ*N*)phenyl-κ*C*
 mhbp – *N*-(3-hydrazinyl-3-oxopropyl)-4'-methyl-2,2'-bipyridine-4-carboxamide
 MMA – methyl methacrylate
 MLCT – metal-to-ligand charge transfer
 MOF – metal-organic framework
 MOL – 2D metal-organic layer
 MPP – 4-methyl-2-phenylpyridine
 mtppc – 2-(pyridin-2-yl-κ*N*)-4-(9-carbazolyl)phenyl-κ*C*
 N3 – *cis*-di(isothiocyanato)bis(2,2'-bipyridyl-4,4'-dicarboxylato)ruthenium(II) dihydrate
 NDI – 1,4,5,8-naphthalenediimide
 NHPI – *N*-hydroxyphthalimide
 NP – nanoparticle
 PAMAM – polyamidoamine
 pbp – 4-phenyl-2-[6-(pyridin-2-yl-κ*N*)-pyridin-2-yl-κ*N*]phenyl-κ*C*
 PC – photocatalyst
 PCET – proton-coupled electron transfer

PET-RAFT – photoinduced electron/energy transfer reversible addition–fragmentation chain transfer
 PFPPN – poly{(9,9-dihexylfluorene)-*alt*-[5,5'-(2,2'-bipyridine)]}-*graft*-poly(*N*-isopropylacrylamide)
 phen – 1,10-phenanthroline
 phim – 2-(1*H*-phenanthro[9,10-*d*]imidazol-2-yl)-3,5-difluorophenol residue
 Phphen – 4,7-diphenyl-1,10-phenanthroline
 PIB – polyisobutylene
 PINO – phthalimide *N*-oxide
 PMB – 4-methoxybenzyl ether
 PNIPAM – poly(*N*-isopropylacrylamide) residue
 POF – porous organic framework
 ppy – 2-(pyridin-2-yl- κN)phenyl- κC
ptppc-R – 2-(5-R-pyridin-2-yl- κN)-5-(9-carbazolyl)phenyl- κC (R = H (*ptppc*-H), CF₃ (*ptppc*-F))
 PVA – polyvinyl alcohol
 py – pyridine
 Pyc – lead ruthenate pyrochlore
 qpy – 2,2':6,2'':6'':2'''-quaterpyridine
 RAFT – reversible addition–fragmentation chain transfer
 rGO – reduced graphene oxide
 ROS – reactive oxygen species
 S – styrene
 SAED – selected area electron diffraction
 SAXS – synchrotron small-angle X-ray scattering
 SBU – secondary building units
 SEM – scanning electron microscopy
 TAS – transient absorption spectroscopy
 TEA – triethylamine
 TEM – transmission electron microscopy
 TEOA – triethanolamine
 TEOS – tetraethoxysilane
 TEMPO – (2,2,6,6-tetramethylpiperidine-1)-oxyl
 TEPB – 1,3,5-tris(4-ethynylphenyl)benzene
 TEPM – tetrakis(4-ethynylphenyl)methane
 TFA – trifluoroacetic acid
 THF – tetrahydrofuran
 THIQ – tetrahydroisoquinoline
 TME – tetramethylethylene
 TOF – turnover frequency
 TON – turnover number
 tpy – 2,2':6',2''-terpyridine
 tpy-1 – 4'-(4-methylphenyl)-2,2':6',2''-terpyridine
 tpy-2 – 4'-(4-methoxyphenyl)-2,2':6',2''-terpyridine
 vbpy – 4-(but-3-en-1-yl)-4'-methyl-2,2'-bipyridine
 vppy – 2-(pyridin-2-yl- κN)-5-vinylphenyl- κC
 VATMPY complexes – visible light-active transition metal complexes with tris(diimine)s
 XAFS – X-ray absorption fine structure
 XANES – X-ray absorption near edge structure
 XPS – X-ray photoelectron spectroscopy
 XRD – X-ray powder diffraction

References

- [1] N. Hoffmann, Photochemical Reactions as Key Steps in Organic Synthesis, *Chem. Rev.* 108 (2008) 1052–1103, <https://doi.org/10.1021/cr0680336>.
- [2] D.M. Schultz, T.P. Yoon, Solar Synthesis: Prospects in Visible Light Photocatalysis, *Science* 343 (2014) 1239176, <https://doi.org/10.1126/science.1239176>.
- [3] J.M.R. Narayanam, C.R.J. Stephenson, Visible Light Photoredox Catalysis: Applications in Organic Synthesis, *Chem. Soc. Rev.* 40 (2011) 102–113, <https://doi.org/10.1039/B913880N>.
- [4] C.K. Prier, D.A. Rankic, D.W.C. MacMillan, Visible Light Photoredox Catalysis with Transition Metal Complexes: Applications in Organic Synthesis, *Chem. Rev.* 113 (2013) 5322–5363, <https://doi.org/10.1021/cr300503r>.
- [5] J.-R. Chen, X.-Q. Hu, L.-Q. Lu, W.-J. Xiao, Exploration of Visible-Light Photocatalysis in Heterocycle Synthesis and Functionalization: Reaction Design and Beyond, *Acc. Chem. Res.* 49 (2016) 1911–1923, <https://doi.org/10.1021/acs.accounts.6b00254>.
- [6] S. Dadashi-Silab, S. Doran, Y. Yagci, Photoinduced Electron Transfer Reactions for Macromolecular Syntheses, *Chem. Rev.* 116 (2016) 10212–10275, <https://doi.org/10.1021/acs.chemrev.5b00586>.
- [7] L. Marzo, S.K. Pagire, O. Reiser, B. König, Visible-Light Photocatalysis: Does It Make a Difference in Organic Synthesis? *Angew. Chem. Int. Ed.* 57 (2018) 10034–10072, <https://doi.org/10.1002/anie.201709766>.
- [8] F. Strieth-Kalthoff, M.J. James, M. Teders, L. Pitzer, F. Glorius, Energy Transfer Catalysis Mediated by Visible Light: Principles, Applications, Directions, *Chem. Soc. Rev.* 47 (2018) 7190–7202, <https://doi.org/10.1039/C8CS00054A>.
- [9] E. Meggers, Asymmetric Catalysis Activated by Visible Light, *Chem. Commun.* 51 (2015) 3290–3301, <https://doi.org/10.1039/C4CC09268F>.
- [10] K. Teegardin, J.I. Day, J. Chan, J. Weaver, Advances in Photocatalysis: A Microreview of Visible Light Mediated Ruthenium and Iridium Catalyzed Organic Transformations, *Org. Process Res. Dev.* 20 (2016) 1156–1163, <https://doi.org/10.1021/acs.oprd.6b00101>.
- [11] D. Sun, Z. Li, Metal-Organic Frameworks (MOFs) for Photocatalytic Organic Transformations, in: H. Yamashita, H. Li (Eds.), *Nanostructured Photocatalysts: Advanced Functional Materials*, Springer International Publishing, Cham, 2016, pp. 523–535.
- [12] Y. Horiuchi, T. Toyao, M. Matsuoka, Metal–Organic Framework (MOF) and Porous Coordination Polymer (PCP)-Based Photocatalysts, in: H. Yamashita, H. Li (Eds.), *Nanostructured Photocatalysts: Advanced Functional Materials*, Springer International Publishing, Cham, 2016, pp. 479–489.
- [13] S.-N. Zhao, G. Wang, D. Poelman, P. Van Der Voort, Metal Organic Frameworks Based Materials for Heterogeneous Photocatalysis, *Molecules*, 23 (2018), 2947, <https://doi.org/10.3390/molecules23112947>.
- [14] K. Mori, H. Yamashita, Silica-Supported Metal Complex Photocatalysts, in: H. Yamashita, H. Li (Eds.), *Nanostructured Photocatalysts. Nanostructure Science and Technology*, Springer, Cham, 2016, pp. 465–477.
- [15] F. Bella, C. Gerbaldi, C. Barolo, M. Grätzel, Aqueous Dye-Sensitized Solar Cells, *Chem. Soc. Rev.* 44 (2015) 3431–3473, <https://doi.org/10.1039/C4CS00456F>.
- [16] D.L. Ashford, M.K. Gish, A.K. Vannucci, M.K. Brennaman, J.L. Templeton, J.M. Papanikolas, T.J. Meyer, Molecular Chromophore–Catalyst Assemblies for Solar Fuel Applications, *Chem. Rev.* 115 (2015) 13006–13049, <https://doi.org/10.1021/acs.chemrev.5b00229>.

- [17] B. Pashaei, H. Shahroosvand, M. Graetzel, M.K. Nazeeruddin, Influence of Ancillary Ligands in Dye-Sensitized Solar Cells, *Chem. Rev.* 116 (2016) 9485–9564, <https://doi.org/10.1021/acs.chemrev.5b00621>.
- [18] T.J. Meyer, M.V. Sheridan, B.D. Sherman, Mechanisms Of Molecular Water Oxidation in Solution and on Oxide Surfaces, *Chem. Soc. Rev.* 46 (2017) 6148–6169, <https://doi.org/10.1039/C7CS00465F>.
- [19] X. Ding, L. Zhang, Y. Wang, A. Liu, Y. Gao, Design of Photoanode-Based Dye-Sensitized Photoelectrochemical Cells Assembling with Transition Metal Complexes for Visible Light-Induced Water Splitting, *Coord. Chem. Rev.* 357 (2018) 130–143, <https://doi.org/https://doi.org/10.1016/j.ccr.2017.10.020>.
- [20] F. Niu, D. Wang, F. Li, Y. Liu, S. Shen, T.J. Meyer, Hybrid Photoelectrochemical Water Splitting Systems: From Interface Design to System Assembly, *Adv. Energy Mater.* 10 (2020) 1900399, <https://doi.org/10.1002/aenm.201900399>.
- [21] M.-N. Collomb, D.V. Morales, C.N. Astudillo, B. Dautreppe, J. Fortage, Hybrid Photoanodes for Water Oxidation Combining a Molecular Photosensitizer with a Metal Oxide Oxygen-Evolving Catalyst, *Sustainable Energy Fuels* 4 (2020) 31–49, <https://doi.org/10.1039/C9SE00597H>.
- [22] P. Gómez-Romero, C. Sanchez, Hybrid Materials, Functional Applications. An Introduction, Functional Hybrid Materials, in: P. Gómez-Romero and C. Sanchez (Eds), *Functional Hybrid Materials*, Wiley Online Books, 2003, pp. 1–14, <https://doi.org/doi:10.1002/3527602372.ch1>.
- [23] K. Mori, K. Kagohara, H. Yamashita, Synthesis of Tris(2,2'-bipyridine)iron(II) Complexes in Zeolite Y Cages: Influence of Exchanged Alkali Metal Cations on Physicochemical Properties and Catalytic Activity, *J. Phys. Chem. C* 112 (2008) 2593–2600, <https://doi.org/10.1021/jp709571v>.
- [24] M. Martis, K. Mori, H. Yamashita, Control of Physicochemical Properties and Catalytic Activity of Tris(2,2'-Bipyridine)Iron(II) Encapsulated Within the Zeolite Y Cavity by Alkaline Earth Metal Cations, *Dalton Trans.* 43 (2014) 1132–1138, <https://doi.org/10.1039/C3DT52408F>.
- [25] K. Mori, M. Kawashima, K. Kagohara, H. Yamashita, Influence of Exchanged Alkali Metal Cations within Zeolite Y Cages on Spectroscopic and Photooxidation Properties of the Incorporated Tris(2,2'-bipyridine)ruthenium(II) Complexes, *J. Phys. Chem. C* 112 (2008) 19449–19455, <https://doi.org/10.1021/jp807210q>.
- [26] Bratermen, Z.P. Xu, F. Yarberry, Layered Double Hydroxides (LDHs), in: S. M. Auerbach, K.A. Carrado, P.K. Dutta (Eds.), *Handbook of Layered Materials*, Marcel Dekker Inc., New York, 2004, pp. 373–474. <https://doi.org/10.1201/9780203021354.ch8>.
- [27] S. Fujita, H. Sato, N. Kakegawa, A. Yamagishi, Enantioselective Photooxidation of a Sulfide by a Chiral Ruthenium(II) Complex Immobilized on a Montmorillonite Clay Surface: The Role of Weak Interactions in Asymmetric Induction, *J. Phys. Chem. B* 110 (2006) 2533–2540, <https://doi.org/10.1021/jp055254r>.
- [28] T.L. Pettit, M.A. Fox, Photoassisted Oxygenation of Olefins: an Exchanged Zeolite as a Heterogeneous Photosensitizer, *J. Phys. Chem.* 90 (1986) 1353–1354, <https://doi.org/10.1021/j100398a029>.
- [29] B. Tambosco, K. Segura, C. Seyrig, D. Cabrera, M. Port, C. Ferroud, Z. Amara, Outer-Sphere Effects in Visible-Light Photochemical Oxidations with Immobilized and Recyclable Ruthenium Bipyridyl Salts, *ACS Catal.* 8 (2018) 4383–4389, <https://doi.org/10.1021/acscatal.8b00890>.
- [30] K. Mori, M. Kawashima, M. Che, H. Yamashita, Enhancement of the Photoinduced Oxidation Activity of a Ruthenium(II) Complex Anchored on Silica-Coated Silver

- Nanoparticles by Localized Surface Plasmon Resonance, *Angew. Chem. Int. Ed.* 49 (2010) 8598–8601, <https://doi.org/10.1002/anie.201004942>.
- [31] X. Yang, T. Liang, J. Sun, M.J. Zaworotko, Y. Chen, P. Cheng, Z. Zhang, Template-Directed Synthesis of Photocatalyst-Encapsulating Metal–Organic Frameworks with Boosted Photocatalytic Activity, *ACS Catal.* 9 (2019) 7486–7493, <https://doi.org/10.1021/acscatal.9b01783>.
- [32] H. He, W. Li, Z. Xie, X. Jing, Y. Huang, Ruthenium Complex Immobilized on Mesoporous Silica as Recyclable Heterogeneous Catalyst for Visible Light Photocatalysis, *Chem. Res. Chin. Univ.* 30 (2014) 310–314, <https://doi.org/10.1007/s40242-014-3367-9>.
- [33] Z. Hao, S. Li, J. Sun, S. Li, F. Zhang, Efficient Visible-Light-Driven Depolymerization of Oxidized Lignin to Aromatics Catalyzed by an Iridium Complex Immobilized on Mesocellular Silica Foams, *Appl. Catal., B* 237 (2018) 366–372, <https://doi.org/https://doi.org/10.1016/j.apcatb.2018.05.072>.
- [34] K. Feng, M.-L. Peng, D.-H. Wang, L.-P. Zhang, C.-H. Tung, L.-Z. Wu, Silica- and Polymer-Supported Platinum(II) Polypyridyl Complexes: Synthesis and Application in Photosensitized Oxidation of Alkenes, *Dalton Trans.* (2009) 9794–9799, <https://doi.org/10.1039/B916488J>.
- [35] A. Jana, J. Mondal, P. Borah, S. Mondal, A. Bhaumik, Y. Zhao, Ruthenium Bipyridyl Tethered Porous Organosilica: a Versatile, Durable and Reusable Heterogeneous Photocatalyst, *Chem. Commun.* 51 (2015) 10746–10749, <https://doi.org/10.1039/C5CC03067F>.
- [36] K. Feng, R.-Y. Zhang, L.-Z. Wu, B. Tu, M.-L. Peng, L.-P. Zhang, D. Zhao, C.-H. Tung, Photooxidation of Olefins under Oxygen in Platinum(II) Complex-Loaded Mesoporous Molecular Sieves, *J. Am. Chem. Soc.* 128 (2006) 14685–14690, <https://doi.org/10.1021/ja0648256>.
- [37] K. Mori, K. Watanabe, M. Kawashima, M. Che, H. Yamashita, Anchoring of Pt(II) Pyridyl Complex to Mesoporous Silica Materials: Enhanced Photoluminescence Emission at Room Temperature and Photooxidation Activity using Molecular Oxygen, *J. Phys. Chem. C* 115 (2011) 1044–1050, <https://doi.org/10.1021/jp105577f>.
- [38] K. Mori, K. Watanabe, Y. Terai, Y. Fujiwara, H. Yamashita, Hybrid Mesoporous-Silica Materials Functionalized by Pt^{II} Complexes: Correlation between the Spatial Distribution of the Active Center, Photoluminescence Emission, and Photocatalytic Activity, *Chem. Eur. J.* 18 (2012) 11371–11378, <https://doi.org/10.1002/chem.201200959>.
- [39] K. Mori, M. Tottori, K. Watanabe, M. Che, H. Yamashita, Photoinduced Aerobic Oxidation Driven by Phosphorescence Ir(III) Complex Anchored to Mesoporous Silica, *J. Phys. Chem. C* 115 (2011) 21358–21362, <https://doi.org/10.1021/jp208357e>.
- [40] S. Földner, R. Mild, H.I. Siegmund, J.A. Schroeder, M. Gruber, B. König, Green-Light Photocatalytic Reduction Using Dye-Sensitized TiO₂ And Transition Metal Nanoparticles, *Green. Chem.* 12 (2010) 400–406, <https://doi.org/10.1039/B918140G>.
- [41] K. Hanson, M.K. Brennaman, H. Luo, C.R.K. Glasson, J.J. Concepcion, W. Song, T.J. Meyer, Photostability of Phosphonate-Derivatized, Ru^{II} Polypyridyl Complexes on Metal Oxide Surfaces, *ACS Appl. Mater. Interfaces* 4 (2012) 1462–1469, <https://doi.org/10.1021/am201717x>.
- [42] P. Farràs, C. Di Giovanni, J.N. Clifford, E. Palomares, A. Llobet, H₂ Generation and Sulfide to Sulfoxide Oxidation with H₂O and Sunlight with a Model Photoelectrosynthesis Cell, *Coord. Chem. Rev.* 304-305 (2015) 202–208, <https://doi.org/https://doi.org/10.1016/j.ccr.2014.10.007>.
- [43] P. Farràs, C. Di Giovanni, J.N. Clifford, P. Garrido-Barros, E. Palomares, A. Llobet, Light Driven Styrene Epoxidation and Hydrogen Generation Using H₂O As an Oxygen Source in

- a Photoelectrosynthesis Cell, *Green. Chem.* 18 (2016) 255–260, <https://doi.org/10.1039/C5GC01589H>.
- [44] S. Li, Z.-J. Li, H. Yu, M.R. Sytu, Y. Wang, D. Beeri, W. Zheng, B.D. Sherman, C.G. Yoo, G. Leem, Solar-Driven Lignin Oxidation via Hydrogen Atom Transfer with a Dye-Sensitized TiO₂ Photoanode, *ACS Energy Lett.* 5 (2020) 777–784, <https://doi.org/10.1021/acseenergylett.9b02391>.
- [45] W. Song, A. Ito, R.A. Binstead, K. Hanson, H. Luo, M.K. Brennaman, J.J. Concepcion, T.J. Meyer, Accumulation of Multiple Oxidative Equivalents at a Single Site by Cross-Surface Electron Transfer on TiO₂, *J. Am. Chem. Soc.* 135 (2013) 11587–11594, <https://doi.org/10.1021/ja4032538>.
- [46] W. Song, A.K. Vannucci, B.H. Farnum, A.M. Lapidés, M.K. Brennaman, B. Kalanyan, L. Alibabaei, J.J. Concepcion, M.D. Losego, G.N. Parsons, T.J. Meyer, Visible Light Driven Benzyl Alcohol Dehydrogenation in a Dye-Sensitized Photoelectrosynthesis Cell, *J. Am. Chem. Soc.* 136 (2014) 9773–9779, <https://doi.org/10.1021/ja505022f>.
- [47] P. Kumar, S. Varma, S.L. Jain, A TiO₂ Immobilized Ru(II) Polyazaine Complex: a Visible-Light Active Photoredox Catalyst for Oxidative Cyanation of Tertiary Amines, *J. Mater. Chem. A* 2 (2014) 4514–4519, <https://doi.org/10.1039/C3TA14783E>.
- [48] R.I. Teixeira, N.C. de Lucas, S.J. Garden, A.E. Lanterna, J.C. Scaiano, Glass Wool Supported Ruthenium Complexes: Versatile, Recyclable Heterogeneous Photoredox Catalysts, *Catal. Sci. Technol.* 10 (2020) 1273–1280, <https://doi.org/10.1039/C9CY02479D>.
- [49] A. Kumar, P. Kumar, S. Paul, S.L. Jain, Visible Light Assisted Reduction of Nitrobenzenes Using Fe(Bpy)₃²⁺/rGO Nanocomposite as Photocatalyst, *Appl. Surf. Sci.* 386 (2016) 103–114, <https://doi.org/https://doi.org/10.1016/j.apsusc.2016.05.139>.
- [50] X. Li, Z. Hao, F. Zhang, H. Li, Reduced Graphene Oxide-Immobilized Tris(bipyridine)ruthenium(II) Complex for Efficient Visible-Light-Driven Reductive Dehalogenation Reaction, *ACS Appl. Mater. Interfaces* 8 (2016) 12141–12148, <https://doi.org/10.1021/acsami.6b01100>.
- [51] A. Kumar, P. Kumar, C. Joshi, S. Ponnada, A.K. Pathak, A. Ali, B. Sreedhar, S.L. Jain, A [Fe(bpy)₃]²⁺ Grafted Graphitic Carbon Nitride Hybrid for Visible Light Assisted Oxidative Coupling of Benzylamines under Mild Reaction Conditions, *Green. Chem.* 18 (2016) 2514–2521, <https://doi.org/10.1039/C5GC02090E>.
- [52] K. Mori, D. Tatsumi, T. Iwamoto, Y. Masui, M. Onaka, H. Yamashita, Ruthenium(II)–Bipyridine/NanoC₃N₄ Hybrids: Tunable Photochemical Properties by Using Exchangeable Alkali Metal Cations, *Chem. Asian J.* 13 (2018) 1348–1356, <https://doi.org/10.1002/asia.201800397>.
- [53] A. Kumar, P. Kumar, A.K. Pathak, A.N. Chokkapu, S.L. Jain, Carbon Nitride Grafted Cobalt Complex (Co@npg-C₃N₄) for Visible Light-Assisted Esterification of Aldehydes, *ChemistrySelect* 2 (2017) 3437–3443, <https://doi.org/10.1002/slct.201602031>.
- [54] X. Wang, W. Lu, Z.-Y. Gu, Z. Wei, H.-C. Zhou, Topology-Guided Design of an Anionic Bor-Network for Photocatalytic [Ru(Bpy)₃]²⁺ Encapsulation, *Chem. Commun.* 52 (2016) 1926–1929, <https://doi.org/10.1039/C5CC08614K>.
- [55] I.-H. Choi, S. Yoon, S. Huh, S.-J. Kim, Y. Kim, Photophysical Properties and Heterogeneous Photoredox Catalytic Activities of Ru(bpy)₃@InBTB MOF, *Chem. Eur. J.* 26 (2020) 14580–14584, <https://doi.org/10.1002/chem.202003743>.
- [56] X. Zhang, X. Zhang, J.A. Johnson, Y.-S. Chen, J. Zhang, Highly Porous Zirconium Metal–Organic Frameworks with β-UH₃-like Topology Based on Elongated Tetrahedral Linkers, *J. Am. Chem. Soc.* 138 (2016) 8380–8383, <https://doi.org/10.1021/jacs.6b04608>.
- [57] J. Pang, S. Yuan, J.-S. Qin, C.T. Lollar, N. Huang, J. Li, Q. Wang, M. Wu, D. Yuan, M. Hong, H.-C. Zhou, Tuning the Ionicity of Stable Metal–Organic Frameworks through Ionic

- Linker Installation, *J. Am. Chem. Soc.* 141 (2019) 3129–3136, <https://doi.org/10.1021/jacs.8b12530>.
- [58] Y. Isaka, Y. Kondo, Y. Kuwahara, K. Mori, H. Yamashita, Incorporation of a Ru Complex into an Amine-Functionalized Metal–Organic Framework for Enhanced Activity In Photocatalytic Aerobic Benzyl Alcohol Oxidation, *Catal. Sci. Technol.* 9 (2019) 1511–1517, <https://doi.org/10.1039/C8CY02599A>.
- [59] Y.-X. Tan, S.-X. Lin, C. Liu, Y. Huang, M. Zhou, Q. Kang, D. Yuan, M. Hong, Boosting Photocatalytic Cross-Dehydrogenative Coupling Reaction by Incorporating [Ru^{II}(Bpy)₃] into a Radical Metal–Organic Framework, *Appl. Catal., B* 227 (2018) 425–432, <https://doi.org/https://doi.org/10.1016/j.apcatb.2018.01.048>.
- [60] C. Wang, Z. Xie, K.E. deKrafft, W. Lin, Doping Metal–Organic Frameworks for Water Oxidation, Carbon Dioxide Reduction, and Organic Photocatalysis, *J. Am. Chem. Soc.* 133 (2011) 13445–13454, <https://doi.org/10.1021/ja203564w>.
- [61] W.A. Maza, A.J. Morris, Photophysical Characterization of a Ruthenium(II) Tris(2,2'-bipyridine)-Doped Zirconium UiO-67 Metal–Organic Framework, *J. Phys. Chem. C* 118 (2014) 8803–8817, <https://doi.org/10.1021/jp501140r>.
- [62] A. Santiago-Portillo, H.G. Baldoví, E. Carbonell, S. Navalón, M. Álvaro, H. García, B. Ferrer, Ruthenium(II) Tris(2,2'-bipyridyl) Complex Incorporated in UiO-67 as Photoredox Catalyst, *J. Phys. Chem. C* 122 (2018) 29190–29199, <https://doi.org/10.1021/acs.jpcc.8b07204>.
- [63] X. Yu, S.M. Cohen, Photocatalytic Metal–Organic Frameworks for the Aerobic Oxidation of Arylboronic Acids, *Chem. Commun.* 51 (2015) 9880–9883, <https://doi.org/10.1039/C5CC01697E>.
- [64] Y.-Y. Zhu, G. Lan, Y. Fan, S.S. Veroneau, Y. Song, D. Micheroni, W. Lin, Merging Photoredox and Organometallic Catalysts in a Metal–Organic Framework Significantly Boosts Photocatalytic Activities, *Angew. Chem. Int. Ed.* 57 (2018) 14090–14094, <https://doi.org/10.1002/anie.201809493>.
- [65] H. Yang, H. Fei, A Generic and Facile Strategy to Fabricate Metal–Organic Framework Films on TiO₂ Substrates for Photocatalysis, *Dalton Trans.* 46 (2017) 2751–2755, <https://doi.org/10.1039/C7DT00082K>.
- [66] X. Yu, S.M. Cohen, Photocatalytic Metal–Organic Frameworks for Selective 2,2,2-Trifluoroethylation of Styrenes, *J. Am. Chem. Soc.* 138 (2016) 12320–12323, <https://doi.org/10.1021/jacs.6b06859>.
- [67] Y. Quan, G. Lan, Y. Fan, W. Shi, E. You, W. Lin, Metal–Organic Layers for Synergistic Lewis Acid and Photoredox Catalysis, *J. Am. Chem. Soc.* 142 (2020) 1746–1751, <https://doi.org/10.1021/jacs.9b12593>.
- [68] R. Xu, T. Drake, G. Lan, W. Lin, Metal–Organic Layers Catalyze Photoreactions without Pore Size and Diffusion Limitations, *Chem. Eur. J.* 24 (2018) 15772–15776, <https://doi.org/10.1002/chem.201803635>.
- [69] X.-H. Li, L.Z. Wu, L.P. Zhang, C.-H. Tung, C.-M. Che, Luminescence and Photocatalytic Properties of a Platinum(II)–Quaterpyridine Complex Incorporated in Nafion Membrane, *Chem. Commun.* (2001) 2280–2281, <https://doi.org/10.1039/B105601H>.
- [70] D. Zhang, L.-Z. Wu, Q.-Z. Yang, X.-H. Li, L.-P. Zhang, C.-H. Tung, Versatile Photosensitization System for ¹O₂-Mediated Oxidation of Alkenes Based on Nafion-Supported Platinum(II) Terpyridyl Acetylde Complex, *Org. Lett.* 5 (2003) 3221–3224, <https://doi.org/10.1021/ol035012e>.
- [71] J.-M. Zen, S.-L. Liou, A.S. Kumar, M.-S. Hsia, An Efficient and Selective Photocatalytic System for the Oxidation of Sulfides to Sulfoxides, *Angew. Chem. Int. Ed.* 42 (2003) 577–579, <https://doi.org/10.1002/anie.200390166>.

- [72] G. Zhang, I.Y. Song, T. Park, W. Choi, Recyclable and Stable Ruthenium Catalyst for Free Radical Polymerization at Ambient Temperature Initiated by Visible Light Photocatalysis, *Green. Chem.* 14 (2012) 618–621, <https://doi.org/10.1039/C2GC16409D>.
- [73] L. Li, C. Cui, W. Su, Y. Wang, R. Wang, Hollow Click-Based Porous Organic Polymers for Heterogenization of $[\text{Ru}(\text{Bpy})_3]^{2+}$ through Electrostatic Interactions, *Nano Res.* 9 (2016) 779–786, <https://doi.org/10.1007/s12274-015-0957-x>.
- [74] W.-J. Yoo, S. Kobayashi, Efficient Visible Light-Mediated Cross-Dehydrogenative Coupling Reactions of Tertiary Amines Catalyzed by a Polymer-Immobilized Iridium-Based Photocatalyst, *Green. Chem.* 16 (2014) 2438–2442, <https://doi.org/10.1039/C4GC00058G>.
- [75] J. Ma, F. Strieth-Kalthoff, T. Dalton, M. Freitag, J.L. Schwarz, K. Bergander, C. Daniliuc, F. Glorius, Direct Dearomatization of Pyridines via an Energy-Transfer-Catalyzed Intramolecular [4+2] Cycloaddition, *Chem* 5 (2019) 2854–2864, <https://doi.org/10.1016/j.chempr.2019.10.016>.
- [76] J.-L. Wang, C. Wang, K.E. deKrafft, W. Lin, Cross-Linked Polymers with Exceptionally High $\text{Ru}(\text{Bipy})_3^{2+}$ Loadings for Efficient Heterogeneous Photocatalysis, *ACS Catal.* 2 (2012) 417–424, <https://doi.org/10.1021/cs300027n>.
- [77] L. Pan, M.-Y. Xu, L.-J. Feng, Q. Chen, Y.-J. He, B.-H. Han, Conjugated Microporous Polycarbazole Containing Tris(2-Phenylpyridine)Iridium(III) Complexes: Phosphorescence, Porosity, and Heterogeneous Organic Photocatalysis, *Polym. Chem.* 7 (2016) 2299–2307, <https://doi.org/10.1039/C5PY01955A>.
- [78] H.-P. Liang, Q. Chen, B.-H. Han, Cationic Polycarbazole Networks as Visible-Light Heterogeneous Photocatalysts for Oxidative Organic Transformations, *ACS Catal.* 8 (2018) 5313–5322, <https://doi.org/10.1021/acscatal.7b04494>.
- [79] C. Wang, Z. Xie, K.E. deKrafft, W. Lin, Light-Harvesting Cross-Linked Polymers for Efficient Heterogeneous Photocatalysis, *ACS Appl. Mater. Interfaces* 4 (2012) 2288–2294, <https://doi.org/10.1021/am3003445>.
- [80] Z.-Y. Xu, Y. Luo, D.-W. Zhang, H. Wang, X.-W. Sun, Z.-T. Li, Iridium Complex-Linked Porous Organic Polymers for Recyclable, Broad-Scope Photocatalysis of Organic Transformations, *Green. Chem.* 22 (2020) 136–143, <https://doi.org/10.1039/C9GC03688A>.
- [81] Y. Luo, Z.-Y. Xu, H. Wang, X.-W. Sun, Z.-T. Li, D.-W. Zhang, Porous $\text{Ru}(\text{bpy})_3^{2+}$ -Linked Polymers for Recyclable Photocatalysis of Enantioselective Alkylation of Aldehydes, *ACS Macro Lett.* 9 (2020) 90–95, <https://doi.org/10.1021/acsmacrolett.9b00872>.
- [82] Z. Xie, C. Wang, K.E. deKrafft, W. Lin, Highly Stable and Porous Cross-Linked Polymers for Efficient Photocatalysis, *J. Am. Chem. Soc.*, 133 (2011) 2056–2059, <https://doi.org/10.1021/ja109166b>.
- [83] C.-A. Wang, Y.-F. Han, K. Nie, Y.-W. Li, Porous Organic Frameworks With Mesopores and $[\text{Ru}(\text{Bpy})_3]^{2+}$ Ligand Built-In as a Highly Efficient Visible-Light Heterogeneous Photocatalyst, *Mater. Chem. Front.* 3 (2019) 1909–1917, <https://doi.org/10.1039/C9QM00316A>.
- [84] F. Peng, P. Zhi, H. Ji, H. Zhao, F.-Y. Kong, X.-Z. Liang, Y.-M. Shen, Visible Light Mediated Cyclization of Tertiary Anilines with Maleimides Using a Supported Iridium Complex Catalyst, *RSC Adv.* 7 (2017) 19948–19953, <https://doi.org/10.1039/C7RA01045A>.
- [85] P. Zhi, Z.-W. Xi, D.-Y. Wang, W. Wang, X.-Z. Liang, F.-F. Tao, R.-P. Shen, Y.-M. Shen, Vilsmeier–Haack Reagent Mediated Synthetic Transformations with an Immobilized Iridium Complex Photoredox Catalyst, *New J. Chem.* 43 (2019) 709–717, <https://doi.org/10.1039/C8NJ05288C>.
- [86] C. Monterde, R. Navarro, M. Iglesias, F. Sánchez, Fluorine-Phenanthroimidazole Porous Organic Polymer: Efficient Microwave Synthesis and Photocatalytic Activity, *ACS Appl. Mater. Interfaces* 11 (2019) 3459–3465, <https://doi.org/10.1021/acsmi.8b18053>.

- [87] M. Liras, M. Pintado-Sierra, M. Iglesias, F. Sánchez, A Deprotection Strategy of a BODIPY Conjugated Porous Polymer to Obtain a Heterogeneous (Dipyrrin)(bipyridine)ruthenium(II) Visible Light Photocatalyst, *J. Mater. Chem. A* 4 (2016) 17274–17278, <https://doi.org/10.1039/C6TA07696C>.
- [88] Y. Huang, X.R. Zhang, S. Ye, J.L. Li, X. Li, T. Cai, Robust Hollow Nanocomposites With Ruthenium–Bipyridine Complexes for Heterogeneous Catalysis of Logic-Controlled RAFT Polymerization, *Nanoscale* 11 (2019) 13502–13510, <https://doi.org/10.1039/C9NR04664J>.
- [89] Y.-P. Wu, B. Yang, J. Tian, S.-B. Yu, H. Wang, D.-W. Zhang, Y. Liu, Z.-T. Li, Postmodification of a Supramolecular Organic Framework: Visible-Light-Induced Recyclable Heterogeneous Photocatalysis for the Reduction of Azides to Amines, *Chem. Commun.* 53 (2017) 13367–13370, <https://doi.org/10.1039/C7CC08824H>.
- [90] Y.-P. Wu, M. Yan, h.-Z. ZGao, J.-L. Hou, H. Wang, D.-W. Zhang, J. Zhang, Z.-T. Li, Ruthenium(II)-Cored Supramolecular Organic Framework-Mediated Recyclable Visible Light Photoreduction of Azides to Amines and Cascade Formation of Lactams, *Chin. Chem. Lett.* 30 (2019) 1383–1386, <https://doi.org/10.1016/j.ccllet.2019.03.056>.
- [91] X. Wang, S. Blechert, M. Antonietti, Polymeric Graphitic Carbon Nitride for Heterogeneous Photocatalysis, *ACS Catal.* 2 (2012) 1596–1606, <https://doi.org/10.1021/cs300240x>.
- [92] J. Zhu, P. Xiao, H. Li, S.A.C. Carabineiro, Graphitic Carbon Nitride: Synthesis, Properties, and Applications in Catalysis, *ACS Appl. Mater. Interfaces* 6 (2014) 16449–16465, <https://doi.org/10.1021/am502925j>.
- [93] Handbook of Graphene Set: Composites, E. Celasco, A.N. Chaika, T. Stauber, M. Zhang, C. Ozkan, C. Ozkan, U. Ozkan, B. Palys, S.W. Harun (Eds.), Vol. IV, Scrivener Publishing LLC Wiley Online Books, 2019, [DOI:10.1002/9781119468455](https://doi.org/10.1002/9781119468455).
- [94] Zeolites And Catalysis: Synthesis, Reactions and Applications, J. Čejka, A. Corma, S. Zones (Eds.), Wiley-VCH Weinheim, 2010, [DOI:10.1002/9783527630295](https://doi.org/10.1002/9783527630295).
- [95] W. Stöber, A. Fink, Controlled Growth of Monodisperse Silica Spheres in the Micron Size Range, *J. Colloid Interface Sci.* 26 (1968) 62–69 [https://doi.org/10.1016/0021-9797\(68\)90272-5](https://doi.org/10.1016/0021-9797(68)90272-5).
- [96] K.L. Materna, R.H. Crabtree, G.W. Brudvig, Anchoring Groups for Photocatalytic Water Oxidation on Metal Oxide Surfaces, *Chem. Soc. Rev.* 46 (2017) 6099–6110, <https://doi.org/10.1039/C7CS00314E>.
- [97] P. Péchy, F.P. Rotzinger, M.K. Nazeeruddin, O. Kohle, S.M. Zakeeruddin, R. Humphry-Baker, M. Grätzel, Preparation of Phosphonated Polypyridyl Ligands to Anchor Transition-Metal Complexes on Oxide Surfaces: Application for the Conversion of Light to Electricity with Nanocrystalline TiO₂ Films, *J. Chem. Soc., Chem. Commun.* (1995) 65–66, <https://doi.org/10.1039/C39950000065>.
- [98] M.K. Nazeeruddin, A. Kay, I. Rodicio, R. Humphry-Baker, E. Mueller, P. Liska, N. Vlachopoulos, M. Graetzel, Conversion of Light to Electricity by *cis*-X₂bis(2,2'-bipyridyl-4,4'-dicarboxylate)ruthenium(II) Charge-Transfer Sensitizers (X = Cl⁻, Br⁻, I⁻, CN⁻, and SCN⁻) on Nanocrystalline Titanium Dioxide Electrodes, *J. Am. Chem. Soc.* 115 (1993) 6382–6390, <https://doi.org/10.1021/ja00067a063>.
- [99] J.-L. Wang, C. Wang, W. Lin, Metal–Organic Frameworks for Light Harvesting and Photocatalysis, *ACS Catal.* 2 (2012) 2630–2640, <https://doi.org/10.1021/cs3005874>.
- [100] L. Zeng, X. Guo, C. He, C. Duan, Metal–Organic Frameworks: Versatile Materials for Heterogeneous Photocatalysis, *ACS Catal.* 6 (2016) 7935–7947, <https://doi.org/10.1021/acscatal.6b02228>.
- [101] Y. Horiuchi, T. Toyao, M. Matsuoka, Metal–Organic Framework (MOF) and Porous Coordination Polymer (PCP)-Based Photocatalysts, in: H. Yamashita, H. Li (Eds.),

- Nanostructured Photocatalysts. *Nanostructure Science and Technology.*, Springer, Cham, 2016, pp. 479–489.
- [102] D. Sun, Z. Li Metal–Organic Frameworks (MOFs) for Photocatalytic Organic Transformations., in: H. Yamashita, H. Li (Eds.), *Nanostructured Photocatalysts. Nanostructure Science and Technology.*, Springer, Cham, 2016, pp. 523–535.
- [103] X. Yu, L. Wang, S.M. Cohen, Photocatalytic Metal–Organic Frameworks for Organic transformations, *CrystEngComm* 19 (2017) 4126–4136, <https://doi.org/10.1039/C7CE00398F>.
- [104] A. Dhakshinamoorthy, Z. Li, H. Garcia, Catalysis and Photocatalysis by Metal Organic frameworks, *Chem. Soc. Rev.* 47 (2018) 8134–8172, <https://doi.org/10.1039/C8CS00256H>.
- [105] T. Zhang, Y. Jin, Y. Shi, M. Li, J. Li, C. Duan, Modulating photoelectronic performance of metal–organic frameworks for premium photocatalysis, *Coord. Chem. Rev.* 380 (2019) 201–229, <https://doi.org/https://doi.org/10.1016/j.ccr.2018.10.001>.
- [106] A. Dhakshinamoorthy, A.M. Asiri, H. Garcia, 2D Metal–Organic Frameworks as Multifunctional Materials in Heterogeneous Catalysis and Electro/Photocatalysis, *Adv. Mater.* 31 (2019) 1900617, <https://doi.org/10.1002/adma.201900617>.
- [107] M. Dan-Hardi, C. Serre, T. Frot, L. Rozes, G. Maurin, C. Sanchez, G. Férey, A New Photoactive Crystalline Highly Porous Titanium(IV) Dicarboxylate, *J. Am. Chem. Soc.* 131 (2009) 10857–10859, <https://doi.org/10.1021/ja903726m>.
- [108] M. Sohail, Y.-N. Yun, E. Lee, S.K. Kim, K. Cho, J.-N. Kim, T.W. Kim, J.-H. Moon, H. Kim, Synthesis of Highly Crystalline NH₂-MIL-125 (Ti) with S-Shaped Water Isotherms for Adsorption Heat Transformation, *Cryst. Growth Des.* 17 (2017) 1208–1213, <https://doi.org/10.1021/acs.cgd.6b01597>.
- [109] W.A. Maza, A.J. Haring, S.R. Ahrenholtz, C.C. Epley, S.Y. Lin, A.J. Morris, Ruthenium(II)-Polypyridyl Zirconium(IV) Metal–Organic Frameworks as a New Class of Sensitized Solar Cells, *Chem. Sci.* 7 (2016) 719–727, <https://doi.org/10.1039/C5SC01565K>.
- [110] R. Dai, F. Peng, P. Ji, K. Lu, C. Wang, J. Sun, W. Lin, Electron Crystallography Reveals Atomic Structures of Metal–Organic Nanoplates with M₁₂(μ³-O)₈(μ³-OH)₈(μ²-OH)₆ (M = Zr, Hf) Secondary Building Units, *Inorg. Chem.* 56 (2017) 8128–8134, <https://doi.org/10.1021/acs.inorgchem.7b00845>.
- [111] K. Lu, C. He, N. Guo, C. Chan, K. Ni, G. Lan, H. Tang, C. Pelizzari, Y.-X. Fu, M.T. Spiotto, R.R. Weichselbaum, W. Lin, Low-Dose X-Ray Radiotherapy–Radiodynamic Therapy via Nanoscale Metal–Organic Frameworks Enhances Checkpoint Blockade Immunotherapy, *Nat. Biomed. Eng.* 2 (2018) 600–610, <https://doi.org/10.1038/s41551-018-0203-4>.
- [112] C.-H. Tung, J.-Q. Guan, Remarkable Product Selectivity in Photosensitized Oxidation of Alkenes within Nafion Membranes, *J. Am. Chem. Soc.* 120 (1998) 11874–11879, <https://doi.org/10.1021/ja9816842>.
- [113] J. Tian, Z.-Y. Xu, D.-W. Zhang, H. Wang, S.-H. Xie, D.-W. Xu, Y.-H. Ren, H. Wang, Y. Liu, Z.-T. Li, Supramolecular Metal–Organic Frameworks That Display High Homogeneous and Heterogeneous Photocatalytic Activity for H₂ Production, *Nat. Commun.* 7 (2016) 11580, <https://doi.org/10.1038/ncomms11580>.
- [114] D.C. Fabry, M.A. Ronge, M. Rueping, Immobilization and Continuous Recycling of Photoredox Catalysts in Ionic Liquids for Applications in Batch Reactions and Flow Systems: Catalytic Alkene Isomerization by Using Visible Light, *Chem. Eur. J.* 21 (2015) 5350–5354, <https://doi.org/10.1002/chem.201406653>.
- [115] N. Priyadarshani, Y. Liang, J. Suriboot, H.S. Bazzi, D.E. Bergbreiter, Recoverable Reusable Polyisobutylene (PIB)-Bound Ruthenium Bipyridine (Ru(PIB-bpy)₃Cl₂)

- Photoredox Polymerization Catalysts, *ACS Macro Lett.* 2 (2013) 571–574, <https://doi.org/10.1021/mz400232y>.
- [116] Y. Liang, D.E. Bergbreiter, Visible Light Mediated Photoredox Reactions Catalyzed by Recyclable PIB-Bound Ruthenium Photoredox Catalysts, *Catal. Sci. Technol.* 6 (2016) 215–221, <https://doi.org/10.1039/C5CY01287B>.
- [117] D. Rackl, P. Kreitmeier, O. Reiser, Synthesis of a Polyisobutylene-Tagged *Fac*-Ir(Ppy)₃ Complex and its Application as Recyclable Visible-Light Photocatalyst in a Continuous Flow Process, *Green. Chem.* 18 (2016) 214–219, <https://doi.org/10.1039/C5GC01792K>.
- [118] X. Zhang, Y. Li, X. Hao, K. Jin, R. Zhang, C. Duan, Recyclable Alkylated Ru(bpy)₃²⁺ Complex as a Visible-Light Photoredox Catalyst for Perfluoroalkylation, *Tetrahedron* 74 (2018) 1742–1748, <https://doi.org/https://doi.org/10.1016/j.tet.2018.01.040>.
- [119] X. Zhang, Y. Li, X. Hao, K. Jin, R. Zhang, C. Duan, Recyclable Alkylated *Fac*-Ir(Ppy)₃ Complex as a Visible-Light Photoredox Catalyst for the Synthesis of 3-Trifluoromethylated and 3-Difluoroacetylated Coumarins, *Tetrahedron* 74 (2018) 7358–7363, <https://doi.org/https://doi.org/10.1016/j.tet.2018.10.075>.
- [120] M.-j. Bu, C. Cai, F. Gallou, B.H. Lipshutz, Pqs-Enabled Visible-Light Iridium Photoredox Catalysis in Water at Room Temperature, *Green. Chem.* 20 (2018) 1233–1237, <https://doi.org/10.1039/C7GC03866F>.
- [121] J. Guerra, D. Cantillo, C.O. Kappe, Visible-Light Photoredox Catalysis Using a Macromolecular Ruthenium Complex: Reactivity and Recovery by Size-Exclusion Nanofiltration in Continuous Flow, *Catal. Sci. Technol.* 6 (2016) 4695–4699, <https://doi.org/10.1039/C6CY00070C>.
- [122] G. Centi, S. Perathoner, Selective Oxidation—Industrial, in: *Encyclopedia of Catalysis*, Wiley Online Books, 2002, <https://doi.org/doi:10.1002/0471227617.eoc188>.
- [123] F.H. Wolfgang, K. Felix, Oxidation Reactions in the Synthesis of Fine and Intermediate Chemicals Using Environmentally Benign Oxidants and the Right Reactor System, *Pure Appl. Chem.* 72 (2000) 1273–1287, <https://doi.org/https://doi.org/10.1351/pac200072071273>.
- [124] A. Maldotti, A. Molinari, R. Amadelli, Photocatalysis with Organized Systems for the Oxofunctionalization of Hydrocarbons by O₂, *Chem. Rev.* 102 (2002) 3811–3836, <https://doi.org/10.1021/cr010364p>.
- [125] R.A. Sheldon, E Factors, *Green Chemistry and Catalysis: an Odyssey*, *Chem. Commun.* (2008) 3352–3365, <https://doi.org/10.1039/B803584A>.
- [126] J. Chen, J. Cen, X. Xu, X. Li, The Application of Heterogeneous Visible Light Photocatalysts in Organic Synthesis, *Catal. Sci. Technol.* 6 (2016) 349–362, <https://doi.org/10.1039/C5CY01289A>.
- [127] V. Blanchard, Z. Asbai, K. Cottet, G. Boissonnat, M. Port, Z. Amara, Continuous Flow Photo-oxidations Using Supported Photocatalysts on Silica, *Org. Process Res. Dev.* 24 (2020), 822–826, <https://doi.org/10.1021/acs.oprd.9b00420>.
- [128] T. Punniyamurthy, S. Velusamy, J. Iqbal, Recent Advances in Transition Metal Catalyzed Oxidation of Organic Substrates with Molecular Oxygen, *Chem. Rev.* 105 (2005) 2329–2364, <https://doi.org/10.1021/cr050523v>.
- [129] T. Mori, M. Takamoto, Y. Tate, J. Shinkuma, T. Wada, Y. Inoue, Photoinduced Electron Transfer Oxidation of *α*-Methylstyrene with Molecular Oxygen Sensitized by Dimethoxybenzenes: A Non-Singlet-Oxygen Mechanism, *Tetrahedron Lett.* 42 (2001) 2505–2508, [https://doi.org/https://doi.org/10.1016/S0040-4039\(01\)00213-1](https://doi.org/https://doi.org/10.1016/S0040-4039(01)00213-1).
- [130] A.A. Ghogare, A. Greer, Using Singlet Oxygen to Synthesize Natural Products and Drugs, *Chem. Rev.* 116 (2016) 9994–10034, <https://doi.org/10.1021/acs.chemrev.5b00726>.

- [131] J. Turconi, F. Grioret, R. Guevel, G. Oddon, R. Villa, A. Geatti, M. Hvala, K. Rossen, R. Göller, A. Burgard, Semisynthetic Artemisinin, the Chemical Path to Industrial Production, *Org. Process Res. Dev.* 18 (2014) 417–422, <https://doi.org/10.1021/op4003196>.
- [132] J. Li, W. Ma, Y. Huang, M. Cheng, J. Zhao, J.C. Yu, A Highly Selective Photooxidation Approach Using O₂ in Water Catalyzed by Iron(II) Bipyridine Complex Supported on NaY Zeolite, *Chem. Commun.* (2003) 2214–215, <https://doi.org/10.1039/B306538C>.
- [133] K. Gollnick, A. Griesbeck, Singlet Oxygen Photooxygenation of Furans: Isolation and Reactions of (4+2)-Cycloaddition Products (Unsaturated sec.-Ozonides), *Tetrahedron* 41 (1985) 2057–2068, [https://doi.org/https://doi.org/10.1016/S0040-4020\(01\)96576-7](https://doi.org/https://doi.org/10.1016/S0040-4020(01)96576-7).
- [134] Y. Su, L. Zhang, N. Jiao, Utilization of Natural Sunlight and Air in the Aerobic Oxidation of Benzyl Halides, *Org. Lett.* 13 (2011) 2168–2171, <https://doi.org/10.1021/ol2002013>.
- [135] C. Li, M.Z. Hoffman, Oxidation of Phenol by Singlet Oxygen Photosensitized by the Tris(2,2'-bipyridine)ruthenium(II) Ion, *J. Phys. Chem. A* 104 (2000) 5998–6002, <https://doi.org/10.1021/jp9937104>.
- [136] K. Singh, S.J. Staig, J.D. Weaver, Facile Synthesis of Z-Alkenes via Uphill Catalysis, *J. Am. Chem. Soc.* 136 (2014) 5275–5278, <https://doi.org/10.1021/ja5019749>.
- [137] C.-Y. Xiong, H.-J. Wang, W.-B. Liang, Y.-L. Yuan, R. Yuan, Y.-Q. Chai, Luminescence-Functionalized Metal–Organic Frameworks Based on a Ruthenium(II) Complex: A Signal Amplification Strategy for Electrogenenerated Chemiluminescence Immunosensors, *Chem. Eur. J.* 21 (2015) 9825–9832, <https://doi.org/10.1002/chem.201500909>.
- [138] Y. Zhang, Q. Xiao, Y. Bao, Y. Zhang, S. Bottle, S. Sarina, B. Zhaorigetu, H. Zhu, Direct Photocatalytic Conversion of Aldehydes to Esters Using Supported Gold Nanoparticles under Visible Light Irradiation at Room Temperature, *J. Phys. Chem. C* 118 (2014) 19062–19069, <https://doi.org/10.1021/jp505552v>.
- [139] *The Chemistry of Phenols*, Z. Rappoport (Ed.), Wiley-VCH, Weinheim, Germany, 2003.
- [140] I.G.T.M. Penders, Z. Amara, R. Horvath, K. Rossen, M. Poliakoff, M.W. George, Photocatalytic Hydroxylation of Arylboronic Acids Using Continuous Flow Reactors, *RSC Adv.* 5 (2015) 6501–6504, <https://doi.org/10.1039/C4RA15588B>.
- [141] J. Börgel, L. Tanwar, F. Berger, T. Ritter, Late-Stage Aromatic C–H Oxygenation, *J. Am. Chem. Soc.* 140 (2018) 16026–16031, <https://doi.org/10.1021/jacs.8b09208>.
- [142] L. Hao, G. Ding, D.A. Deming, Q. Zhang, Recent Advances in Green Synthesis of Functionalized Phenols from Aromatic Boronic Compounds, *Eur. J. Org. Chem.* 2019 (2019) 7307–7321, <https://doi.org/10.1002/ejoc.201901303>.
- [143] E. Baciocchi, T.D. Giacco, F. Elisei, M.F. Gerini, M. Guerra, A. Lapi, P. Liberali, Electron Transfer and Singlet Oxygen Mechanisms in the Photooxygenation of Dibutyl Sulfide and Thioanisole in MeCN Sensitized by *N*-Methylquinolinium Tetrafluoroborate and 9,10-Dicyanoanthracene. The Probable Involvement of a Thiadioxirane Intermediate in Electron Transfer Photooxygenations, *J. Am. Chem. Soc.* 125 (2003) 16444–16454, <https://doi.org/10.1021/ja037591o>.
- [144] S.M. Bonesi, I. Manet, M. Freccero, M. Fagnoni, A. Albini, Photosensitized Oxidation of Sulfides: Discriminating between the Singlet-Oxygen Mechanism and Electron Transfer Involving Superoxide Anion or Molecular Oxygen, *Chem. Eur. J.* 12 (2006) 4844–4857, <https://doi.org/https://doi.org/10.1002/chem.200501144>.
- [145] F. Su, S.C. Mathew, L. Möhlmann, M. Antonietti, X. Wang, S. Blechert, Aerobic Oxidative Coupling of Amines by Carbon Nitride Photocatalysis with Visible Light, *Angew. Chem. Int. Ed.* 50 (2011) 657–660, <https://doi.org/10.1002/anie.201004365>.
- [146] H. Bartling, A. Eisenhofer, B. König, R.M. Gschwind, The Photocatalyzed Aza-Henry Reaction of *N*-Aryltetrahydroisoquinolines: Comprehensive Mechanism, H[•]- versus H⁺-Abstraction, and Background Reactions, *J. Am. Chem. Soc.* 138 (2016) 11860–11871, <https://doi.org/10.1021/jacs.6b06658>.

- [147] A.G. Condie, J.C. González-Gómez, C.R.J. Stephenson, Visible-Light Photoredox Catalysis: Aza-Henry Reactions via C–H Functionalization, *J. Am. Chem. Soc.* 132 (2010) 1464–1465, <https://doi.org/10.1021/ja909145y>.
- [148] M. Rueping, S. Zhu, R.M. Koenigs, Photoredox Catalyzed C–P Bond Forming Reactions – Visible Light Mediated Oxidative Phosphonylations of Amines, *Chem. Commun.* 47 (2011) 8679–8681, <https://doi.org/10.1039/C1CC12907D>.
- [149] Y.M. Shafran, V.A. Bakulev, V.S. Mokrushin, Synthesis and Properties of α -Aminonitriles, *Russ. Chem. Rev.* 58 (1989) 148–162.
- [150] M. Rueping, S. Zhu, R.M. Koenigs, Visible-Light Photoredox Catalyzed Oxidative Strecker Reaction, *Chem. Commun.*, 47 (2011) 12709–12711, <https://doi.org/10.1039/C1CC15643H>.
- [151] S.F. Martin, Recent Applications of Imines as Key Intermediates in the Synthesis of Alkaloids and Novel Nitrogen Heterocycles, *Pure Appl. Chem.* 81 (2009) 195–204, <https://doi.org/10.1351/PAC-CON-08-07-03>.
- [152] J. Iwanejko, E. Wojaczyńska, Cyclic Imines – Preparation and Application in Synthesis, *Org. Biomol. Chem.* 16 (2018) 7296–7314, <https://doi.org/10.1039/C8OB01874J>.
- [153] X. Lang, H. Ji, C. Chen, W. Ma, J. Zhao, Selective Formation of Imines by Aerobic Photocatalytic Oxidation of Amines on TiO₂, *Angew. Chem. Int. Ed.* 50 (2011) 3934–3937, <https://doi.org/10.1002/anie.201007056>.
- [154] M. Rueping, C. Vila, A. Szadkowska, R.M. Koenigs, J. Fronert, Photoredox Catalysis as an Efficient Tool for the Aerobic Oxidation of Amines and Alcohols: Bioinspired Demethylations and Condensations, *ACS Catal.* 2 (2012) 2810–2815, <https://doi.org/10.1021/cs300604k>.
- [155] X.-W. Lan, N.-X. Wang, Y. Xing, Recent Advances in Radical Difunctionalization of Simple Alkenes, *Eur. J. Org. Chem.* 2017 (2017) 5821–5851, <https://doi.org/10.1002/ejoc.201700678>.
- [156] L. Li, M. Huang, C. Liu, J.-C. Xiao, Q.-Y. Chen, Y. Guo, Z.-G. Zhao, 2,2,2-Trifluoroethylation of Styrenes with Concomitant Introduction of a Hydroxyl Group from Molecular Oxygen by Photoredox Catalysis Activated by Visible Light, *Org. Lett.* 17 (2015) 4714–4717, <https://doi.org/10.1021/acs.orglett.5b02177>.
- [157] M.R. Heinrich, Intermolecular Olefin Functionalisation Involving Aryl Radicals Generated from Arenediazonium Salts, *Chem. Eur. J.* 15 (2009) 820–833, <https://doi.org/10.1002/chem.200801306>.
- [158] D. Prasad Hari, T. Hering, B. König, The Photoredox-Catalyzed Meerwein Addition Reaction: Intermolecular Amino-Arylation of Alkenes, *Angew. Chem. Int. Ed.* 53 (2014) 725–728, <https://doi.org/10.1002/anie.201307051>.
- [159] S.K. Pagire, S. Paria, O. Reiser, Synthesis of β -Hydroxysulfones from Sulfonyl Chlorides and Alkenes Utilizing Visible Light Photocatalytic Sequences, *Org. Lett.* 18 (2016) 2106–2109, <https://doi.org/10.1021/acs.orglett.6b00734>.
- [160] Z. Li, H. Song, R. Guo, M. Zuo, C. Hou, S. Sun, X. He, Z. Sun, W. Chu, Visible-Light-Induced Condensation Cyclization to Synthesize Benzimidazoles Using Fluorescein as a Photocatalyst, *Green. Chem.* 21 (2019) 3602–3605, <https://doi.org/10.1039/C9GC01359H>.
- [161] X. Ju, D. Li, W. Li, W. Yu, F. Bian, The Reaction of Tertiary Anilines with Maleimides under Visible Light Redox Catalysis, *Adv. Synth. Catal.* 354 (2012) 3561–3567, <https://doi.org/10.1002/adsc.201200608>.
- [162] H. Sun, C. Yang, F. Gao, Z. Li, W. Xia, Oxidative C–C Bond Cleavage of Aldehydes via Visible-Light Photoredox Catalysis, *Org. Lett.* 15 (2013) 624–627, <https://doi.org/10.1021/ol303437m>.

- [163] R. Ananthkrishnan, S. Gazi, $[\text{Ru}(\text{bpy})_3]^{2+}$ Aided Photocatalytic Synthesis of 2-Arylpyridines via Hantzsch Reaction Under Visible Irradiation And Oxygen Atmosphere, *Catal. Sci. Technol.* 2 (2012) 1463–1471, <https://doi.org/10.1039/C2CY20050C>.
- [164] T. Koike, M. Akita, Photoinduced Oxyamination of Enamines and Aldehydes with TEMPO Catalyzed by $[\text{Ru}(\text{bpy})_3]^{2+}$, *Chem. Lett.* 38 (2009) 166–167, <https://doi.org/10.1246/cl.2009.166>.
- [165] W. Su, Y. Weng, L. Jiang, Y. Yang, L. Zhao, Z. Chen, Z. Li, J. Li, Recent Progress in the Use of Vilsmeier-Type Reagents, *Org. Prep. Proced. Int.* 42 (2010) 503–555, <https://doi.org/10.1080/00304948.2010.513911>.
- [166] A.P. Rajput, P.D. Girase, Review article on Vilsmeier Haack reaction, *Int. Pharm., Chem. Biol. Sci.* 3 (2013) 25–43.
- [167] C. Dai, J.M.R. Narayanam, C.R.J. Stephenson, Visible-Light-Mediated Conversion of Alcohols to Halides, *Nat. Chem.* 3 (2011) 140–145, <https://doi.org/10.1038/nchem.949>.
- [168] M.D. Konieczynska, C. Dai, C.R.J. Stephenson, Synthesis of Symmetric Anhydrides Using Visible Light-Mediated Photoredox Catalysis, *Org. Biomol. Chem.* 10 (2012) 4509–4511, <https://doi.org/10.1039/C2OB25463H>.
- [169] A.K. Yadav, V.P. Srivastava, L.D.S. Yadav, Visible-Light-Mediated Efficient Conversion of Aldoximes and Primary Amides into Nitriles, *RSC Adv.* 4 (2014) 4181–4186, <https://doi.org/10.1039/C3RA46553E>.
- [170] T. Koike, M. Akita, Visible-Light-Induced Photoredox Catalysis: an Easy Access to Green Radical Chemistry, *Synlett* 24 (2013) 2492–2505, <https://doi.org/10.1055/s-0033-1339874>.
- [171] A.K. Yadav, V.P. Srivastava, L.D.S. Yadav, An Easy Access to Unsymmetrical Ureas: A Photocatalytic Approach to the Lossen Rearrangement, *RSC Adv.* 4 (2014) 24498–24503, <https://doi.org/10.1039/C4RA03805C>.
- [172] B.P. Fors, C.J. Hawker, Control of a Living Radical Polymerization of Methacrylates by Light, *Angew. Chem. Int. Ed.* 51 (2012) 8850–8853, <https://doi.org/10.1002/anie.201203639>.
- [173] G. Zhang, I.Y. Song, K.H. Ahn, T. Park, W. Choi, Free Radical Polymerization Initiated and Controlled by Visible Light Photocatalysis at Ambient Temperature, *Macromolecules* 44 (2011) 7594–7599, <https://doi.org/10.1021/ma201546c>.
- [174] J. Shao, Y. Huang, Q. Fan, Visible Light Initiating Systems for Photopolymerization: Status, Development and Challenges, *Polym. Chem.* 5 (2014) 4195–4210, <https://doi.org/10.1039/C4PY00072B>.
- [175] J. Xu, S. Shanmugam, C. Fu, K.-F. Aguey-Zinsou, C. Boyer, Selective Photoactivation: From a Single Unit Monomer Insertion Reaction to Controlled Polymer Architectures, *J. Am. Chem. Soc.* 138 (2016) 3094–3106, <https://doi.org/10.1021/jacs.5b12408>.
- [176] Y.-N. Zhou, J.-J. Li, Y.-Y. Wu, Z.-H. Luo, Role of External Field in Polymerization: Mechanism and Kinetics, *Chem. Rev.* 120 (2020) 2950–3048, <https://doi.org/10.1021/acs.chemrev.9b00744>.
- [177] M.A. Ischay, M.E. Anzovino, J. Du, T.P. Yoon, Efficient Visible Light Photocatalysis of [2+2] Enone Cycloadditions, *J. Am. Chem. Soc.* 130 (2008) 12886–12887, <https://doi.org/10.1021/ja805387f>.
- [178] J. Du, T.P. Yoon, Crossed Intermolecular [2+2] Cycloadditions of Acyclic Enones via Visible Light Photocatalysis, *J. Am. Chem. Soc.* 131 (2009) 14604–14605, <https://doi.org/10.1021/ja903732v>.
- [179] J. Du, L.R. Espelt, I.A. Guzei, T.P. Yoon, Photocatalytic Reductive Cyclizations of Enones: Divergent Reactivity of Photogenerated Radical and Radical Anion Intermediates, *Chem. Sci.*, 2 (2011) 2115–2119, <https://doi.org/10.1039/C1SC00357G>.

- [180] A. Böhm, T. Bach, Radical Reactions Induced by Visible Light in Dichloromethane Solutions of Hünig's Base: Synthetic Applications and Mechanistic Observations, *Chem. Eur. J.* 22 (2016) 15921–15928, <https://doi.org/10.1002/chem.201603303>.
- [181] D.A. Nicewicz, D.W.C. MacMillan, Merging Photoredox Catalysis With Organocatalysis: the Direct Asymmetric Alkylation of Aldehydes, *Science* 322 (2008) 77–80, <https://doi.org/10.1126/science.1161976>.
- [182] J.M.R. Narayanam, J.W. Tucker, C.R.J. Stephenson, Electron-Transfer Photoredox Catalysis: Development of a Tin-Free Reductive Dehalogenation Reaction, *J. Am. Chem. Soc.* 131 (2009) 8756–8757, <https://doi.org/10.1021/ja9033582>.
- [183] R.S. Andrews, J.J. Becker, M.R. Gagné, Intermolecular Addition of Glycosyl Halides to Alkenes Mediated by Visible Light, *Angew. Chem. Int. Ed.* 49 (2010) 7274–7276, <https://doi.org/10.1002/anie.201004311>.
- [184] M.-j. Bu, G.-p. Lu, C. Cai, Visible-Light Photoredox Catalyzed Cyclization of Aryl Alkynoates for the Synthesis of Trifluoromethylated Coumarins, *Catal. Commun.* 114 (2018) 70–74, <https://doi.org/https://doi.org/10.1016/j.catcom.2018.06.009>.
- [185] X. Yu, P. Dai, Y.-C. Zhu, P. Teng, W.-H. Zhang, C. Deng, Metal-free, Visible-Light-Mediated Direct Csp²-H Radical Mono- and Bis-trifluoromethylation of Coumarins and Bioactivity Evaluation, *ChemCatChem* 10 (2018) 5115–5118, <https://doi.org/https://doi.org/10.1002/cctc.201801332>.
- [186] E.F.V. Scriven, K. Turnbull, Azides: Their Preparation and Synthetic Uses, *Chem. Rev.* 88 (1988) 297–368, <https://doi.org/10.1021/cr00084a001>.
- [187] Y. Chen, A.S. Kamlet, J.B. Steinman, D.R. Liu, A Biomolecule-Compatible Visible-Light-Induced Azide Reduction from a DNA-Encoded Reaction-Discovery System, *Nat. Chem.* 3 (2011) 146–153, <https://doi.org/10.1038/nchem.932>.
- [188] T. Hirao, J. Shiori, N. Okahata, Ruthenium–Bipyridine Complex-Catalyzed Photo-Induced Reduction of Nitrobenzenes with Hydrazine, *Bull. Chem. Soc. Jpn.* 77 (2004) 1763–1764, <https://doi.org/10.1246/bcsj.77.1763>.
- [189] J.D. Nguyen, E.M. D'Amato, J.M.R. Narayanam, C.R.J. Stephenson, Engaging Unactivated Alkyl, Alkenyl and Aryl Iodides in Visible-Light-Mediated Free Radical Reactions, *Nat. Chem.*, 4 (2012) 854–859, <https://doi.org/10.1038/nchem.1452>.
- [190] A.R.P. Henderson, J.R. Kosowan, T.E. Wood, The Truce-Smiles Rearrangement and Related Reactions: a Review, *Can. J. Chem.* 95 (2017) 483–504, <https://doi.org/10.1139/cjc-2016-0594>.
- [191] D. Alpers, K.P. Cole, C.R.J. Stephenson, Visible Light Mediated Aryl Migration by Homolytic C–N Cleavage of Aryl Amines, *Angew. Chem. Int. Ed.* 57 (2018) 12167–12170, <https://doi.org/10.1002/anie.201806659>.
- [192] J.D. Nguyen, B.S. Matsuura, C.R.J. Stephenson, A Photochemical Strategy for Lignin Degradation at Room Temperature, *J. Am. Chem. Soc.* 136 (2014) 1218–1221, <https://doi.org/10.1021/ja4113462>.
- [193] A. Rahimi, A. Azarpira, H. Kim, J. Ralph, S.S. Stahl, Chemoselective Metal-Free Aerobic Alcohol Oxidation in Lignin, *J. Am. Chem. Soc.* 135 (2013) 6415–6418, <https://doi.org/10.1021/ja401793n>.
- [194] I.P. Beletskaya, V.P. Ananikov, Transition-Metal-Catalyzed C–S, C–Se, and C–Te Bond Formation via Cross-Coupling and Atom-Economic Addition Reactions, *Chem. Rev.* 111 (2011) 1596–1636, <https://doi.org/10.1021/cr100347k>.
- [195] M.S. Oderinde, M. Frenette, D.W. Robbins, B. Aquila, J.W. Johannes, Photoredox Mediated Nickel Catalyzed Cross-Coupling of Thiols With Aryl and Heteroaryl Iodides via Thiyl Radicals, *J. Am. Chem. Soc.* 138 (2016) 1760–1763, <https://doi.org/10.1021/jacs.5b11244>.
- [196] M. Jouffroy, C.B. Kelly, G.A. Molander, Thioetherification via Photoredox/Nickel Dual Catalysis, *Org. Lett.* 18 (2016) 876–879, <https://doi.org/10.1021/acs.orglett.6b00208>.

- [197] K.L. Skubi, T.R. Blum, T.P. Yoon, Dual Catalysis Strategies in Photochemical Synthesis, *Chem. Rev.* 116 (2016) 10035–10074, <https://doi.org/10.1021/acs.chemrev.6b00018>.
- [198] X. Lang, J. Zhao, X. Chen, Cooperative Photoredox Catalysis, *Chem. Soc. Rev.* 45 (2016) 3026–3038, <https://doi.org/10.1039/C5CS00659G>.
- [199] S. Mukherjee, J.W. Yang, S. Hoffmann, B. List, Asymmetric Enamine Catalysis, *Chem. Rev.* 107 (2007) 5471–5569, <https://doi.org/10.1021/cr0684016>.
- [200] R. Ciriminna, R. Delisi, Y.-J. Xu, M. Pagliaro, Toward the Waste-Free Synthesis of Fine Chemicals with Visible Light, *Org. Process Res. Dev.* 20 (2016) 403–408, <https://doi.org/10.1021/acs.oprd.5b00424>.
- [201] Y. Su, N.J.W. Straathof, V. Hessel, T. Noël, Photochemical Transformations Accelerated in Continuous-Flow Reactors: Basic Concepts and Applications, *Chem. Eur. J.* 20 (2014) 10562–10589, <https://doi.org/10.1002/chem.201400283>.
- [202] D. Cambié, C. Bottecchia, N.J.W. Straathof, V. Hessel, T. Noël, Applications of Continuous-Flow Photochemistry in Organic Synthesis, Material Science, and Water Treatment, *Chem. Rev.* 116 (2016) 10276–10341, <https://doi.org/10.1021/acs.chemrev.5b00707>.
- [203] J. Griffiths, K.-Y. Chu, C. Hawkins, Photosensitised Oxidation of 1-Naphthols, *J. Chem. Soc., Chem. Commun.* (1976) 676–677, <https://doi.org/10.1039/C39760000676>.
- [204] S.-y. Takizawa, R. Aboshi, S. Murata, Photooxidation of 1,5-Dihydroxynaphthalene with Iridium Complexes as Singlet Oxygen Sensitizers, *Photochem. Photobiol. Sci.* 10 (2011) 895–903, <https://doi.org/10.1039/C0PP00265H>.
- [205] Z. Amara, J.F.B. Bellamy, R. Horvath, S.J. Miller, A. Beeby, A. Burgard, K. Rossen, M. Poliakoff, M.W. George, Applying Green Chemistry to the Photochemical Route to Artemisinin, *Nat. Chem.* 7 (2015) 489–495, <https://doi.org/10.1038/nchem.2261>.
- [206] F.R. Bou-Hamdan, P.H. Seeberger, Visible-Light-Mediated Photochemistry: Accelerating Ru(Bpy)₃²⁺-Catalyzed Reactions in Continuous Flow, *Chem. Sci.* 3 (2012) 1612–1616, <https://doi.org/10.1039/C2SC01016J>.
- [207] M. Antonietti, A. Savateev, Splitting Water by Electrochemistry and Artificial Photosynthesis: Excellent Science but a Nightmare of Translation? *Chem. Rec.* 18 (2018) 969–972, <https://doi.org/10.1002/tcr.201700062>.
- [208] C. Di Giovanni, A. Poater, J. Benet-Buchholz, L. Cavallo, M. Solà, A. Llobet, Dinuclear Ru–Aqua Complexes for Selective Epoxidation Catalysis Based on Supramolecular Substrate Orientation Effects, *Chem. Eur. J.* 20 (2014) 3898–3902, <https://doi.org/10.1002/chem.201304699>.